Winter 2022

# DEVELOPMENT OF A CONTINUOUS-TENSION-COMPRESSION MACHINE FOR TESTING THIN SHEET METAL

Jacqueline McNally
*University of New Hampshire, Durham*

# DEVELOPMENT OF A CONTINUOUS-TENSION-COMPRESSION MACHINE FOR TESTING THIN SHEET METAL

BY

Jacqueline K. McNally

B.S. Mechanical Engineering, University of New Hampshire, 2017

THESIS

Submitted to the University of New Hampshire

in Partial Fulfillment of

the Requirements for the Degree of

Master of Science

in

Mechanical Engineering

December, 2022

*This page intentionally left blank*

This thesis has been examined and approved in partial fulfillment of the requirements for the degree of Master of Science in Mechanical Engineering by:

Thesis/Dissertation Director, Yannis Korkolis,

Associate Professor of Mechanical Engineering, Ohio State University

Jinjin Ha,

Assistant Professor of Mechanical Engineering

May-Win Thein,

Professor of Mechanical and Ocean Engineering

On September 28, 2022

Original approval signatures are on file with the University of New Hampshire Graduate School.

*This page intentionally left blank*

# TABLE OF CONTENTS

TABLE OF CONTENTS ..... i

LIST OF TABLES ..... iv

LIST OF FIGURES ..... v

ABSTRACT ..... xi

CHAPTER 1 Introduction ..... 1

1.1. Motivation ..... 1

1.2. Previous Research ..... 5

1.2.1. Pure Compression with Anti-buckling Device ..... 7

1.2.2. Laminated Specimens ..... 8

1.2.3. Addition of Rigid Support Plates ..... 8

1.2.4. Constant-Force Support Systems ..... 10

1.3. Outline of Thesis ..... 12

CHAPTER 2 Machine Design ..... 15

2.1. Introduction ..... 15

2.2. Overall Concept ..... 15

2.3. Detailed Design ..... 19

2.3.1. Comb-die Assembly ..... 21

2.3.2. Blank-Holding Assembly ..... 24

2.3.3. Horizontal Load Train Assembly ..... 29

2.4. Analysis of Critical Components ..... 30

2.4.1. Major Bolts and Pins ..... 30

2.4.2. Ball Housing Assembly ..... 33

2.4.3. Compliance of Moving Comb-die Assembly ..... 35

CHAPTER 3 Data Acquisition and Controller ..... 39
3.1. Introduction ..... 39
3.2. System Architecture ..... 39
3.2.1. Large Strain Readings ..... 42
3.3. Controller Program ..... 45
3.3.1. Controller Overview ..... 45
3.3.2. Layout of User Intereface ..... 47
3.3.3. Test Options ..... 53
3.3.4. Calibration of Machine ..... 57
CHAPTER 4 Machine Verification ..... 59
4.1. Introduction ..... 59
4.2. Initial Checks ..... 59
4.2.1. Stability of Signals with Time ..... 59
4.2.2. Comparison of Input vs. Output ..... 61
4.3. Verifying Results from the CTC Machine ..... 65
4.3.1. Comparing CTC Machine to MTS ..... 66
4.3.2. Comparing Two CTC Machines ..... 68
4.3.3. Specimen Geometry Verification ..... 73
4.4. Friction Compensation ..... 76
4.4.1. Friction Internal to the Machine ..... 76
4.4.2. Friction Between Specimen and Machine ..... 79
4.4.3. Friction Compensation during CTC Testing ..... 82
CHAPTER 5 Material Behavior under Cyclic Loading ..... 87
5.1. Introduction ..... 87

5.2. Aluminum Alloy AA6022-T43 ..... 87
5.3. Extra Deep Drawing Quality (EDDQ) Steel ..... 89
5.4. JAC-270D Steel ..... 94
5.5. DP590 and DP1180 Dual-Phase Steels ..... 96
5.5.1. DP1180 steel ..... 97
5.5.2. DP590 vs. DP1180 Steels ..... 103
5.6. DP980 Dual-Phase Steel ..... 104
CHAPTER 6 Material Modeling Under Cyclic Loading ..... 111
6.1. Introduction ..... 111
6.2. Theoretical Underpinnings ..... 111
6.2.1. Categorization and Behavior of Chaboche Parameters ..... 114
6.2.2. Algorithm to Automatically Determine Chaboche Parameters ..... 116
6.3. Parameter identification for DP980 steel ..... 124
CHAPTER 7 Conclusions and Future Work ..... 131
7.1. Introduction ..... 131
7.2. Conclusions ..... 131
7.3. Hardware Improvements ..... 133
7.4. Machine Control Program Improvements ..... 134
REFERENCES ..... 135
APPENDIX A Additional Calculation Information ..... 139
APPENDIX B Reference Documents ..... 145
APPENDIX C Additional Material Results ..... 147

# LIST OF TABLES

Table 2.1: Characteristics of Machine ..... 19

Table 2.2: List of off-the-shelf components ..... 20

Table 2.3: List of Critical Bolt and Pin Calculations ..... 32

Table 2.4: Ball Housing Assembly Calculation Results ..... 33

Table 3.1: Electrical information for instrumentation ..... 40

Table 3.2: Excel driven test parameters ..... 55

Table 4.1: Parameters used in cyclic test comparison of CTC to TUAT machine ..... 69

Table 5.1 : Parameters for AA6022-T43 5x cycle test ..... 88

Table 5.2 : Parameters for EDDQ 4.5x cycle test ..... 90

Table 5.3 : Parameters for JAC-270D 1x cycle test ..... 95

Table 5.4 : Parameters for DP1180 cyclic tests on CTC ..... 99

Table 5.5 : Parameters for DP980 tests on CTC ..... 104

Table 5.6 : R-value of DP980 of pure tension and prestrain then tension ..... 108

Table 6.1 : Initial parameters for Chaboche optimization algorithm. ..... 118

Table 6.2 : Remaining Parameters for DP980 Chaboche optimization algorithm ..... 124

Table 6.3 : Chaboche terms determined for DP980 [17] ..... 125

# LIST OF FIGURES

Figure 1.1: Frame of a Volvo XC90 [1]. ..... 2

Figure 1.2: CAFE requirements for vehicle fuel efficiency [2]. ..... 2

Figure 1.3: Difference in elastic recovery (springback) between various materials [3]. ... 3

Figure 1.4: Springback of two materials using the same die [4]. Even though both steels have the same yield stress (350 MPa), the DP steel has a UTS of 600 MPa, vs. 450 MPa for the HSLA, and thus exhibits higher springback. ..... 4

Figure 1.5: Simulation versus experiment of sheet metal forming [5]. ..... 5

Figure 1.6: Types of deformation and buckling when testing thin sheet metal [6]. ..... 6

Figure 1.7: Early examples of supporting specimens during compression [7]. ..... 7

Figure 1.8: Representation of testing a thick specimen created from several thin specimens [8]. ..... 8

Figure 1.9: Device using several support plates to prevent buckling [9]. ..... 9

Figure 1.10: Device using a diagonally-split support plate to prevent buckling [10]. ..... 9

Figure 1.11: Device using a hydraulic fixture for support against buckling [6]. ..... 10

Figure 1.12: (a) Anti-buckling device using intermeshing pairs of upper and lower dies. (b) Testing machine using this idea [11]. ..... 11

Figure 1.13: CTC machine described in this thesis. ..... 12

Figure 2.1: Isometric view of the CTC machine and layout of its key features. ..... 17

Figure 2.2: Specimen aligned in machine, which is shown in the open condition. ..... 18

Figure 2.3: Specimen drawing. ..... 18

Figure 2.4: Comb-die assembly – side view. ..... 21

Figure 2.5: Top view of the lower dies, showing the comb teeth meshing and the location of the strain-gauge. ..... 22

Figure 2.6: Quick-release grip assembly sequence. ..... 24

Figure 2.7: Dimensions of vertical heights of assembly. 25
Figure 2.8: Ball housing assembly. 26
Figure 2.9: Air Controller Assembly. 27
Figure 2.10: Compressed air circuit, identifying the major components. 28
Figure 2.11: Horizontal load train. 29
Figure 2.12: Outline of bolt and pin calculation areas. 31
Figure 2.13: Expanded bolt and pin areas. 32
Figure 2.14: Ball Housing Assembly compression FEA. 34
Figure 2.15: Ball Housing Assembly tension FEA. 35
Figure 2.16: Photograph of comb-die assembly, to explain its compliance. 36
Figure 3.1: Location of electrical box in relation to CTC Machine. 41
Figure 3.2: Electrical Architecture of CTC Machine. 42
Figure 3.3: Offset Circuit Boards. 43
Figure 3.4: Snapshot of strain conversion calculator. 45
Figure 3.5: Front panel of program. 48
Figure 3.6: Region 1 – Top banner of front panel. 49
Figure 3.7: Region 1 – Control region of program. 49
Figure 3.8: Settings tab in control region. 50
Figure 3.9: Region 3 – Hydraulic pump monitoring. 51
Figure 3.10: Region 4 – Specimen Variables and Extra settings. 52
Figure 3.11: Region 5 – Graphing region. 53
Figure 3.12: Tension or compression test panel. 54
Figure 3.13: Standard min-max strain cyclic test. 56
Figure 3.14: Variable min-max strain cyclic test to failure. 56

Figure 3.15: Input voltage command vs. output velocity for the proportional valve used in the CTC machine..... 58

Figure 4.1: Stability of force signal at rest, with hydraulics on or off. ..... 60

Figure 4.2: Stability of displacement signal at rest, with hydraulics on or off. ..... 61

Figure 4.3: Displacement vs. time of saw-tooth verification test at a velocity of 0.06 mm/s, showing input (dashed red line) and output (solid blue line). ..... 62

Figure 4.4: Overlapped multiple cycles (between 220 and 750 seconds, see Figure 4.3) from displacement vs. time of saw-tooth verification test at a velocity of .06 mm/s. Also included is the input signal. The machine is repeatably following the input command very well. ..... 63

Figure 4.5: One displacement vs. time cycle from each saw-tooth test. ..... 64

Figure 4.6: Force vs. displacement of saw-tooth verification tests at different velocities ranging from .03 - .18 mm/s (same colors as in previous figure). ..... 65

Figure 4.7: Comparing MTS to CTC machine with AA6022-T43 ASTM E8 uniaxial tension specimens..... 67

Figure 4.8: Comparing MTS to CTC machine with EDDQ steel ASTM E8 uniaxial tension specimens..... 68

Figure 4.9: Tension-compression-tension test between CTC machine to TUAT machine. The data shown are raw, i.e., not compensated for friction. ..... 70

Figure 4.10: Compression-tension-compression test between CTC machine to TUAT machine. The data shown are raw, i.e., not compensated for friction..... 70

Figure 4.11: Magnified view of Figure 4.9, showing slight buckling in both CTC machines. The data shown are raw, i.e., not compensated for friction. ..... 71

Figure 4.12: Comparing results from the two CTC machines in elastic-plastic transition regions. The data shown are raw, i.e., not compensated for friction. ..... 72

Figure 4.13: Comparing ASTM E8 to CTC specimens on CTC machine using AA6022-T43. ..... 74

Figure 4.14: Zoomed-in portion of comparing ASTM E8 to CTC specimens on CTC machine, using AA6022-T43. ..... 74

Figure 4.15: Comparing ASTM E8 to CTC specimens on CTC machine using EDDQ steel..... 75

Figure 4.16: Machine friction at various blank-holding pressures over the majority of the stroke. ..... 78

Figure 4.17: Modified CTC specimen for friction testing. ..... 80

Figure 4.18: Decrease in friction by using Teflon sheets and lubrication at 12.5 kN (2,810 lbs) blank-holding force. ..... 81

Figure 4.19: Reduction of specimen gouging by use of Teflon sheets. ..... 82

Figure 4.20: Strain from friction tests performed. ..... 83

Figure 4.21: Comparing blank-holding tensile test to conventional tensile test. ..... 84

Figure 5.1: AA6022-T43 5x cycle test. ..... 89

Figure 5.2 EDDQ 4.5x cycle test. ..... 91

Figure 5.3 Comparison of starting in tension vs. compression ..... 91

Figure 5.4 Comparison of reversal stress when starting in tension vs. compression of EDDQ 4.5x cycle test. ..... 92

Figure 5.5 Engineering stress vs. strain comparison of EDDQ and AA6022-T43 in early cycles. ..... 93

Figure 5.6 True stress vs. plastic strain comparison of EDDQ and AA6022-T43 in early cycles. ..... 94

Figure 5.7 JAC-270D tension-compression-tension test. ..... 95

Figure 5.8 Comparison of starting in tension vs. compression of ..... 96

Figure 5.9 Reduced width specimen for DP1180 testing. ..... 97

Figure 5.10 Comparing an in-plane buckled specimen (lower) vs. barreled (upper). .... 98

Figure 5.11 DP1180 full cycle test. Note that 3 tests are overlapped here. ..... 100

Figure 5.12 DP1180 multiple cycle test. ..... 100

Figure 5.13 DP1180 multiple cycle test negative strain side. ..... 101

Figure 5.14 DP1180 pure compression versus tension test, indicating significant tension-compression asymmetry. ..... 102

Figure 5.15 DP590 vs. DP1180 pure tension and pure compression tests. ..... 103

Figure 5.16 Comparing pure compression of different orientations of DP980. ..... 105

Figure 5.17 Prestrain in compression then tension of DP980. Tests performed along the rolling and transverse directions. ..... 106

Figure 5.18 R-Value comparison between rolling and transverse direction of DP980 after prestrain. ..... 107

Figure 5.19 T-C-Tension to failure of DP980 at various prestrains. ..... 109

Figure 6.1 The cumulative action of each back-stress term on the agreement of the prediction with the experiment [20]. ..... 115

Figure 6.2 Flow chart for Chaboche algorithm for DP980. ..... 117

Figure 6.3 Agreement between prediction and experiment for the initial Chaboche values used in this work, for DP980 steel. Significant discrepancies after the first load reversal are seen. ..... 119

Figure 6.4 Fit of calculated curve after the plastic tangent modulus at large strains is matched to the experimental one. ..... 120

Figure 6.5 Fit of calculated curve with $S$ and $\alpha(1)$ determined. ..... 122

Figure 6.6 Fit of calculated curve with all terms determined. ..... 123

Figure 6.7 Fit of calibrated curves against DP980 TCTF experimental results. ..... 126

Figure 6.8 Prediction of the 0%-1.5%-0%-10% DP980 TCTF test using the manually-optimized material parameters. ..... 127

Figure 6.9 Prediction of the 0%-3%-0%-10% DP980 TCTF test using the manually-optimized material parameters. ..... 128

Figure 6.10 Prediction of the DP980 compression-to-tension-to-failure test using the manually-optimized material parameters..... 129

Figure 6.11 Prediction of the DP980 pure compression test using the manually-optimized material parameters. ..... 130

Figure A 1 Ball housing assembly tension FEA Mesh displayed with mesh details .... 139

Figure A 2 Ball housing assembly compression FEA Mesh displayed with mesh details 140

Figure A 3 Compliance of comb dies labeling major features ..... 141

Figure A 4 Compliance of comb dies calculations 1 ..... 142

Figure A 5 Compliance of comb dies calculations 2 ..... 143

Figure A 6 Compliance of comb dies calculations 3 ..... 144

Figure B 1 Hydraulic safety information..... 145

Figure B 2 Bosh Rexroth guide rail information ..... 146

Figure B 3 Tychoway information ..... 146

Figure C 1 EDDQ 5x cycle test starting in compression. ..... 147

Figure C 2 JAC-270D cycle test starting in compression. ..... 148

Figure C 3 DP1180 Load-unload test overlayed on tension test. ..... 149

Figure C 4 DP1180 Pure compression test. ..... 150

Figure C 5 DP590 Load-unload test overlayed on tension test. ..... 151

Figure C 6 DP590 1x cycle starting in tension. ..... 152

Figure C 7 DP590 Multiple cycle test. ..... 153

# ABSTRACT

DEVELOPMENT OF A CONTINUOUS-TENSION-COMPRESSION MACHINE

FOR TESTING THIN SHEET METAL

BY

Jacqueline K. McNally

This thesis details the design and manufacturing of a custom testing machine for thin sheet metal undergoing continuous tension-compression (CTC) loading. The CTC machine concept is based on using a set of intermeshing dies to continuously support the thin sheet specimen against buckling during the test. The upper set of dies are held in place by a pneumatic actuator of 25 kN capacity. The dies can move freely relative to one another, so that both tension and compression can be performed in the same setup. A hydraulic actuator of 50 kN capacity displaces one side of the intermeshed dies. The stroke of the actuator is 63.5 mm, and based on the geometry of the CTC machine and specimen selected, that results into 20% strain in compression and 75% in tension. Strain is measured on the specimen itself using high-elongation strain gages, capable of reaching up to 20-30%, depending on the material. However, based on the hardware currently used, only +/- 5% strain can be read; this is an issue that can be easily fixed with updates to measurement hardware.

Chapter 1, which is the introduction, includes the motivation behind this work, as well as other concepts that have been implemented to achieve similar results. Chapter 2 describes the mechanical design of the CTC machine. It includes details of the machine

design and functionality, and the strength calculations performed to verify its correct and safe operation. Chapter 3 details the custom data acquisition and control system that was developed. It includes details of the sensors and circuity used for the CTC machine. It also discusses the user interface of the control software, and the pre-programmed functionality of the CTC machine. Chapter 4 describes a full suite of verification tests that were performed on both the CTC machine and CTC specimen geometry, to ensure that the data acquired is accurate and reliable. After the verification testing, Chapter 5 describes a series of cyclic experiments performed on a variety of thin metallic sheets. The research chapters of the thesis are capped by Chapter 6, which discusses a non-linear kinematic hardening model of the Chaboche family, which can be used to replicate the results of the cyclic experiments. Finally, Chapter 7 provides a summary of this work, the main conclusions, as well as proposed future extensions and improvements of the CTC machine.

Returning to Chapter 4, the verification tests performed for the CTC machine itself involve tension tests on ASTM E8 specimens using both the present machine and a MTS Landmark 370 servohydraulic loading frame. The agreement is found to be excellent. The CTC specimen geometry is different from the standard ASTM E8 dogbone specimen one, to further prevent buckling during compression. It is confirmed though that the CTC specimen geometry provides identical results to the standard ASTM E8 during tension testing. In summary, the results listed in Chapter 4 show favorable agreement between the two machines, as well as the two specimen geometries.

The cyclic experiments discussed in Chapter 5 are performed on a variety of thin metallic sheets: aluminum alloy AA6022-T43 as well as EDDQ, JAC-270D, DP590,

DP980 and DP1180 steels. An example of a cyclic experiment is: straining a specimen in tension to +1% engineering strain, reverse loading to -1%, forward loading to +3%, etc. as in -3%, +5%, -5%, then back to 0%. Another experiment is cyclic loading between two equal and opposite strain values, e.g., +/- 2%, for N number of cycles. A noticeable trend with all the materials tested is the amount of tension/compression asymmetry, i.e., where the compressive flow stress is higher than the one in tension for pure compression or tension tests.

The Chaboche model in Chapter 6, is calibrated for DP980 steel. An automated parameter determination algorithm, implemented in Matlab, is also described. The code produced is meant to provide the user with an initial best fit to the experiment, so that the user can then improve the fit further as desired, e.g., by manual adjustments. It is expected that utilizing this model in numerical simulations of sheet metal forming processes that include unloading and/or cyclic loading can yield accurate predictions of the springback expected.

*This page intentionally left blank*

# CHAPTER 1
# INTRODUCTION

## 1.1. Motivation

The question that must be asked for any task is why is that task necessary. In this case, why was designing and building a custom material testing machine for continuous tension-compression of thin sheets necessary to do. The simple answer is that there is not a commercially available machine that can perform the testing desired, but this does not address the reason this testing needs to be performed in the first place. Ultimately the purpose of this task is to provide material forming characteristics of sheet metal to manufacturers so that improved designs can be produced where it would have been impossible otherwise. These improved designs can range from airplanes down to the vehicles we drive every day.

The industry that gains the greatest benefit from this research is the car industry because the majority of the frame (see Figure 1.1) and outer panels are made out of sheet metal. Since the car industry has been under pressure to increase fuel efficiency of their products, as seen in Figure 1.2, the fastest solution is to reduce the overall weight of the vehicle. By switching mild steel sheets with a lighter alloy that provides similar strengths, the vehicles will become lighter yet still exhibit the same safety criteria. Similarly, by swapping mild steel for higher-strength steels will permit down-gaging, i.e., use of thinner sheets.

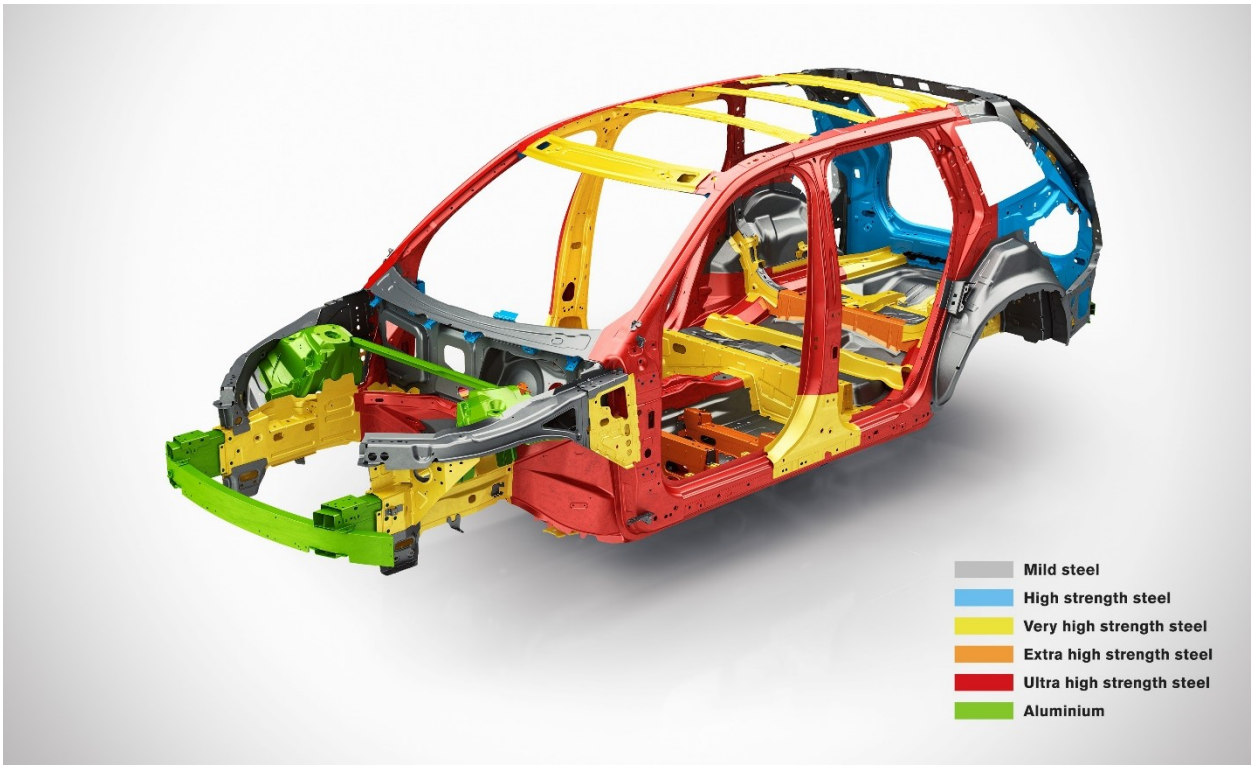


Figure 1.1: Frame of a Volvo XC90 [1].

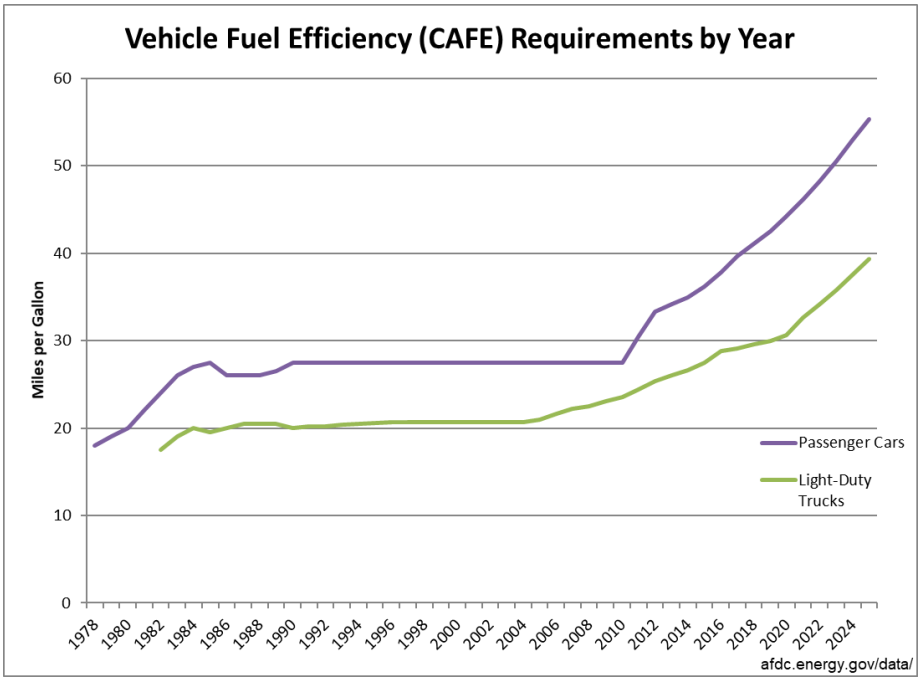


Figure 1.2: CAFE requirements for vehicle fuel efficiency [2].

The issue with simply switching materials is that the dies used to form the sheets are designed for the springback of the original material. This difference in springback can be seen in Figure 1.3 which show tension tests loaded to the same strain. Even though both materials are steel, the elastic recovery after unloading (i.e., springback) is still different between the two since the higher strength steel will have more recovery than the mild steel.

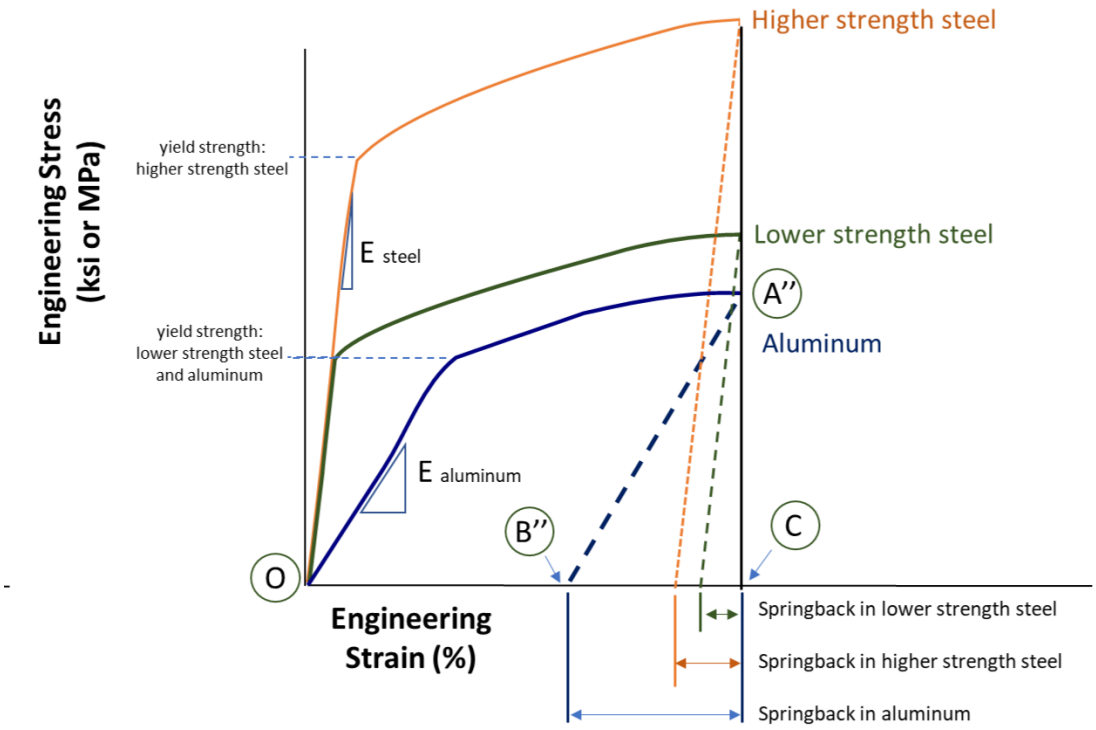


Figure 1.3: Difference in elastic recovery (springback) between various materials [3].

This difference in springback results in parts not meeting final dimensional requirements, as seen in Figure 1.4, when the dies are not adjusted for the new material. The process of re-making these dies is not only costly but also requires numerous

iterations to obtain the correct dimensional parts since most stampings that would be replaced are made in a progressive die that has multiple stages. These stages all tie into each other where a change in a previous stage could affect a later stage and cascade from there.


Figure 1.4: Springback of two materials using the same die [4]. Even though both steels have the same yield stress (350 MPa), the DP steel has a UTS of 600 MPa, vs. 450 MPa for the HSLA, and thus exhibits higher springback.

To reduce the cost of making dies, accurate simulations are needed. These simulations can use data produced from this machine to allow manufacturers to better predict what the dies need to look like. Sheet forming involves repeated loading and reverse loading, hence understanding the material behavior under tension-compression cycles is necessary. An example of how this simulation would look in comparison to actual results can be seen in Figure 1.5.

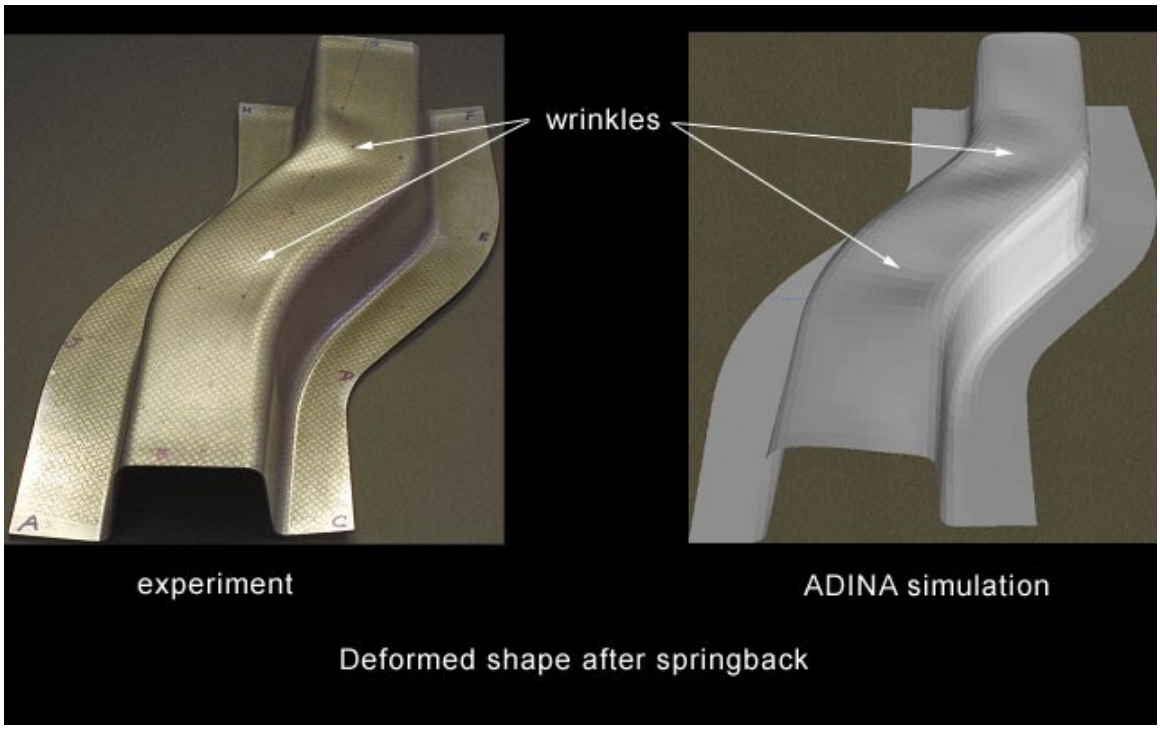


Figure 1.5: Simulation versus experiment of sheet metal forming [5].

## 1.2. Previous Research

Before diving into the machine that was designed, it's important to have an appreciation of the designs that came before. There have been numerous designs that have been made over the years to obtain the same data, with each design having a unique solution. These solutions will be discussed, starting with adapations onto existing equipment, to unique machines built. The last solution discussed will be the design produced by Professor Toshihiko Kuwabara from The University of Agriculture and Technology (TUAT). Ultimately the biggest challenge that the different solutions are looking to resolve is preventing the specimen from buckling as seen in Figure 1.6.

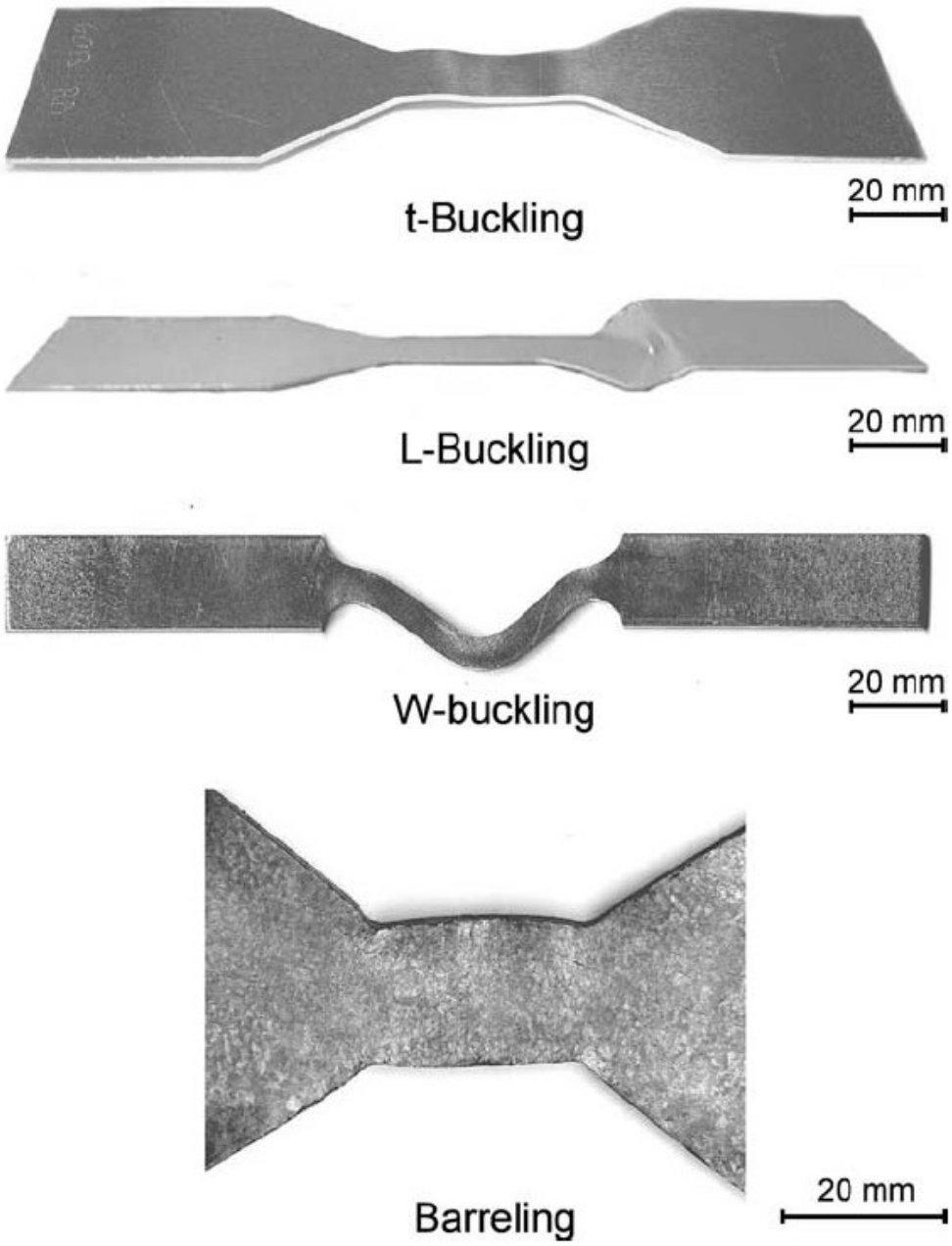


Figure 1.6: Types of deformation and buckling when testing thin sheet metal [6].

### 1.2.1. Pure Compression with Anti-buckling Device

Before diving into testing the cyclic behavior of thin sheet metal, the pure compression tests performed by the National Advisory Committee for Aeronautics (NACA) has some of the first examples of adding support to the specimen to prevent buckling during compression. Figure 1.7 shows an example of using a guide fixture to prevent buckling of thin sheet metal. The device was used to only look at pure compression tests and did not facilitate any provisions to switch to tension.

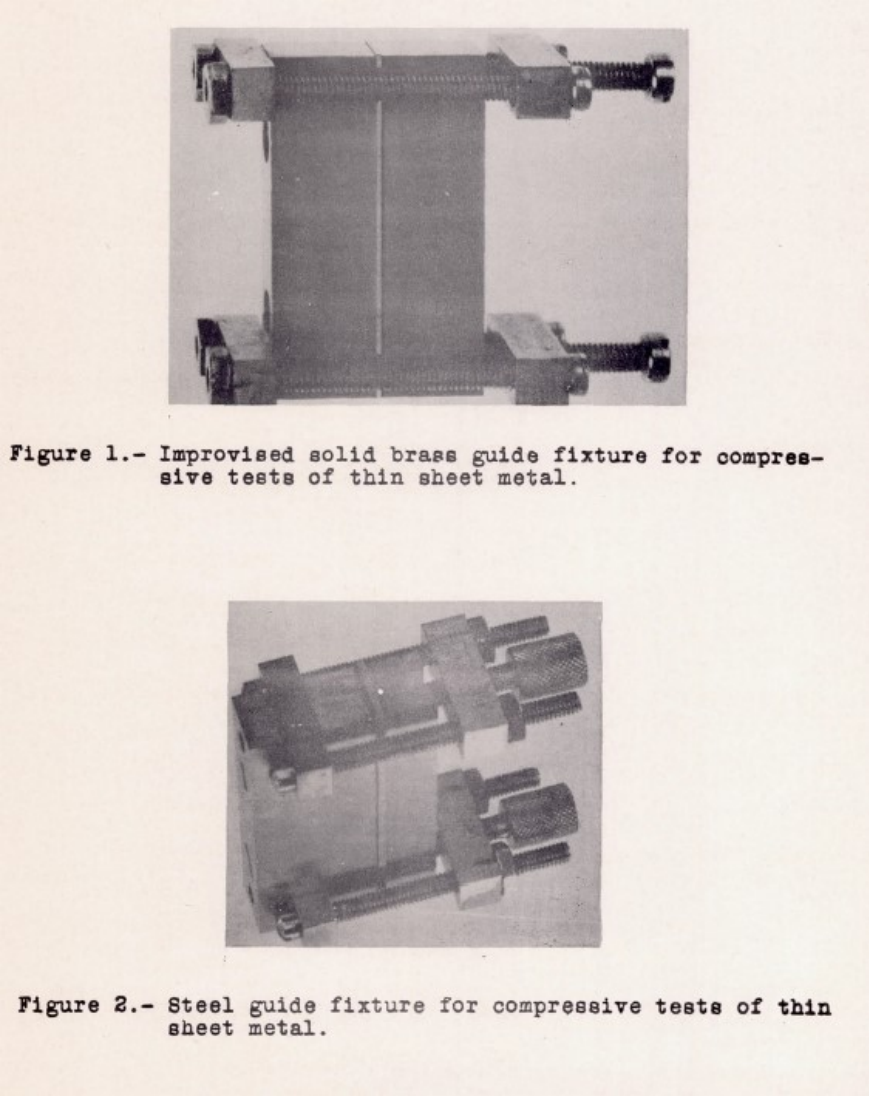

Figure 1.- Improvised solid brass guide fixture for compressive tests of thin sheet metal.

Figure 2.- Steel guide fixture for compressive tests of thin sheet metal.

Figure 1.7: Early examples of supporting specimens during compression [7].

### 1.2.2. Laminated Specimens

The first example that has been used to test the cyclic nature of thin sheet metal is to glue multiple pieces together to create a single thick specimen. This has been done by F. Yoshida [8] with the addition of an anti-buckling device, so that large strains could be reached reliably. This method produces reliable results with low influence from the anti-buckling device, but requires significantly more material to be used.

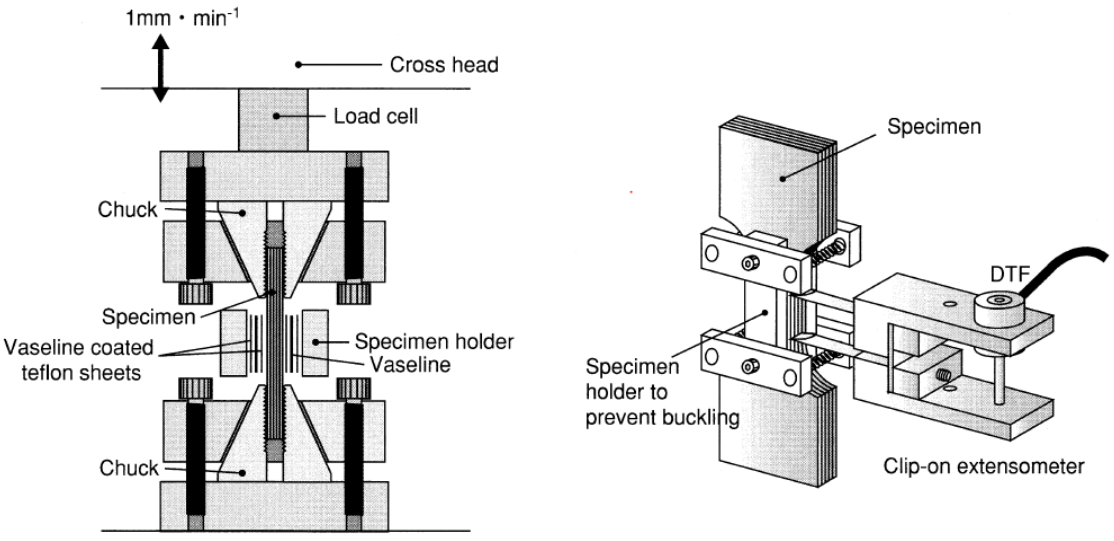


Fig. 4. Schematic illustrations of in-plane cyclic tension–compression tests of sheet metals.

Figure 1.8: Representation of testing a thick specimen created from several thin specimens [8].

### 1.2.3. Addition of Rigid Support Plates

Other solutions that have been produced add a support plate, similar to Figure 1.8 as seen in Figure 1.9 and Figure 1.10. The support plate achieves close to the same desired goal of preventing buckling but isn't able to maintain a consistent pressure. The inconsistent pressure can cause issues with the test data being skewed from tensile data, as well as do not provide sufficient support during large strains.

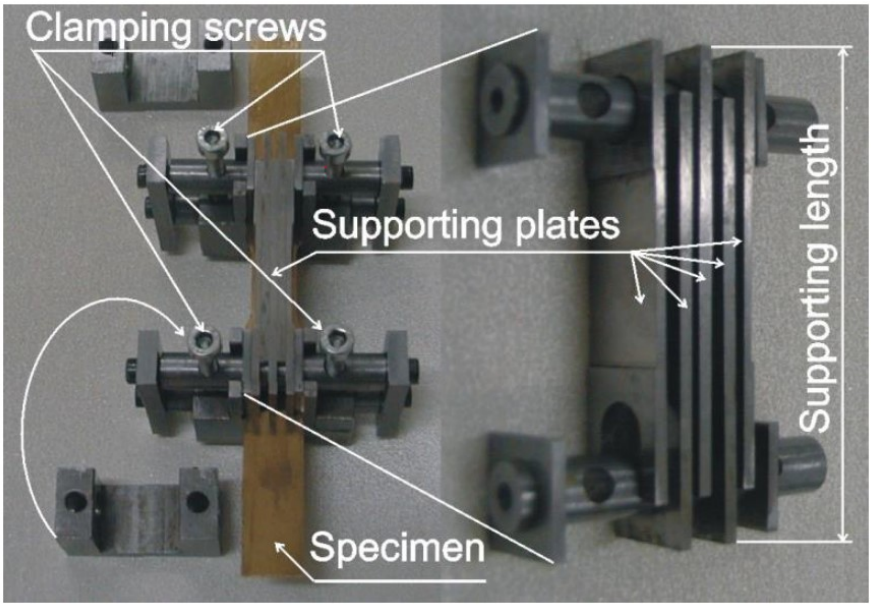


Figure 1.9: Device using several support plates to prevent buckling [9].

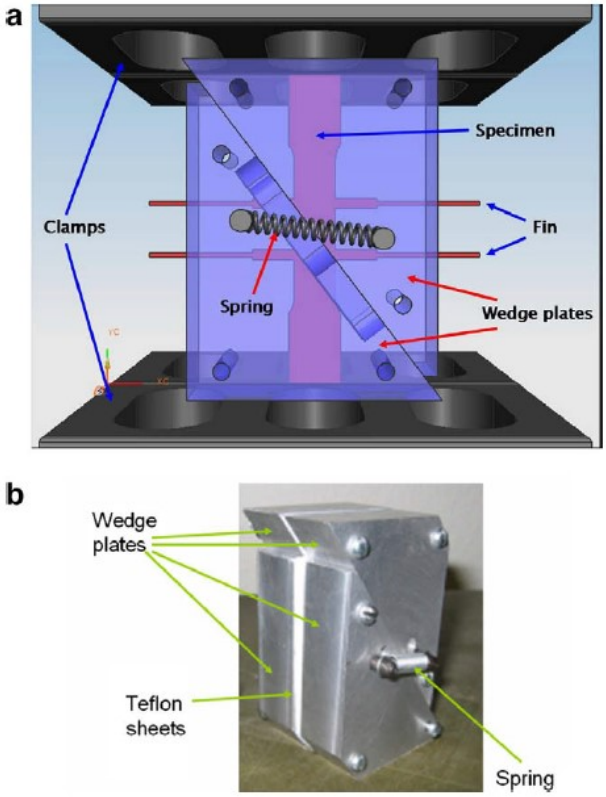


Figure 1.10: Device using a diagonally-split support plate to prevent buckling [10].

### 1.2.4. Constant-Force Support Systems

The last type of solution is using constant-force support by way of hydraulics or pneumatics. With the previous designs discussed, the holding force applied to the specimen will change as the specimen thickness changes. This change in the holding force can contaminate the test data, and make their interpretation dubious; whereas with a constant-force support system, the device will automatically compensate for the change in specimen thickness. The first example, shown in Figure 1.11, showcases the addition of a hydraulic fixture to an existing tensile testing machine. While this achieves the constant support that is needed, there are a few issues that can still occur. The biggest area of concern with this design is buckling of the specimen that emerges from the supported region during compression.

Figure 1.11: Device using a hydraulic fixture for support against buckling [6].

The other solution is to design a machine specifically for this type of testing that uses a consistent support. Figure 1.12 depicts such a machine that was designed to support a thin specimen under large compression. This machine, designed by Toshihiko Kuwabara, was the reference for the design that will be explained throughout this thesis. The key feature is that the upper and lower dies mesh in pairs using comb-shaped teeth, providing continuous support to the specimen, with no large gaps in specimen coverage, so that buckling cannot occur any time during testing. The comb teeth are wide enough for strength, but narrow enough so that the specimen cannot be extruded between the teeth. In addition to using a lubricant, Teflon sheets are used to further reduce friction, so that there is less noise in the data. With this type of design the majority of shortcomings of other solutions are resolved, of course at the expense of designing and building a custom machine and its controller, from scratch.

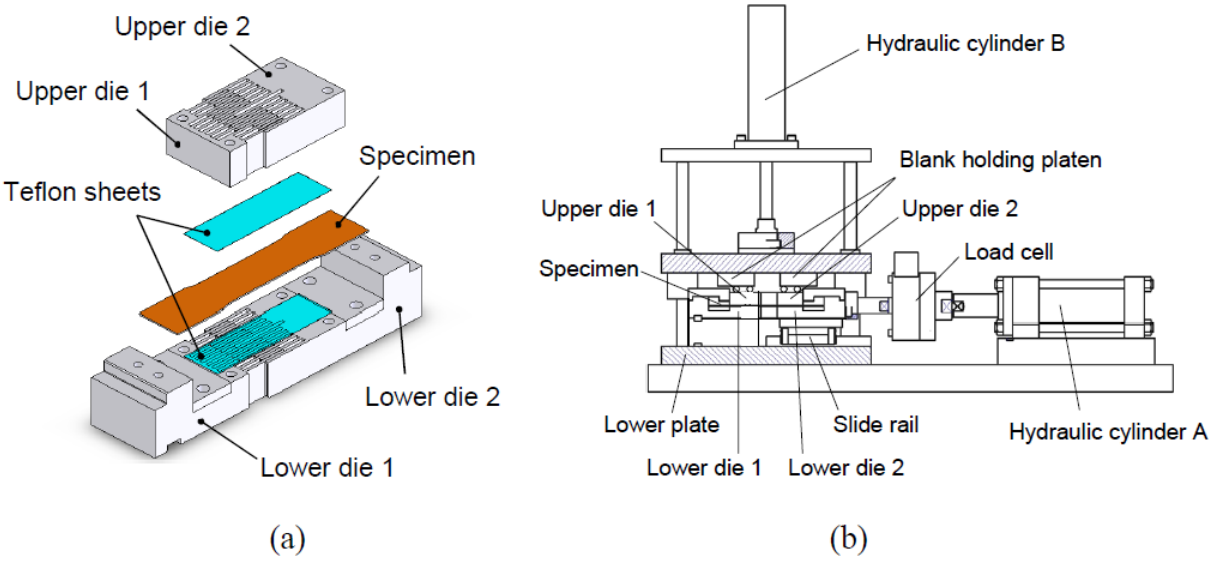


Figure 1.12: (a) Anti-buckling device using intermeshing pairs of upper and lower dies. (b) Testing machine using this idea [11].

## 1.3. Outline of Thesis

The present thesis will describe the machine that was designed, built, and tested based on the concept shown in Figure 1.12. A photograph of this machine is shown in Figure 1.13.

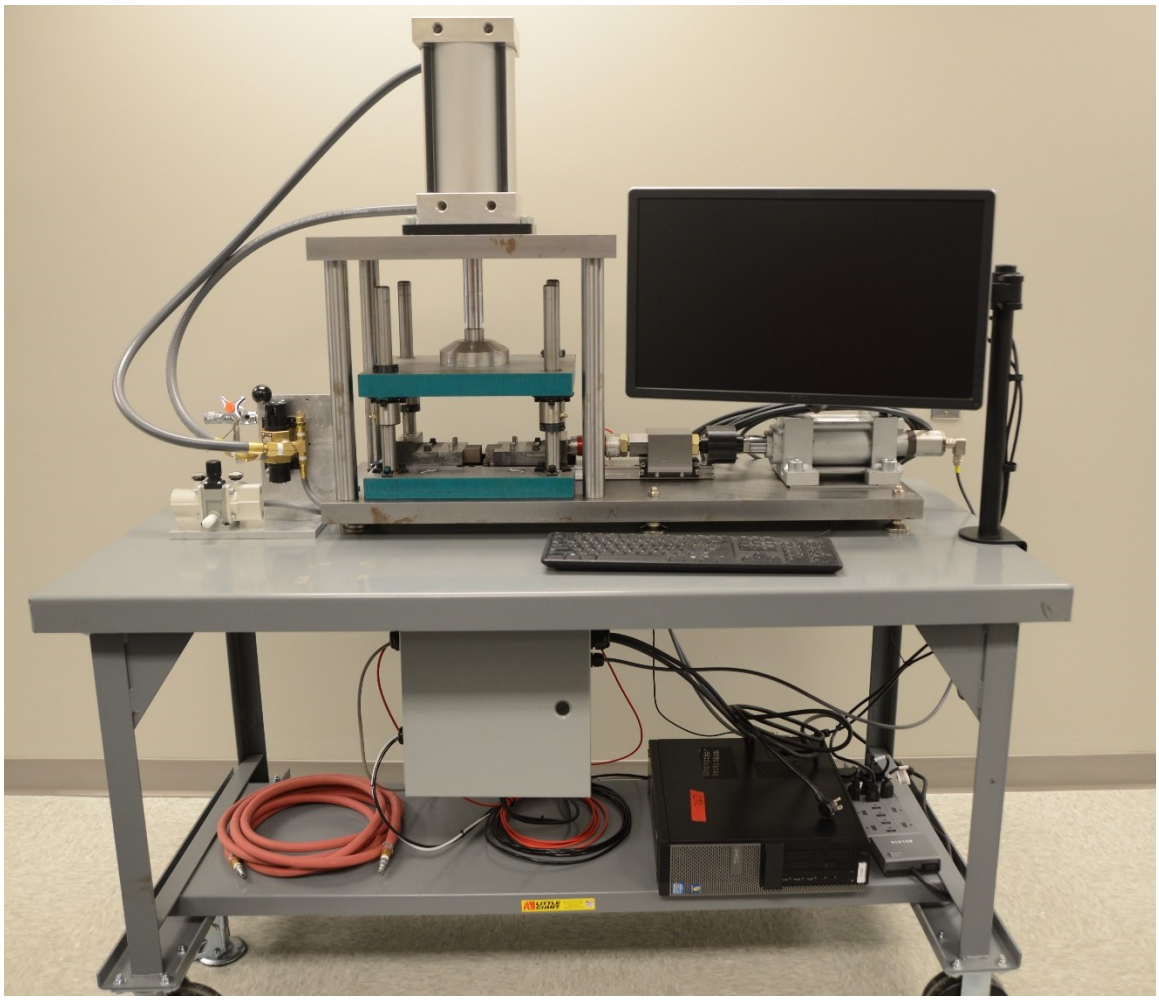

Figure 1.13: CTC machine described in this thesis.

The overall flow of this paper is as follows. CHAPTER 2 details the mechanical design of the machine, to withstand the loads expected during operation, and limit the deflections so that meaningful data can be obtained. CHAPTER 3 explains the data acquisition and

control system that was designed and built for this machine. CHAPTER 4 presents the series of experiments performed to verify the proper behavior of this machine. CHAPTER 5 includes a series of novel scientific data that have been obtained with this machine, by performing cyclic tension-compression experiments on a variety of metal sheets. CHAPTER 6 uses that information to calibrate a non-linear kinematic hardening rule that captures the responses obtained experimentally. CHAPTER 7 discusses conclusions and future work, as well as suggestions on how to further evolve the design from where it stands currently. Finally, APPENDIX A, APPENDIX B, and APPENDIX C include additional details that were left out of the main body of work.

*This page intentionally left blank*

# CHAPTER 2
# MACHINE DESIGN

## 2.1. Introduction

In this chapter, the focus will be on the mechanical aspects of the testing machine. This will start with an overview of the concept and progress into details of how the machine operates and how the basic components were designed. Then a section on critical calculations performed to ensure the machine will work as intended is discussed. Overall, this chapter discusses all the basic mechanical features of the testing machine that would be required to create a duplicate machine.

## 2.2. Overall Concept

As discussed in the previous Chapter, the fundamental problem that should be addressed during compression testing of thin sheets is the avoidance of buckling. In Section 1.2, three basic approaches were discussed: 1) reinforcing the specimen itself, e.g., by gluing multiple sheets together, 2) creating an anti-buckling device to be used with a universal testing machine, 3) creating a specialized machine. The third path was chosen in this research. The design of the machine is inspired by the ones at the Kuwabara group at Tokyo University of Agriculture and Technology.

In this machine outlined in Figure 2.1. The specimen is horizontal within the comb-die assembly; its ends are held by manually-tightened serrated grips; one set of grips is stationary on the machine; the other set is able to slide on a linear bearing; that load train is controlled by a hydraulic cylinder, and contains a load-cell; strain is measured during testing by a strain-gauge attached on the specimen. To prevent buckling during compression, the machine has dies with intermeshing comb-shaped teeth, supported by constant backing force (termed “blank-holding force”). That force is provided by a pneumatic actuator, supported on a portal frame. To ensure alignment, the supporting comb-dies are attached to a custom die-set. The reason this design was chosen is because it provides support to the entire specimen throughout the testing. This was deemed advantageous from the performance point of view. It should be emphasized that although this machine follows the same concept as the Kuwabara group design, the detail design is novel, and includes a few key changes made to improve upon the existing machine.

One of the changes is the specimen alignment method within the machine, as seen in Figure 2.2. This is accomplished by the two locating pins shown in the figure. By having one position be a locating feature and the opposite end be a slot, the possibility of accidental pre-loading of the specimen is significantly reduced. An added benefit of this layout is that manufacturing this specimen with tight tolerances is achievable and reproducible. The dimensions of the specimen used in this machine are given in Figure 2.3. The specimen has a stubbier geometry than a standard tensile dog-bone specimen. An investigation of its behavior is described in Section 4.3.3.

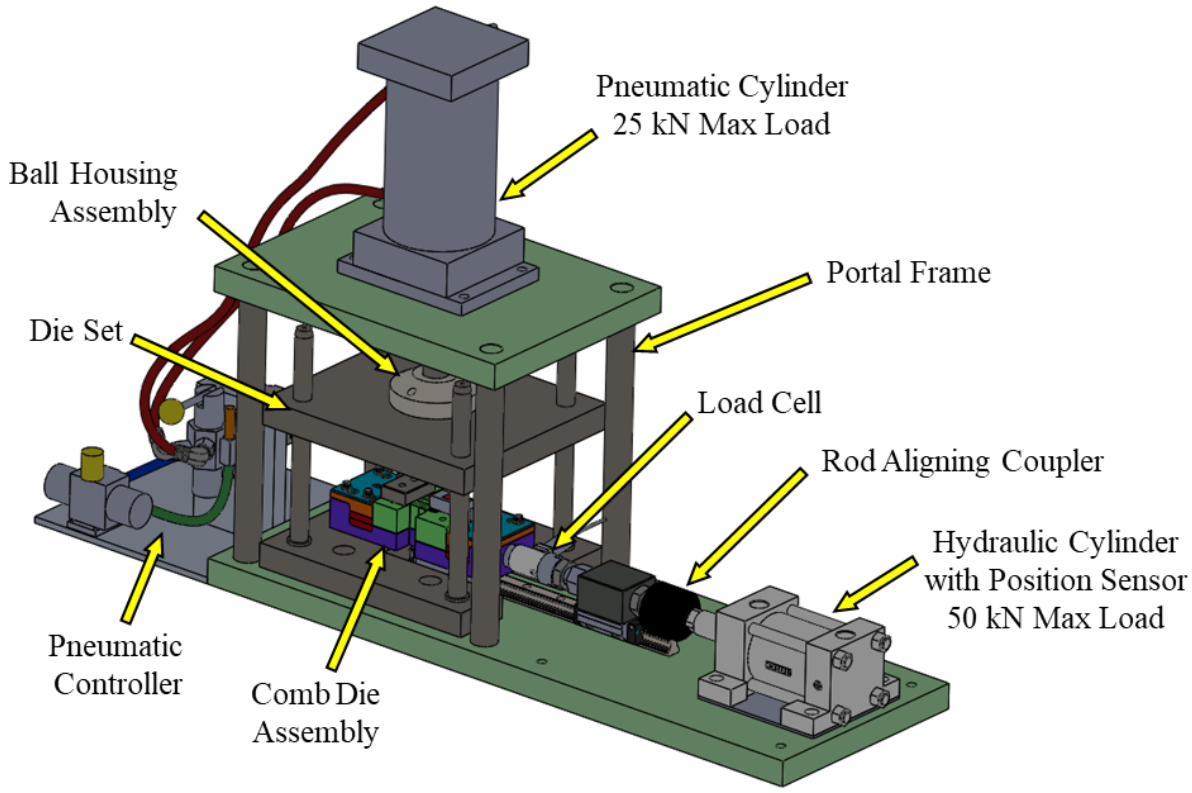


Figure 2.1: Isometric view of the CTC machine and layout of its key features.

The list of core characteristics for the CTC machine can be found in Table 2.1 which was used as the basis for designing. The maximum horizontal and vertical load were chosen to cover the wide array of materials and various thicknesses that could be tested. In addition to these characteristics, other requirements were added to make usability of the machine easy and intuitive, which will be explained further in Section 2.3.

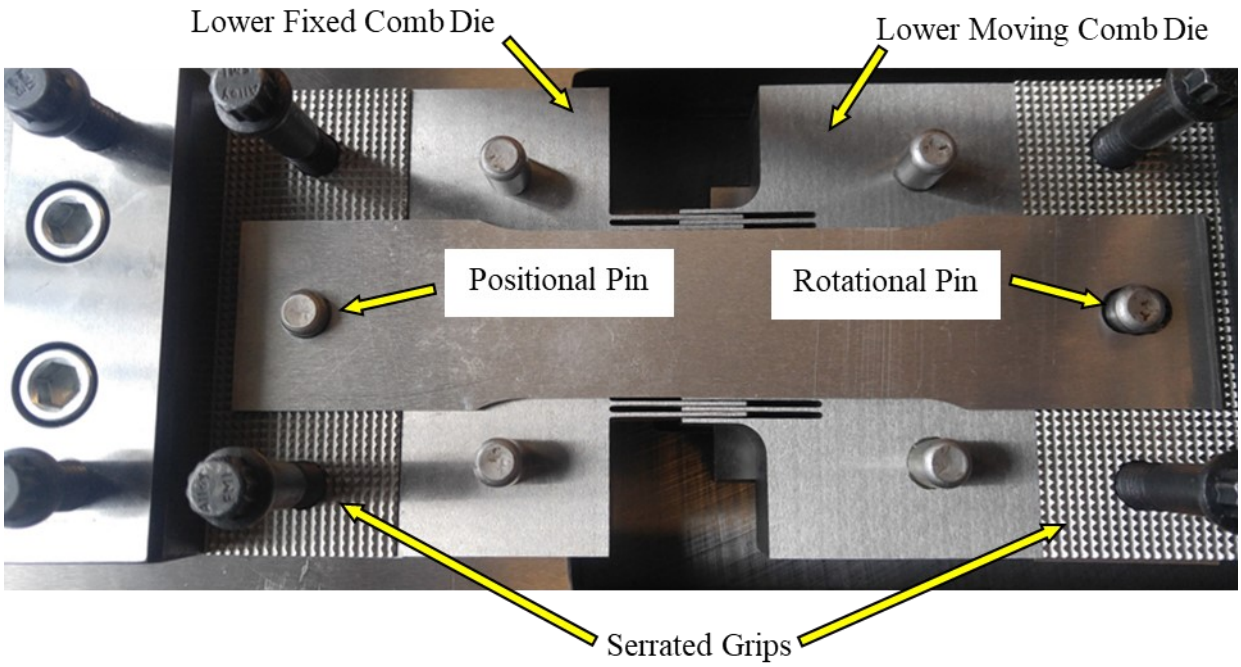


Figure 2.2: Specimen aligned in machine, which is shown in the open condition.

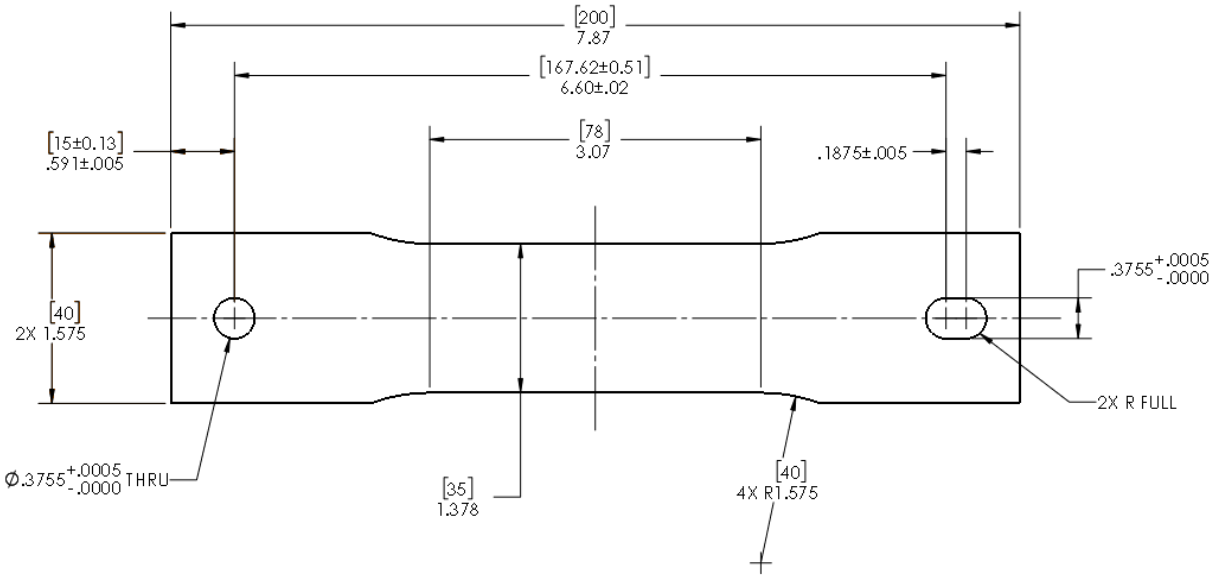


Figure 2.3: Specimen drawing.

Table 2.1: Characteristics of Machine

| CHARACTERISTIC | VALUE |
|---|---|
| MAXIMUM HORIZONTAL LOAD | 50 kN [11,240 lbs] |
| MAXIMUM VERTICAL (BLANK-HOLDING) LOAD | 25 kN [5,620 lbs] |
| MAXIMUM COMPRESSION STROKE | 16 mm [0.630 in] |
| MAXIMUM TENSILE STOKE | 60 mm [2.362 in] |
| MINIMUM AIR SUPPLY PRESSURE | 5.5 bar [80 psi] |

## 2.3. Detailed Design

Before diving into the details of the major assemblies, it should be stated that the premise of the whole design was to alleviate user hindrance. What this means is reducing the number of steps required to perform a test and designing in a way that makes the design intuitive to use. Designing in this manner allows for users in the future to be able to run tests with little to no issues stemming from using the machine incorrectly. The largest factors that pertain to this are: 1) keeping the machine self-contained as much as possible and, 2) only requiring additional input from simple sources such as an air supply line.

Using Figure 2.1 as a layout reference, details of each major assembly will be discussed next. The corresponding calculations will be covered in Section 0. A list of off the shelf components and their pertinent information can be found in Table 2.2.

Table 2.2: List of off-the-shelf components

| NAME OF COMPONENT | RELEVANT INFORMATION |
|---|---|
| **LOAD CELL** | Load Capacity = 88.96 kN [20,000 lbs]<br>FUTEK LCB450 \| FSH00712 |
| **HYDRAULIC CYLINDER** | Pressure Capacity = 206.8 bar [3,000 psi]<br>Load Capacity = 90.9 kN [20,433 lbs]<br>Bore = 82.55 mm [3.25 in]<br>Rod = 44.45 mm [1.75 in]<br>Stroke = 63.5 mm [2.50 in]<br>Sheffer \| 3-1/4 HH FHF 1.75 CC KY |
| **POSITIONAL SENSOR** | Stroke = +/- 32 mm<br>BALLUFF \| BTL7 A501 M0064 Z-S32 |
| **ROD-ALIGNING COUPLER** | Load Capacity = 86.41 kN [19,425 lbs]<br>Sheffer \| RAC-0100 |
| **BOSCH REXROTH GUIDE RAIL** | Load Capacity = 47.30 kN [10,633 lbs]<br>Bosch Rexroth \| R165323922 |
| **TYCHOWAY ROLLER BEARING** | Load Capacity = 35.23 kN [7,920 lbs]<br>Bosch Rexroth \| R987144824 |
| **PNEUMATIC CYLINDER** | Pressure Capacity = 17.3 bar [250 psi]<br>Load Capacity = 31.43 kN [7,065 lbs]<br>Bore = 152.40 mm [6.00 in]<br>Rod = 34.93 mm [1.375 in]<br>Stroke = 203.20 mm [8.00 in]<br>Motion Controls \| K1375600SE SL8 RA3 MJ |
| **AIR DIRECTIONAL SWITCH** | Max Pressure = 17.3 bar [250 psi]<br>Lexair Inc. \| BRL-2D-1/4-AIR-TYPE I |
| **AIR AMPLIFIER** | Set Pressure Range = 2–20 bar [29–290psi]<br>SMC Corporation \| VBA11A-02 |

### 2.3.1. Comb-die Assembly

Starting with the core of the machine seen in Figure 2.4, the comb-dies are heavily influenced from the works of Kuwabara [11]. In regard to the naming convention going forward, the half of the assembly opposite of the hydraulic cylinder is considered fixed and the other half is regarded as moving. To have optimum support of the specimen and reduce potential for extruding between the teeth, the width of each tooth (see Figure 2.2) is 1 mm and the spacing in-between each tooth is .15 mm. To accommodate the strain gauge that will be glued on the specimen and be used as the main means of acquiring strain during testing, the center tooth is wider (3.7 mm instead of 1 mm) and its length is shorter than its surrounding teeth on the upper moving die.

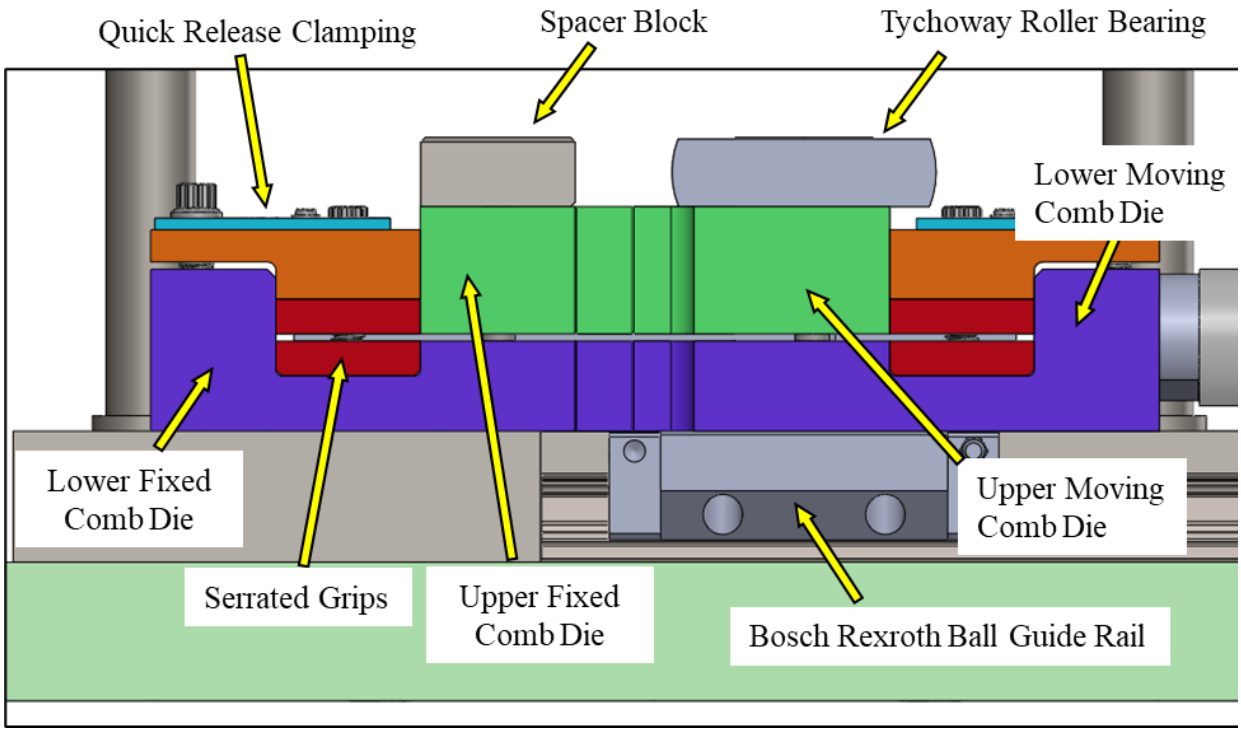


Figure 2.4: Comb-die assembly – side view.

This shorter length prevents the possibility of peeling the strain gauge off of the specimen, and also provides a channel for routing the gauge wires, as seen in Figure 2.5. The fixed comb-die also has a slot for the strain gauge wire to lie and stay recessed from parts that could possibly tear its wires.

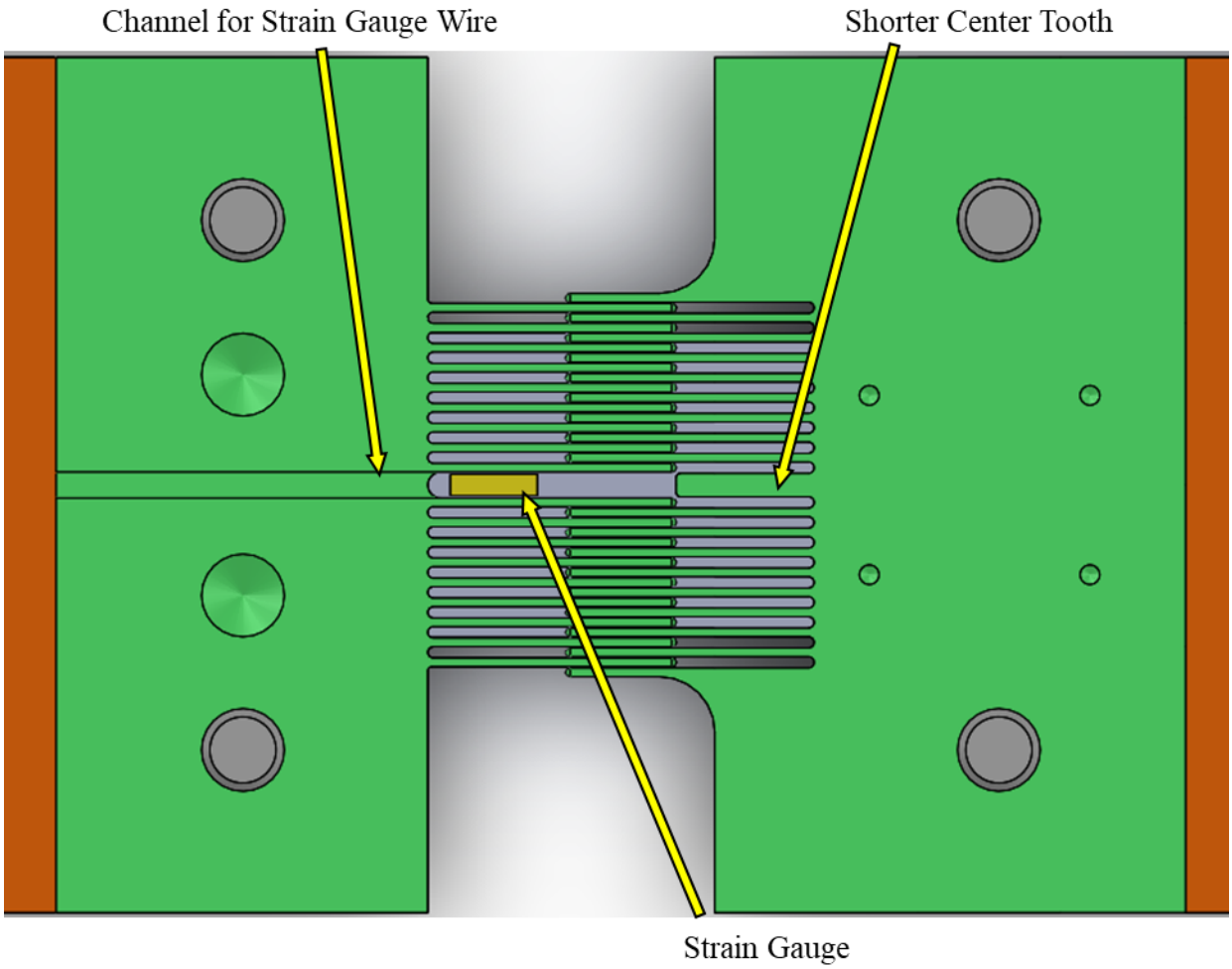


Figure 2.5: Top view of the lower dies, showing the comb teeth meshing and the location of the strain-gauge.

To allow for optimal alignment, all surfaces that contribute to the height are ground to the required height after initial fit-up of the machine. Additional adjustment of the machine can be made by using shims if the adjustment required is greater than 13 μm. This

flexibility in alignment of the machine ensures repeatable and reliable specimen alignment. Furthermore, components such as the serrated grips (see Figure 2.4) have the capability to be shimmed to a specific height. By allowing numerous ways to adjust alignment, the impact of misalignment is, for the most part, foregone.

To allow for the comb-dies to move while under large vertical loads with little vertical displacement, a Bosch-Rexroth ball guide rail and Tychoway roller bearing were selected. The Tychoway roller bearing allows for infinite linear movement with a very stiff vertical compliance, and the Bosch-Rexroth ball guide rail is precision-made to significantly reduce the amount of vertical linear movement when high loads are applied. To transfer the blank-holding force provided by the pneumatic cylinder onto the specimen (see Figure 2.1), the upper die contacts the spacer block and Tychoway roller bearing (see Figure 2.4) simultaneously, which transfers the load through the upper comb-dies onto the specimen. Although the vertical displacement on the moving side of the comb-die assembly is about 11 μm (as specified in the product catalog), for a 1 mm thick specimen this would be about 1% of its thickness. This can cause issues with gouging the specimen, which is addressed in Section 0. Both components used on the moving side of the comb-die assembly are attached to their respective upper and lower comb-dies, to ensure alignment is held and for ease of use with respect to the Tychoway roller bearing.

Another feature of the comb-die assembly is a quick-release clamping plate to allow for faster installation of the specimen, seen in Figure 2.6. Not only does this reduce the fatigue a user can experience running multiple tests, but its design allows for less wear on the threads. Since the user does not need to remove the screws to mount a specimen, the threads experience far less erosion over time, which increases the life of the comb-

dies. The clamping screws only need to be backed out a few turns which allows for the transfer plate to then be slid back and release the clamping assembly.

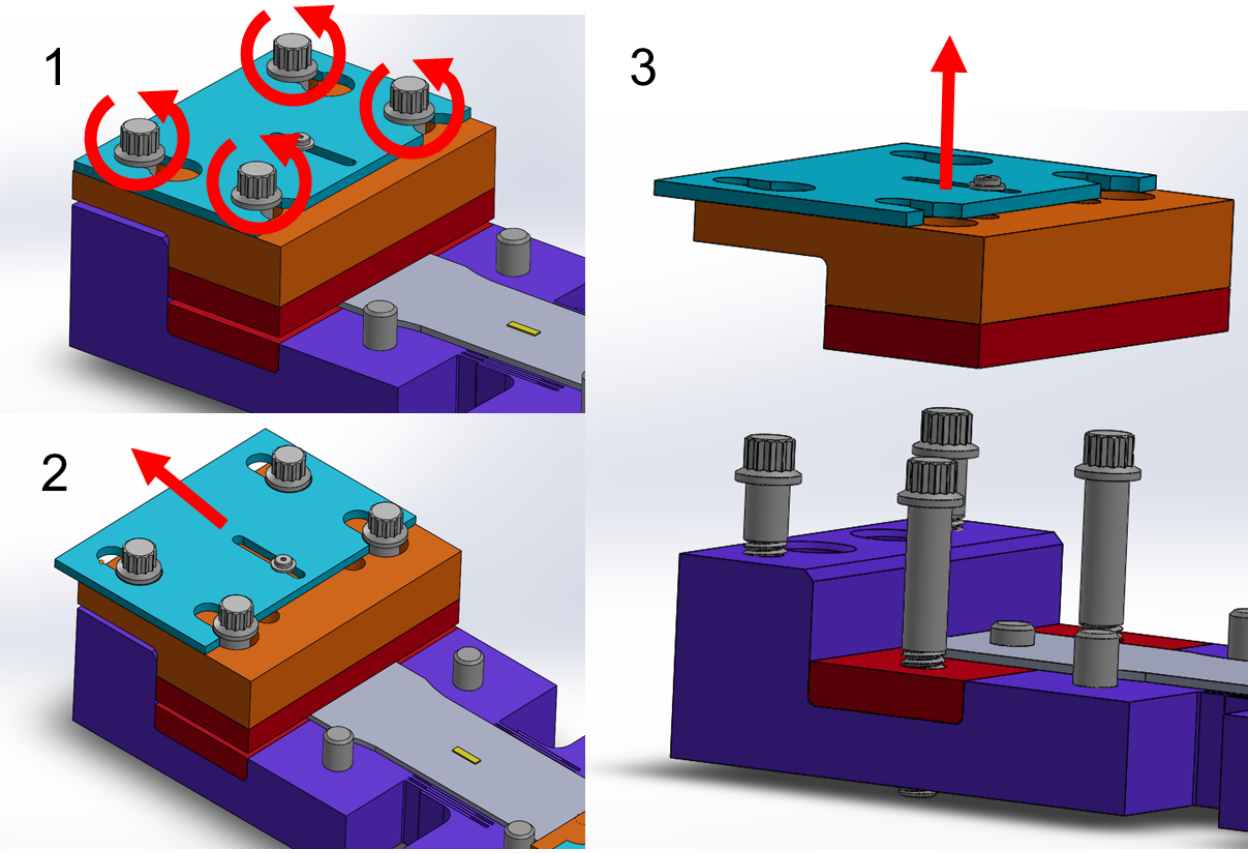


Figure 2.6: Quick-release grip assembly sequence.

### 2.3.2. Blank-Holding Assembly

With reference to Figure 2.1, the next major assembly is the one that transfers the vertical blank holding force onto the specimen and ensures that the force is vertical with little to no horizontal force component (i.e., loss). This assembly consists of the portal frame, pneumatic cylinder, die-set, and ball housing assembly. Compressed air is supplied to the pneumatic cylinder, which generates a force that is transferred through the ball housing assembly and the die-set onto the comb-dies (see Fig. 2.1). Not only does the frame need to withstand the BHF applied, but the overall height is critical, to

allow the user to have plenty of clearance when operating between the die set and comb-dies. Figure 2.7 shows the overall height of the assembly and the clearance allowed for the user to operate in the comb-die space.

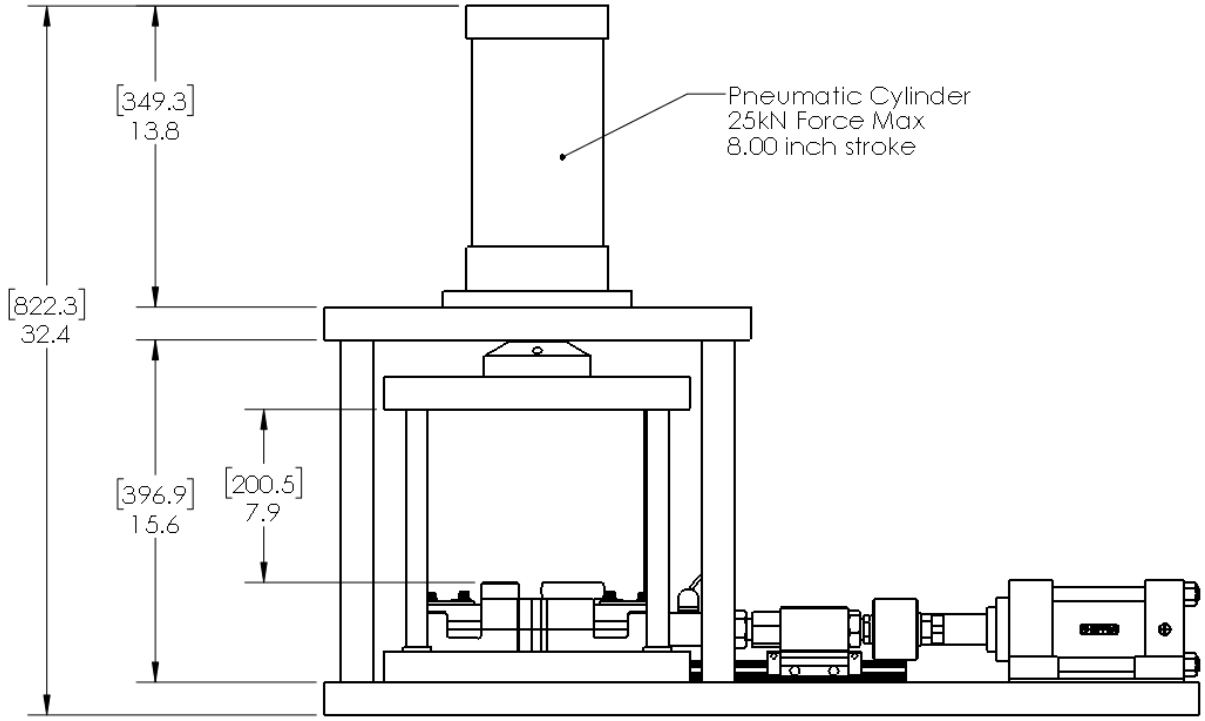


Figure 2.7: Dimensions of vertical heights of assembly.

To reduce stress from off-center loading or bending moments caused from a hard connection between the pneumatic cylinder rod and the upper plate of the die-set, a ball is used to transfer the load. By allowing the ball to center itself with respect to the pneumatic cylinder, as seen in Figure 2.8, no bending moments can be transferred to the internal components of the pneumatic cylinder, alleviating dragging during actuation. The assembly is of course designed to also lift the upper plate of the die-set off the comb-dies. As shown in Figure 2.8, a small clearance is provided between the piston rod and the ball

housing. Hence, when the direction of motion of the pneumatic cylinder is changed, that gap is closed, the force on the bearing ball is released, and the die-set can open without again causing any unwanted bending moments.

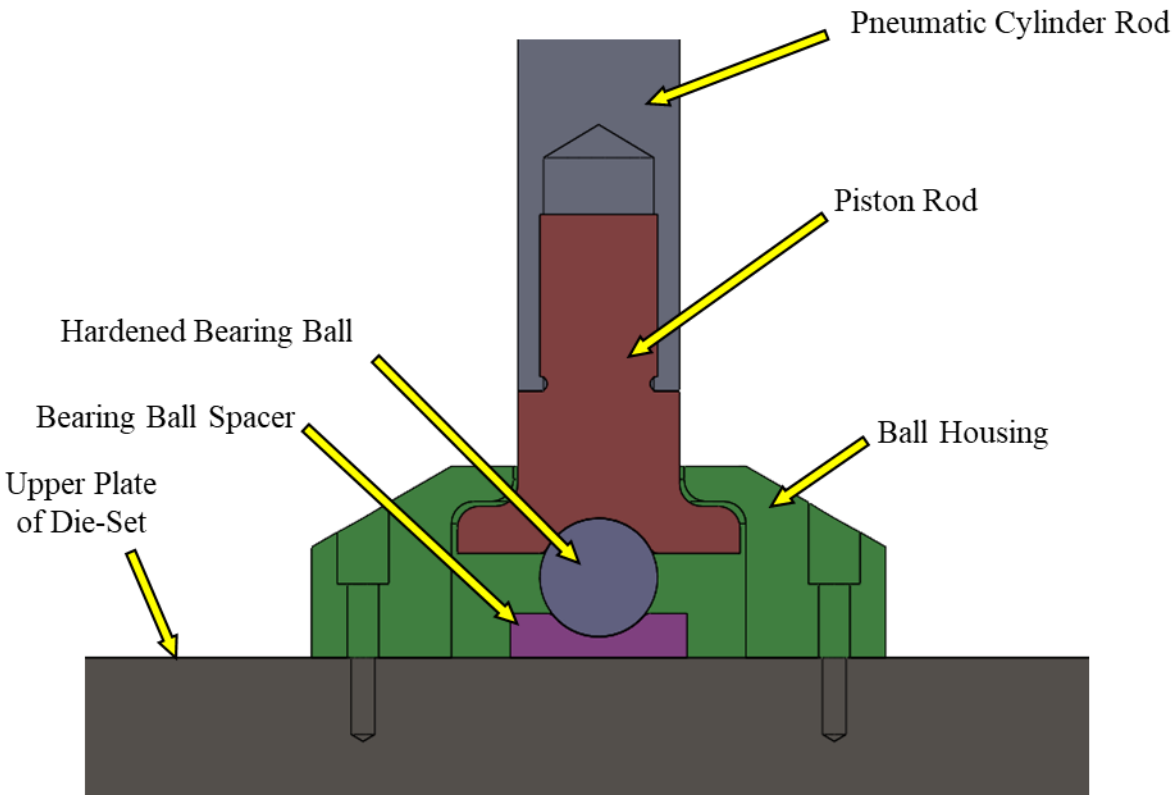


Figure 2.8: Ball housing assembly.

The force to push down on the specimen is provided by compressed air. The air controller assembly is outlined in Figure 2.9. Standard shop air is fed into the assembly and amplified for use in the pneumatic cylinder since the standard shop air pressure is insufficient for the range of BH forces specified. Typical pressure of shop air ranges between 5.9 – 6.9 bar (85 – 100 psi), which would cause this 152.4 mm bore cylinder (see Table 2.2) to generate between 10 – 13 kN. This is about half of what is required (see Table 2.1). Hence a pressure intensifier (a.k.a. booster) was added in the circuit.

Following the path of the air outlined in Figure 2.10, the air supply is fed into a booster with a built-in regulator, where pressure can be adjusted accordingly and reach pressures up to 20 bar (290 psi). Since 20 bar is well above the maximum that would be needed for operation according to the machine specs on Table 2.1, and furthermore it surpasses the pressure rating of the pneumatic cylinder (Table 2.2), a relief valve set at 15.5 bar (225 psi) is installed after the air booster and before the control switch. Due to the design of the control switch, if the pneumatic cylinder is pressurized further because of the specimen attempting to buckle, the relief valve will actuate if needed.

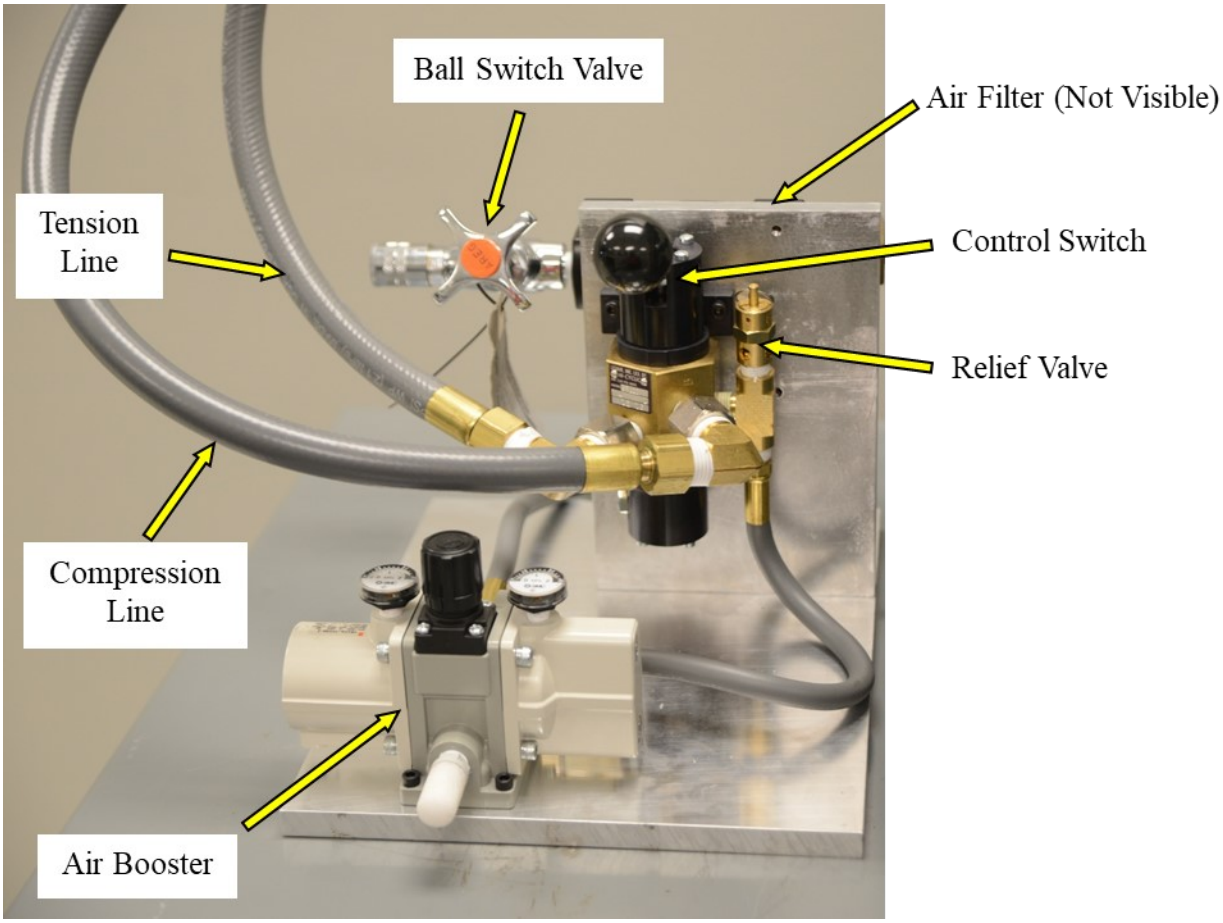


Figure 2.9: Air Controller Assembly.

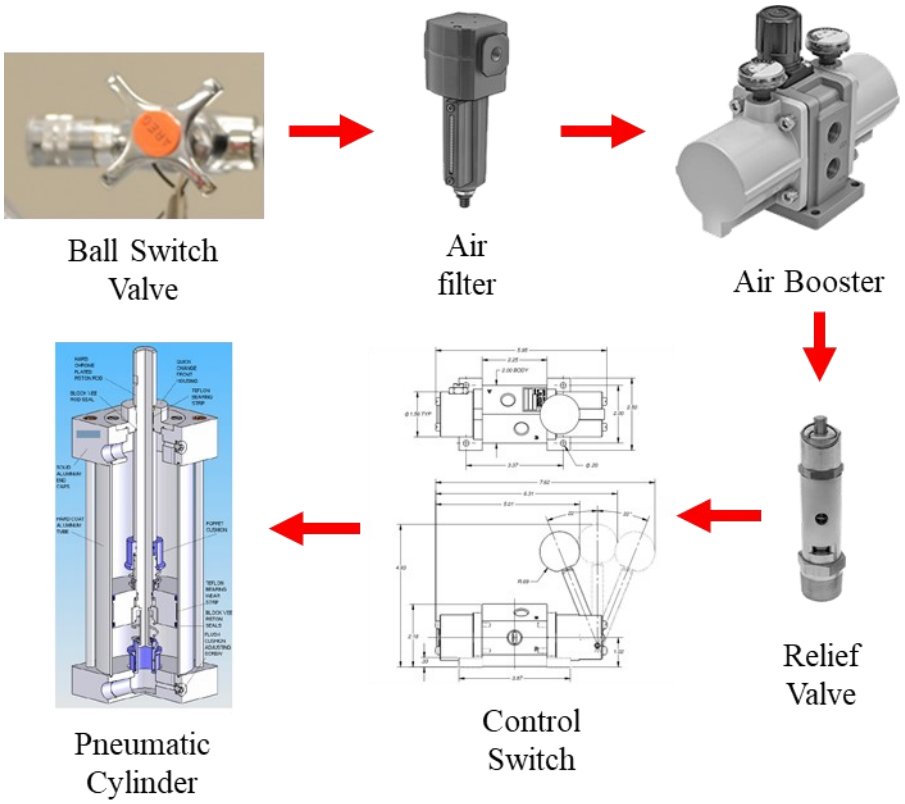


Figure 2.10: Compressed air circuit, identifying the major components.

The blank-holding pressure (BHP) used during a test is taken as 1.5% of the yield stress of the material. This is the value typically used in sheet metal forming to prevent wrinkling of the flange during stamping. This pressure is multiplied by the specimen area supported by the comb dies (i.e., the area between the gripping inserts in Figure 2.2), to provide the blank-holding force (BHF). From the latter, the air pressure used in the pneumatic cylinder (see Figure 2.1) is determined. The BHP applied on the specimen corresponds to a through-thickness stress, so that the specimen will not be under pure uniaxial loading. However, the difference is minimal between a pure uniaxial test versus including multiaxial loading using von Mises as the yield criterion. This difference is around 2% at small strains of around .001 and decreases even further to under .7% as the stress continues to grow.

### 2.3.3. Horizontal Load Train Assembly

To transfer load from the hydraulic cylinder to the specimen, a load train was created as seen in Figure 2.11. Starting from the hydraulic cylinder on the right and moving towards the comb-die assembly, the first connection is the rod-aligning coupler, which allows an angular misalignment of 10° and a lateral offset of the axes of 3.175 mm (1/8”). These misalignment allowances aide in vastly reducing cylinder wear and rotational loads on the ball guide rail. The rod-aligning coupler is then attached to the coupler block, which eliminates any remaining extraneous forces on the load cell other than the axial one, by transferring them to the ball guide rail instead of the remaining of the load train to the left. By reducing extraneous forces on the load cell, the accuracy of the sensor is improved and additional compensation for these forces is not needed.

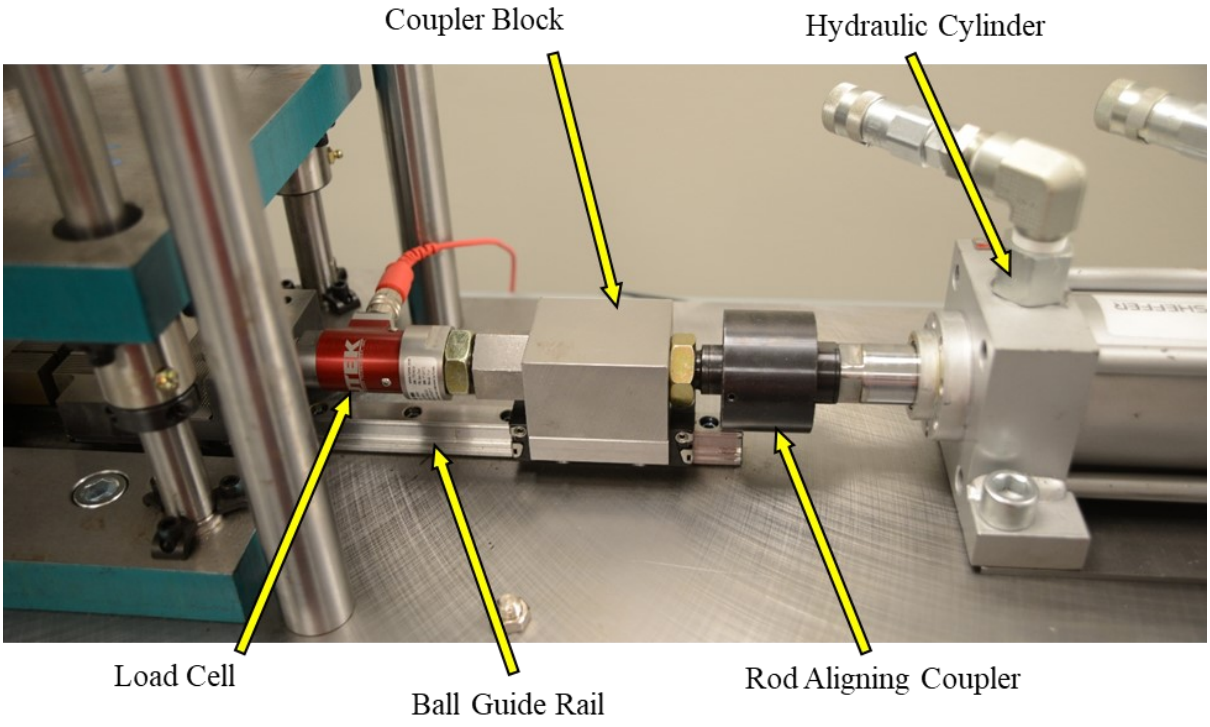


Figure 2.11: Horizontal load train.

## 2.4. Analysis of Critical Components

### 2.4.1. Major Bolts and Pins

The majority of the calculations performed for this machine are related to basic bolt and pin strength calculations. In Table 2.3, the critical bolt and pin calculations are listed, along with their corresponding safety factors. Figure 2.12 and Figure 2.13 show where the labels are located within the machine. For the bolts outlined in labels 1 and 3, the same style bolt that is used to clamp the hydraulic cylinder to the base plate was used. The same premise was made for the threads covered in label 2 and the weakest link within the horizontal load train is the rod-aligning coupler. This simplified calculations as the bolts used for the hydraulic cylinder are already calculated for a safety factor of 3 from the manufacturer for this style of mounting (APPENDIX B). Out of all the calculations performed, the lowest safety factor is the rod-aligning coupler which was intentional. The rod-aligning coupler is designed to be the failure point as to save the other parts that are loaded by the hydraulic cylinder.

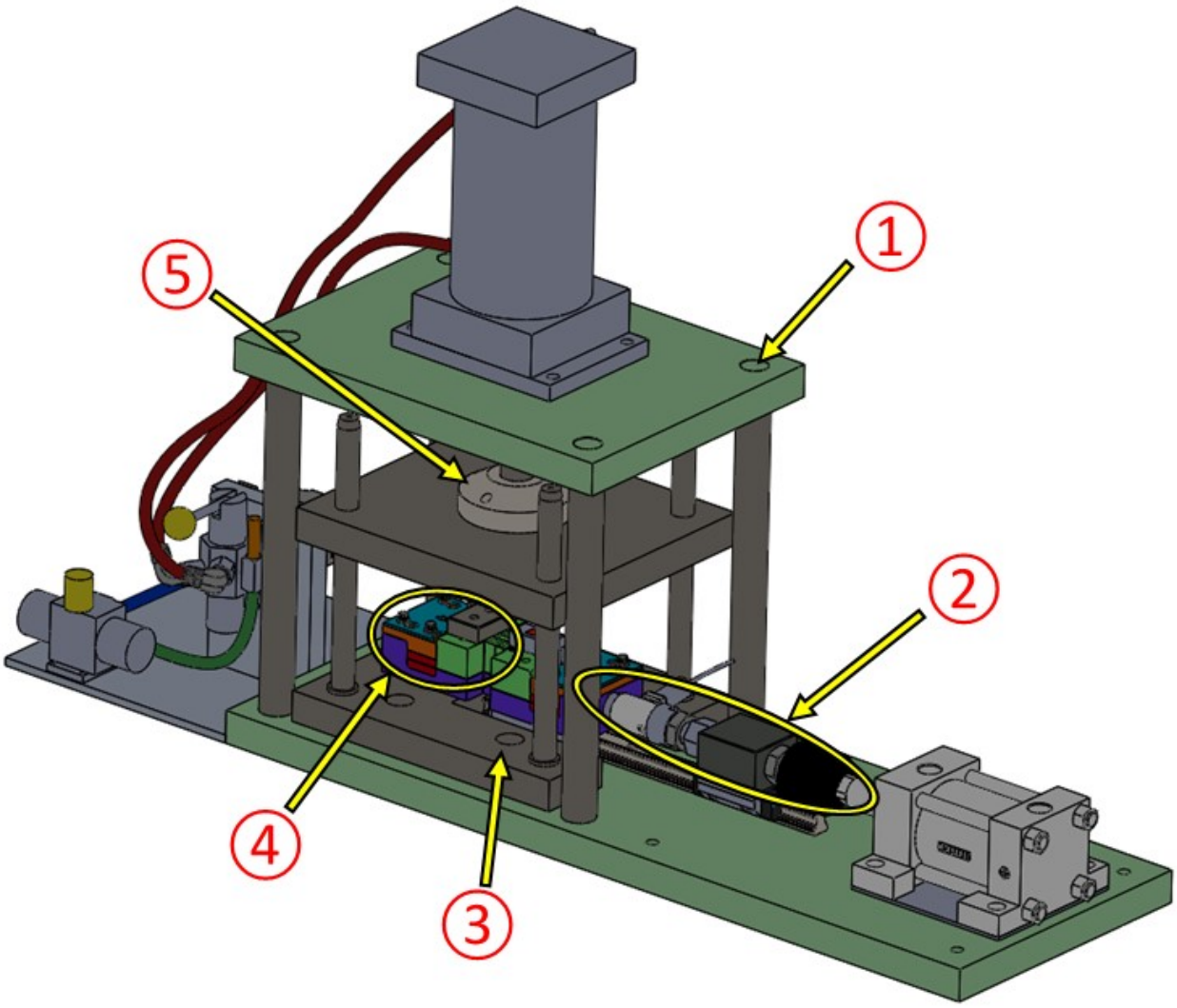


Figure 2.12: Outline of bolt and pin calculation areas.

Table 2.3: List of Critical Bolt and Pin Calculations

| Label # | Type of Loading | Load | Safety Factor |
|---|---|---|---|
| **1** | Tension | 25 kN | >5 |
| **2** | Tension/Compression | 50 kN | 1.73 |
| **3** | Shear | 50 kN | 3.00 |
| **4.1** | Shear | 50 kN | 2.05 |
| **4.2** | Tension | 36 kN | 3.25 |
| **5** | Tension | 25 kN | 3.85 |

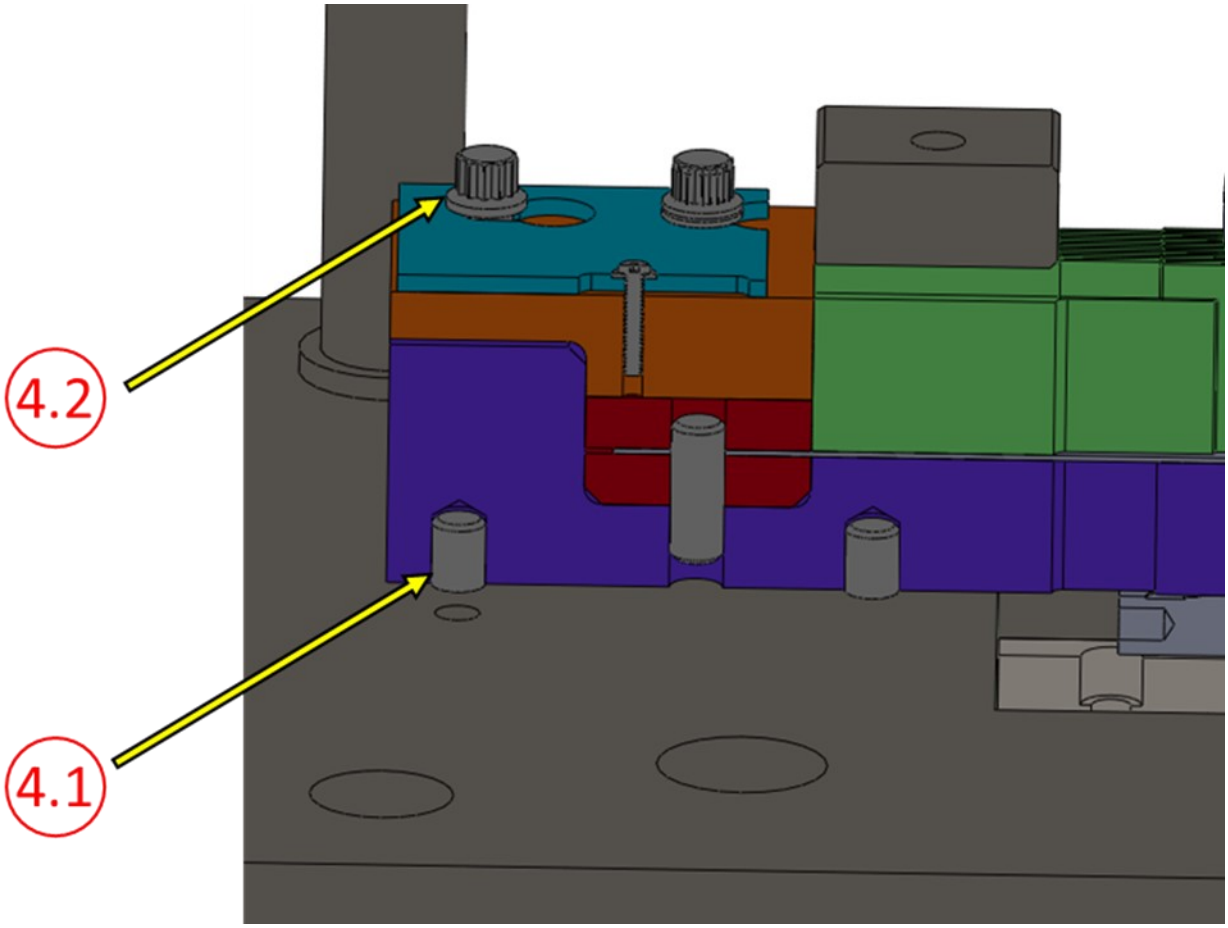


Figure 2.13: Expanded bolt and pin areas.

### 2.4.2. Ball Housing Assembly

Another area of major calculations performed was on the ball housing assembly, refer to Figure 2.8, since the whole assembly is custom parts. A combination of hand calculations and finite element analysis (FEA) were performed on the assembly, using a force of 25 kN (the maximum the cylinder can apply) for both tension and compression. For the FEA simulations, the commercial package SolidWorks was used. All simulations used the solid mesh option (mesh can be found in APPENDIX A), and a linearly-elastic material behavior was assumed, using E = 210 Gpa and v=0.3.

The summary of results from these calculations can be found in Table 2.4. In reality, the tension load will never reach 25 kN and since there is not a requirement on minimizing the weight, it was simpler to develop an over-designed assembly rather than spending time to reduce weight and increase cost of the design.

Table 2.4: Ball Housing Assembly Calculation Results

| Component Name | Material | UTS [12] [13] | Safety Factor |
|---|---|---|---|
| **BALL HOUSING** | 1117 Steel | 485 MPa | 5.05 |
| **PISTON ROD TENSION** | 1117 Steel | 485 MPa | 4.27 |
| **PISTON ROD COMPRESSION** | 1117 Steel | 485 MPa | 2.02 |
| **HARDENED BEARING BALL** | S2 Steel | 2000 MPa | 8.00 |
| **BEARING BALL SPACER** | 1117 Steel | 485 MPa | 1.61 |

Starting with the compression load on the assembly, the assembly was quartered for the FEA analysis, due to symmetry. The set-up of the analysis had the following features: the bearing ball spacer had a roller constraint on the bottom surface, the load was applied through the threads of the piston rod, i.e., as a shear force on the corresponding cylindrical part, and there was a global contact of no penetration allowed. From this simulation, the von Mises equivalent stress seen in Figure 2.14 is used to calculate the safety factors. Out of the three parts in this simulation, the lowest safety factor was the bearing ball spacer. Although the bearing ball spacer had a lower than desired safety factor, the fail-safe of the design is that if the part failed then it would be contained inside of the ball housing.

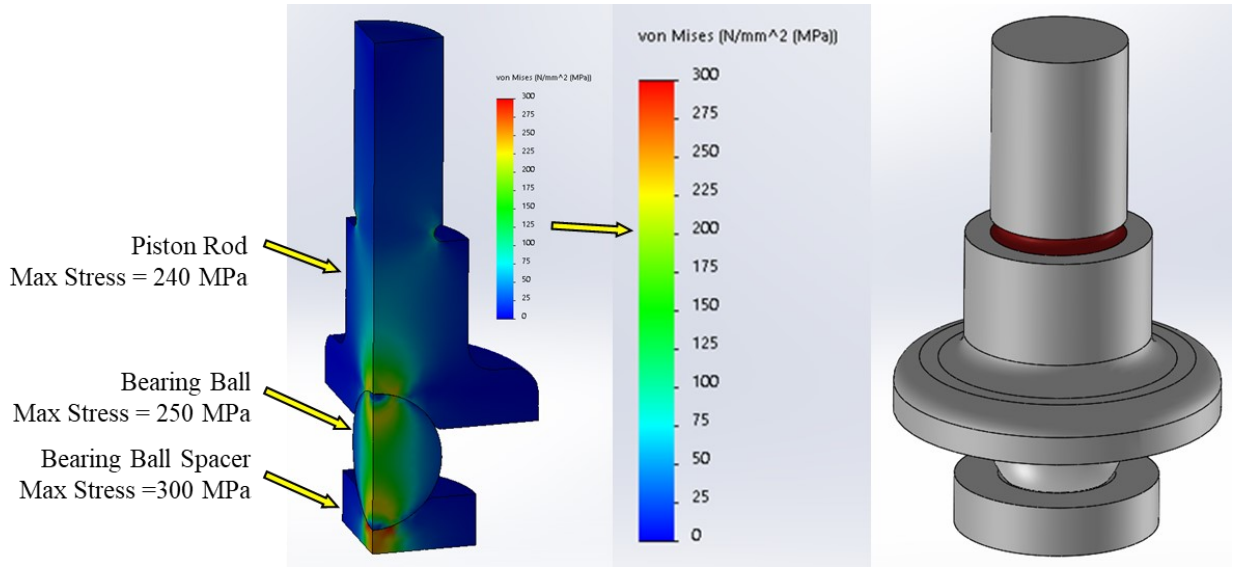


Figure 2.14: Ball Housing Assembly compression FEA.

For the tension FEA on the assembly, the model was again quartered due to symmetry. The set-up for this analysis had the same constraints as the compression FEA, except that a roller constraint was applied to the bottom of the ball housing instead of the

ball bearing spacer. The results from the tension FEA can be seen in Figure 2.15. As expected, the results in the tension direction are significantly less than in the compression one due to difference in cross sectional area where the contact occurs. The question can be raised as to why thicknesses were not adjusted to decrease stress in the compression direction. The reasoning behind this decision is such the component that would fail would be the ball bearing spacer and that part is considerably easier to replace than the ball housing or piston rod. Furthermore, that would be a much safer failure than on one of the tension components.

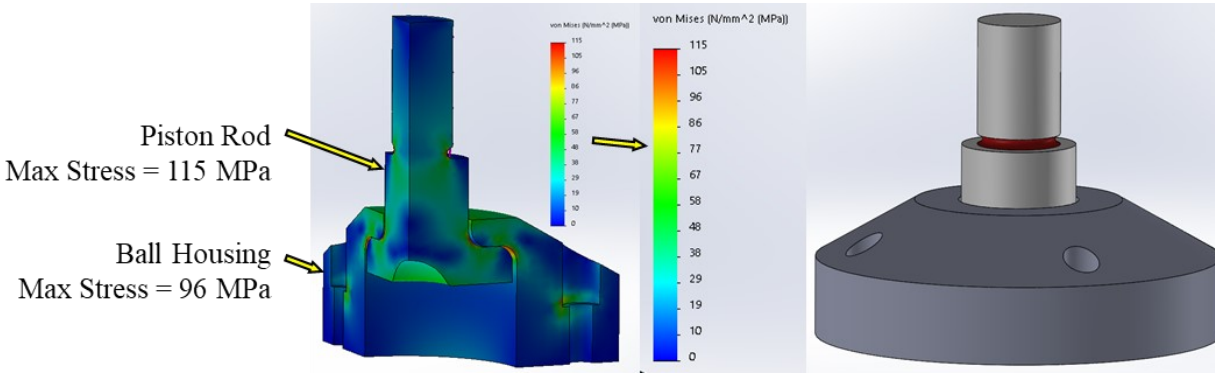


Figure 2.15: Ball Housing Assembly tension FEA.

### 2.4.3. Compliance of Moving Comb-die Assembly

The last major calculation that will be covered is the deflection of the comb-dies under vertical loading. Since one side of the comb-die assembly is fixed and the other is moving, the compliance of each side is different when the same vertical load is applied. Although this deviation is smaller than the diameter of a human hair (~.01 mm), the discrepancy is enough to cause unwanted gouging on the specimen. Looking at Figure 2.16 and Figure 2.4, the moving side of the assembly (indicated as “2” in the figure) has the Tychoway

Roller Bearing and Bosch Rexroth Ball Guide, which inherently have some compliance under a vertical load which is greater than the stacked steel blocks on the fixed side (or "1").

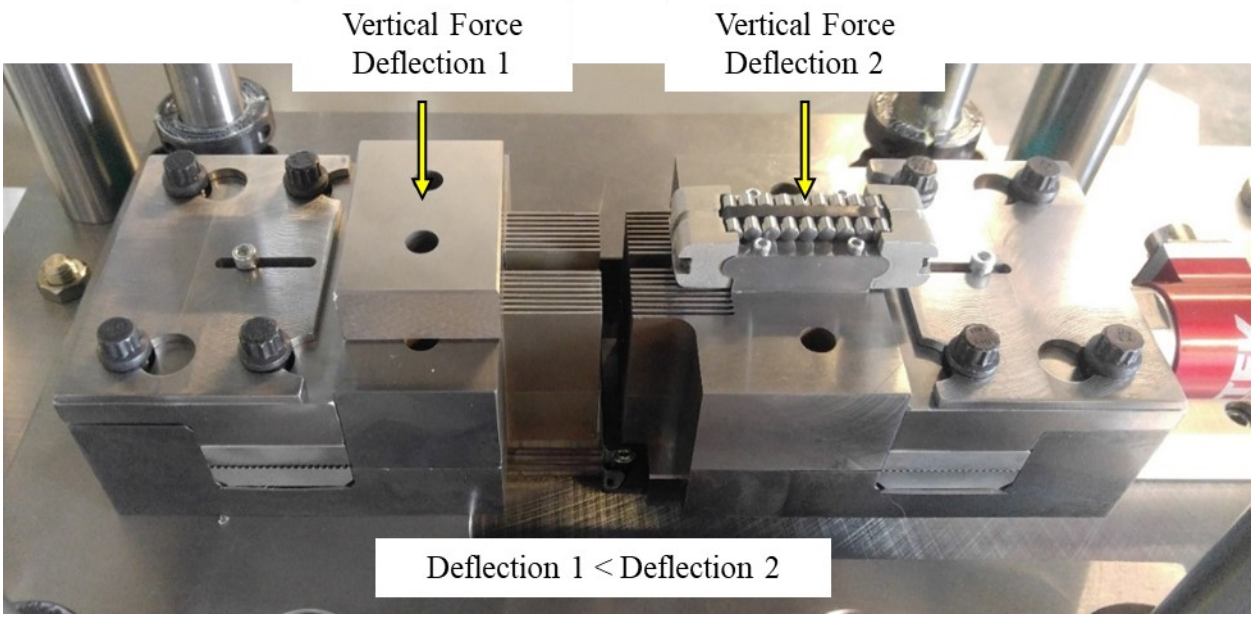


Figure 2.16: Photograph of comb-die assembly, to explain its compliance.

What is of interest is to assess the height difference of the two assemblies (moving and fixed) under the specimen. Then, with reference to Figure 2.4, the compliance of the Bosch Rexroth Ball Guide should be compared to that of the lower plate of the die-set (shown in grey in that figure). Using Equation (2.1) on that component,

$$\delta = \frac{FL}{EA} \tag{2.1}$$

where "F" is the vertical load applied (divided by 2), "L" the thickness of the component, "E" the elastic modulus (210 Gpa for steel) and "A" the area of contact, the maximum deviation between these two sides at 25 kN (or 12.5 kN one each side) loading is found

to be about $10\ \mu m$. This value produces the offset required on the moving comb-die so that when half the blank force loading (12.5 kN) is applied then the comb-dies are co-planar. This offset was produced by leaving stock on the moving side, assembling the machine, measuring the difference, then grinding the material until the offset desired is achieved. The complete hand calculations can be found APPENDIX A.

*This page intentionally left blank*

# CHAPTER 3
# DATA ACQUISITION AND CONTROLLER

## 3.1. Introduction

Continuing the details of the machine's design, this chapter will focus on the electrical and programming aspects. This chapter will start with the overall system architecture of the electrical components and how the components are situated with respect to each other and to the machine. After the hardware is discussed, the chapter will end with how the controller was programmed and designed to interact with all the electrical components.

## 3.2. System Architecture

Before the system could be wired and programmed, all the hardware needed to be determined. When choosing the measuring devices required for the machine, most of the details are covered from the core characteristics of the machine detailed in Table 2.2. The signal acquisition from these measuring devices is obtained through a USB connection and a NI chassis with several DAQ cards installed. Not only does the NI chassis obtain measured signals but also controls the horizontal movement and pump pressure of the machine by way of the directional and relief valve installed on the hydraulic pump which will be explained in Section 3.3.

Table 3.1: Electrical information for instrumentation

| NAME OF COMPONENT | RELEVANT INFORMATION |
|---|---|
| **USB220 – LOAD CELL READER** | Sampling Rate = Up to 4800 SPS<br>Computer Connection = USB 2.0<br>Model USB220 \| FSH03927 |
| **NI 9185 – DAQ CHASSIS** | Card Capacity = 4<br>Computer Connection = Ethernet Cable |
| **NI 9237 – BRIDGE COMPLETION** | Voltage Limit = +/- 5 V<br>Input Range = +/- 25mV/V<br>Max Sampling = 50 kS/s/ch |
| **NI 9263 – ANALOG OUTPUT** | Voltage Limit = +/- 10 V<br>Number of Outputs = 4<br>Max Sampling = 100 kS/s/ch |
| **NI 9215 – ANALOG INPUT** | Voltage Limit = +/- 10 V<br>Number of Inputs = 4<br>Max Sampling = 100 kS/s/ch |
| **DIRECTIONAL VALVE** | Power Supply = 24 V<br>Input Limit = +/- 10 V<br>Rexroth \| 4WREE6E04-2X/G24K31/A1V |
| **RELIEF VALVE** | Power Supply = 24 V<br>Input Limit = 0 – 10 V<br>Rexroth \| DBETE-6X/200G24K31A1V |

The primary goal with designing the electrical system was to keep the wiring as simple and organized as possible. By doing so, the system will have reduced signal interference, be easier to modify later, and prevent accidental damage to the hardware during maintenance. This was achieved by laying out all the hardware and creating an electrical box to house hardware not already mounted to the machine. The location of the electrical box is housed directly underneath the machine so that the equipment is accessible yet offset from the edges of the cart to prevent accidental damage as seen in Figure 1.1.

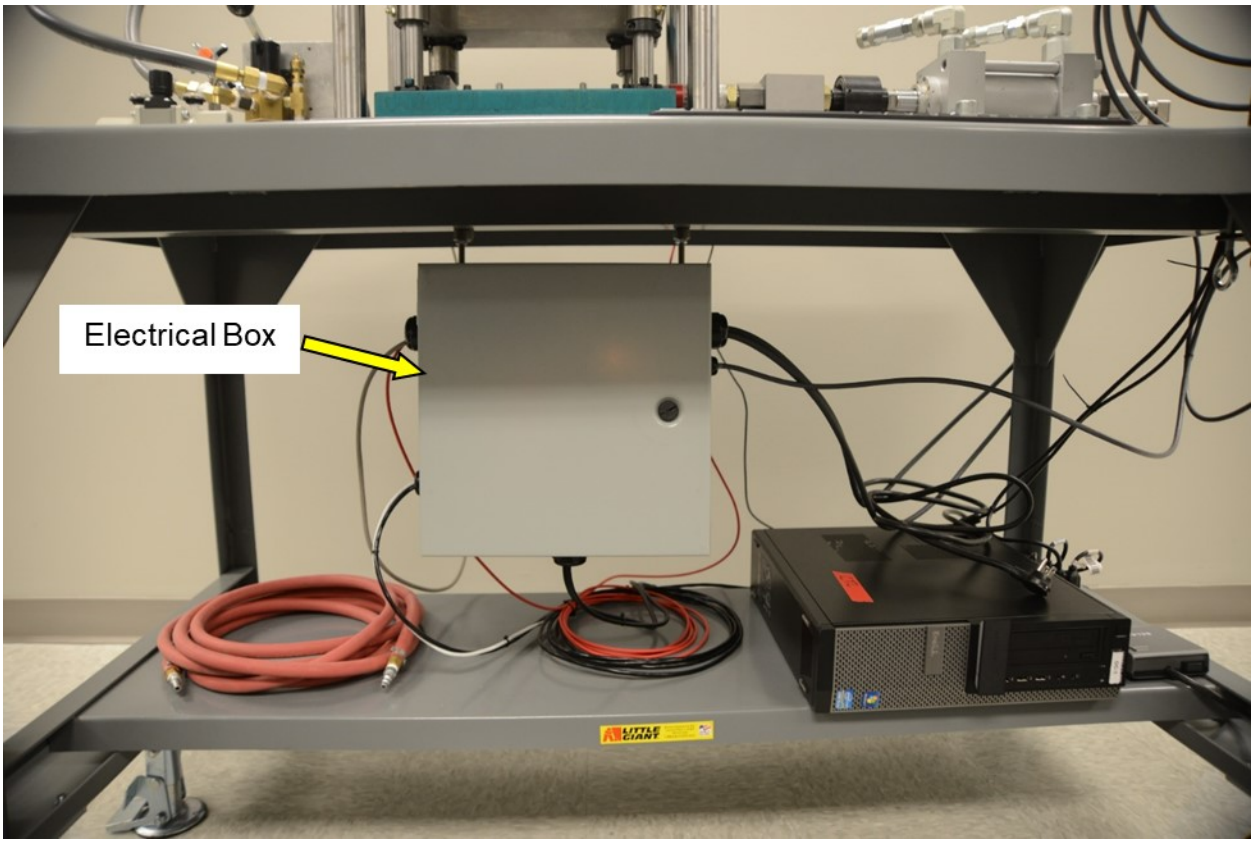


Figure 3.1: Location of electrical box in relation to CTC Machine.

Looking at Figure 3.2, a simple electrical architecture is shown with a view from behind the machine which showcases the electrical box as being the center for all the wiring. By having the electrical box mounted in a hanging position, the cables can be fed through any direction required from the box. The strain reader can be seen fed in between the pillars of the frame since the wires will be fed out near that area. This also keeps the device protected since its location is kept away from the user's working area while installing the specimen.

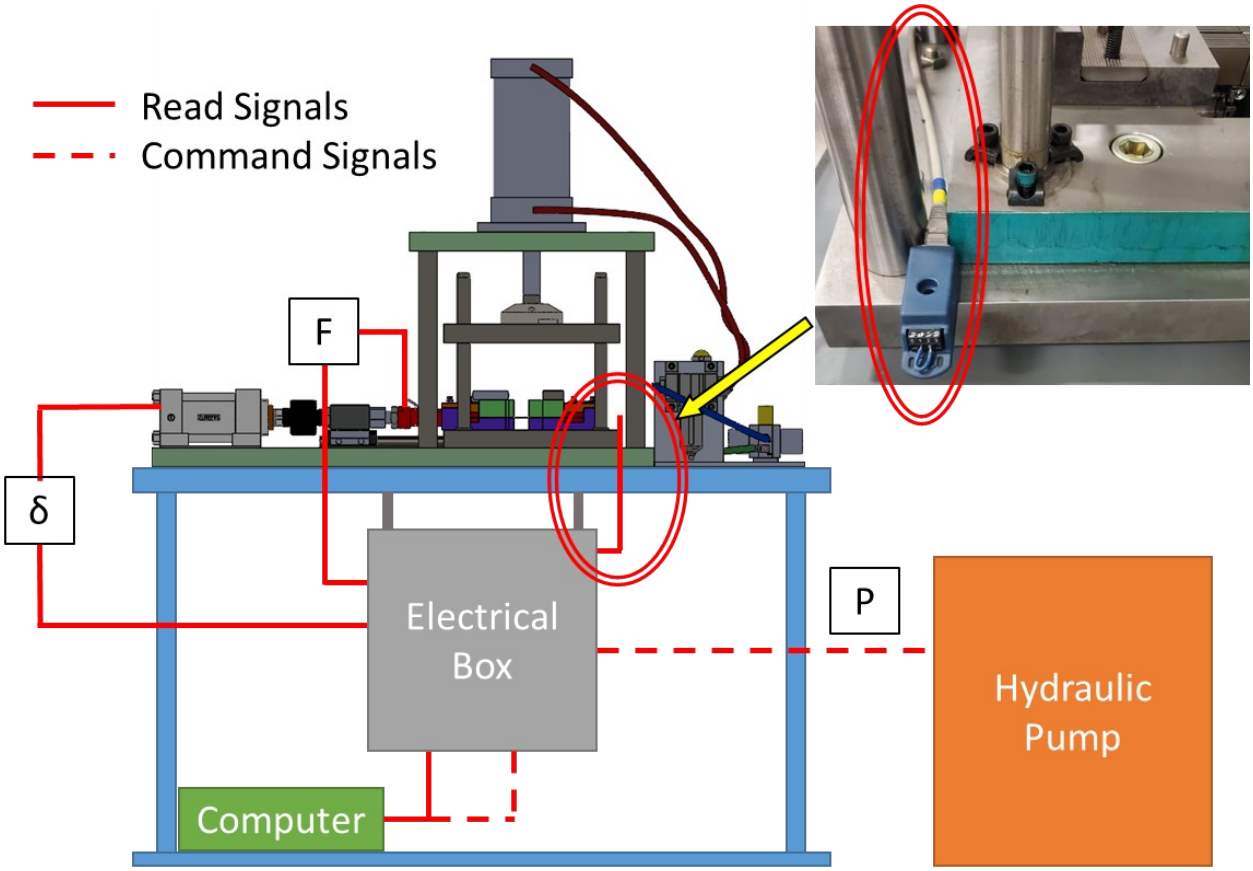


Figure 3.2: Electrical Architecture of CTC Machine.

### 3.2.1. Large Strain Readings

One aspect of the electrical hardware that was overlooked when initially designing the electrical system is that the NI Bridge Completion Card can only read about +/-5% engineering strain. A work-around was created to surpass this shortcoming which allowed large strain tests to be performed on the current strain reader. The work-around was to create two circuit boards as seen in Figure 3.3; one board for offsetting strain in the positive direction and the second board to offset strain in the negative direction. The circuit boards would wire into the existing strain reading device (not at the same time) and the strain gages would then be attached to the circuit board's terminal screws.

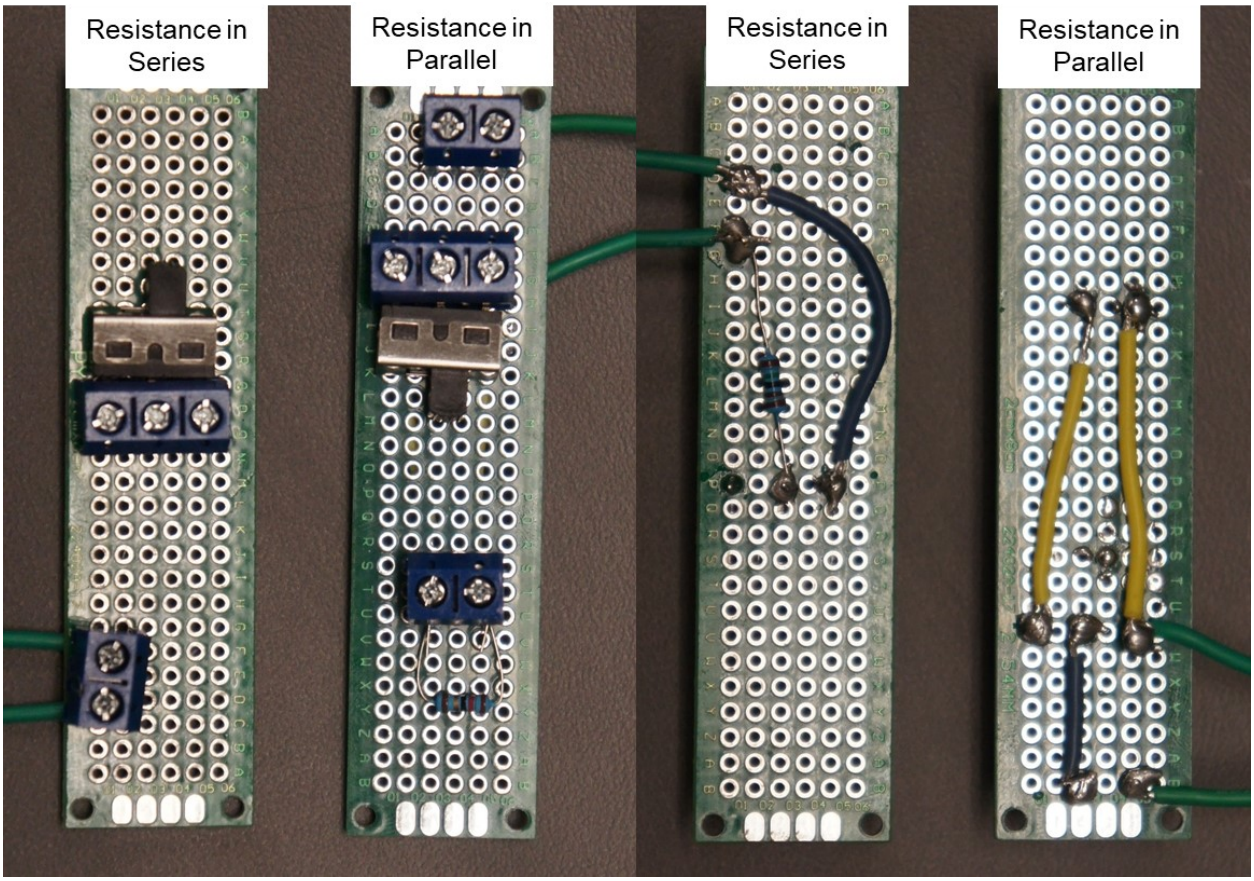


Figure 3.3: Offset Circuit Boards.

When offsetting strain in the positive direction, the circuit board adds a resistor in series with the strain gage. The user will zero the strain gage in the program before physically flipping a switch that offsets the data. The amount of offset can be adjusted by switching out which resistor is used. Fine tune adjustments are not possible with this device since a potentiometer is not installed but for what the circuit board needs to do, it works perfectly for this application. To determine what resistor to use for offsetting Equation (3.1) is used where "$\delta R$" is the resistor required for the offset desired, "$\varepsilon$" is the desired offset strain, "$GF$" is the gage factor provided by the manufacturer, and "$R$" is the strain gage resistance. Once the experimental data is collected, the data simply needs to be shifted linearly by the initial strain value offset created by the circuit board.

$$\delta R = \varepsilon * GF * R \tag{3.1}$$

To offset the data in the negative direction, the circuit board adds a resistor in parallel with the strain gage. The user will follow the same testing procedure as with the previous board but to determine the desired offset resistor, Equation (3.2) is used where "$R_0$" is the resistor required for the desired offset and the remaining terms remain the same. Before a test can be performed with this board, the adjusted limits need to be calculated. To determine the adjusted limits for this board, a quadratic equation will need to be used which will also be used for correcting the experimental data after testing. The quadratic equation is produced through a best fit line comparing the strain produced through typical resistance change of a strain gage versus resistance change of a strain gage with a constant parallel resistance. A spreadsheet (seen in Figure 3.4) was created to perform this calculation quickly and to update the equation when any of the following variables change: resistor used, gage resistance, or gage factor.

$$R_0 = \frac{R(R + \delta R)}{-\delta R} \tag{3.2}$$

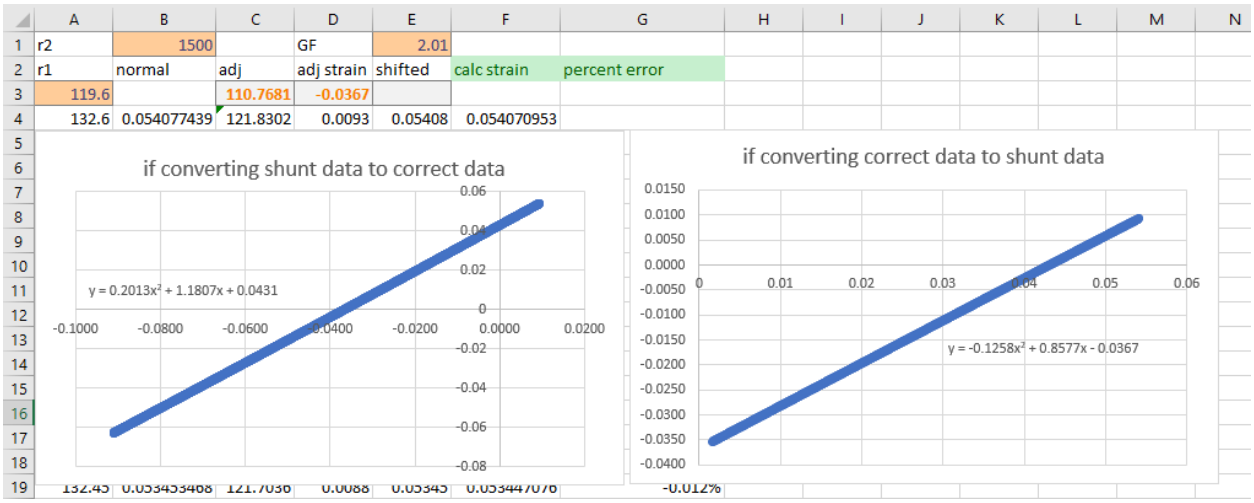


Figure 3.4: Snapshot of strain conversion calculator.

## 3.3. Controller Program

Although there were a few software options to choose from, the decision was to use LabVIEW since the program is widely used at the University. This was ultimately the same reason why an NI chassis was chosen to house the majority of input and output hardware that control the movement of the machine. By using hardware that was compatible with the software, the program is significantly easier to code and modifications in the future will be effortless to implement.

### 3.3.1. Controller Overview

When determining requirements for a controller, there are several layers to consider. The first layer is determining what needs to be read and what needs to be controlled, the next layer is what features are controlled by the user and what features are automated, and the last layer is how will all this information be conveyed to the user. By structuring all these layers, the program runs efficiently and optimizes the use of subroutines.

Looking at the first layer, there are a few key measurements that need to be monitored and recorded. The first being the load cell reading which is fed to the computer by a USB convertor. Since the load reading is not being fed into the NI chassis, the program needs to navigate to the USB port and read the data from there. The manufacturer of the load cell and USB convertor have files to work with from their website that accomplish this within LabVIEW which were used in this program. The strain reading is read through the NI Bridge Completion card and LabVIEW has a subroutine already created to convert the voltage to strain. A significant downfall of using the already created subroutine for reading strain is that the user cannot adjust gage resistance or gage factor while the program is running. To circumvent this, the subroutine was modified so that the user has control over these values on the front panel. Lastly, the position sensor in the hydraulic cylinder is monitored by the NI Analog Input card and the conversion from voltage to distance is accomplished within the program. For what the program needs to control, the directional valve and relief valve on the hydraulic pump are the only signals. Both signals are controlled through the NI Analog Output card.

Looking at what the user will be able to control and what will be automated, the user is able to control the motion of the hydraulic cylinder for manually aligning the specimen and this movement can be adjusted for direction and velocity. Along with controlling the movement of the hydraulic cylinder, the fluid pressure in the pump can also be controlled although this control is semi-automated. The user can input a desired pressure, but the pump does not provide this pressure until the user toggles pressurize pump. This toggle will begin an automated ramp function so that the pump does not jump from no pressure to a high pressure and if the user wishes to adjust the pump pressure after pressurization,

they will need to toggle the reset pressure button and wait for the pressure to ramp down. This safety feature ensures that the pump will not be damaged by jumping pressures and that the user has a chance to check the value entered. The user is also able to control what type of test is to be run through the several test tabs and parameters available for selection on the front panel which is discussed in 3.3.3.

As far as what the user has no control over, these tasks are primarily after the user has initiated a subroutine and is expecting a pre-determined outcome. A few common tasks in this category are holding force, zeroing force and displacement, and turning on graphs which are self-explanatory. Other tasks that the user would often use that are automated would be warming up the machine and calibrating velocity which is further detailed in 3.3.4. The user has no influence over the outcome of these subroutines other than initiating them but there is the option to stop the loop if need be.

The last layer, arguably the most crucial, of conveying all the information to the user, is achieved by having everything the user needs to interact with in a single front panel. Rather than having several panels the user will need to open or navigate, there is one large panel that fills the monitor screen with a test section that has tabs the user can use to access the various machine movement options. The details of how this front panel works and is organized can be found in 3.3.2.

### 3.3.2. Layout of User Intereface

As seen in Figure 3.5 the front panel houses everything the user will need to interact with. Starting counterclockwise from the top of the front panel, the program can be broken up into 5 regions. Each region will be shown individually in this next section and any actuation buttons shown will be described.

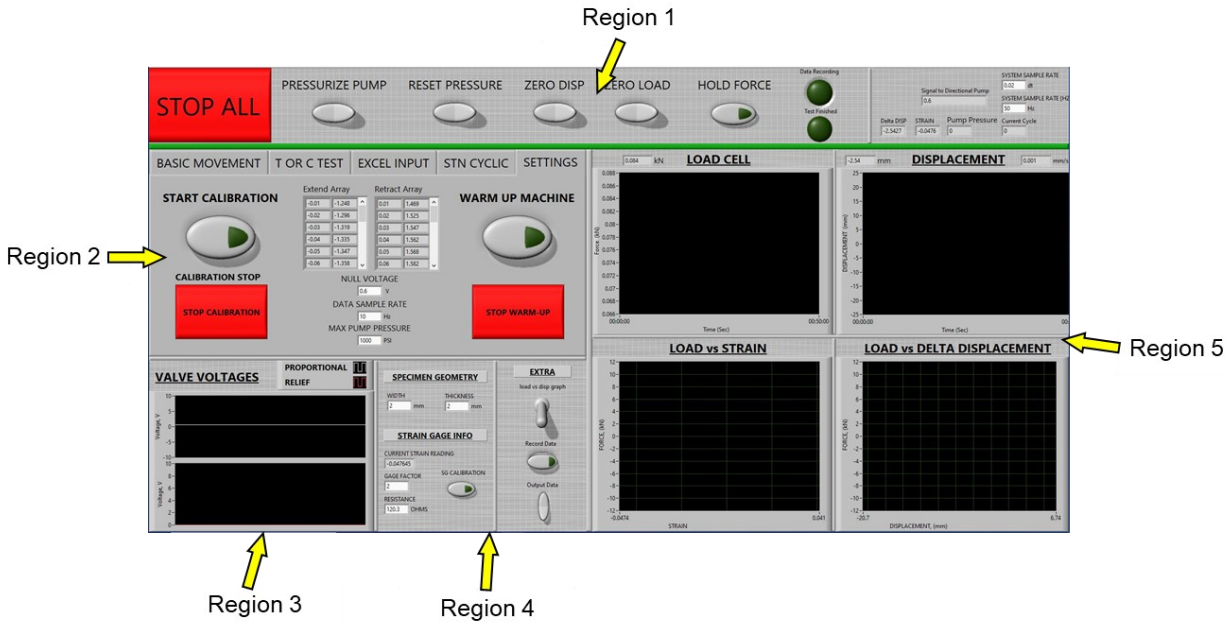


Figure 3.5: Front panel of program.

The first region is the top banner across the whole width of the program, seen in Figure 3.6. Starting from left, the “STOP ALL” button is the overall stop for the program. This shuts down all loops in the program safely as to not cause issues with the hardware. The next two toggles are related to turning the hydraulic pump on and off. As the names suggest, “PRESSURIZE PUMP” ramps the pump pressure up to the user prescribed value and “RESET PRESSURE” ramps the pressure back to zero. The toggles following the pump control are in regard to zeroing the displacement sensor and load cell which are self-explanatory. The last switch, “HOLD FORCE”, is used when the user wishes to place the machine under pseudo force control. The force control is only for holding the current averaged force being read and the user cannot prescribe a desired force to be held.

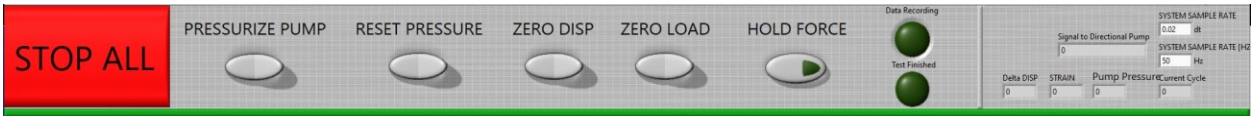


Figure 3.6: Region 1 – Top banner of front panel.

The next region houses all the various control options for the machine as well as the calibration tab, seen in Figure 3.7. The first tab, which is displayed in the figure, is used for basic manual control of the machine. The user can select a direction, turn on the manual movement, and control the velocity at which the machine will travel by using the slider. If the user turns off the manual movement while the velocity is not zero, the program will automatically reset the slider bar to the bottom as to not have the next movement start at a non-zero velocity. The direction switch can only be flipped while the manual movement is turned off as well. The following three tabs are related to testing and are covered in 3.3.3 in detail.

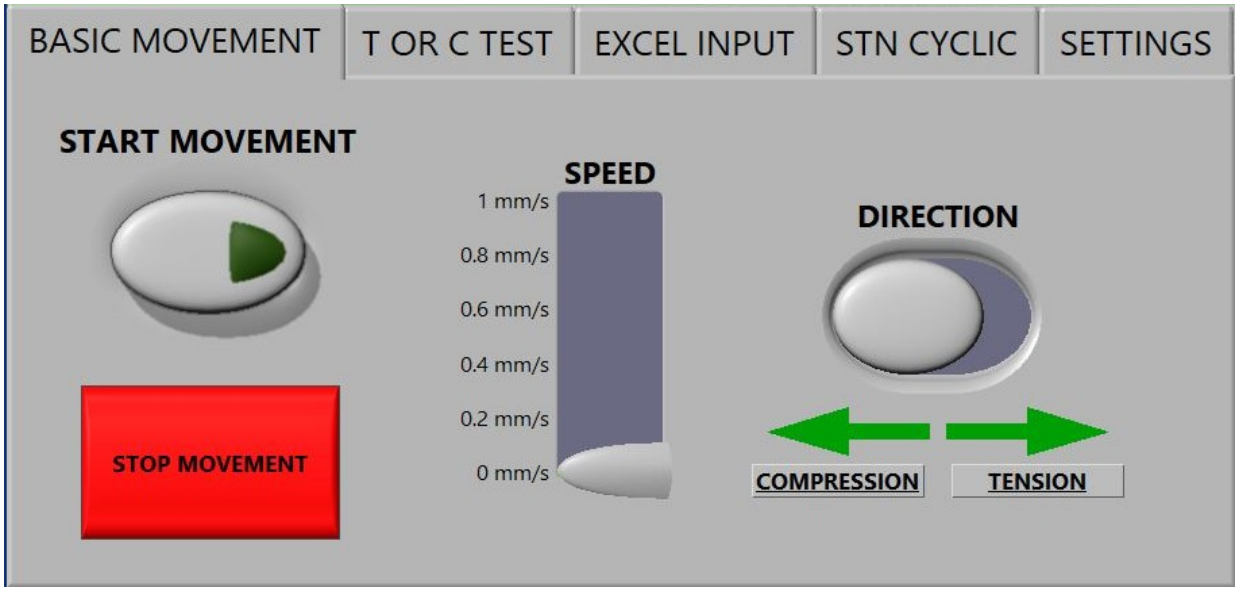


Figure 3.7: Region 1 – Control region of program.

The last tab in this region is related to calibrating and warming up the machine along with prescribing sampling rates and pump pressure. Looking at Figure 3.8, the user can set the null voltage and hydraulic pump pressure. There are more functions in this tab to discuss but the calibration and warm up is covered in 3.3.4.

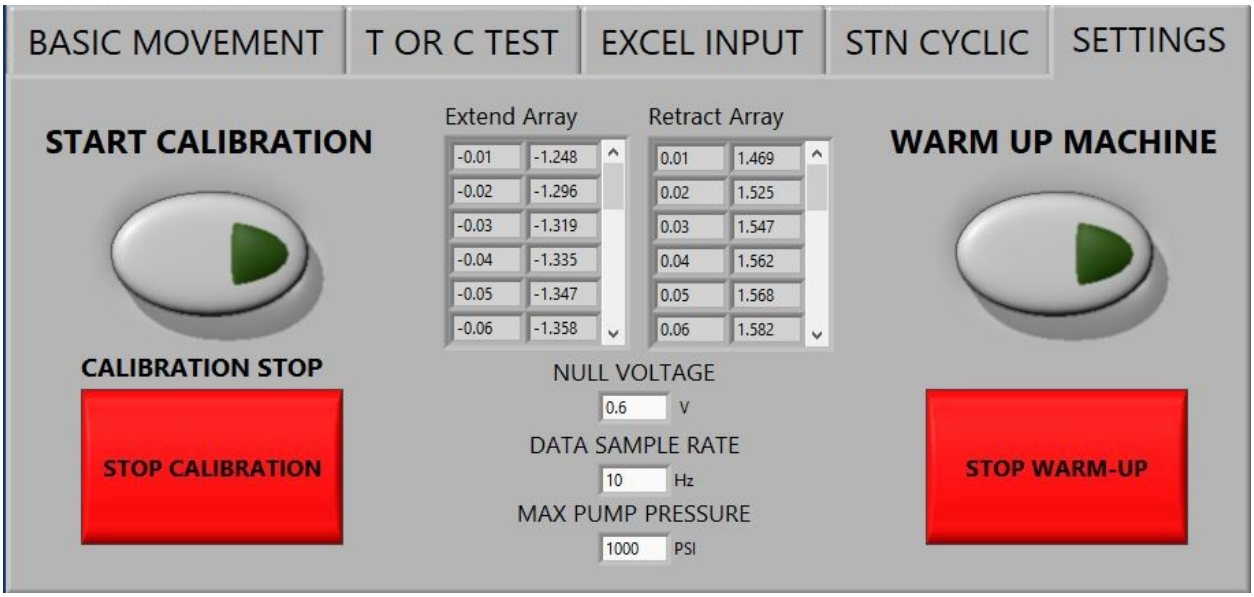


Figure 3.8: Settings tab in control region.

The following region, seen in Figure 3.9, is for monitoring the signal to the hydraulic pump. The upper graph plots the proportional valve signal while the lower graph plots the relief valve signal. This region is not always used but having these inputs monitored as a graph rather than a floating-point value helps to ensure the user what state the machine is currently in and if there are issues with the pump.

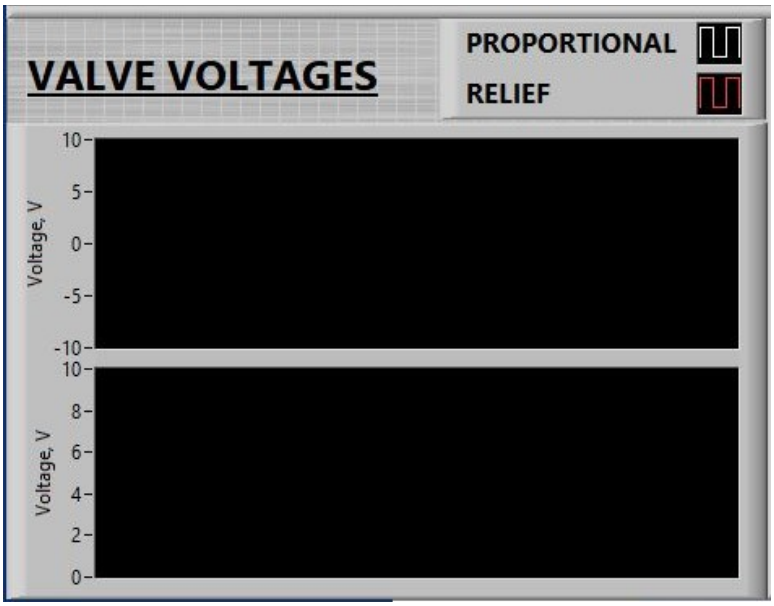

Figure 3.9: Region 3 – Hydraulic pump monitoring.

In addition to the settings tab in the control region, the fourth region can be considered the specimen variables and extra region, seen in Figure 3.10. The reason why this region would be labeled as specimen variables is that the variables controlled in this region have a high likelihood of being modified before each test. Starting with the strain calibration, the user can change the gage factor and gage resistance before selecting the strain calibration toggle. The detailed procedure for calibrating the strain gage can be found in 3.3.4. The sampling rate is also controlled in this region, separate from machine sampling rate, along with the controls for recording data and exporting. The “RECORD DATA” switch can be manually turned on before a test if desired, but the program will automatically flip this switch to active before a test is performed. To stop data recording, the user must manually turn off the “RECORD DATA” switch. 51easonn this switch is not automated to stop recording data is that leaving the data recording at the end of a test, allows the user to run multiple tests in a row on the same specimen without losing data in between tests. The user is free to output the data at any time using the “OUTPUT DATA”

toggle which will prompt the user for a file location and file name. The last switch, “LOAD VS DISP GRAPH”, is more-so for when the test is actively running. This switch will toggle the lower graphs in the last region on and off which is why it is located on the right side of the active test settings region.

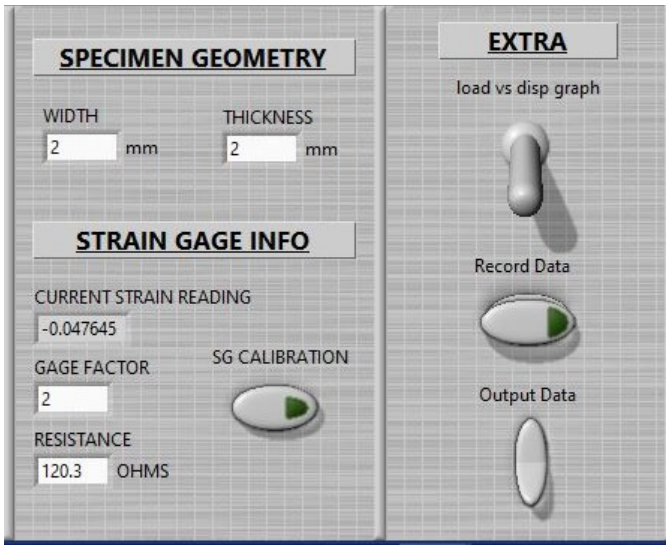


Figure 3.10: Region 4 – Specimen Variables and Extra settings.

The final region of the front panel is the graphing region seen in Figure 3.11. This is where the user can monitor force and displacement readings as well as actively monitoring test results. The load cell and displacement graphs have digital read-outs at the top of the graphs for ease of deciphering. There are not any active controls in this region as the only active control that commands anything in this region is in the active test settings region. Until the “LOAD VS DISP GRAPH” switch is toggled, the lower two graphs will not display any information. When the switch is turned off, the previous information remains but will be wiped out if the user turns the switch back on.

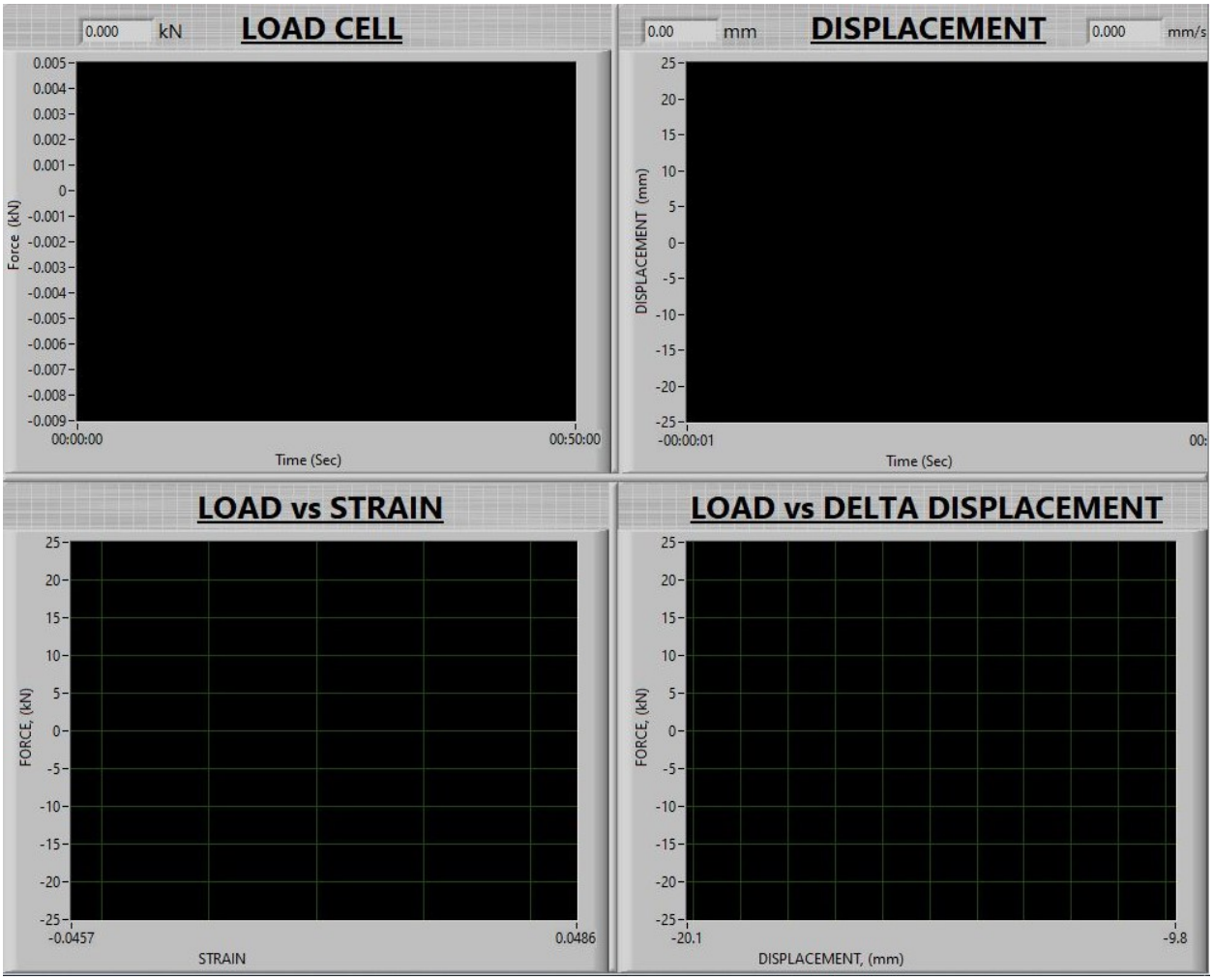


Figure 3.11: Region 5 – Graphing region.

### 3.3.3. Test Options

Looking back at the control region of the program, the first test that is available for the user to use is a simple tension or compression test. This is the most basic test that you can perform on this machine and only requires desired displacement rate and direction the test will perform as seen in Figure 3.12.

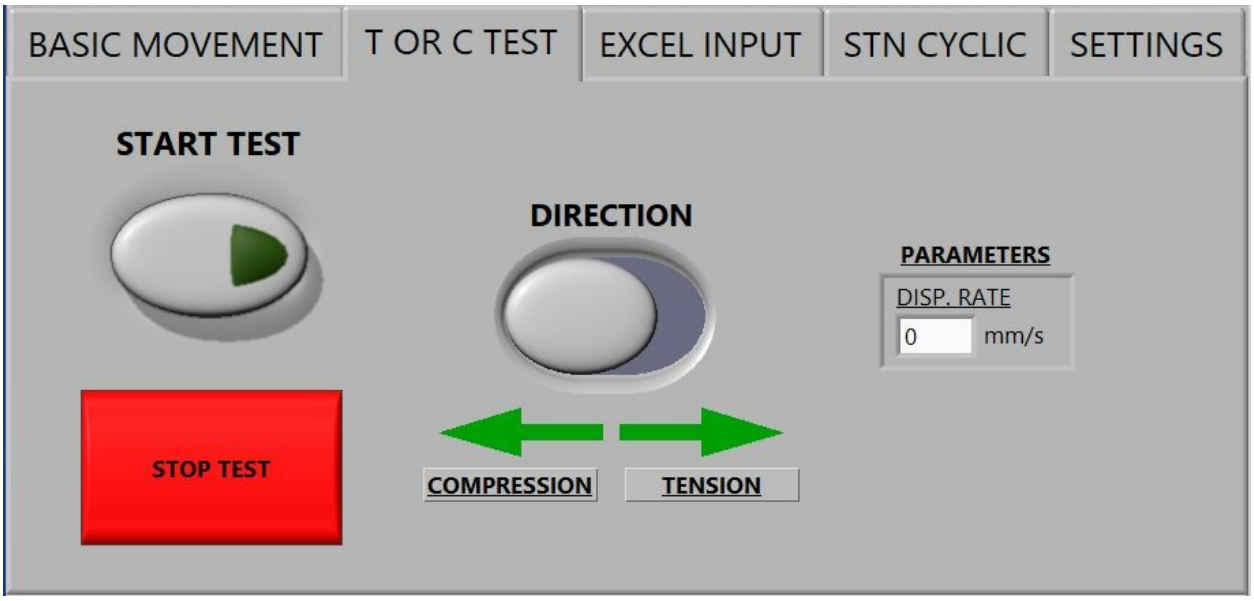


Figure 3.12: Tension or compression test panel.

The next test the user can select is an Excel-driven parameter test. This option is currently not functional, but the goal of this test option is to allow the user to specify any type of loading path which will allow infinite testing combinations. Whether this loading path be driven by force, strain, displacement, or bounce between different options. The way this test option would work is that the user would import an excel sheet that contains two columns. The first column would be an integer that would correlate to a specific control option seen in Table 3.2. The second column would then be the corresponding value for that control option. Once the user specifies displacement rate and begins the test, the program will read one row at a time and continue to the next row once the current row's condition is met.

Table 3.2: Excel driven test parameters

| TYPE INDICATOR INTEGER | RESULTANT CONTROL |
|---|---|
| **1** | Force |
| **2** | Displacement |
| **3** | Strain |

The last test option available to the user is strain controlled cyclic tests. Within this tab there are three additional tabs which slightly varies the tests from one another. The first choice is to perform a simple cyclic test that bounces between a maximum and minimum strain limit for a prescribed number of cycles as seen in Figure 3.13. The user will input the desired displacement rate, maximum strain, minimum strain, and number of cycles in the test panel. The direction toggle directs whether the test will start in tension or compression. The second choice that is available is an incrementing min-max strain cyclic test which bounces between a minimum and maximum strain value, but these values can change after each cycle by a constant amount. The panel looks almost the same as the first test choice but next to the “MAX STRAIN” and “MIN STRAIN” there is an additional input box for the user to specify desired increment amount for each limit and this increment can be positive or negative.

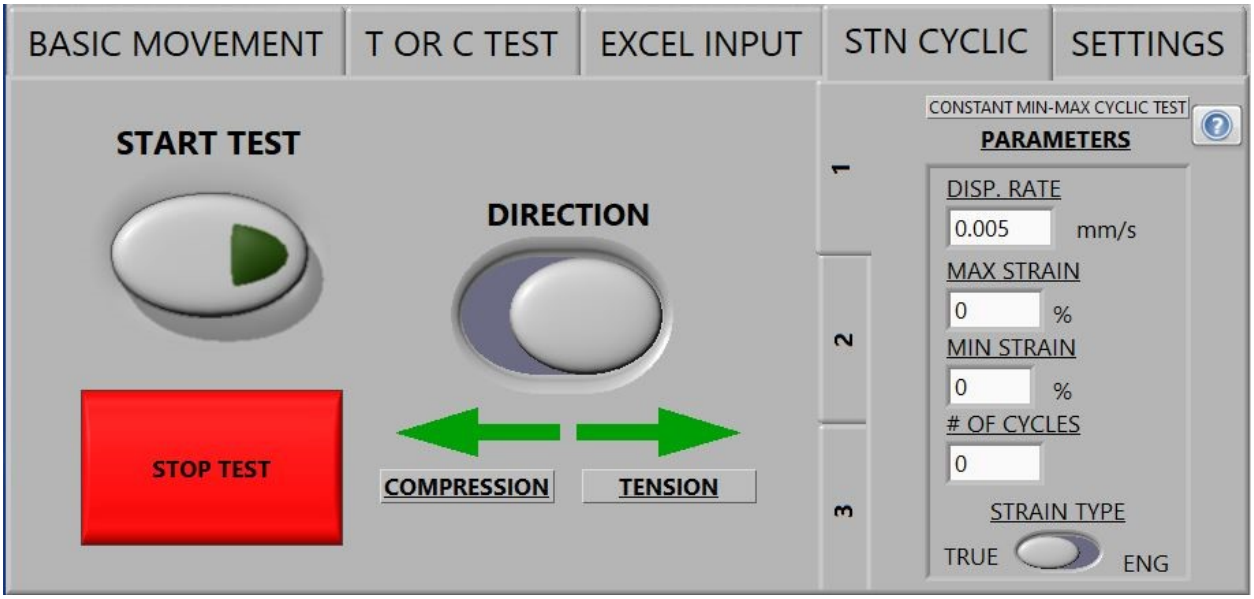


Figure 3.13: Standard min-max strain cyclic test.

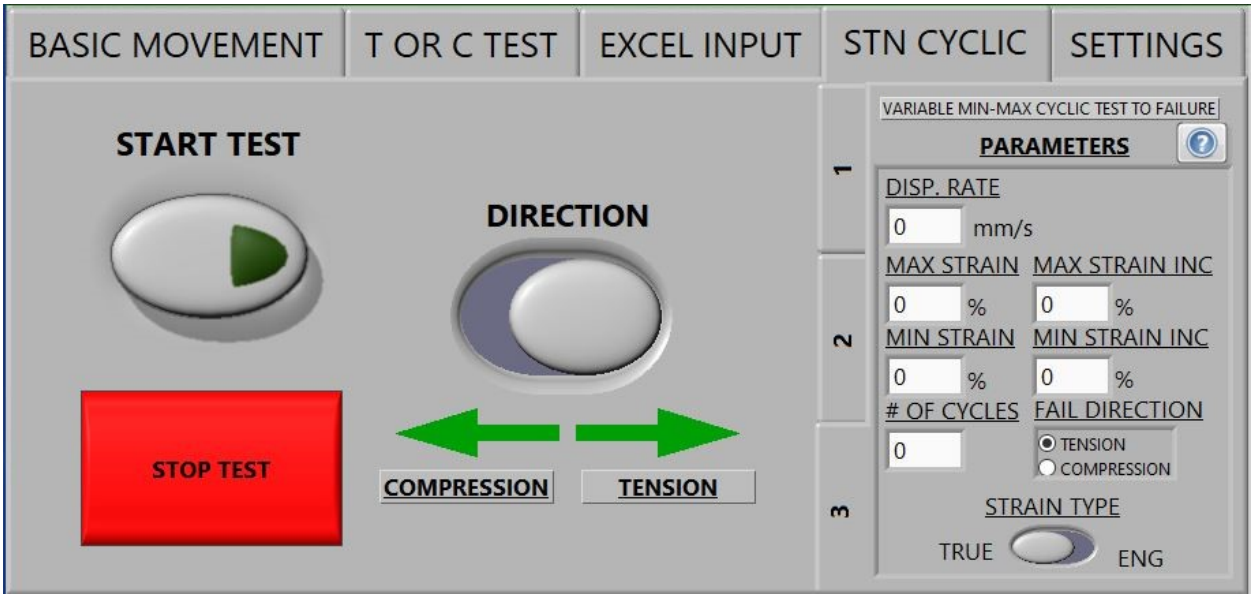


Figure 3.14: Variable min-max strain cyclic test to failure.

The last test choice the user has for strain cyclic tests is a variable min-max strain cyclic test which ends in failing the specimen in tension or compression. This panel can be seen in Figure 3.14 and is essentially the same layout as the second choice but with the added variable of which direction the specimen will fail in.

### 3.3.4. Calibration of Machine

Before any tests are to be performed, the machine must be calibrated. This includes zeroing out the hardware, determining the velocity characteristics of the machine, and warming-up the machine. By not completing one of these steps, the subsequent tests performed could prove to be inconsistent.

Zeroing out the hardware is made simple for the user by having toggle latches for both the load cell and position sensor which will take the current reading and subtract that value from future readings. The strain reading requires to be zeroed once the fixed side of the specimen is clamped and hand pressure is applied to the un-clamped side. If the user zeros the strain reading before installing the specimen, the results will most likely be incorrect due to natural bowing of the specimen outside of the workpiece holder.

To determine velocity characteristics of the machine, a subroutine was created to incrementally increase and decrease the voltage to the directional valve until a certain velocity is achieved in both directions. Before this subroutine is run, the user will need to specify a null voltage value which corresponds to no movement of the hydraulic cylinder. Since the velocity response is non-linear to voltage change, a table is created to store the voltage to velocity conversion values. The voltage-to-velocity conversion can be seen in Figure 3.15 which showcases why a linear conversion cannot be used. Null voltage is the value in which no movement occurs with hydraulic piston, and it is due to the overlap characteristics of the spool of the proportional valve used to control the actuator. With this calibration table, the starting velocity in a test will be closely matched in order to maintain a constant strain-rate.

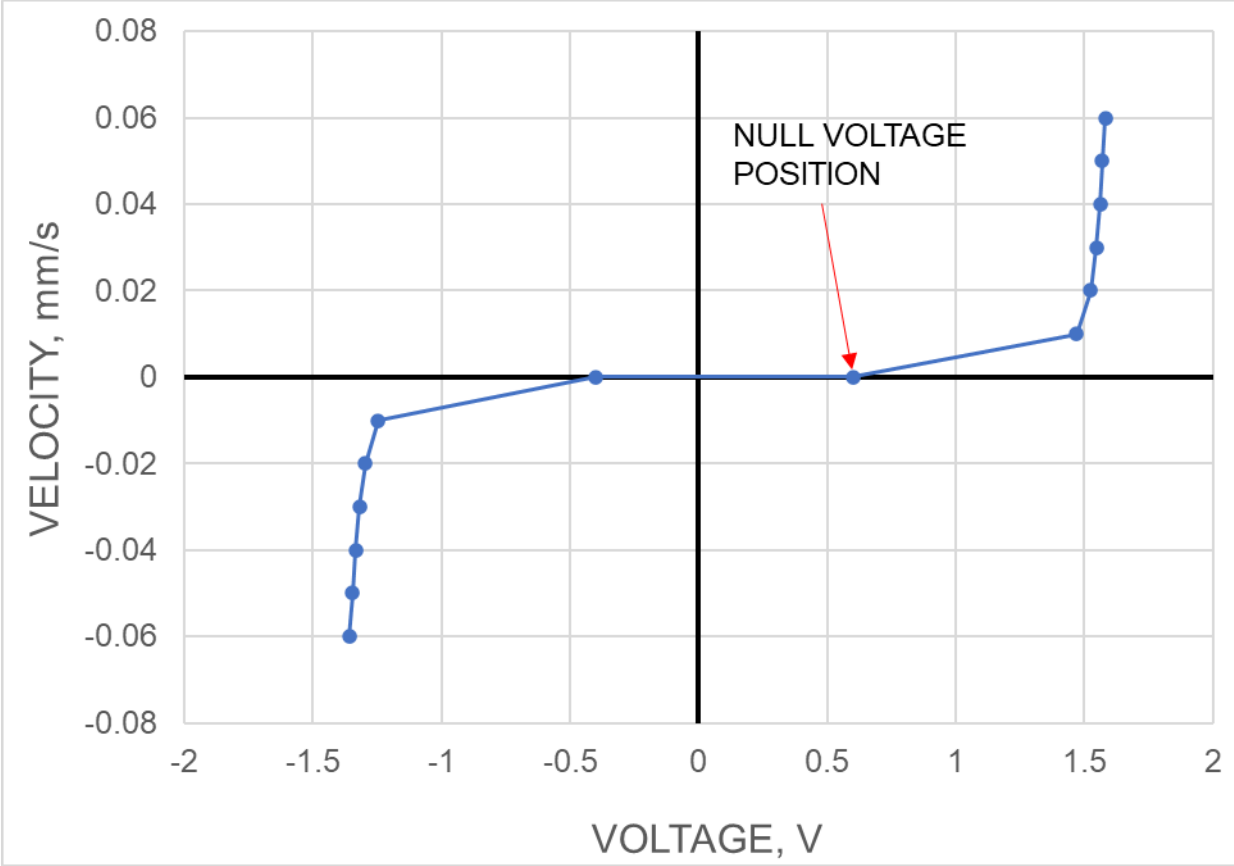


Figure 3.15: Input voltage command vs. output velocity for the proportional valve used in the CTC machine.

Warming up the machine is made simple for the user by having a switch in the settings tab, see Figure 3.8. The warm-up routine for the machine is to cycle the hydraulic cylinder +/- 8 mm (from the middle of the stroke) for 15 cycles, starting at 0 mm/s, ramping up to 1 mm/s by the end of the 1$^{st}$ cycle, and performing the rest of the cycles at that velocity. At the end of the warm-up cycle, a message will pop-up and notify the user that the warm-up is done. The warm-up routine is programmed to always start with the piston being at the middle of the stroke. If the piston is in a different location, then it is programmed to slowly move to the middle of the stroke and then start the routine.

# CHAPTER 4
# MACHINE VERIFICATION

## 4.1. Introduction

The previous chapters have covered how the machine was designed and programmed. This chapter will focus on how the machine was verified to perform as intended. This will begin with analyzing signal stability and the comparison of input commands vs. output results. After verifying that the machine is behaving appropriately, its output will be compared to another testing machine performing the same test on the same material. Along with verifying that both machines provide the same data, the effect of different specimen geometries will be compared as well. Lastly, friction compensation will be discussed, as well as how this issue is mitigated and accounted for in day-to-day testing.

## 4.2. Initial Checks

### 4.2.1. Stability of Signals with Time

Before any test can be performed, it needs to be verified that the output signals are stable and have low noise. The stability of the signal was analyzed by recording data for 30 minutes (1800 s) with the hydraulic pump on after being warmed up, and again with the pump off. The results of these tests can be seen in Figure 4.1 and Figure 4.2. It can

be observed that the at-rest signals can be considered stable, as the force reading fluctuates to within about 15 N (or 0.016% of the rated capacity of 88.96 kN of the load-cell), and the displacement reading moves about 0.014 mm (or 0.022% of full-scale value of 63.5 mm) over the full duration of the recording. The same observations can be made for the amount of noise seen in both readings which is roughly +/- 5 N and +/- 0.002 mm.

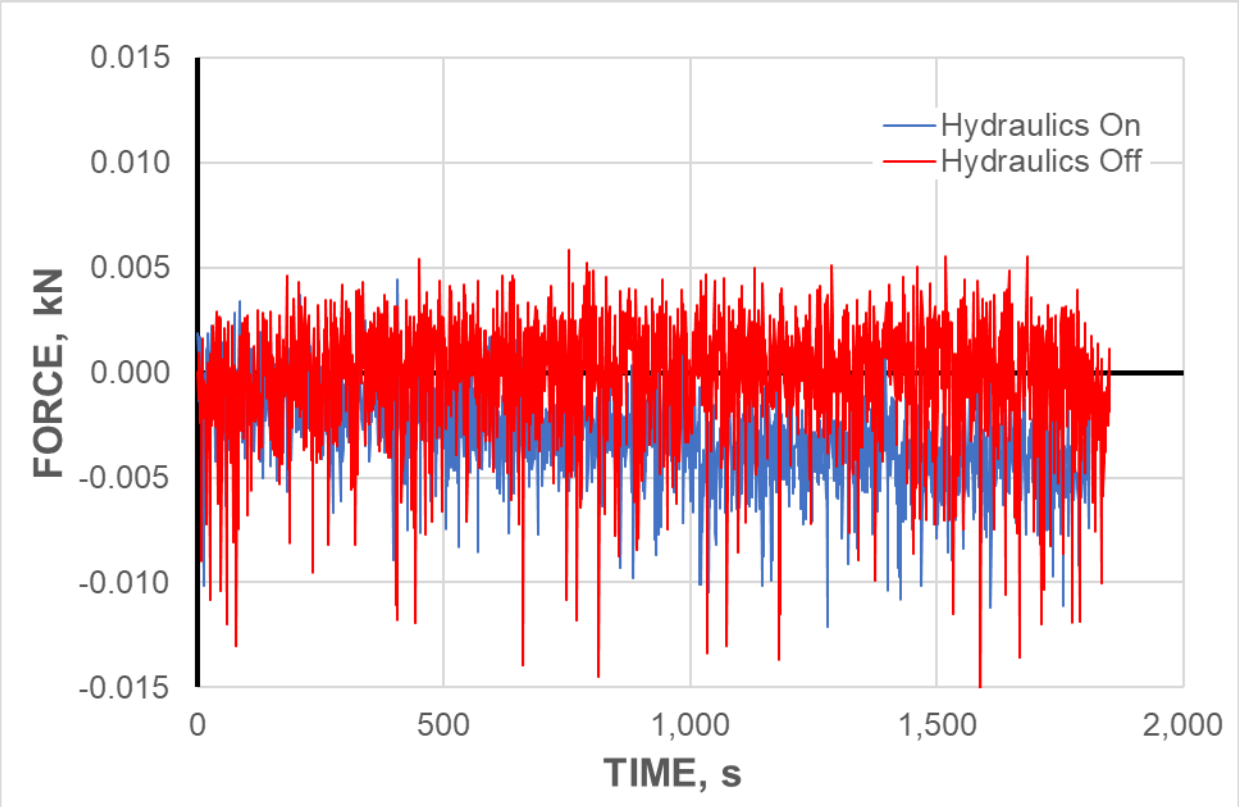


Figure 4.1: Stability of force signal at rest, with hydraulics on or off.

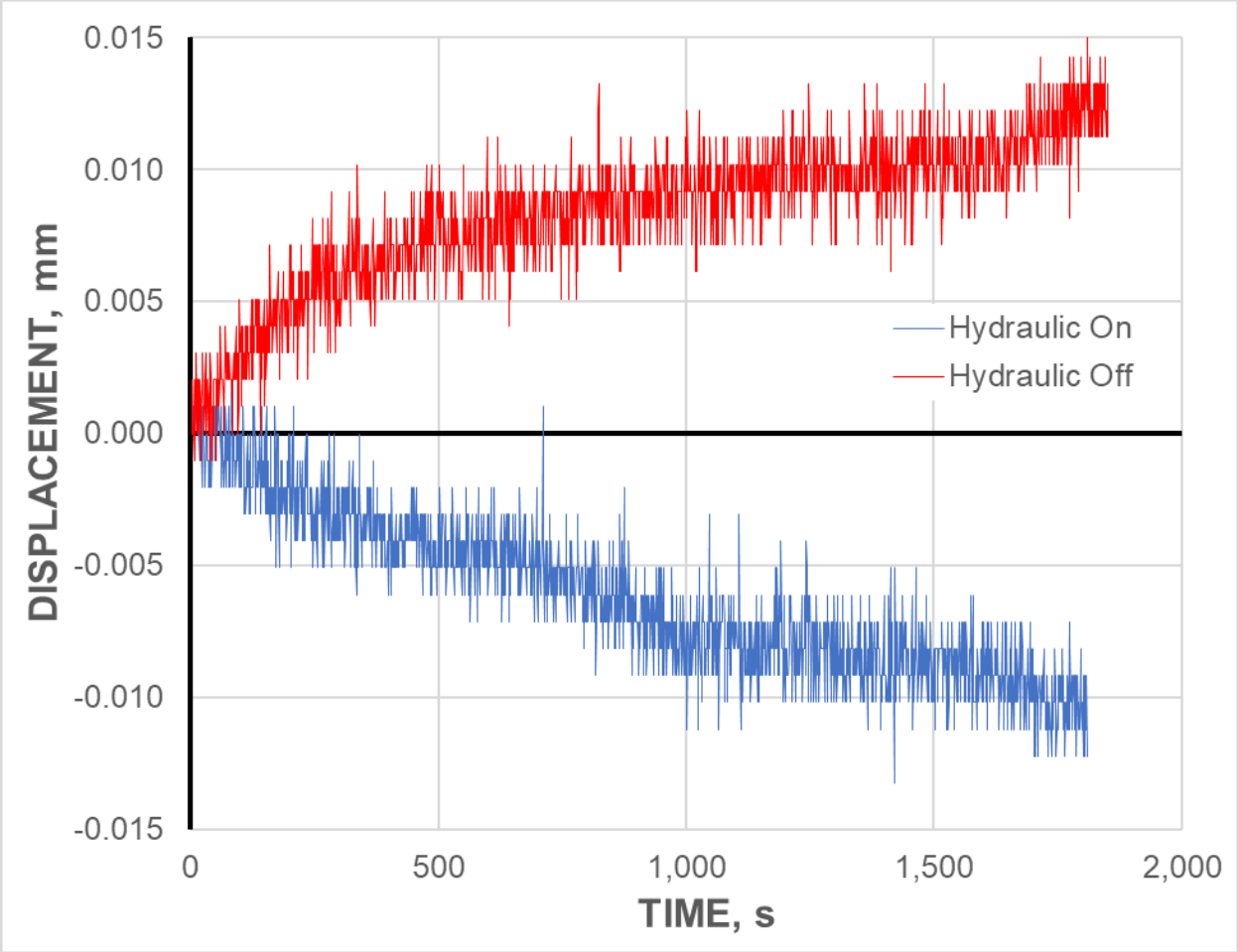


Figure 4.2: Stability of displacement signal at rest, with hydraulics on or off.

### 4.2.2. Comparison of Input vs. Output

To verify that the machine is providing the correct movement based on the input, a simple saw tooth movement test was performed. Before this test, the hydraulics were warmed-up for 15 minutes running a cyclic movement program. The test entailed running the machine in a cyclic fashion, moving between 0 and 3.9 mm, or 0 to 5% strain over the 78 mm gage-length of the CTC specimen. (No specimen was used for this test.) This motion was repeated 5 times to ensure repeatability, and the overall test was repeated several times to compare the results at 4 different crosshead velocities.

Starting with a velocity of 0.06 mm/s, which is the most common velocity used for the CTC specimen, the displacement vs. time is shown in Figure 4.3. Looking at this graph, it can be claimed that the agreement between input and output is excellent. Furthermore, it can be noted that the velocity at the beginning of each direction in the first cycle has a curve before straightening. This curve is due to the voltage to the proportional valve being adjusted to meet the desired velocity of 0.06 mm/s, and will be found in every test to some degree.

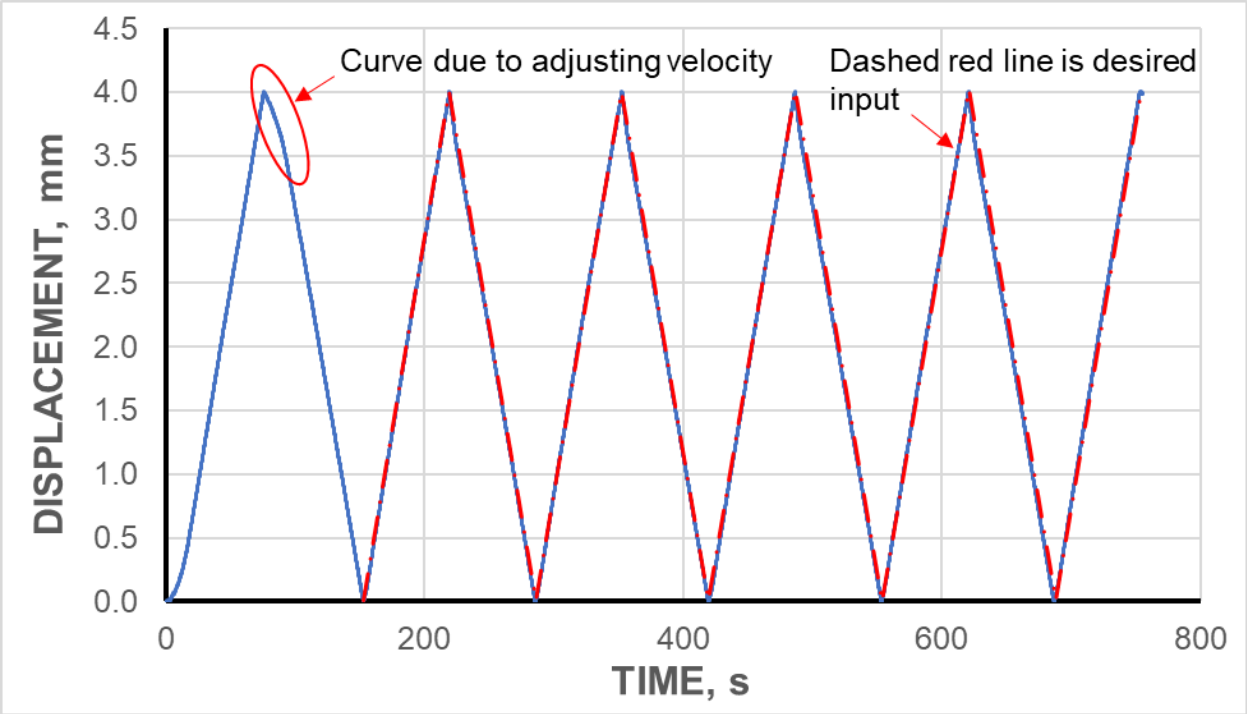


Figure 4.3: Displacement vs. time of saw-tooth verification test at a velocity of 0.06 mm/s, showing input (dashed red line) and output (solid blue line).

Overlapping the cycles from the same test (excluding the 1st cycle), as seen in Figure 4.4, showcases the machine's ability to repeatably reverse direction without overshooting,

as well as to maintain a stable testing velocity. When looking at the tests ran for the other velocities, the same conclusions can be drawn, as seen in Figure 4.5.

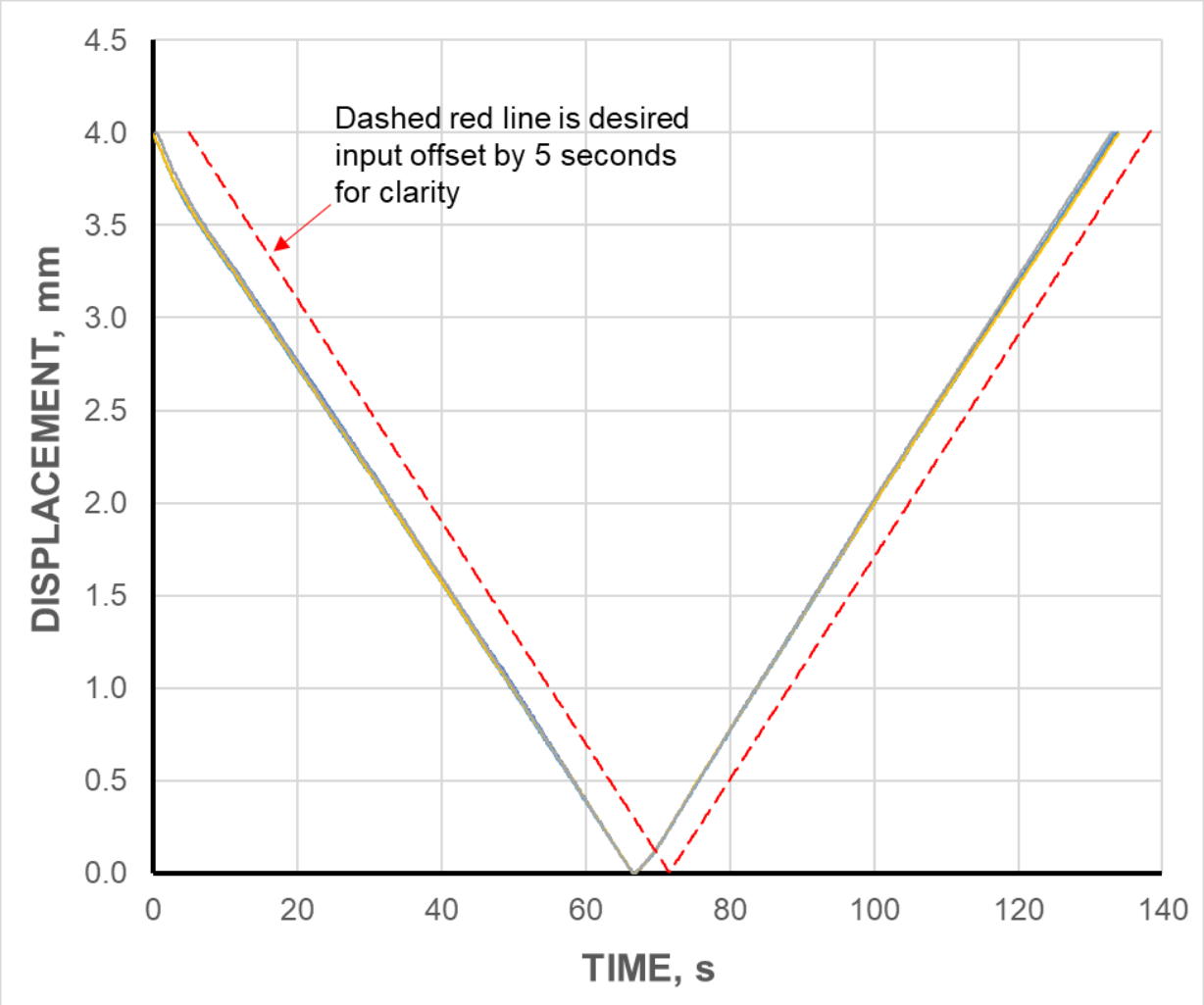


Figure 4.4: Overlapped multiple cycles (between 220 and 750 seconds, see Figure 4.3) from displacement vs. time of saw-tooth verification test at a velocity of .06 mm/s. Also included is the input signal. The machine is repeatably following the input command very well.

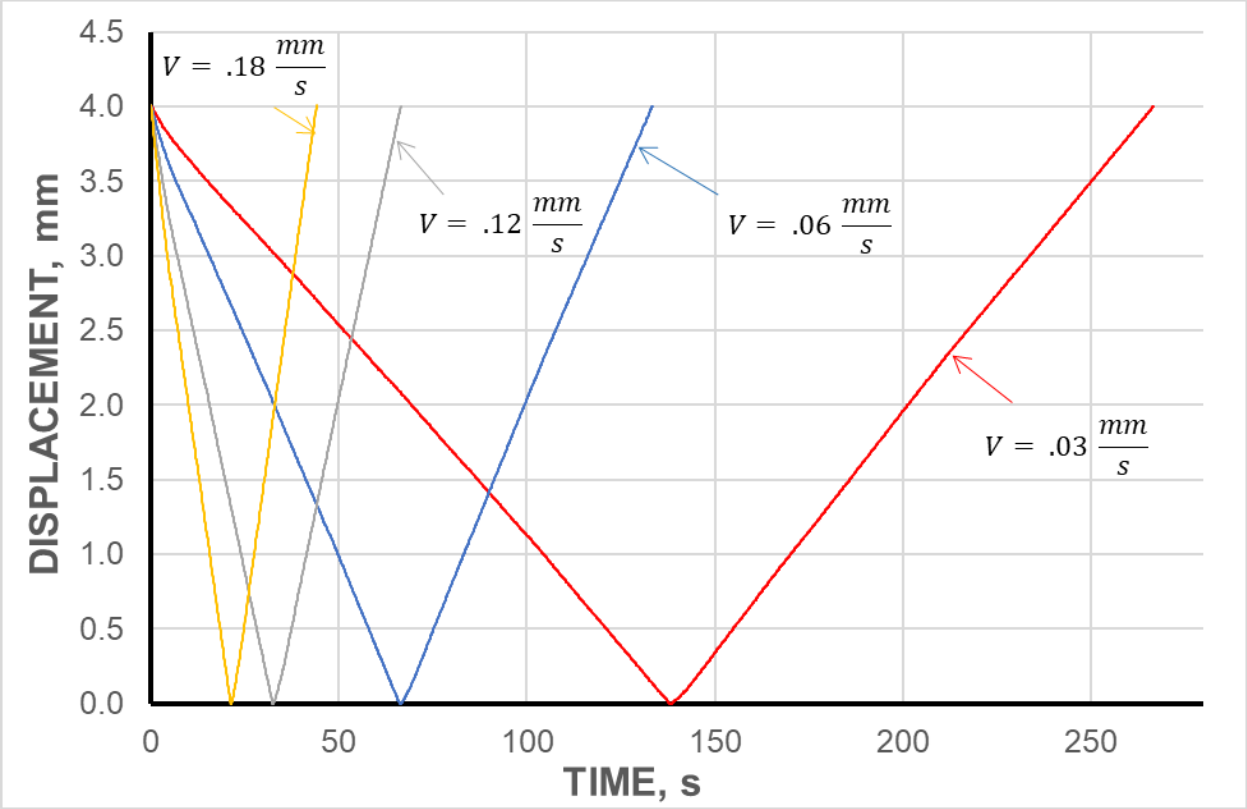


Figure 4.5: One displacement vs. time cycle from each saw-tooth test.

The force recorded in these specimen-free saw-tooth tests is plotted in Figure 4.6. It is observed to have a discrepancy of +/- 15 N from zero, or about +/- 0.03% of the full-scale. The force vs. displacement did not change shape regardless of the velocity that the test was ran at, although the force reading is significantly noisier in tension than compression. This increased noise is most likely due to the rod alignment coupler (see Figure 2.1) because of how the joint is designed, and where the displacement reading is taken: when the joint is in tension it will jolt as it overcomes static friction at low velocities and with no specimen installed. Since the displacement reading is taken at the hydraulic cylinder (see Figure 2.1), this small displacement surge is not seen in that reading but will be seen in the force reading. When in compression, the joint does not engage a flexible member that can induce surging, therefore the noise is not seen. This noise is not seen

as an issue, since it is not seen at higher velocities, or when a specimen is installed. The friction itself will need to be accounted for; that topic is further discussed in Section 4.4.

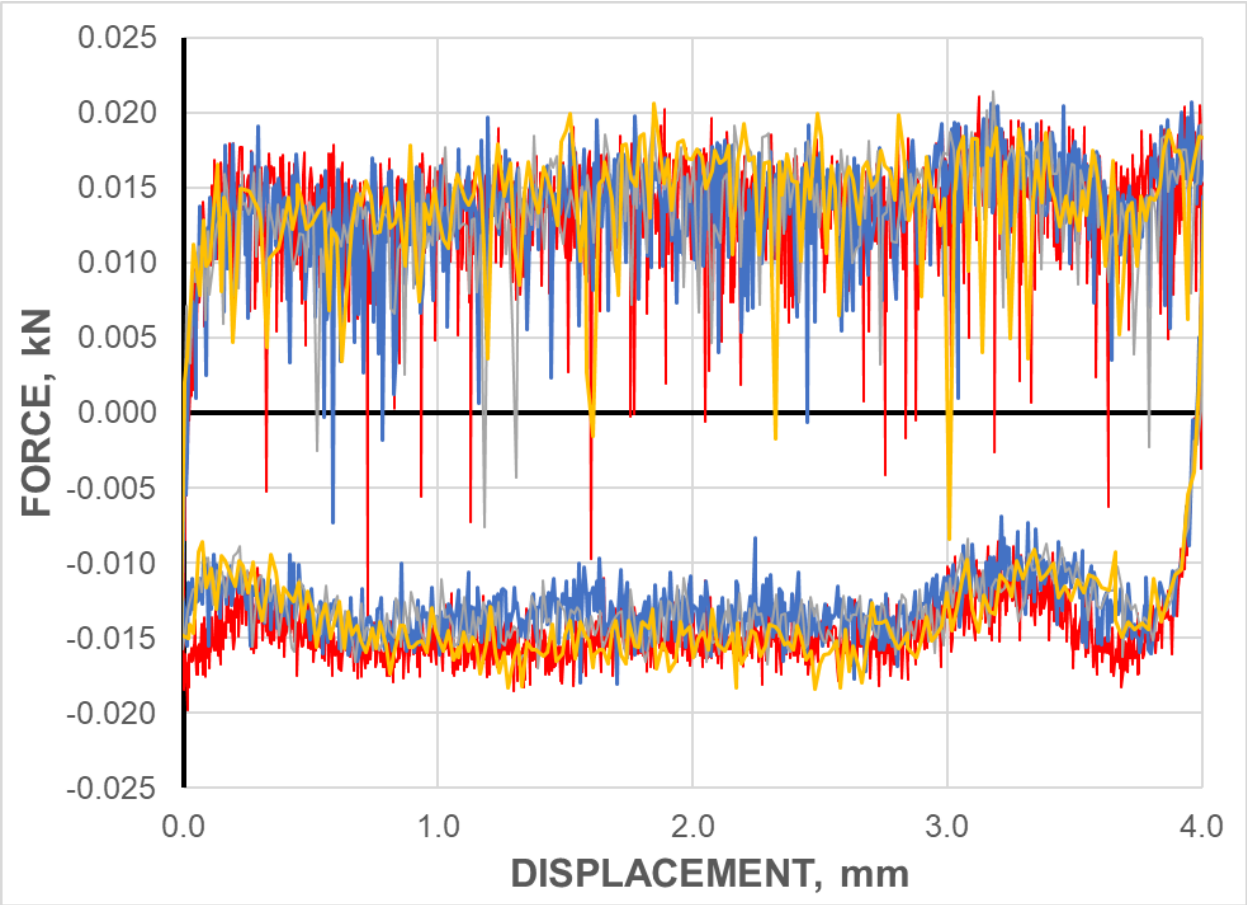


Figure 4.6: Force vs. displacement of saw-tooth verification tests at different velocities ranging from .03 - .18 mm/s (same colors as in previous figure).

## 4.3. Verifying Results from the CTC Machine

Now that we have verified that the CTC machine behaves as intended, i.e., follows the commands of the user with no unwanted or unexpected response and no excessive noise, the next step is to verify the measurement signals with another machine, that is

already verified to be correct, by performing the same test on both machines. In this way, it can be verified that the CTC machine gives accurate results.

The first machine used as the control is an MTS Landmark 370 servo hydraulic testing machine of 250 kN capacity, which will be referred to as “MTS” for the rest of this paper. This verification will be shown once again in Section 4.3.2 by comparing a full cycle test with another CTC machine located with the Kuwabara group at Tokyo University of Agriculture and Technology (TUAT).

### 4.3.1. Comparing CTC Machine to MTS

The test performed to verify the CTC machine is a standard uniaxial tension test following the ASTM E8 standard [14], using a sheet-type specimen from AA6022-T43 (1.2 mm thick). The strain-rate used was 0.0012 /s. The strain was measured using a mechanical extensometer on the MTS and a strain-gage on the CTC (Kyowa KFEM-1-120). When performing the test on the CTC, no blank-holding force was used, and the upper combs (see Figure 2.4) were not installed. This was done to keep the constraints as similar as possible to the MTS. The test was repeated three times for each machine and the results can be seen in Figure 4.7. As mentioned in Section 3.2.1, the strain-gage signal is limited to 5% engineering strain, for DAQ reasons. This does not imply that the CTC machine is not capable of applying larger strains to a specimen.

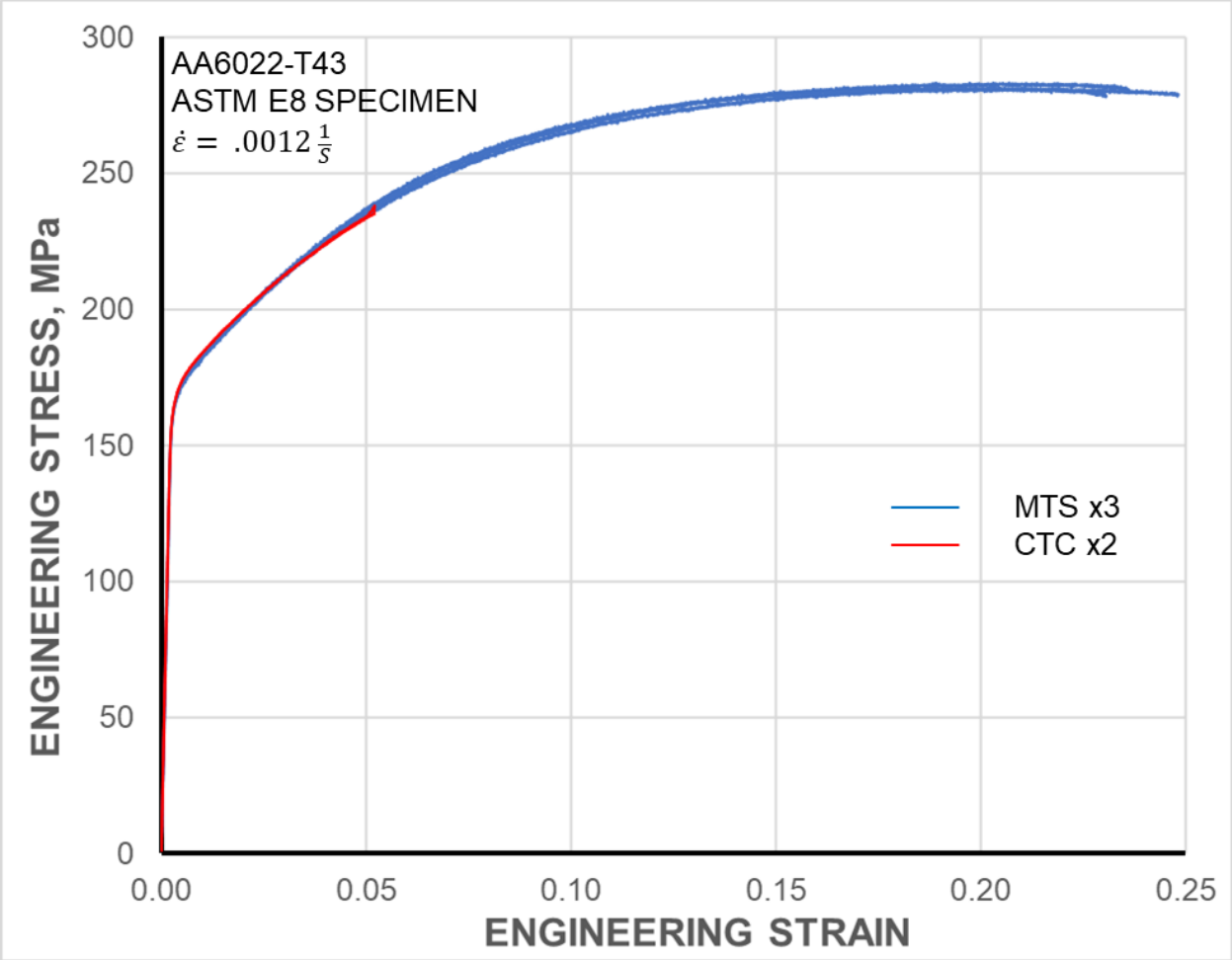


Figure 4.7: Comparing MTS to CTC machine with AA6022-T43 ASTM E8 uniaxial tension specimens.

As seen in the figure above, the agreement between both machines is very good. The third CTC test was omitted due to issues in the elastic region at the beginning of the test which stemmed from the specimen being slightly buckled before the test began. Note that there are slight differences in the rate of plastic work-hardening between the tests ran on the MTS vs. the CTC, but this is most likely due to differences in hardware used for strain acquisition.

As a further test, this comparison was repeated using specimens from Extra Deep-Drawing Quality (EDDQ) steel (1 mm thick). Looking at Figure 4.8, the same agreement between experiments of the two types of machines can be seen, therefore providing assurance the CTC machine produces reliable results.

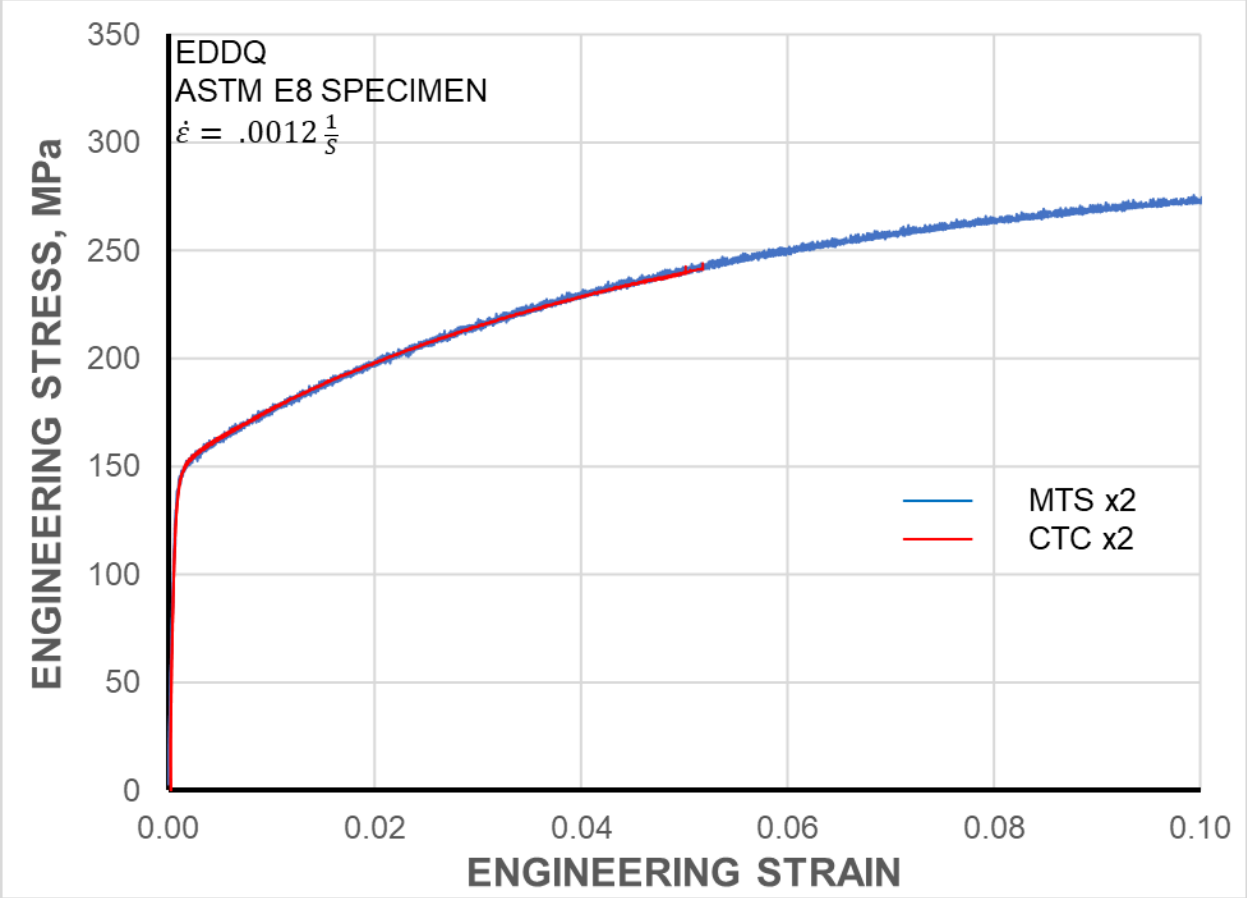


Figure 4.8: Comparing MTS to CTC machine with EDDQ steel ASTM E8 uniaxial tension specimens.

### 4.3.2. Comparing Two CTC Machines

To further verify the agreement seen, the same cyclic tests were performed on JAC-270D (0.8 mm thick) on this CTC machine and the CTC machine located at TUAT. To not

have confusion between the two machines, the CTC machine described within this paper will still be referred to as CTC and the machine located at TUAT will be referred to as TUAT from this point forward.

The cyclic tests performed were +/- 4% true strain for one cycle with one test type starting in tension and the other starting in compression. “One cycle” in these tests is defined as two load reversals, after the initial prestrain (which is not counted as a half cycle). Therefore, for this test the specimen will be prestrained to 4% then compressed (i.e., “cycled”) to -4% and pulled to +4%, before unloading. As for the parameters used for this testing in the CTC, Table 4.1 presents the applicable information.

Table 4.1: Parameters used in cyclic test comparison of CTC to TUAT machine

| PARAMETER | VALUE |
|---|---|
| BLANK HOLDING FORCE | 6.25 kN (1,405 lbs) |
| DISPLACEMENT VELOCITY | 0.06 mm/s (0.0024 in/s) |
| STRAIN-GAGE USED | KFEM-1-120-C1L1M2R |
| CURE TIME | 4 HOURS |

Initial inspection of Figure 4.9 and Figure 4.10 shows that the agreement between the two machines is very good. The largest discrepancy that can be seen clearly, is the difference in the transition from elastic to plastic strain after load reversal, which could be due to a few reasons, but this was not of immense concern. It should also be noted that the data in all the graphs comparing the two machines is raw data that is not corrected for machine friction, as it was not clear how this is done at TUAT.

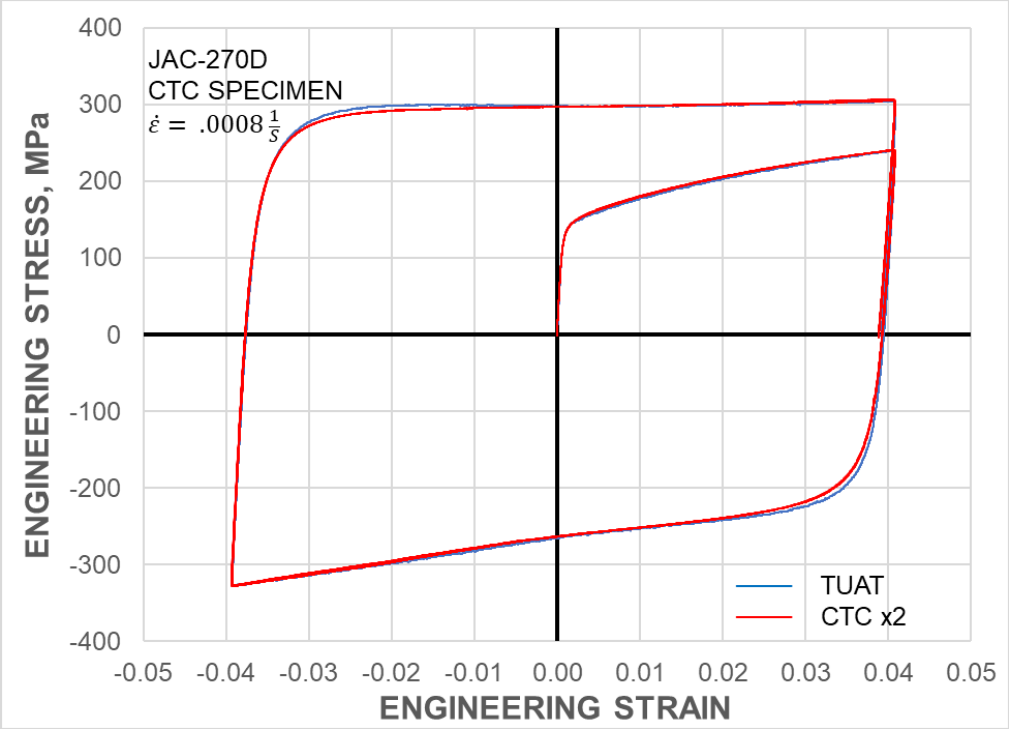


Figure 4.9: Tension-compression-tension test between CTC machine to TUAT machine. The data shown are raw, i.e., not compensated for friction.

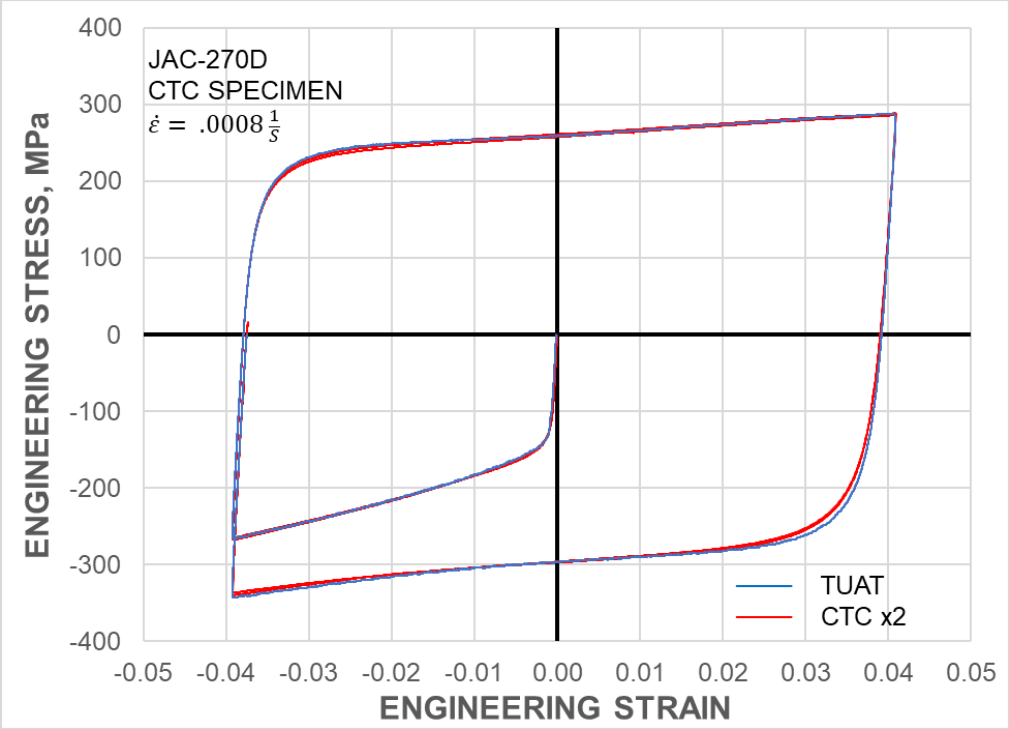


Figure 4.10: Compression-tension-compression test between CTC machine to TUAT machine. The data shown are raw, i.e., not compensated for friction.

Looking at Figure 4.11, which is a zoomed-in portion of Figure 4.9, it can be seen there is a small cusp (less than 2% of the max. stress recorded in these tests) in the data for both machines at the same strain. This is theorized to be due to slight buckling of the specimen since the gripped areas of the specimen will not thin as much as the gage section would. This creates a small gap that the specimen can buckle within but is unavoidable with these machine designs. Still, as can be seen from Figure 4.9 and Figure 4.10, this does not have any impact on the quality of the test results obtained with either of the two machines.

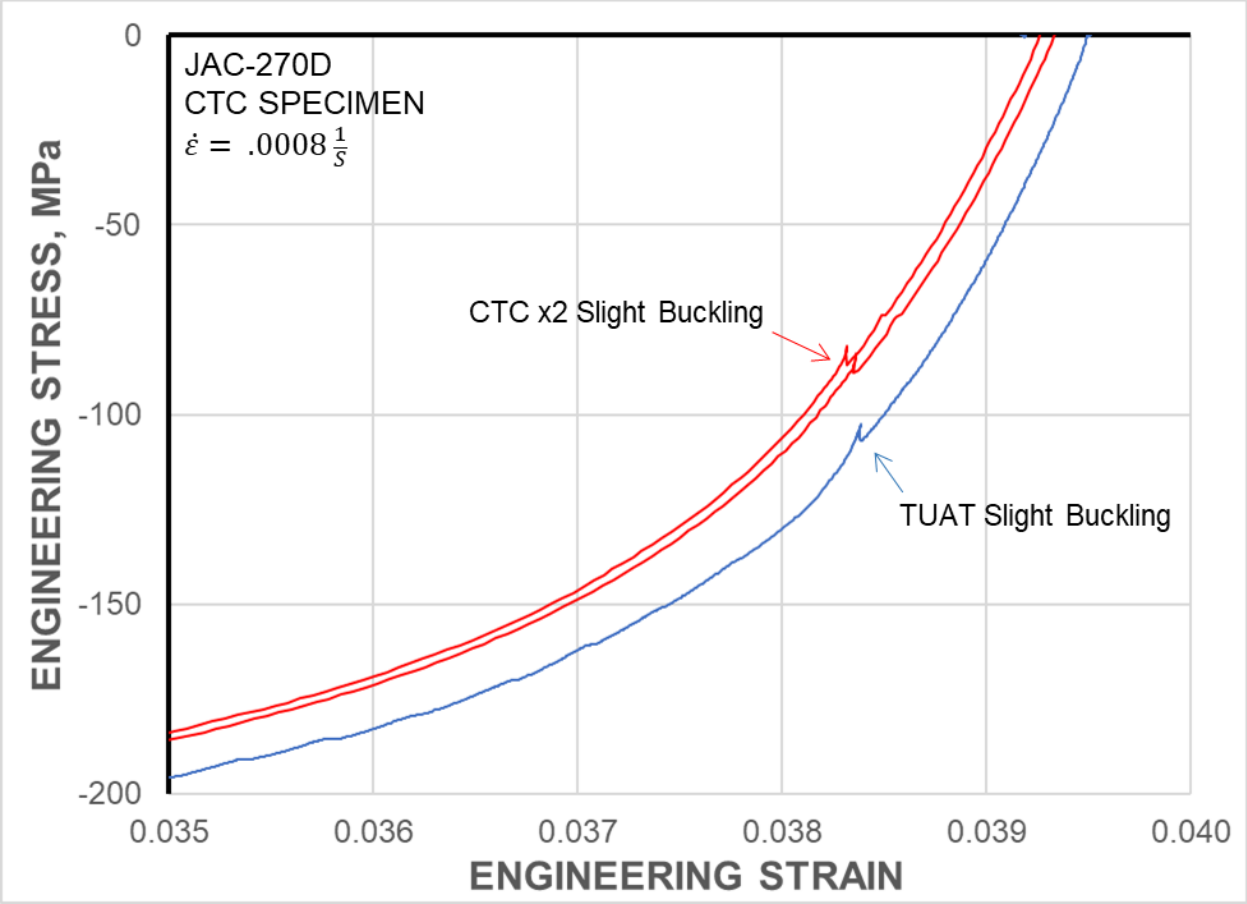


Figure 4.11: Magnified view of Figure 4.9, showing slight buckling in both CTC machines. The data shown are raw, i.e., not compensated for friction.

Figure 4.12 displays a zoomed in portion of Figure 4.9, with the unloading data removed for clarity. It can be observed that the measurements from the machines before the elastic-plastic transition and after the plastic knee in the curve are nearly overlapped. The data begins to deviate between the CTC and TUAT machine around -50 MPa and continue to deviate to a total max. difference of about 14 MPa. After this point, the data re-converges to nearly the same trend until the next elastic-plastic transition where the same phenomenon occurs.

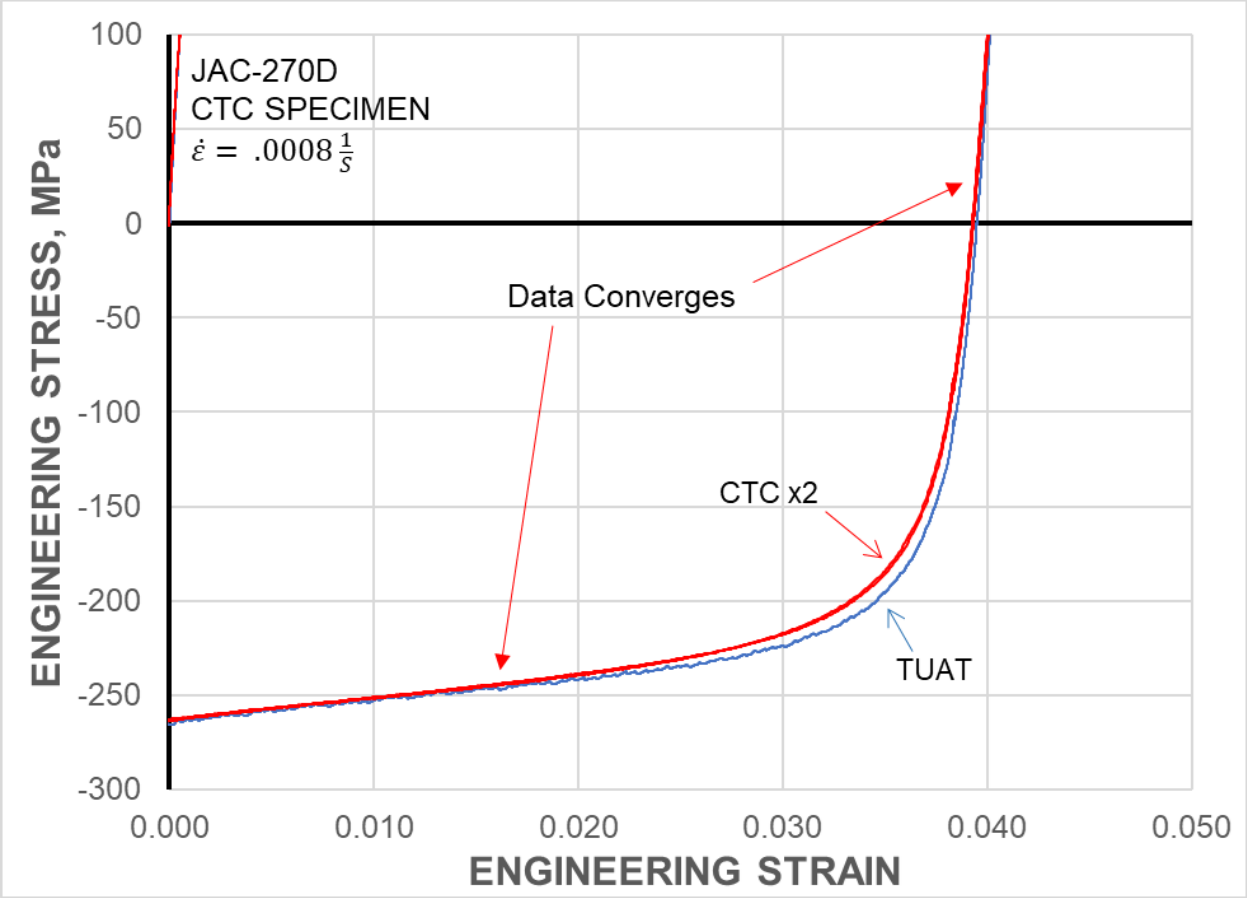


Figure 4.12: Comparing results from the two CTC machines in elastic-plastic transition regions. The data shown are raw, i.e., not compensated for friction.

### 4.3.3. Specimen Geometry Verification

Now that the CTC machine is verified to provide accurate results, the next task is to verify the CTC specimen will give comparable results to ASTM E8 specimens. Recall that the CTC specimen has a significantly different aspect ratio of the in-plane dimensions of the gage-section, in comparison to the standard ASTM one (e.g., see Figure 2.3 and Figure 1 in ASTM E8 [14]). For that comparison, two tension tests were done on the CTC machine: one using the ASTM specimen, and the other the CTC one. No upper comb dies were used. The strain was measured in both cases with strain-gages. The displacement rate was set to 0.06 mm/s. It should be noted that this was a mistake, since the two specimens have different gage-lengths (50 mm for the ASTM E8 and 78 mm for the CTC one). Therefore, by not adjusting the velocity, the strain-rate between the two specimens is somewhat different (0.0012 /s for the ASTM E8 vs. 0.0008 /s for the CTC one). However, this difference is almost a negligible issue, due to the magnitude of the strain-rate and the use of a 6xxx aluminum alloy, which is not rate-sensitive in that range (e.g., has an m-value between 0.001 and 0.002 [15]). Looking at Figure 4.13, there is a minute but constant separation between the ASTM and CTC specimen in the plastic range. This difference is about 1% and can be due to a combination of specimen-to-specimen variation and the 33% difference in the strain-rate. Looking at Figure 4.14, one of the CTC specimens overlapped the ASTM E8 specimen until the strain-gage peeled off, which terminated that specific test early.

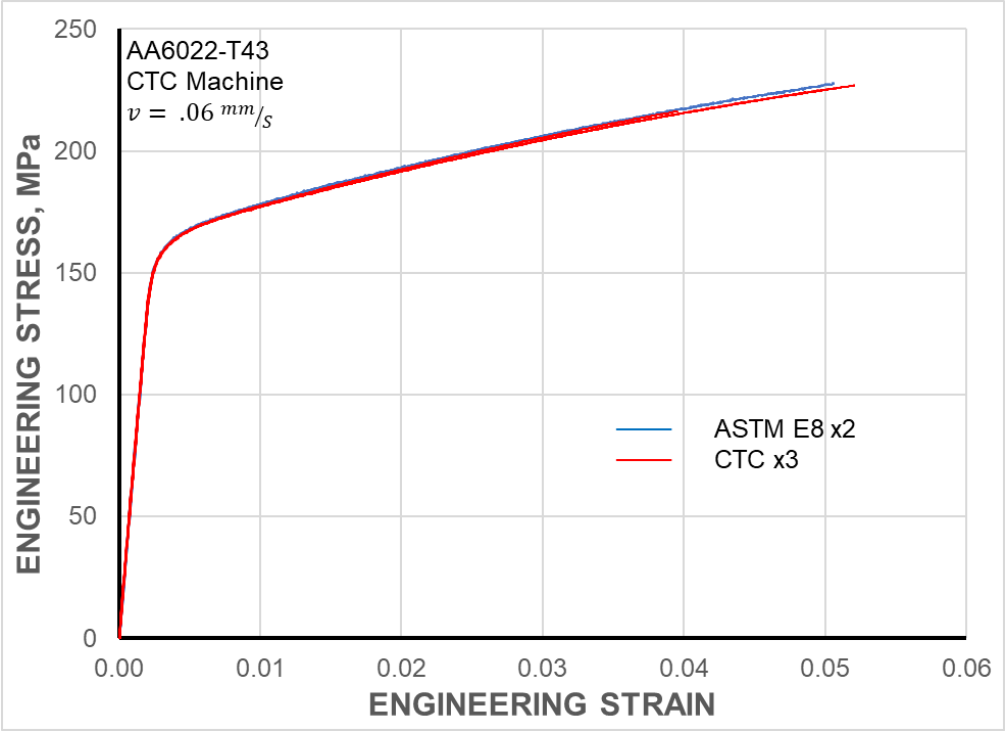


Figure 4.13: Comparing ASTM E8 to CTC specimens on CTC machine using AA6022-T43.

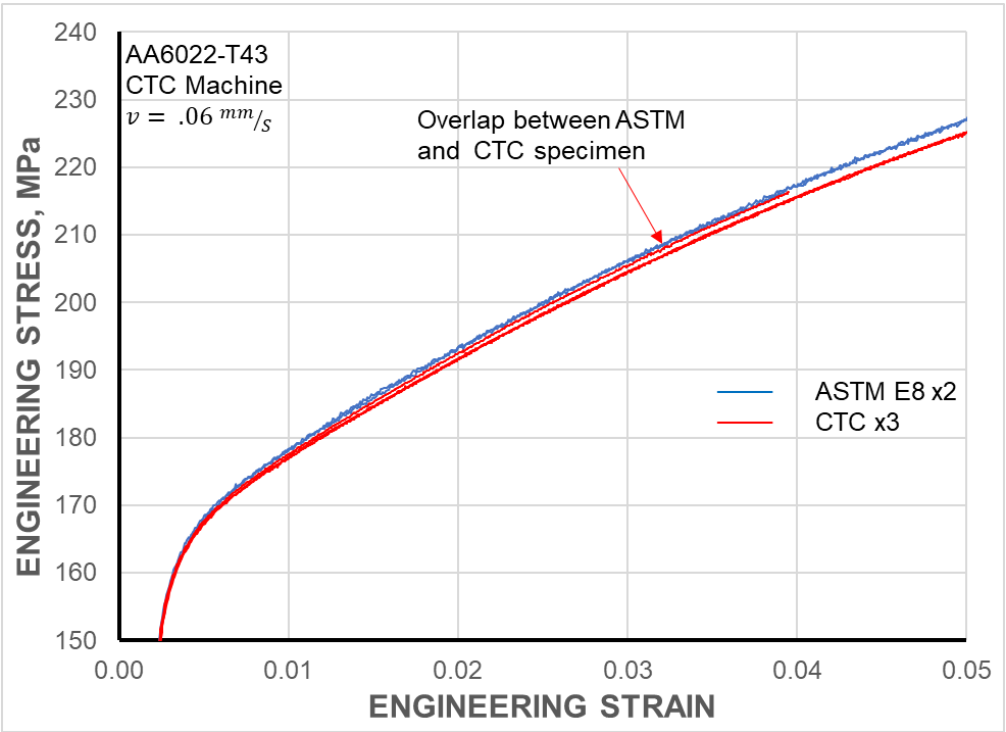


Figure 4.14: Zoomed-in portion of comparing ASTM E8 to CTC specimens on CTC machine, using AA6022-T43.

Repeating the test using EDDQ, the same results can be found in Figure 4.15. The difference between the two specimen types is still about 1%, which is presumably due to the same issues stated previously. A drop in the stress can be seen in one of the CTC specimen tests, due to the grip slipping and re-engaging the specimen. The occurrence lasted one second and did not affect the data after this point, since it reconverged with the other test.

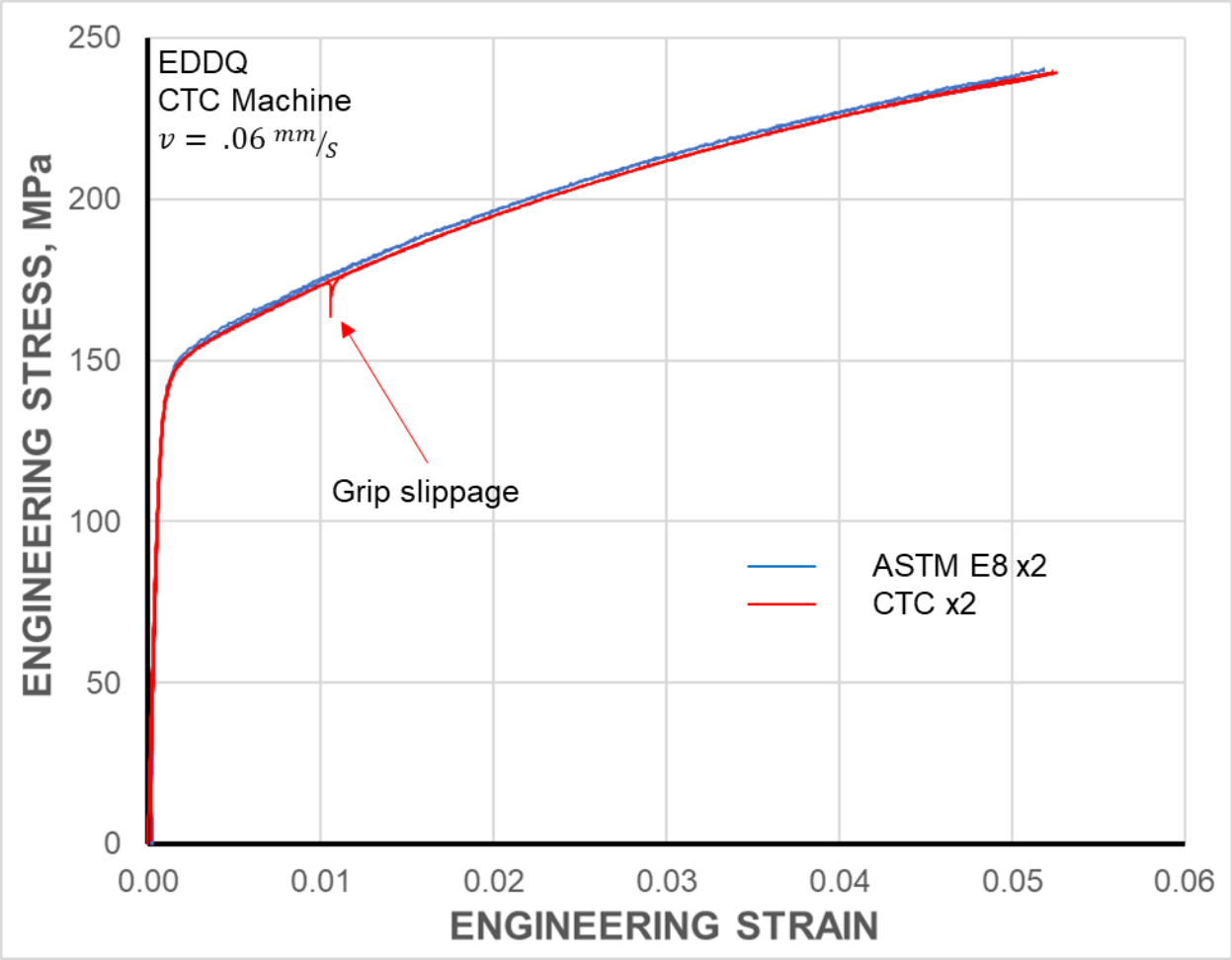


Figure 4.15: Comparing ASTM E8 to CTC specimens on CTC machine using EDDQ steel.

## 4.4. Friction Compensation

An inherent problem with how this machine operates is friction between the specimen and comb dies, as well as between the moving parts of the machine itself. These two are tackled separately in this section, and a method to compensate for the friction is described.

### 4.4.1. Friction Internal to the Machine

The friction within the machine was seen back in Section 4.2.2, where the friction corresponded to about +/- 15 N (or +/- 0.03% of the full-scale) in the horizontal direction. This is a small amount in comparison to the loads seen from testing, and is further confirmed from Figure 4.7 and Figure 4.8, which show almost no difference between the MTS and CTC tension tests.

To ensure there is not a significant increase to the machine-induced friction when blank-holding is applied, a study was conducted to observe the sensitivity of the horizontal force to the blank-holding one. This study was performed by installing the upper comb die assemblies without a specimen and cycling the machine at decreasing blank-holding loads starting at 12.5 kN (2,810 lbs), i.e., 25% of the full capacity, all the way down to zero. The machine would go through one “tension-compression” cycle (i.e., the cylinder retracting and then extending) at a time; after that, the user would decrease the blank-holding pressure by 1.38 bar (20 psi), which translates to about 2.5 kN (565 lbs), and repeat the cycle. When the pressure became zero, the machine performed one more cycle, with the upper plate of the die set (see Figure 2.1) resting on the upper comb dies (i.e., self-weight), and one more with that plate lifted. Each cycle started with the comb

teeth fully engaged, and retracted the hydraulic cylinder so that the comb teeth became fully disengaged.

The results are seen in Figure 4.16. The machine friction can be broken into two parts depending on whether the comb teeth are engaged, as well as whether the system is in tension or compression. Starting at zero displacement (i.e., comb teeth fully engaged) and retracting the actuator, there is a slight decrease in friction as the teeth progressively disengage. After 30 mm of displacement the comb teeth are fully disengaged, and this results in a constant friction force. Similarly, when the direction reverses, initially there is a constant force (i.e., between 50 mm and 30 mm). Upon the teeth re-engaging at 30 mm, the force starts to rise (in absolute terms) again, until the end of the stroke (actuator fully extended, i.e., zero displacement). For the maximum blank-holding force, this change of friction force is about 20 N (4.5 lbs) from fully engaged to fully disengaged, for either direction.

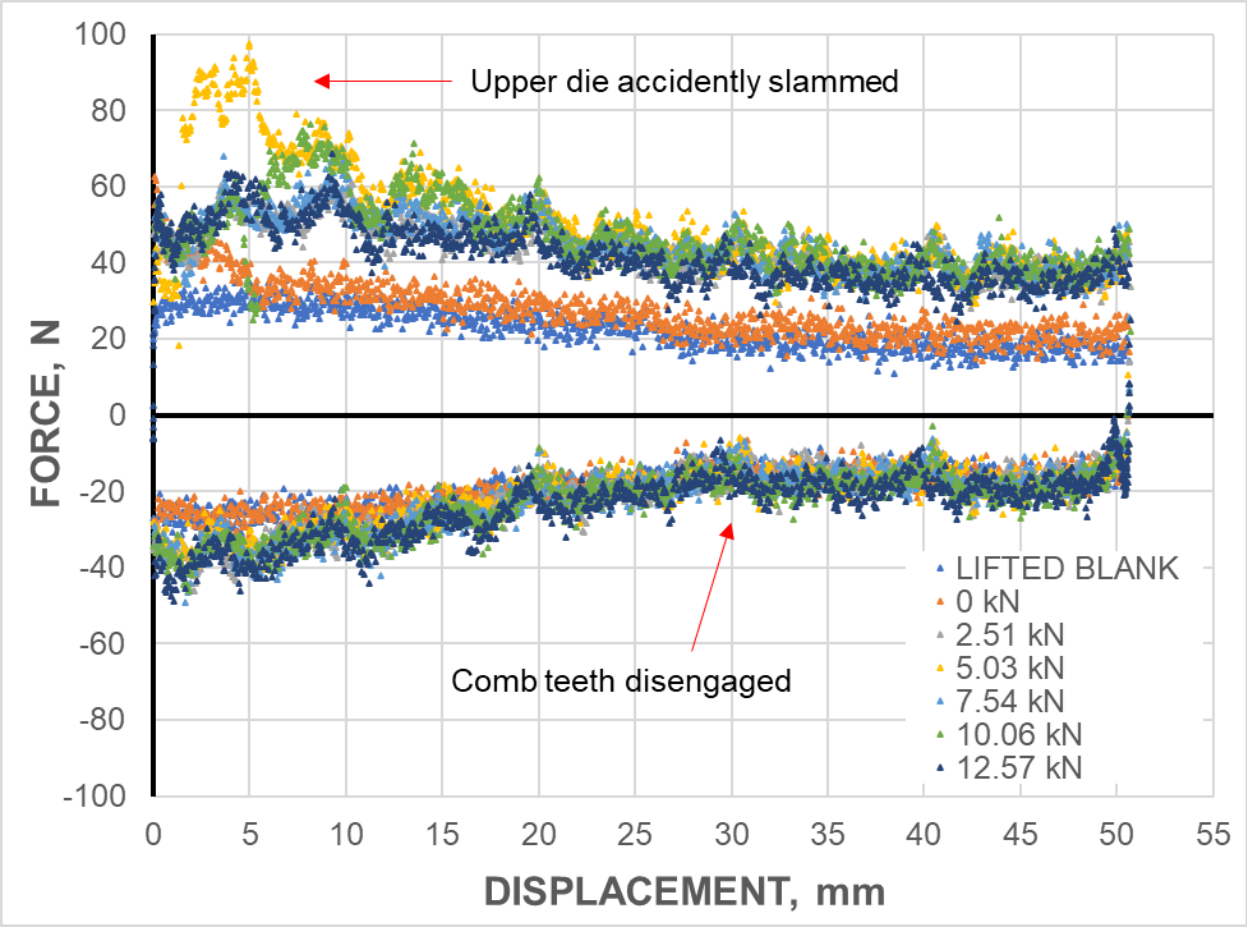


Figure 4.16: Machine friction at various blank-holding pressures over the majority of the stroke.

The friction in tension with the comb teeth fully disengaged (i.e., displacement values over 30 mm), is about 17 N (3.8 lbs) over that of compression (using absolute values). Looking at the maximum difference possible from this study, adding the two parts of friction together, produces a deviation of 37 N (8.3 lbs). What this implies is if the data is adjusted towards the x-axis using only the tension data of the higher loading, the compression data can have up to 37 N (8.3 lbs) of error. This error value can either be a significant issue or negligible, depending on the material tested and cross-section used.

### 4.4.2. Friction Between Specimen and Machine

The previous results were obtained without a specimen and indicate a very limited effect of friction on the machine behavior. The greater potential issue is the friction due to the blank-holding force from supporting the specimen. This was investigated by looking at three scenarios: dry, lubricated, and combination of oil lubricant and Teflon sheets. The Teflon sheets used in all tests are 254 μm (0.010 in) thick and the type of lubricant used can be either E-900L ball screw lubricant or anything equivalent. A standard EDDQ steel CTC specimen was modified as shown in Figure 4.17 to allow for large displacements without the rotational pin pulling on the specimen. Using the modified specimen, only the fixed side was gripped, and then the upper comb dies were installed. A blank-holding force was then applied, and the hydraulic cylinder was retracted. Effectively, this caused the moving comb dies (see Figure 2.2 and Figure 2.4) to slide over the stationary specimen. In this way, the force that the load cell (see Figure 2.1) is measuring is equal to the frictional resistance between the comb dies and specimen, as well as the Bosch Rexroth ball guide rail to the track on which it rides on. Two blank-holding forces, 6.25 kN (1,405 lbs) and 12.5 kN (2,810 lbs), were tested for all three scenarios. A velocity of 0.06 mm/s was used in every case.

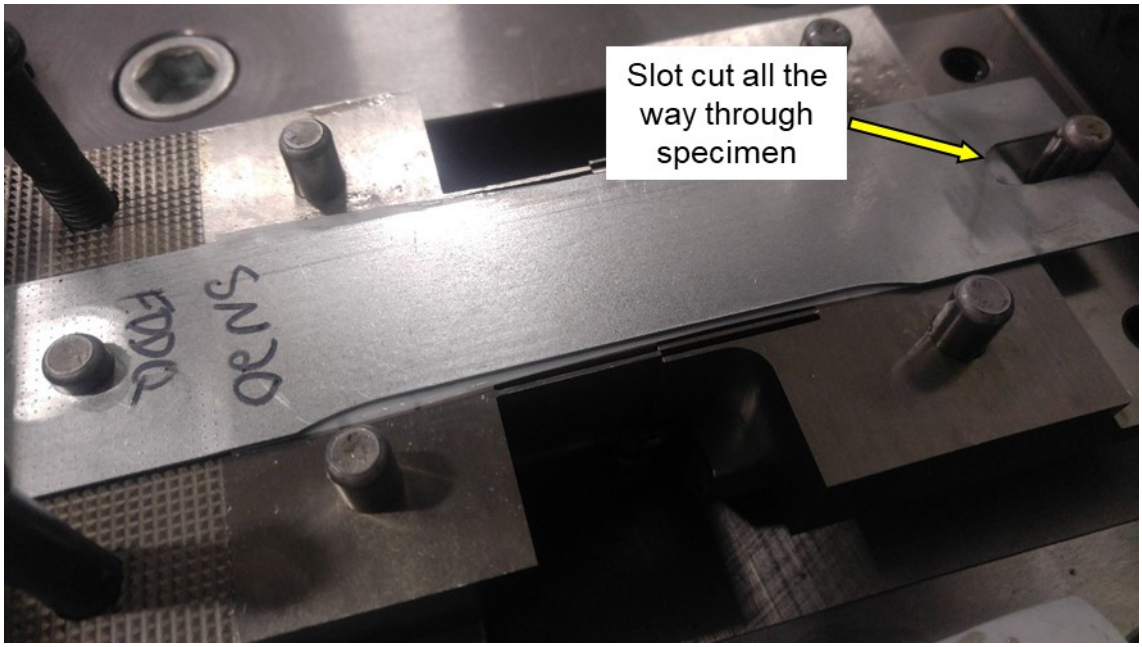


Figure 4.17: Modified CTC specimen for friction testing.

The results are shown in Figure 4.18 for the three lubrication conditions. In every case, there is a steep rise of the frictional resistance. A peak is soon attained (for two of the three conditions). Then the force changes drastically. This signifies the transition from static to kinetic friction. During most of the experiment, the variation of the frictional resistance is limited, indicated that quasi steady-state conditions have been attained. The detailed investigation of the behavior of this tribosystem is beyond the scope of this thesis. It is interesting, however, to contrast the magnitude of the forces measured in this experiment (i.e., order of 2 kN) to that of the specimen-free movement of the machine (order of 15 N and 50 N, see Figure 4.6 and Figure 4.16 respectively). This verifies that the native friction of the machine (i.e., between its own parts) is much lower than what is expected between the specimen and the machine.

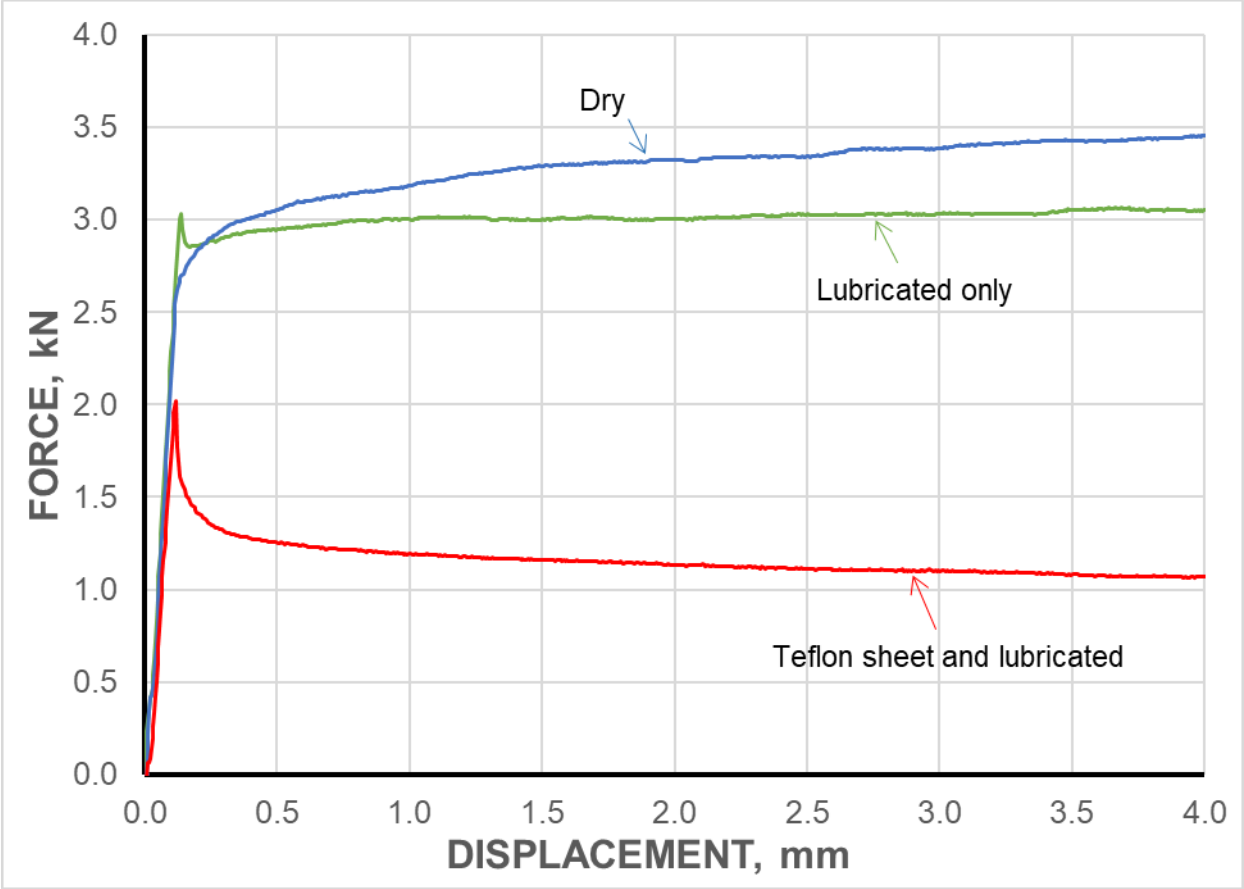


Figure 4.18: Decrease in friction by using Teflon sheets and lubrication at 12.5 kN (2,810 lbs) blank-holding force.

Figure 4.18 displays how the addition of the Teflon sheets reduces the friction between the specimen and comb dies by about 50% for the larger blank-holding force. This same reduction is seen for the lower blank-holding force as well. Furthermore, the Teflon sheet not only provides reduction in friction, but also preserves the surface of the specimen from gouging by the teeth of the comb dies, as seen in Figure 4.19.

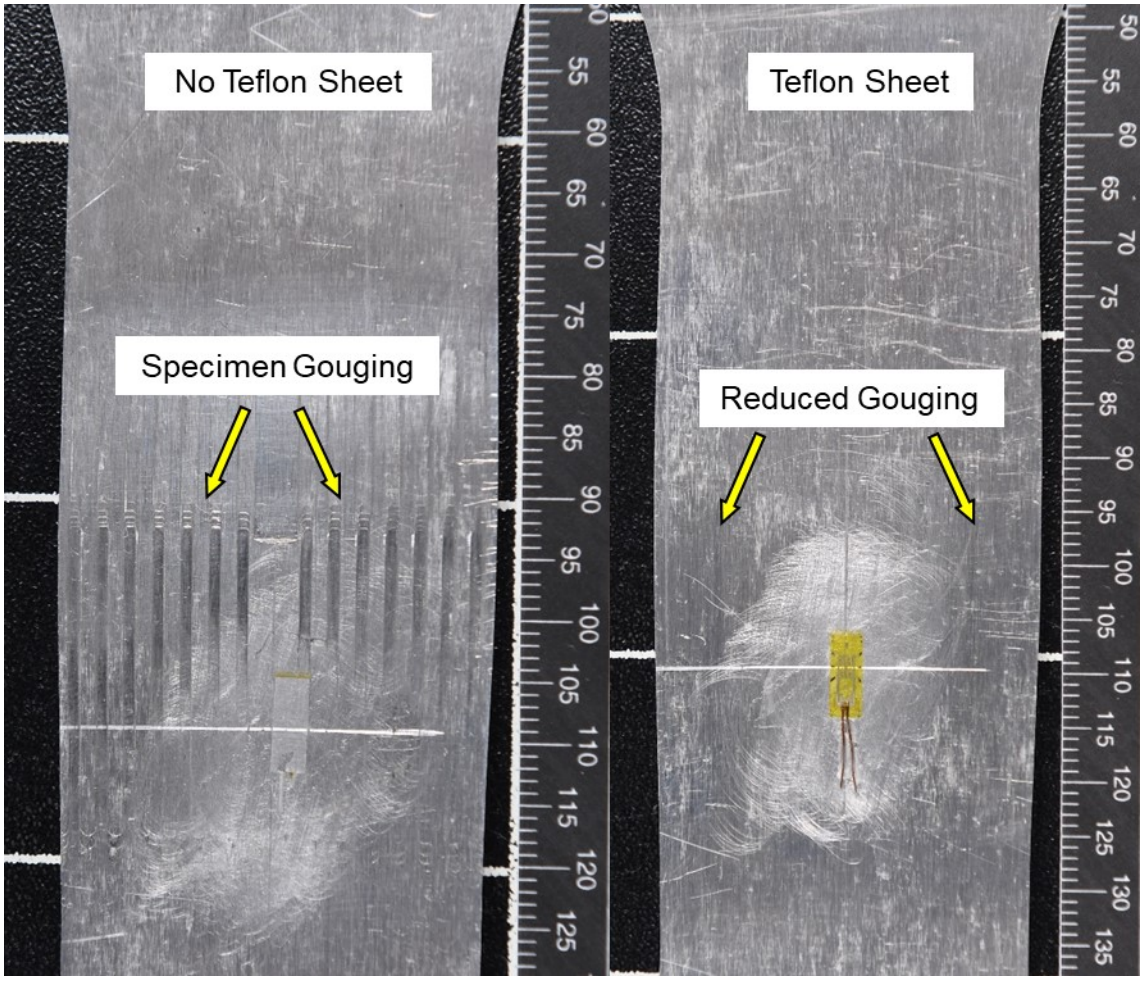


Figure 4.19: Reduction of specimen gouging by use of Teflon sheets.

### 4.4.3. Friction Compensation during CTC Testing

During CTC testing, the specimen will be in contact with the comb-shaped dies, which will be pressed against it by the blank-holding force. In this way, frictional forces will develop between the specimen and the dies. This will mean that the force needed to be applied by the hydraulic cylinder, and measured by the load-cell, will be used not only for straining the specimen, but for overcoming the frictional resistance, as well.

To determine how the force that the hydraulic cylinder is exerting is partitioned between the one that strains the specimen and the frictional resistance between the

specimen and the machine parts, a modified steel specimen (as shown in Figure 4.19) with a strain-gage attached was tested. Teflon sheets and lubricant, and a blank-holding force of 12.5 kN (2,810 lbs) were used. The strain measured during this test is seen in Figure 4.20. The average strain in the plateau region, assuming that the Young's Modulus is 210 GPa, corresponds to about 34 MPa for EDDQ steel, i.e., well within the elastic range (see Figure 4.15). Taking the difference between the engineering stress calculated versus the actual stress seen in the specimen, there is a difference of about 10 MPa. This 10 MPa is attributed to friction between the specimen and the comb-shaped dies.

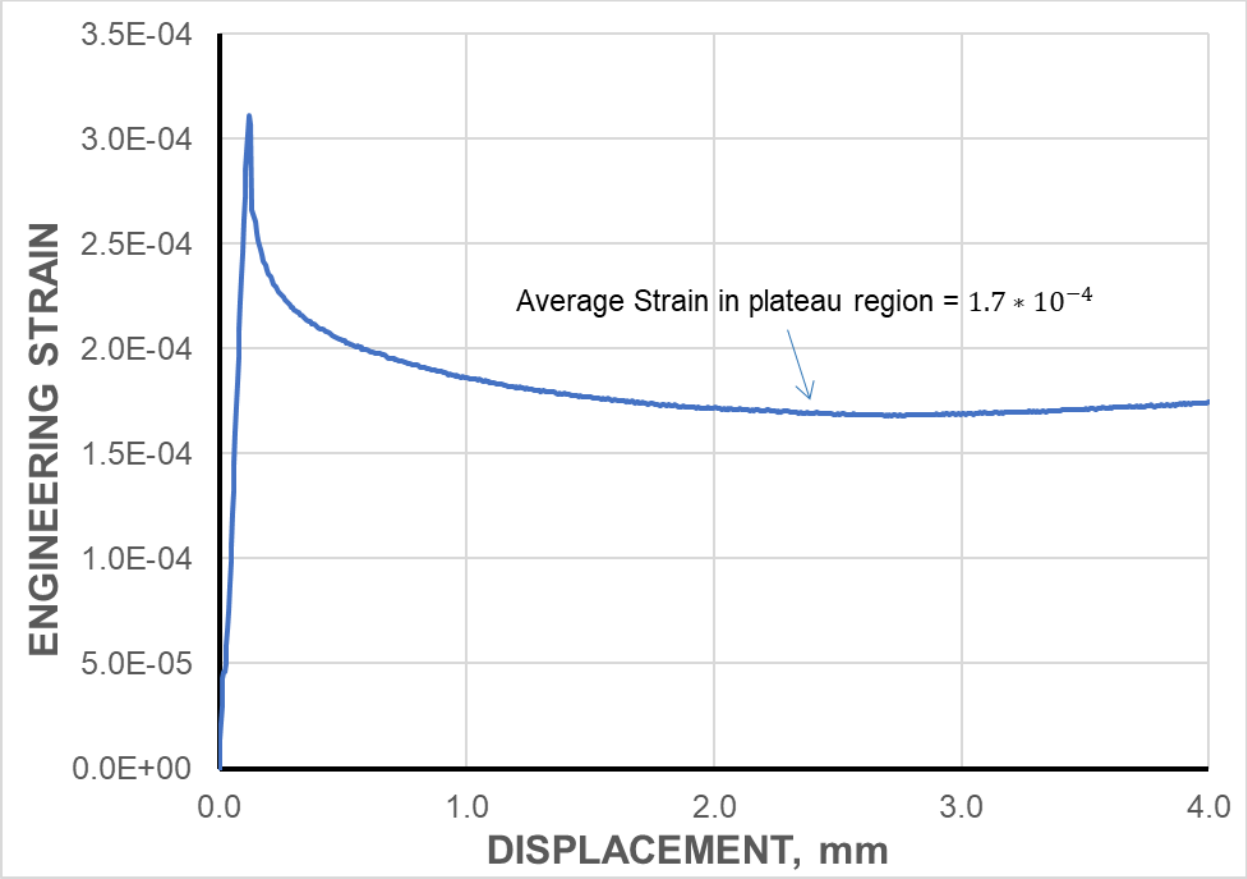


Figure 4.20: Strain from friction tests performed.

To verify this finding, a tensile test was performed on an ASTM E8 specimen of EDDQ steel with the same blank-holding force. This test was then compared to a tensile test without blank-holding force and confirmed to see a difference of about 10 MPa, see Figure 4.21.

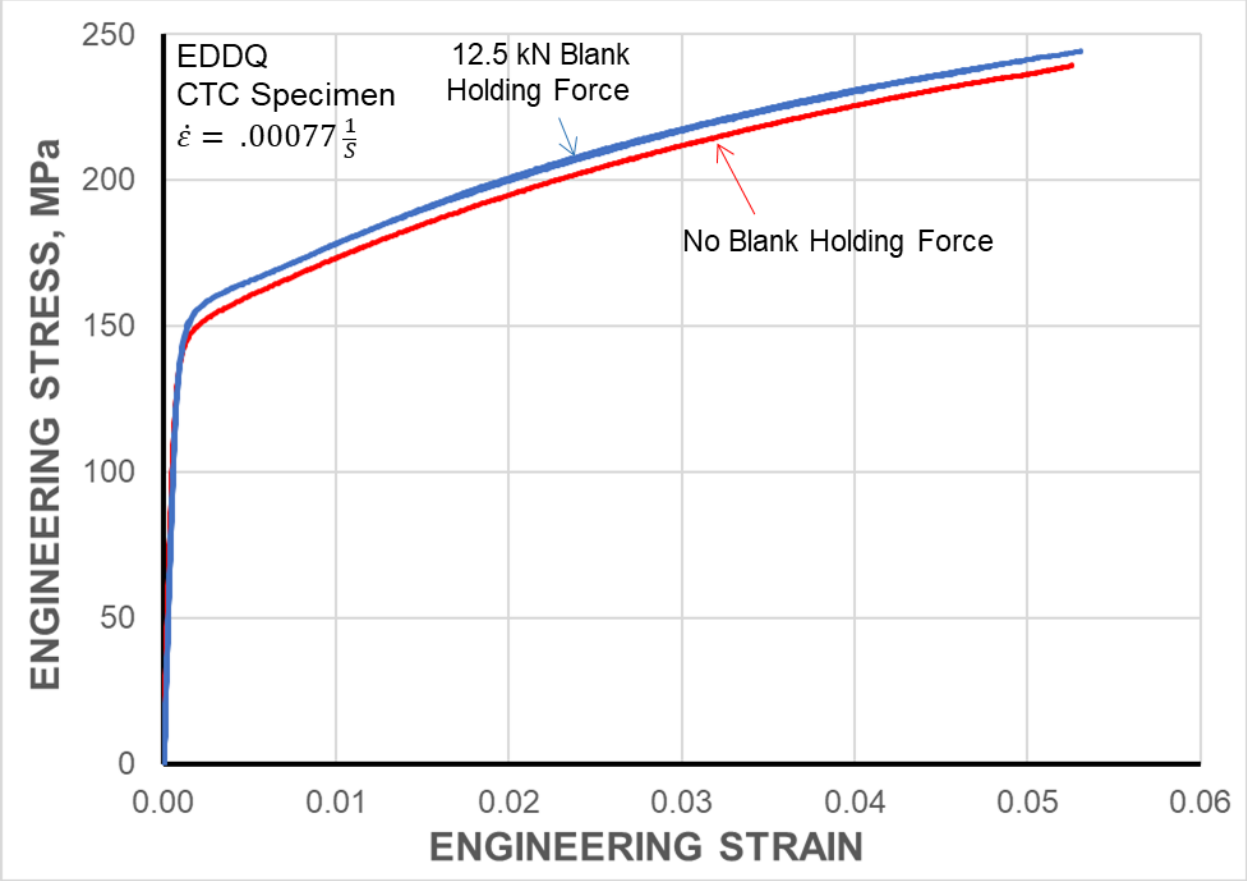


Figure 4.21: Comparing blank-holding tensile test to conventional tensile test.

When repeating the same tests for AA6022-T43, it was found that there are additional dependencies other than the blank-holding force. To facilitate convenient day-to-day testing, an adjustment equation is proposed in this thesis, rather than an exhaustive investigation of every variable that may affect the discrepancy between specimens with

blank-holding force vs. without. This adjustment equation is based off the friction equation seen in Equation (4.1).

$$F_{adj} = \mu * F_{BH} \tag{4.1}$$

where "$F_{adj}$" is the amount of force to adjust the raw data by, "$\mu$" is the Coulomb friction coefficient for the specific material batch and lubrication conditions, and "$F_{BH}$" is the blank-holding force used in the test. The idea is to perform a calibration test to find "$\mu$" for a specific sheet and lubrication scheme, and then use this friction coefficient to correct the force measured during a CTC experiment. (Exact "$\mu$" values for each test will be listed in the next chapter.) To determine what this adjustment needs to be, a tensile test without blank-holding and a tensile test with the desired blank-holding force for future tests will need to be performed. The difference between these tests (e.g., Figure 4.21) will provide the "$F_{adj}$"; then "$\mu$" can be solved for. The raw force data measured from a CTC experiment will then be reduced by using this value of "$\mu$" and the pre-set blank-holding force, to determine the frictional force. In other words, by subtracting the frictional force from the total force measured, the force, and from there the stress, that actually strains the specimen will be computed.

*This page intentionally left blank*

# CHAPTER 5
# MATERIAL BEHAVIOR UNDER CYCLIC LOADING

## 5.1. Introduction

Now that the background of how this CTC machine was designed and validated has been presented, this chapter will cover various cyclic experiments performed. Some of the materials do not have a slew of tests as they were used for initial validation of cyclic testing, but these tests still provide insight on the material's behavior. This chapter will be organized so that the more basic and less extensively tested materials are discussed first, and will end with materials on which research-type experiments were performed. The next chapter will discuss modeling of some of these experiments.

## 5.2. Aluminum Alloy AA6022-T43

Starting with AA6022-T43 for the material tested on this machine, a cyclic test was performed. This test was performed early in the development stages of the CTC machine so there is only one type of cyclic test performed which is 5 cycles starting in tension. The tension results for this material can be found in Figure 4.13. The specimen was cycled with a consistent amplitude of +/- 2% true strain. In this and all the following experiments, the BHF is determined from the specimen area supported by the comb dies (i.e., area between grips in Figure 2.2), multiplied by 1.5% of the yield stress of the material (see Section 2.3.2 for details). The remaining details can be found in Table 5.1.

Table 5.1 : Parameters for AA6022-T43 5x cycle test

| PARAMETER | VALUE |
|---|---|
| BLANK HOLDING FORCE | 6.25 kN (1,405 lbs) |
| FRICTION COEFFICIENT | 0.028 |
| DISPLACEMENT VELOCITY | 0.06 mm/s (0.0024 in/s) |
| STRAIN-GAGE USED | KFEM-1-120-C1L1M2R |
| STRAIN-GAGE CURE TIME | 4 HOURS |

Looking at Figure 5.1, there are a few observations that can be made. The first is that the material cyclically hardens, i.e., the first couple reversals see the largest change (increase) in reversal stress; it then appears to plateau to a constant reversal stress of around 300 MPa for both tension and compression. This plateaued stress of 300 MPa is also higher than the ultimate tensile strength (referred to as UTS from this point forward) from the pure tension test which is 270 MPa (see Figure 4.7). Another observation is that the location of re-yielding in the opposite direction of previous loading has a consistent offset value from where the isotropic value would be expected. This early re-yielding appears to consistently take place about 100 MPa less than the isotropic value after each load reversal. Looking at how the size of the yield surface changes at each cycle, it can also be observed that the yield surface grows about a third from where it started to where the material hardening plateaued. These results indicate that the isotropic hardening assumption is not appropriate for this material, and instead, some form of kinematic or distortional hardening should be used to capture the observations of Figure 5.1.

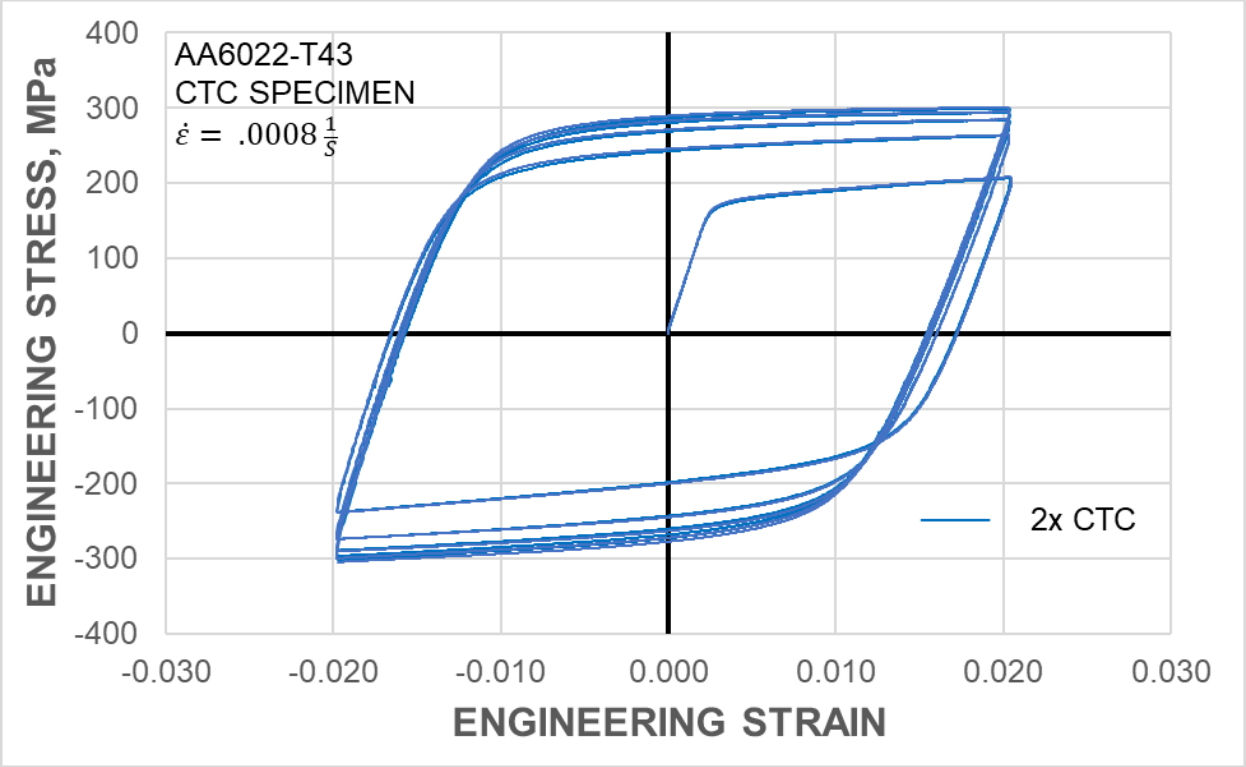


Figure 5.1: AA6022-T43 5x cycle test.

### 5.3. Extra Deep Drawing Quality (EDDQ) Steel

Similar to the AA6022-T43 5x cycle test, EDDQ was tested but only to 4.5x cycles, see Table 5.2. This was due to testing out changes to the control and DAQ program at the time. This experiment showed that the test was being cut short by half a cycle and has since been resolved. Despite that, the data can still be compared with the AA6022-T43 test.

Table 5.2 : Parameters for EDDQ 4.5x cycle test

| PARAMETER | VALUE |
|---|---|
| BLANK HOLDING FORCE | 6.25 kN (1,405 lbs) |
| FRICTION COEFFICIENT | 0.028 |
| DISPLACEMENT VELOCITY | 0.06 mm/s (0.0024 in/s) |
| STRAIN-GAGE USED | KFEM-2-120-C1L1M2R |
| STRAIN-GAGE CURE TIME | 4 HOURS |

As in AA6022-T43, Figure 5.2 shows that EDDQ cyclically hardens in a similar manner of initially showing rapid hardening with the number of cycles and then plateauing quickly. Although EDDQ is following a similar hardening behavior, the material plateaus to a lower stress (260 MPa) than its UTS of 290 MPa (tensile test found in Figure 4.15).

The same test was performed once again but starting in compression rather than in tension. This test can be found by itself in APPENDIX C where the same overall behavior is exhibited. Looking at Figure 5.3, the compression-starting test data is flipped about the x and y axis to observe tension-compression asymmetry of the material. Focusing on the initial stress-strain curve, the two directions show favorable agreement; but after the first reversal the material appears to take different paths for the two starting directions.

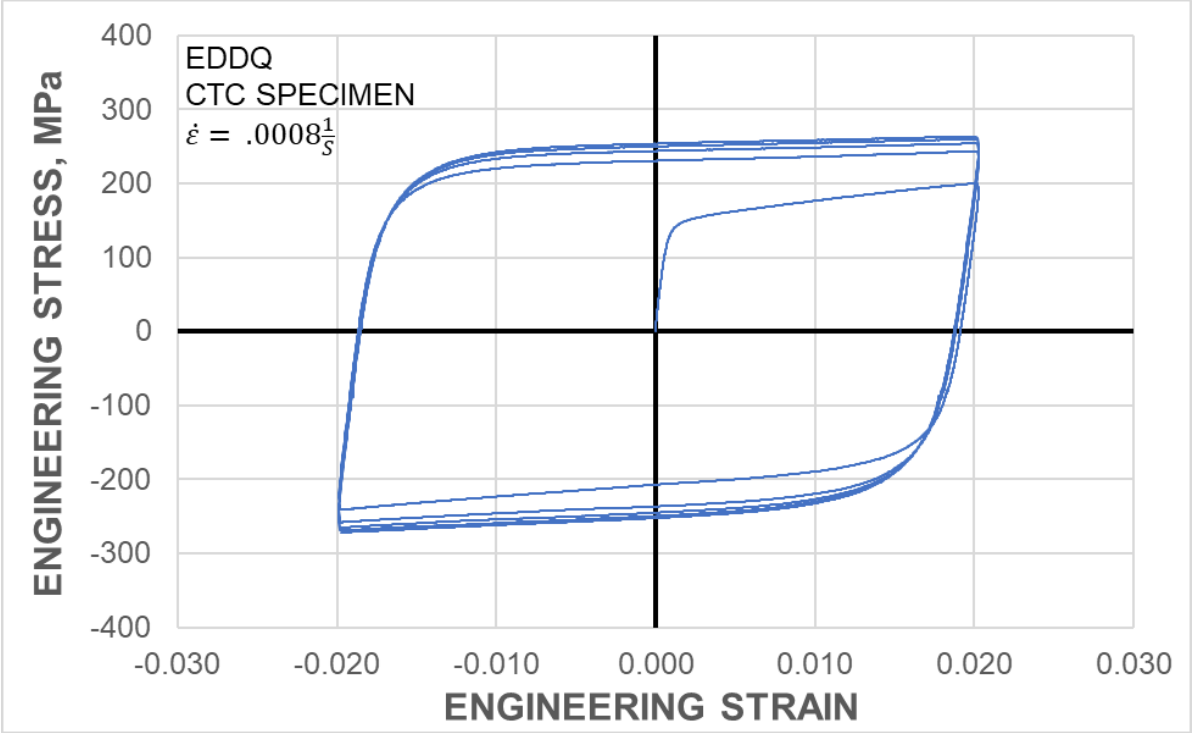


Figure 5.2 EDDQ 4.5x cycle test.

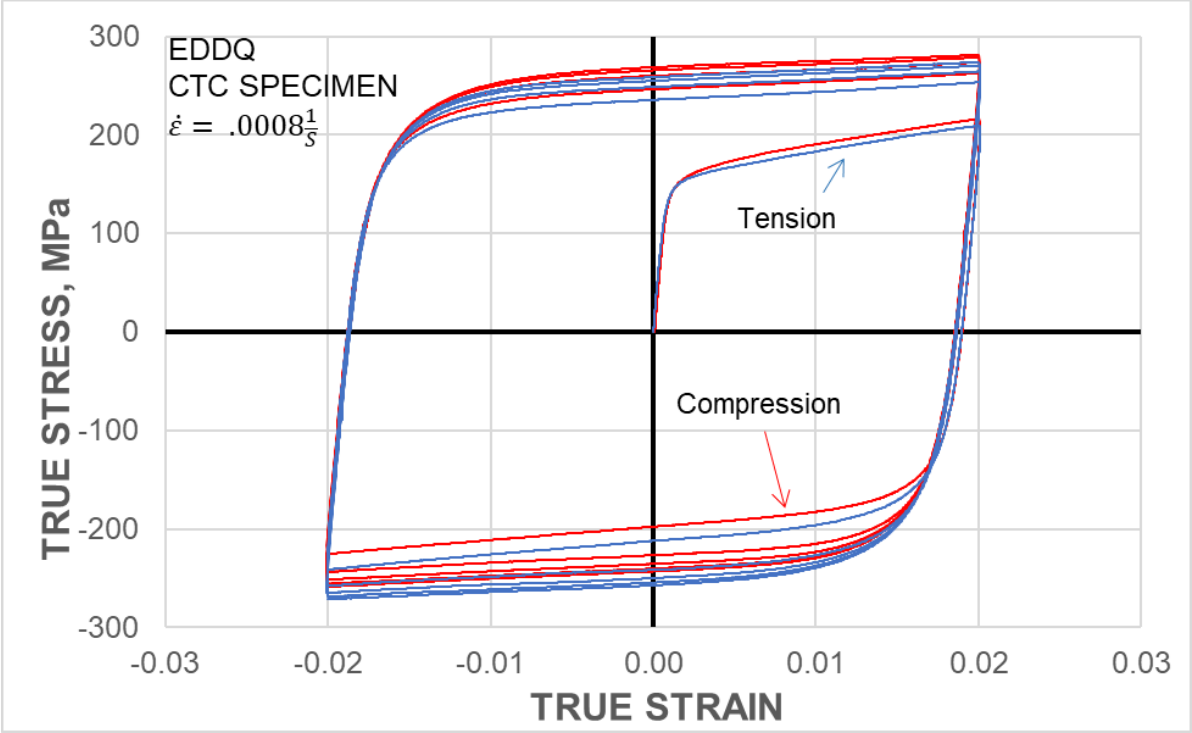


Figure 5.3 Comparison of starting in tension vs. compression of EDDQ 4.5x cycle test.

At the end of the multiple cycles, the compression-starting test is found to be at a slightly higher stress (approx. 15 MPa). It also has a more severe stress difference between reversal points than the tension-starting one. This difference can be seen more clearly in Figure 5.4, where the tension-starting test seems to saturate after 6-7 reversals, whereas the compression-starting one does not, and also retains the asymmetry in tension and compression.

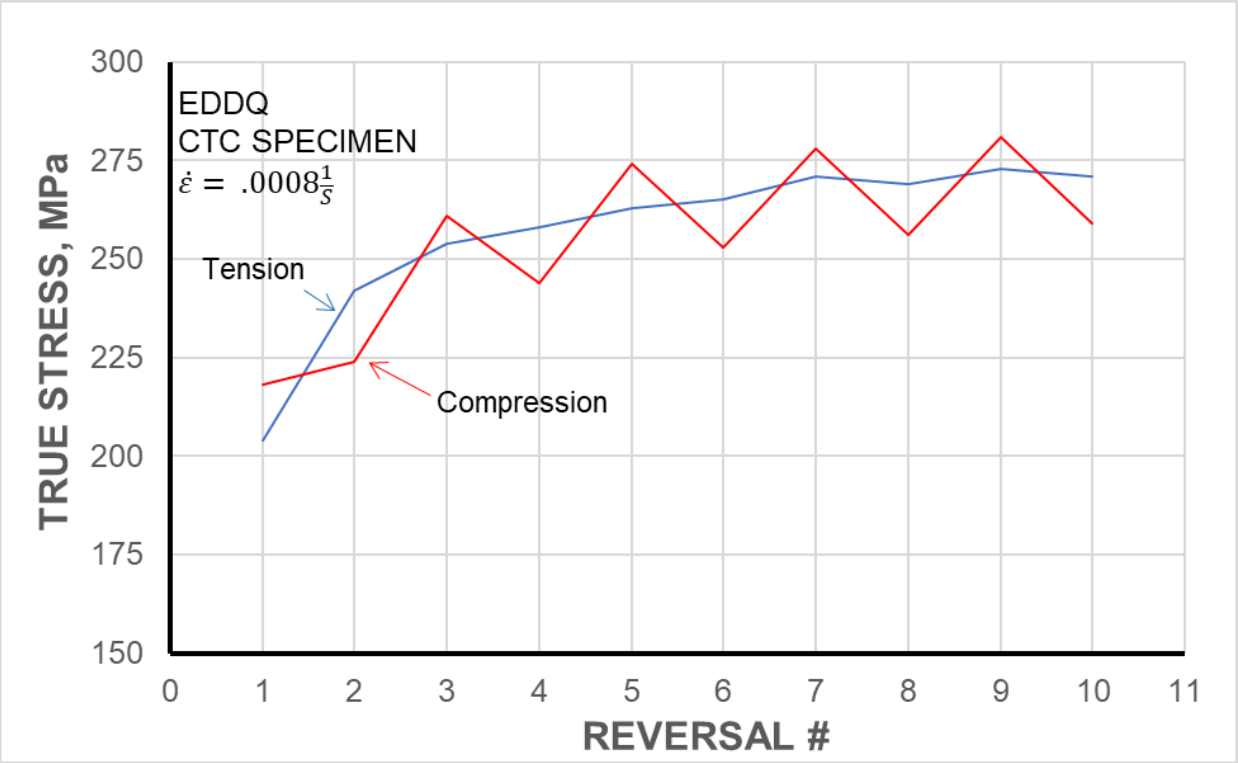


Figure 5.4 Comparison of reversal stress when starting in tension vs. compression of EDDQ 4.5x cycle test.

Comparing the stress-strain response from the beginning to third reversal of both EDDQ and AA6022-T43 in Figure 5.5 and Figure 5.6, a few observations can be made. When comparing engineering stress vs. strain, the stress level in AA6022-T43 matches

the EDDQ one at the first two stress reversals. But once plotted in true stress vs. plastic strain, a different result appears. Due to AA6022-T43 having a lower elastic modulus, the material has a higher elastic strain, therefore lessening the amount of plastic strain in comparison to EDDQ. Another difference can be seen with the plastic tangent modulus or work-hardening rate, where for AA6022-T43 it is larger than EDDQ. Interestingly and somewhat unexpectedly, both materials appear to also exhibit the same amount of Bauschinger effect upon each reversal.

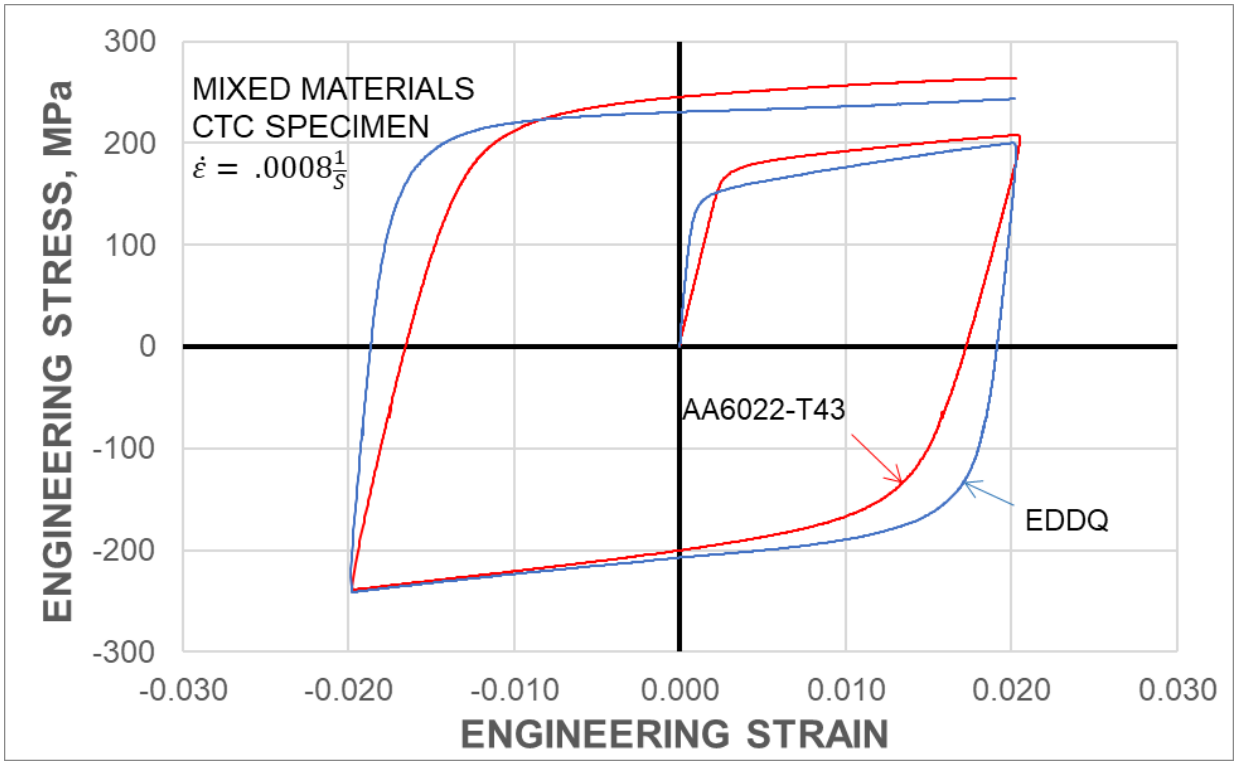


Figure 5.5 Engineering stress vs. strain comparison of EDDQ and AA6022-T43 in early cycles.

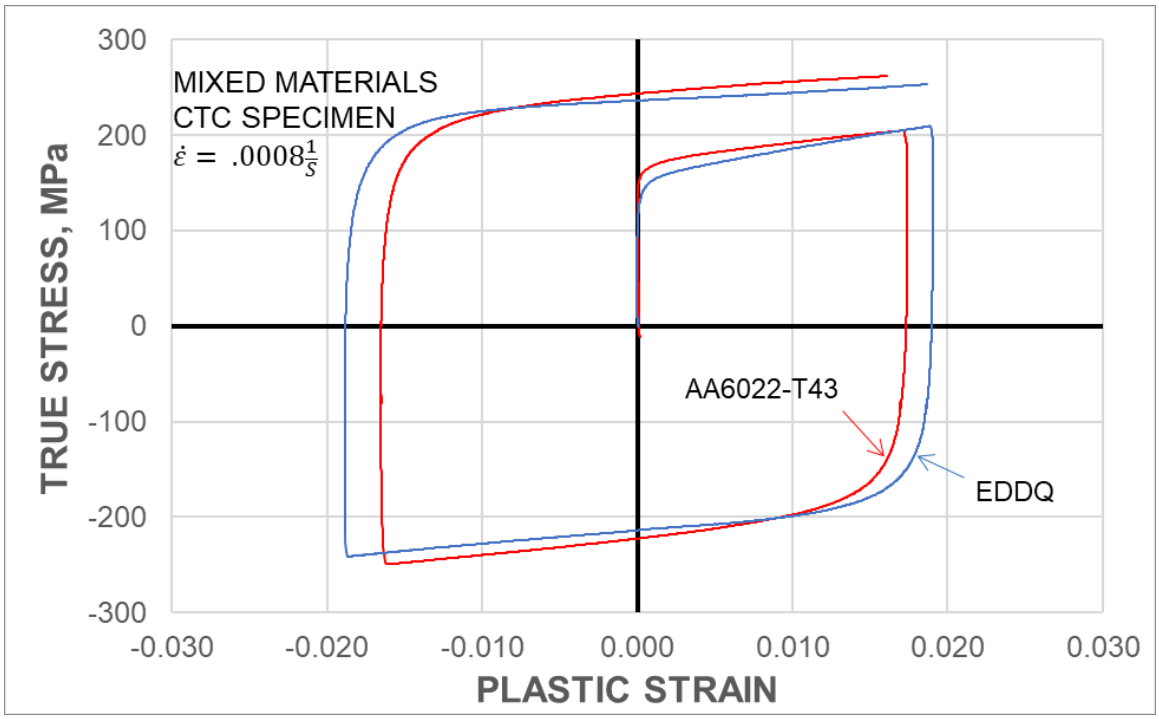


Figure 5.6 True stress vs. plastic strain comparison of EDDQ and AA6022-T43 in early cycles.

## 5.4. JAC-270D Steel

JAC-270D steel has been discussed in earlier chapters for use in comparing this CTC machine to a similar one (see Section 4.3.2), so this section will be for observing specific trends that the material has, using data only from the CTC machine rather than both machines. The tests performed were a 1x cycle test with both starting directions. The testing parameters can be found in Table 5.3.

Looking at Figure 5.7, the same trends appear as what the EDDQ exhibited within the first cycle. Something to note that stands out from previous tests is the small amount of work-hardening stagnation occurring on the first and second reversal between +/-1%. This is also evident in the tests with a compression starting direction found in APPENDIX C.

Table 5.3 : Parameters for JAC-270D 1x cycle test

| PARAMETER | VALUE |
|---|---|
| BLANK HOLDING FORCE | 6.25 kN (1,405 lbs) |
| FRICTION COEFFICIENT | 0.045 |
| DISPLACEMENT VELOCITY | 0.06 mm/s (0.0024 in/s) |
| STRAIN-GAGE USED | KFEM-1-120-C1L1M2R |
| STRAIN-GAGE CURE TIME | 4 HOURS |

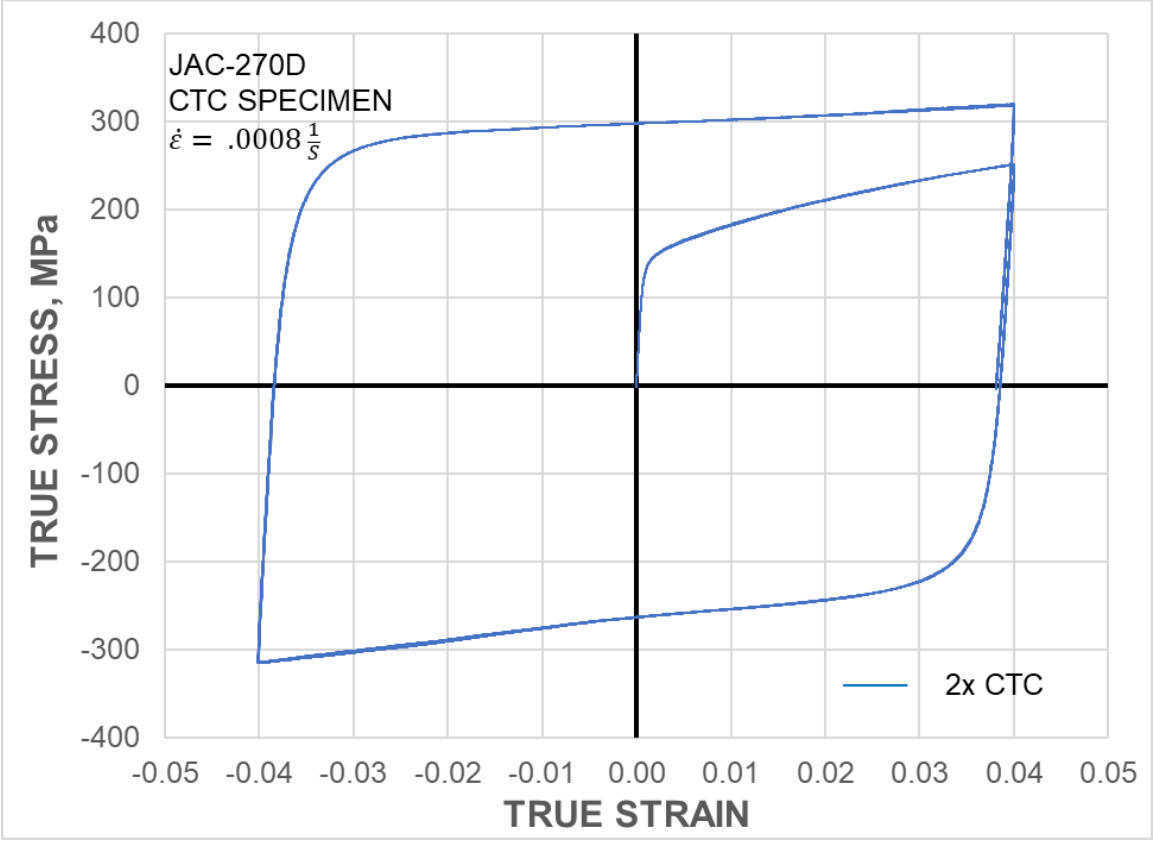


Figure 5.7 JAC-270D tension-compression-tension test.

Following the same procedure as Figure 5.3, Figure 5.8 looks at the tension-compression asymmetry of the material. In this case, the JAC-270D has significantly less

asymmetry than the EDDQ. The only area that seems to deviate is upon the approach of the second load reversal, but the data quickly re-converges after that second load reversal.

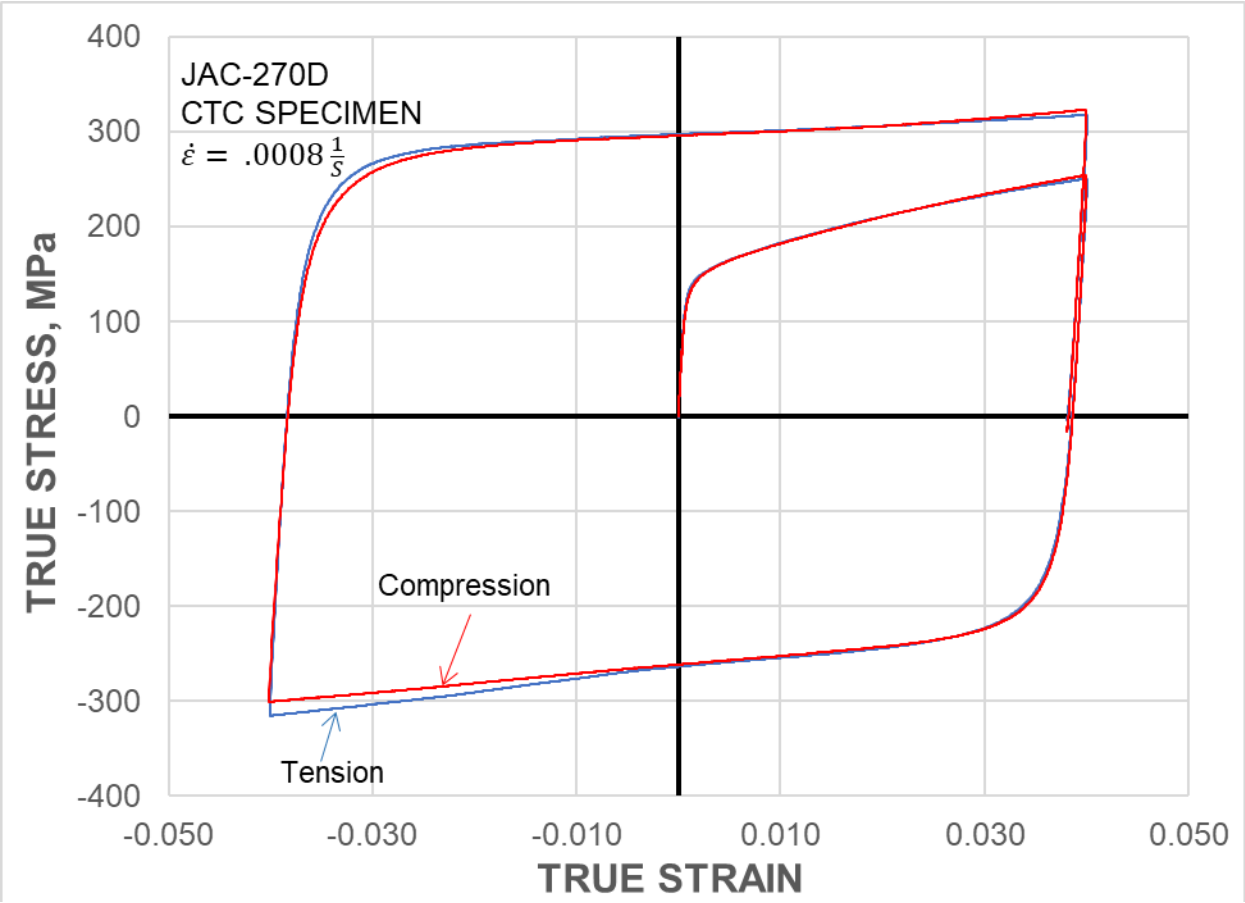


Figure 5.8 Comparison of starting in tension vs. compression of JAC-270D 1x cycle test.

## 5.5. DP590 and DP1180 Dual-Phase Steels

The following sections will cover the testing performed for so that the Yoshida-Uemori model [16] could be calibrated for Dual Phase (DP) 1180. All of the tests performed were requested by a third party except for the pure compression test which was added to further

explore the material's properties. Along with testing DP1180, DP590 was tested to the same extent to further verify the capabilities of the CTC machine.

### 5.5.1. DP1180 steel

Starting with DP1180 since this is the material for which the Y-U model will be calibrated, the specimen gage width needed to be reduced in order to stay within the maximum force capacity of the machine. This reduced gage width can be seen in Figure 5.9 where the width is now 20 mm instead of 35 mm (see Figure 2.3). (Note that 1180 MPa x 20 mm x 1.6 mm = 37.8 kN, vs. 66.2 kN for 35 mm.)

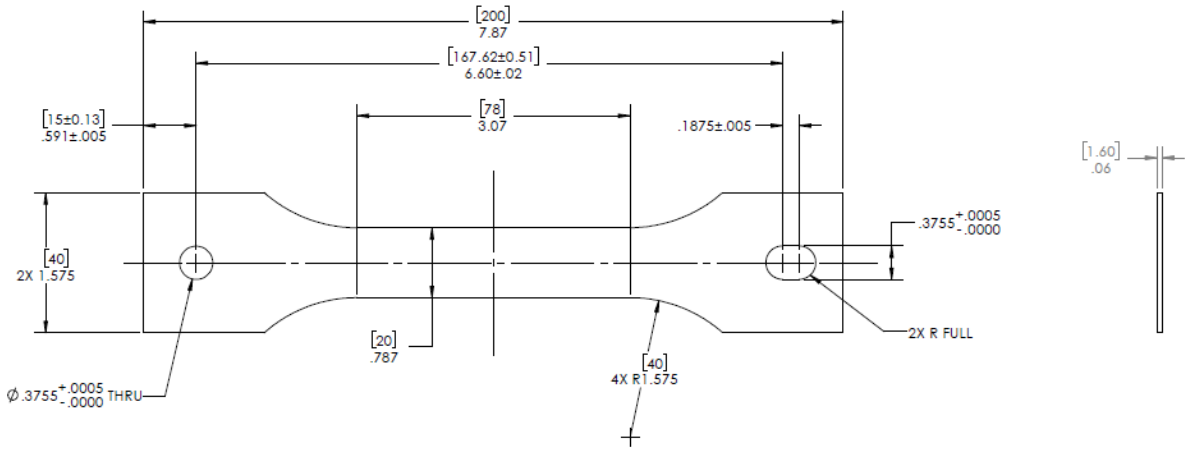


Figure 5.9 Reduced width specimen for DP1180 testing.

With the reduction in gage width, care had to be taken in ensuring the specimen does not buckle in-plane during testing. This was something that could not be directly controlled but rather needed to be noted if the specimen had a bow at the end of a test, since this buckling can induce discrepancies in the data when comparing multiple runs of the same test. For the majority of the tests no buckling occurred, but there were two instances when

it did. Looking at Figure 5.10, the lower specimen is an example of in-plane buckling that can occur and the upper specimen is what would be expected. While no definite conclusion as to why buckling occurred had been reached at, it appears to be related to misalignment between the locating hole and slot in Figure 5.9. At any rate, the in-plane buckling shown in Figure 5.10 is an indication that the out-of-plane buckling suppression features of the CTC machine, which was the primary reason for its design, are working successfully, even close to its maximum axial force rated capacity.

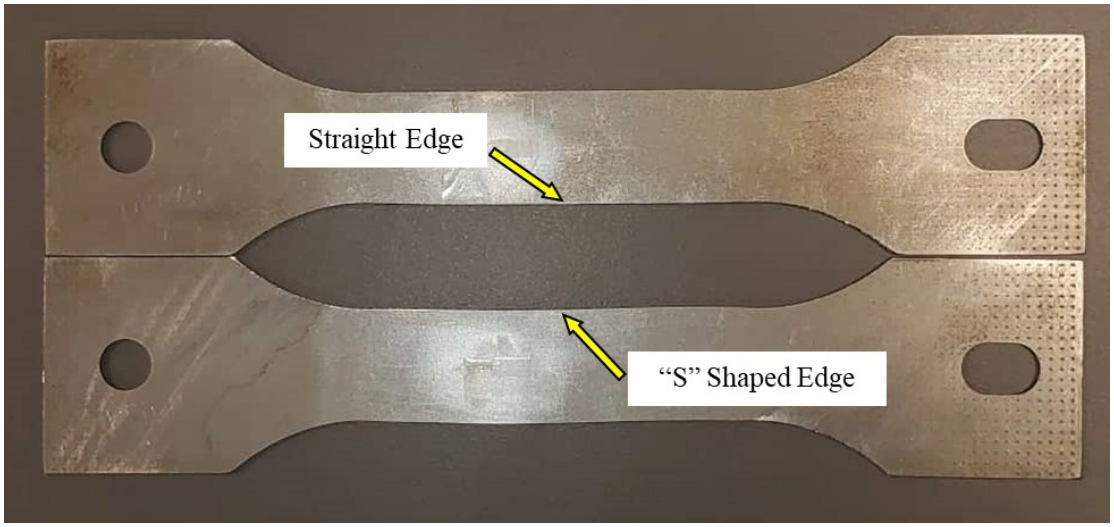


Figure 5.10 Comparing an in-plane buckled specimen (lower) vs. barreled (upper).

For the DP1180 tests performed on the CTC machine with CTC specimens, the parameters used are in Table 5.4. The first of the array of tests performed was a full cycle test which was 1 cycle between +/- 3% engineering strain. The next test was a multiple cycle test which was a total of 3 cycles starting at +/- 1% then +/- 3% and finally ending at +/- 5% engineering strain. The last test performed on the CTC machine was a pure compression test which reached -10% engineering strain. There were a couple of additional tests performed for this project which included a load-unload test and tensile

test. Both of these tests were performed on the MTS machine and, for completeness, can be found in APPENDIX C.

Table 5.4 : Parameters for DP1180 cyclic tests on CTC

| PARAMETER | VALUE |
|---|---|
| BLANK HOLDING FORCE | 20 kN (4,500 lbs) |
| FRICTION COEFFICIENT | 0.020 |
| DISPLACEMENT VELOCITY | 0.095 mm/s (0.0037 in/s) |
| STRAIN-GAGE USED | KFEM-1-120-C1L1M2R |
| STRAIN-GAGE CURE TIME | 24 HOURS |

Starting with the full cycle test performed seen in Figure 5.11, the material does not cyclically harden as much as the previous steels tested in this chapter. Another note is that the elastic-plastic transition upon load reversal is very extensive, and certainly more progressive than during initial yield. Finally, the work-hardening does not appear to saturate at this strain limit, unlike the behavior seen in Figure 5.2 for EDDQ steel.

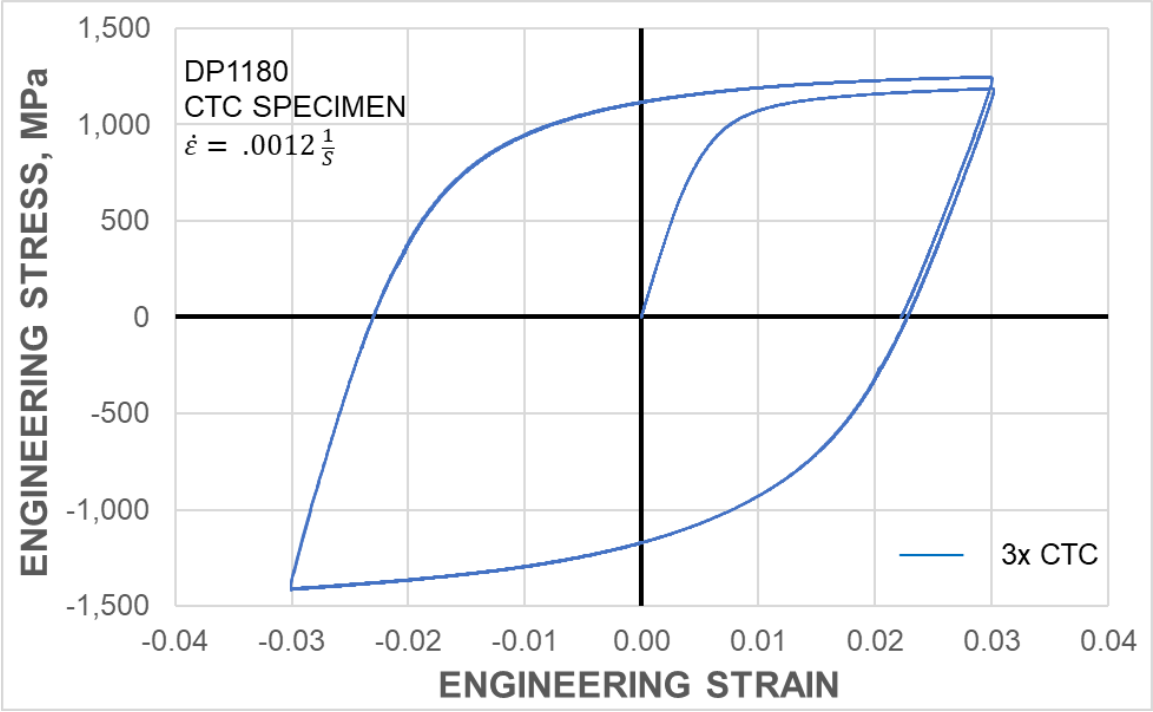


Figure 5.11 DP1180 full cycle test. Note that 3 tests are overlapped here.

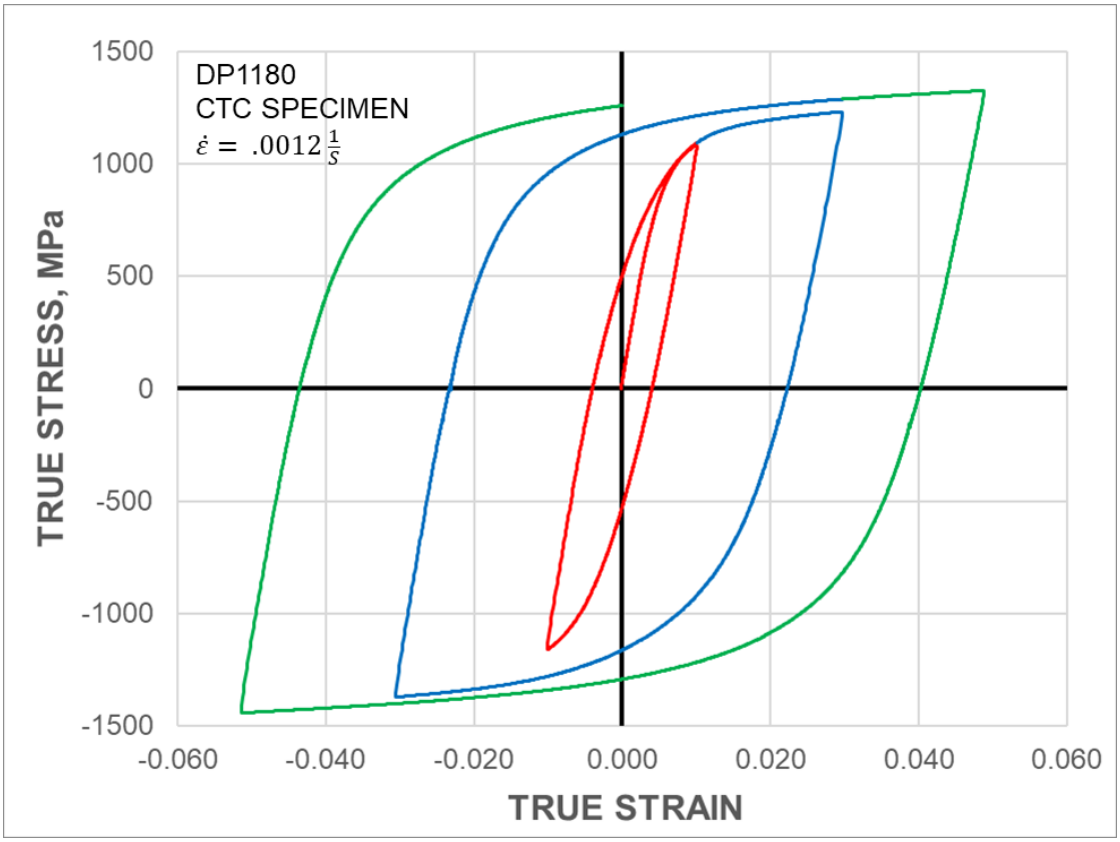


Figure 5.12 DP1180 multiple cycle test.

During the multiple cycle test (see Figure 5.12), the experiment had to stop halfway through the test so that a new strain gage could be applied. This occurred after unloading to zero stress after reaching the -3% strain. The specimen was removed from the machine, and a new strain gage was applied so that the test could continue to +/- 5%. The interruption of the test was for about 24 hours. This transition between gages is barely noticeable; looking at Figure 5.13, it would be hard to notice unless pointed out.

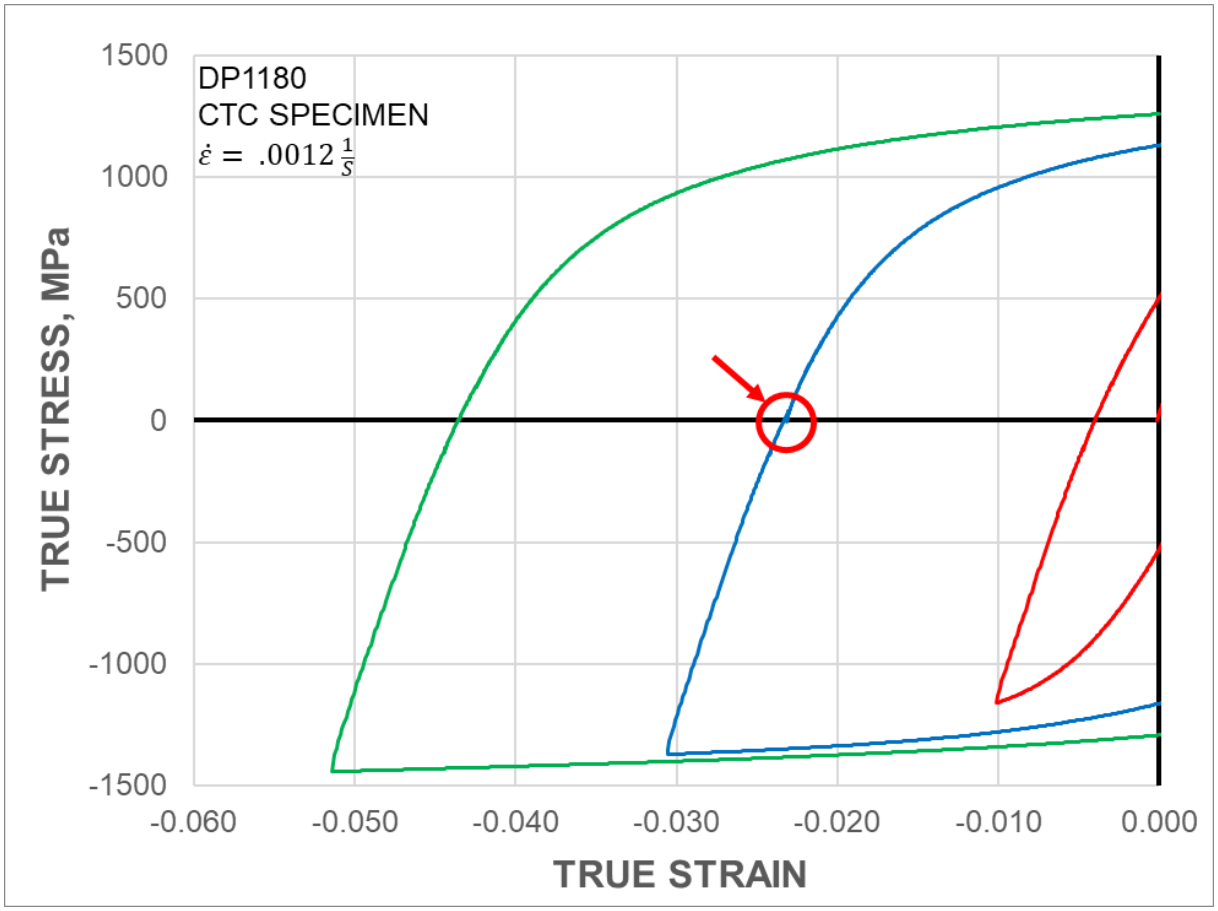


Figure 5.13 DP1180 multiple cycle test negative strain side.

Moving on to the pure compression test performed, the response observed is plotted along with the uniaxial tension one in Figure 5.14. It can be seen that the material has

tension-compression asymmetry. The pure compression test can be seen on its own in APPENDIX C. In particular, while the work-hardening rate is similar in tension and compression, in the latter case the initial yield is higher than in tension. It should be noted that while the tension test in that figure comes from an ASTM dogbone specimen tested on an MTS loading frame, the first part of the cyclic tension-compression tests performed in the CTC (see Figure 5.11) agrees with the ASTM test. This is in agreement with the results discussed in Section 4.3.3.

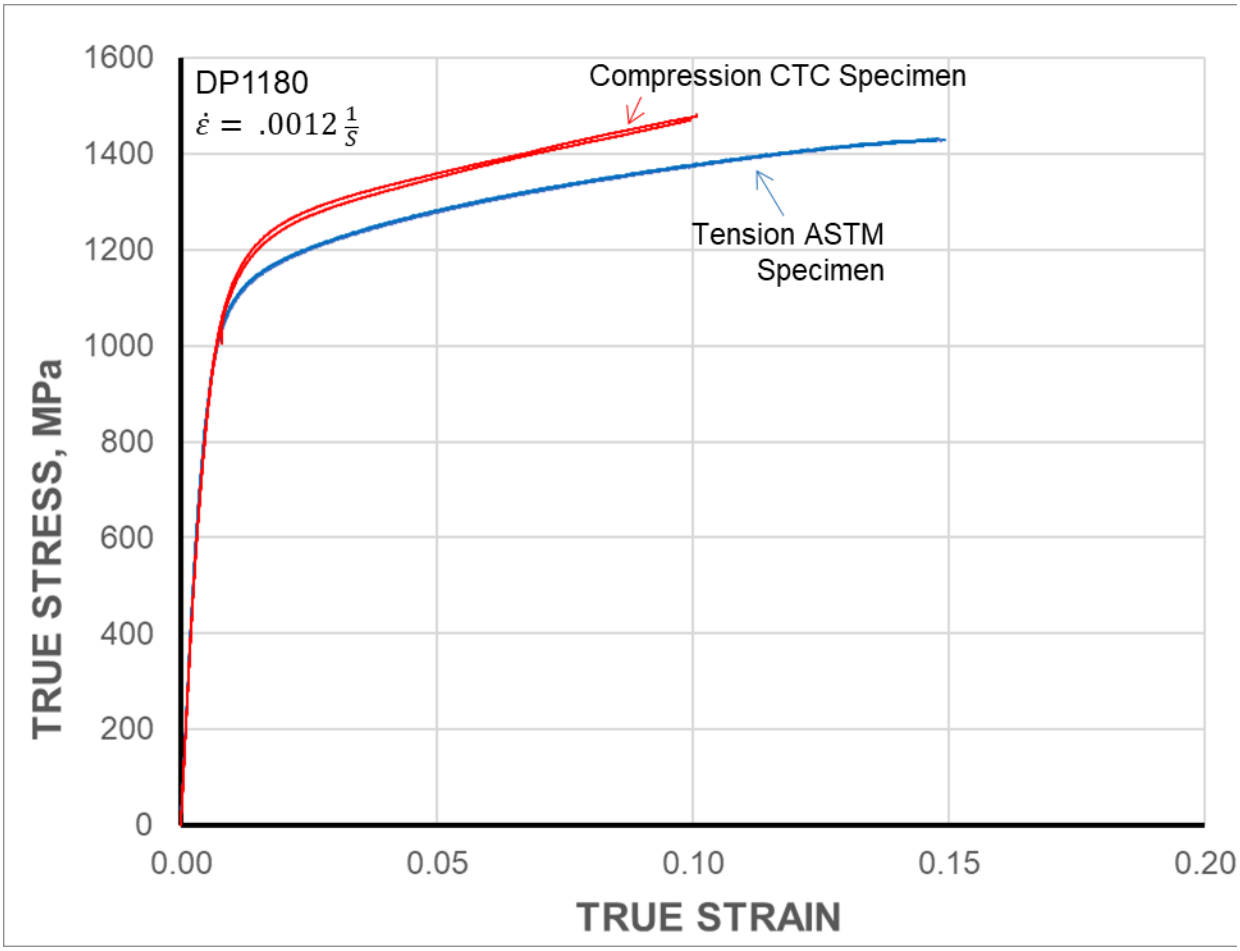


Figure 5.14 DP1180 pure compression versus tension test, indicating significant tension-compression asymmetry.

### 5.5.2. DP590 vs. DP1180 Steels

The same suite of tests as for DP1180 was ran for the second steel, DP590. Comparing the DP590 results with the DP1180 ones from the previous section, the major differences in the materials can be observed. Indicated by the number within the name of the material, DP590 has about half the UTS of DP1180. Figure 5.15 provides the experimental data comparison for a more visual representation. What can also be seen in this figure is the increased ductility of DP590. Not only does this material have a larger strain until failure, but the transition from elastic to plastic deformation takes almost double the strain to reach a constant tangent modulus in tension.

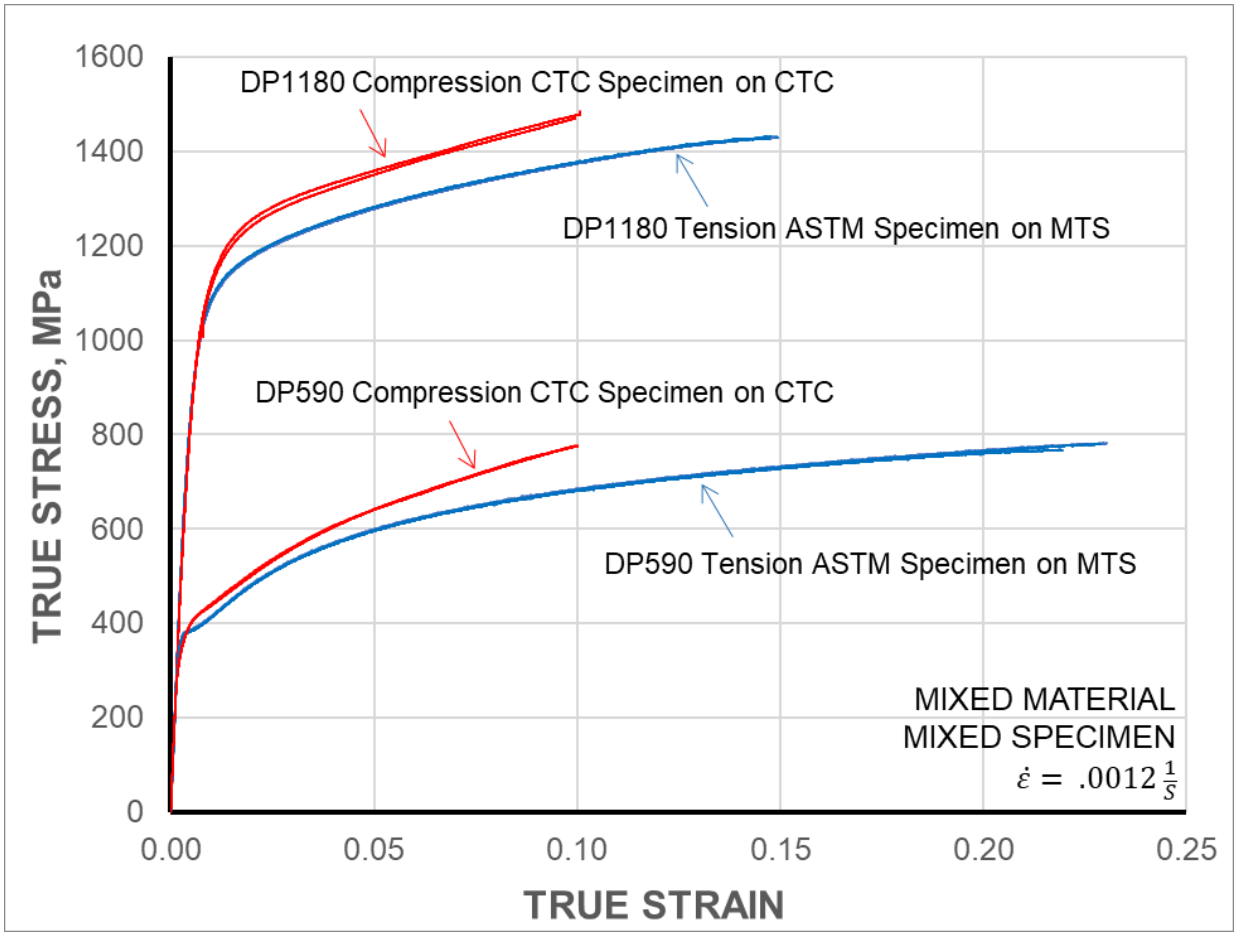


Figure 5.15 DP590 vs. DP1180 pure tension and pure compression tests.

Comparing the compression results of the two materials in Figure 5.15 further verifies the differences between the materials. DP590 appears to have a two-part tangent modulus and the work-hardening stagnation that occurs in the tension test is not seen. Both materials exhibit the same asymmetry behavior where the compression data is higher in stress compared to the tension side. However, unlike DP1180, in DP590 the work-hardening rate is different in tension and compression, so that the difference in the tensile and compressive flow stresses increases with plastic deformation.

## 5.6. DP980 Dual-Phase Steel

The tests performed in this section are focused on CTC-related tests and were used to obtain certain mechanical properties of DP980. The mechanical properties calculated are for use in the Chaboche and HAH model [17]. More tests were performed for that work, but only the CTC-related tests will be covered in-depth here. The testing parameters that apply to all the tests in this section can be found in Table 5.5.

Table 5.5 : Parameters for DP980 tests on CTC

| PARAMETER | VALUE |
|---|---|
| BLANK HOLDING FORCE | 18.86 kN (4,200 lbs) |
| FRICTION COEFFICIENT | RD = .040<br>45° = .020<br>TD = .015 |
| DISPLACEMENT VELOCITY | 0.110 mm/s (0.0043 in/s) |
| STRAIN-GAGE USED | KFEM-2-120-C1L3M2R |
| STRAIN-GAGE CURE TIME | 6 HOURS |

Starting with pure compression, seen in Figure 5.16, three orientations with respect to the rolling direction (RD) were tested. From this test, it can be seen the flow stress increases as the orientation moves away from the rolling direction. Each direction tested appears to exhibit its own unique path and to never cross paths with the other ones.

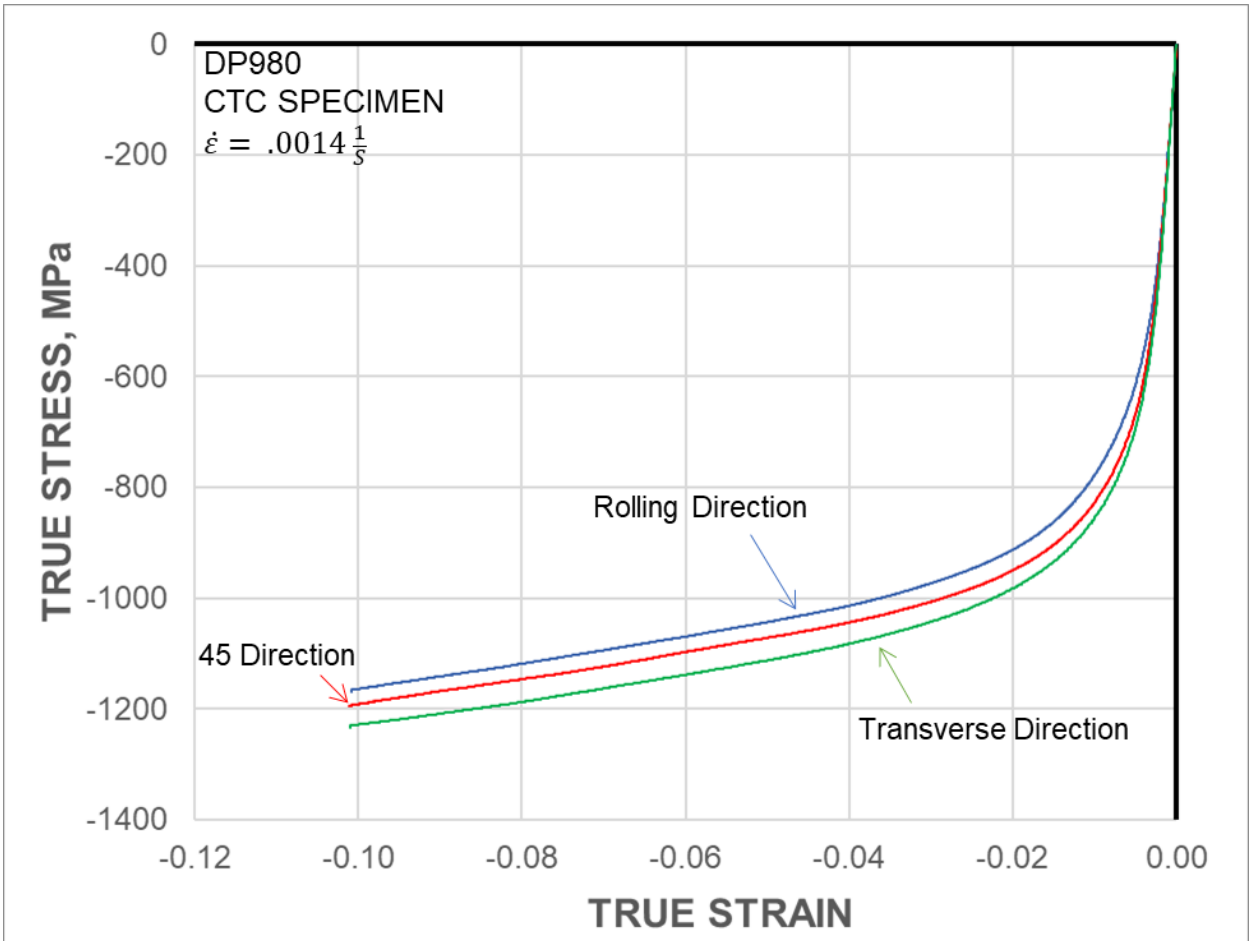


Figure 5.16 Comparing pure compression of different orientations of DP980.

The next few figures shown are combined tests where the specimen starts on the CTC machine and then is transferred to the MTS machine after a certain prestrain. This transfer to the MTS machine allows for measurement of two directions of strain rather than only

one, using Digital Image Correlation, so that the R-values or plastic strain ratio can be computed, see Equation (5.1). Only the rolling and transverse direction were tested in this manner and can be seen in Figure 5.17.

$$R = \frac{d\varepsilon_w^p}{d\varepsilon_t^p} \tag{5.1}$$

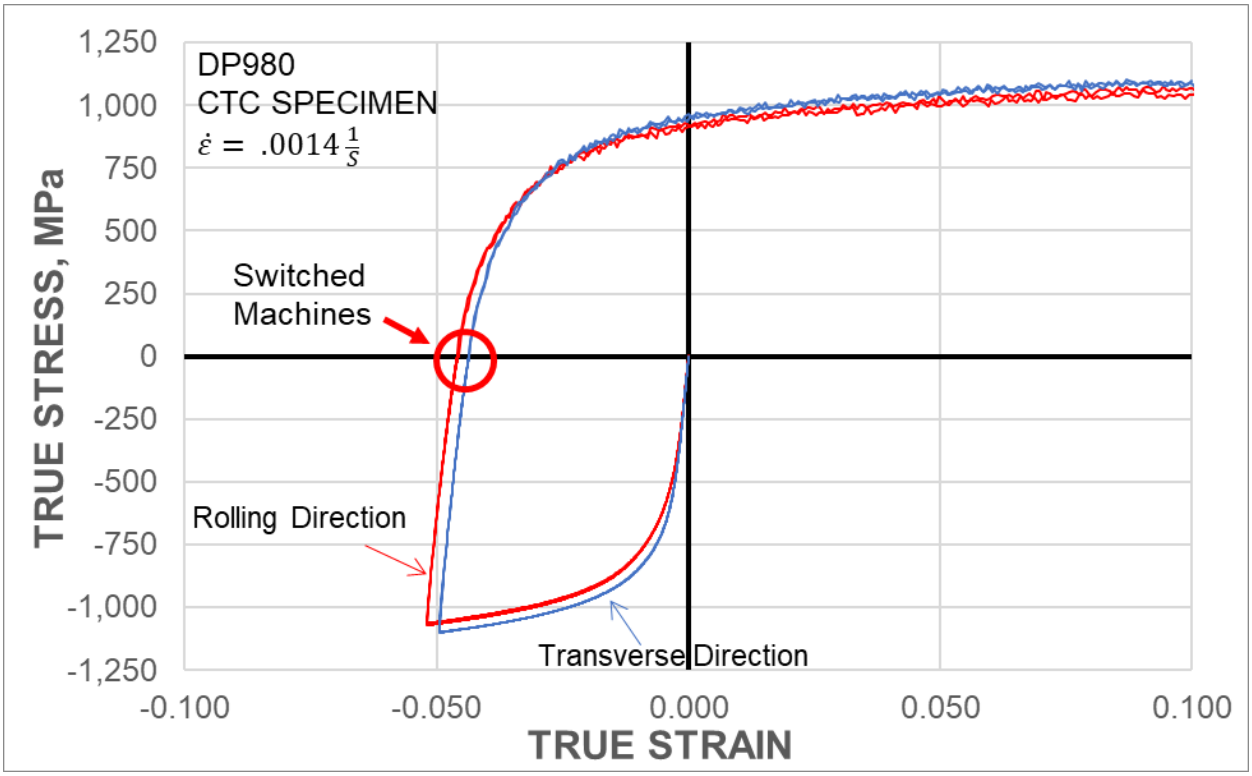


Figure 5.17 Prestrain in compression then tension of DP980. Tests performed along the rolling and transverse directions.

Looking at the data after the specimen switches machines, the R-value graphs were plotted for both directions, as seen in Figure 5.18. It can be seen that the R-values are almost constant with increasing deformation, so that each test and condition can be

represented by a single R-value, instead of the definition in Equation (5.1), which essentially is the instantaneous slope of the width-to-thickness plastic strain ratio plot.

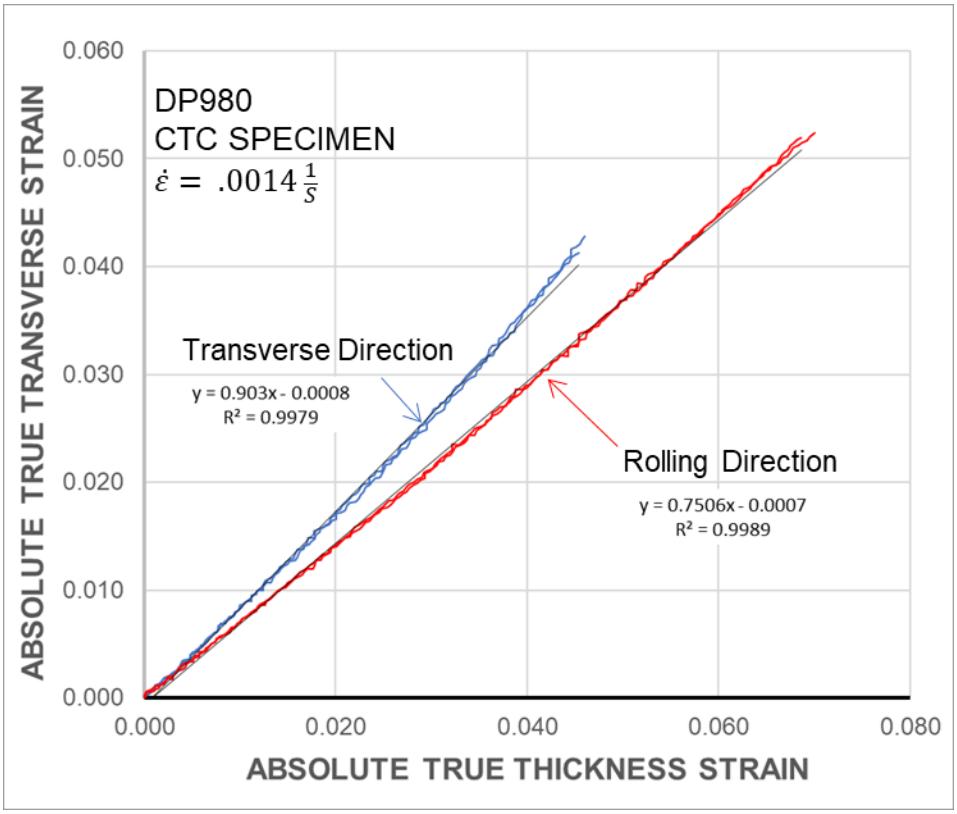


Figure 5.18 R-Value comparison between rolling and transverse direction of DP980 after prestrain.

The R-values are compared in Table 5.6 to a pure tension test performed on the same material, where $R_0$, $R_{45}$, and $R_{90}$ stand for the R-values of the rolling, 45° and transverse directions, respectively. Some amount of planar anisotropy, i.e., different properties in different directions, is visible for this material.

Table 5.6 : R-value of DP980 of pure tension and prestrain then tension

| TERM | PURE TENSION | PRESTRAIN |
|---|---|---|
| $R_0$ | 0.765 | 0.751 |
| $R_{45}$ | 1.107 | - |
| $R_{90}$ | 1.048 | 0.903 |

With the R-values calculated from the pure tension tests, the average plastic anisotropy ratio ($R_m$) can be determined, using Equation (5.2):

$$R_m = \frac{R_0 + R_{90} + 2 * R_{45}}{4} \tag{5.2}$$

Materials having a $R_m$ greater than one, resist thinning (hence $R_m$ is sometimes called "normal anisotropy ratio"), which improves drawing operations. For our DP980, it is calculated to be 1.007, i.e., slightly greater than one. If the same calculation is performed on the prestrained DP980, substituting the pure tension $R_{45}$ for missing data, $R_m$ is found to fall below one, which will mean that the material is prone to thinning after prestraining. While this seems to contradict Figure 5.18, which indicates that the R-values remain constant with plastic straining, it should be recalled that the present case involves a loading reversal, instead of the monotonic loading in Figure 5.18.

The last test covered in this section is prestraining rolling direction specimens to three different values, compressing back to zero strain, then reloading in tension until failure. Figure 5.19 showcases this test and only displays a single set of data for each prestrain to enhance clarity. Comparing the first reversal of each test, the yield surface can be seen

shrinking with increase in plastic prestrain, as well as the Bauschinger effect increasing for each respective cycle. The same applies for the second reversal. After that, all of the prestrain tests converge to roughly the same curve, which also correlates with the monotonic tension curve. This set of data is also used in the next chapter which will be focusing on calibrating a non-linear kinematic hardening model.

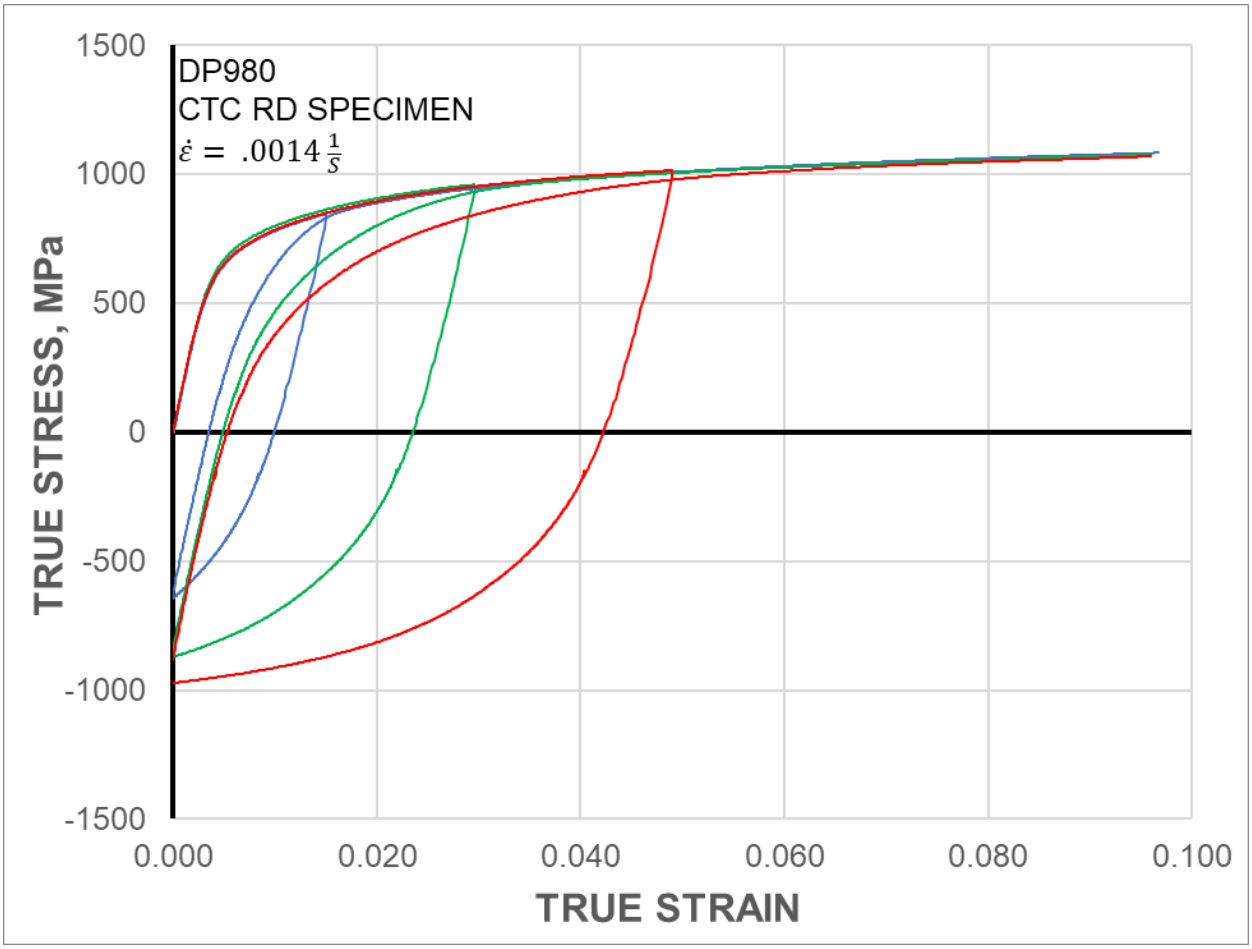


Figure 5.19 T-C-Tension to failure of DP980 at various prestrains.

*This page intentionally left blank*

# CHAPTER 6
# MATERIAL MODELING UNDER CYCLIC LOADING

## 6.1. Introduction

With the previous Chapters discussing the data being obtained from the CTC machine, this Chapter will focus on how this data can be turned into a usable model, that can be used as input in forming simulations. All materials tested exhibit, under cyclic loading, the Bauschinger effect (BE), in addition to a variety of other, material-specific phenomena, such as permanent softening, work-hardening stagnation, etc. [18]. In this Thesis, the BE will be represented by a non-linear kinematic hardening (NLKH) model. The NLKH model chosen is the multi-term Chaboche model [18]. The primary emphasis of this Chapter is an automated procedure for identifying the Chaboche parameters. First, a discussion of how the Chaboche parameters are categorized will be covered; then, we will move on to how to construct an algorithm that automatically optimizes the parameters to give a near-optimal fit. The end of the Chapter will cover what this fitting looks like for the DP980 steel tested previously (see CHAPTER 5).

## 6.2. Theoretical Underpinnings

The code produced from previous work [19] is utilized for this effort. There are multiple versions of this code; the one used for this thesis utilizes $J_2$ Flow Theory (seen in Equation (6.1)) with combined kinematic and isotropic hardening. Extension to a different yield

function, e.g., the Barlat et al. Yld2000-2D can be implemented in a straightforward way [19], but has not been pursued here since most experiments are conducted along the same material orientation. In $J_2$ Flow Theory, the yield function is given by:

$$f = J_2(\sigma_{ij} - \alpha_{ij}) - \sigma_Y = 0 \tag{6.1}$$

where $\sigma_{ij}$ is the stress tensor, $\alpha_{ij}$ the back-stress tensor and $\sigma_Y$ a material property, typically the flow stress in uniaxial tension.

In this work, yielding is associated with deviation from proportionality. Then, as can be seen in the experiments of the previous Chapter, e.g., Figure 5.13, Figure 5.19, etc. during unloading or reverse loading, yielding (i.e., deviation from proportionality) occurs before the zero stress is reached. Comparing the size of these subsequent yield surfaces to the initial one, the conclusion is drawn that the yield surface shrinks during plastic loading. The yield surface shrinkage is captured in this work by Equation (6.2), where $b$ and $Q$ are fitting constants [18].

$$\sigma_Y = \sigma_0 + Q(1 - e^{-bp}) \tag{6.2}$$

The current and initial flow stresses are represented by $\sigma_Y$ and $\sigma_0$, respectively, and $p$ is the equivalent plastic strain. This equation can capture the rapidly shrinking of the initial yield surface when plastic deformation initiates, and the stabilization to a constant size at larger strains. The three material parameters in Equation (6.2) are determined beforehand and will not be altered during the NLKH model calibration.

The Chaboche model used is 4-term, so that the code can be flexible for capturing the behavior of a variety of materials. With this higher-term model, some materials will have no need for this many terms, but will not suffer from the addition. In this work, the additional terms will be maintained for coding convenience, but the calibration can also be done with less terms and the code rewritten to not require all the terms.

Looking now in the NLKH model, the back-stress tensor ($\alpha_{ij}$) is represented by Equation (6.3) as the sum of 4 terms, while the evolution of each term with plastic deformation $p$ is represented by Equation (6.4):

$$d\alpha_{ij} = \sum_{k=1}^{4} d\alpha_{ij}^{(k)} \tag{6.3}$$

$$d\alpha_{ij}^{(k)} = \frac{2}{3} C^{(k)} d\varepsilon_{ij}^{p} - \gamma^{(k)} \alpha_{ij}^{(k)} dp \tag{6.4}$$

where $\varepsilon_{ij}^{p}$ are the components of the plastic strain tensor, and $C^{(k)}$ and $\gamma^{(k)}$ $(k = 1 - 4)$ are pairs of material constants, to be calibrated for the material at hand. It is interesting to note that Equation (6.4) is the same form of differential equation as the one for the isotropic part of hardening, that led to the integrated form seen as Equation (6.2). In that sense, the mathematical dependence of both the isotropic and kinematic components with plastic deformation is identical.

### 6.2.1. Categorization and Behavior of Chaboche Parameters

This section will focus on how the Chaboche parameters are calibrated to capture the stress-strain responses recorded in the cyclic experiments of the previous Chapter. First, in order to create an algorithm that can yield an acceptable prediction of the measured response, one must know how each parameter impacts the overall result.

The parameters can be thought of as pairs of $C^{(k)}$ and $\gamma^{(k)}$, as each set will predominately influence certain portions ($\alpha^{(k)}, k = 1 - 4$) of the predicted curve. Figure 6.1 provides an excellent depiction of how each $\alpha^{(k)}$ term is affecting the predicted response, and of the cumulative $\alpha$ term (Equation (6.5)) which corresponds to $\alpha_X$ in the figure. In this case, there are four back-stress terms that are summed together to produce the cumulative back-stress curve. Equation (6.5) below is essentially Equation (6.3) but written for the uniaxial components only.

$$\alpha = \sum_{k=1}^{4} \alpha^{(k)} \tag{6.5}$$

These four back-stress terms will be referred to as $\alpha^{(1)}$ through $\alpha^{(4)}$ for clarity; each term influences a particular region of the stress-strain curve, which will be explained further.

Following numerical order, $\alpha^{(1)}$ is designated as the initial transition from elastic to plastic. This term is meant to saturate quickly and provide an initial offset for the remaining terms. The terms $\alpha^{(2)}$ and $\alpha^{(4)}$ are curve-fitting terms and will be the primary values to modify for adjusting the fit. The final term to be discussed is $\alpha^{(3)}$, which corresponds to the constant tangent modulus found in the large deformation range. This term has little

impact on the initial elastoplastic transition, but will dictate the entire curve once the three other terms have saturated: looking at Figure 6.1 we find that at larger strains, all the other terms have saturated and no longer contribute to the calculated curve. This means $\alpha^{(3)}$ will be the only term contributing to the shape of the curve then.

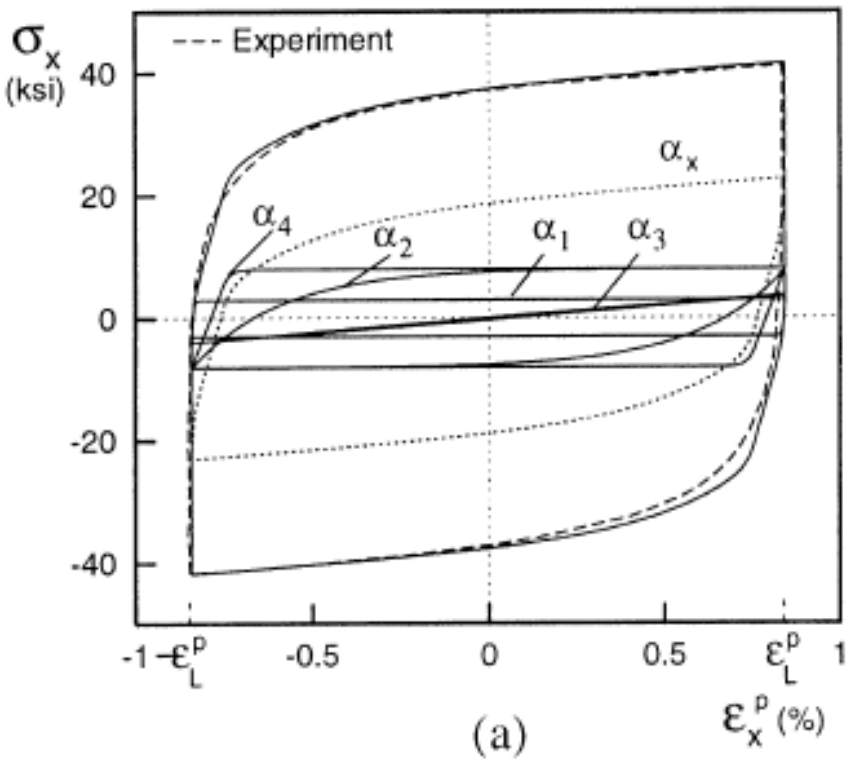


Figure 6.1 The cumulative action of each back-stress term on the agreement of the prediction with the experiment [20].

With reference to Figure 6.1, it can be seen that each $\alpha^{(k)}$ curve is composed of three parts: an initial, seemingly linear part, followed by a curved one, followed by another linear one. The main driver for each $\alpha^{(k)}$ term is the corresponding $\gamma^{(k)}$ (see Equation (6.4)), as this term dictates all shape features of the $\alpha^{(k)}$ curve, i.e., the initial slope, the succeeding

curvature and the saturation stress. The corresponding $C^{(k)}$ value modifies only the saturation stress. For example, with reference to Figure 6.1, if we wish to modify $\alpha^{(4)}$ to look like $\alpha^{(2)}$, modifying only $\gamma^{(4)}$ will change not only the initial slope and curvature, but also the saturation stress, which will require a further adjustment from $C^{(4)}$. A more efficient approach is to maintain the $\frac{C^{(4)}}{\gamma^{(4)}}$ ratio during this process, which will ensure that the resulting $\alpha^{(4)}$ has the same saturation stress as before. This allows the immediate adjustment of the shape of the curve, without needing numerous iterations.

### 6.2.2. Algorithm to Automatically Determine Chaboche Parameters

For a real material behavior, such as those measured in CHAPTER 5, all four terms of the Chaboche NLKH model might be needed. This results in eight Chaboche parameters that need to be determined, just for this model (i.e., beyond the elastic, etc., properties). Hence an algorithm to automatically determine these parameters has been developed and will be described here. As an illustrative example, this algorithm will be explained by calculating the Chaboche parameters appropriate to the DP980 steel sheet discussed in Section 5.6. The experiment that will be used for this purpose is the Tension-Compression-Tension test shown in Figure 5.19 (for the prestrain of 5%).

To calculate and optimize the Chaboche parameters, the algorithm must only focus on these eight parameters and not require changing other material properties. These other parameters, such as the elastic modulus and initial yield stress, need to be determined before proceeding, and set to fixed values throughout. Figure 6.2 showcases what this algorithm looks like, with the numerical values being specific to DP980.

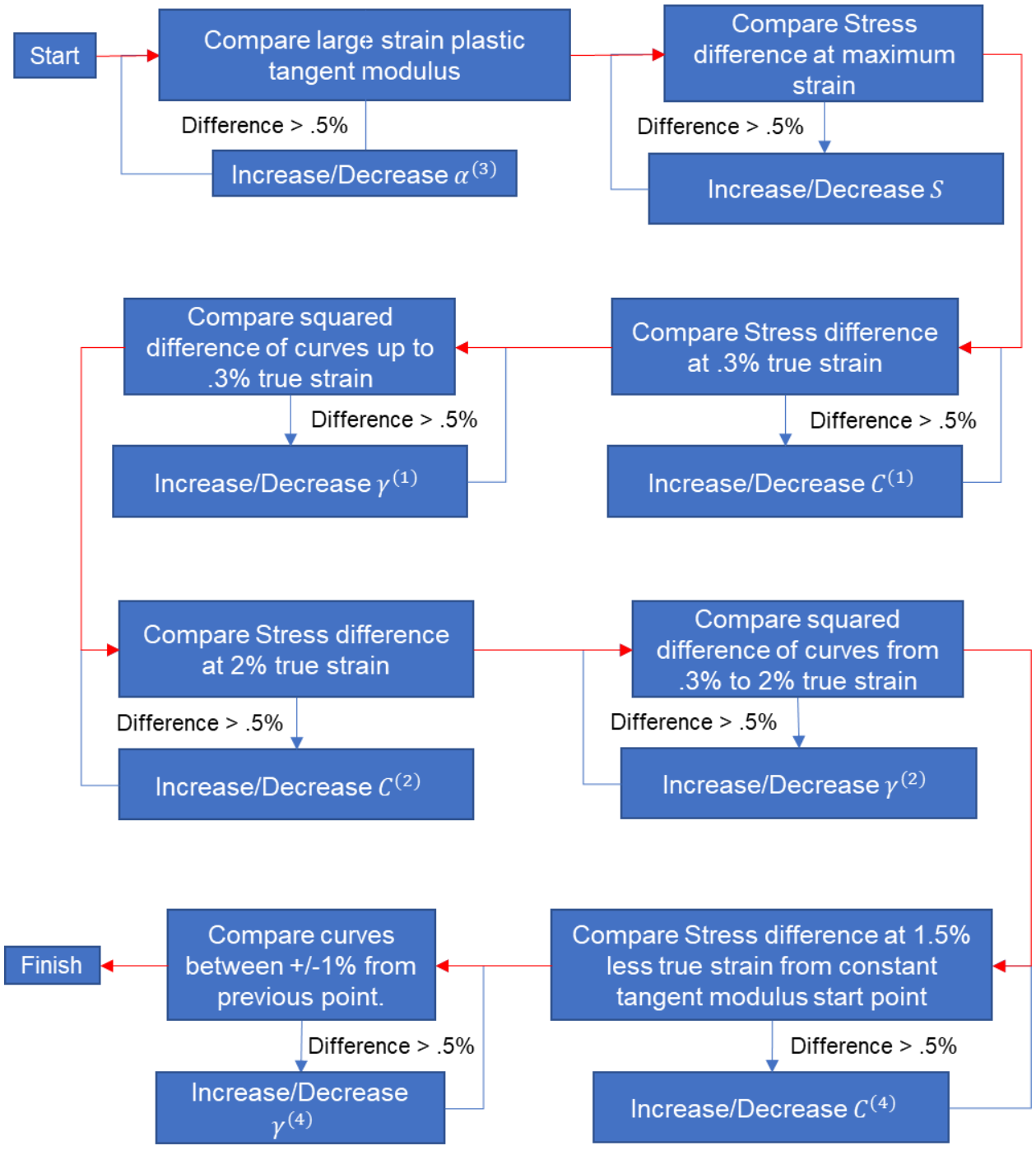


Figure 6.2 Flow chart for Chaboche algorithm for DP980.

The strain values used in Figure 6.2 are specific to the test ran for DP980, except for the .3% strain region which is typically appropriate for most materials. It is advised to start with the same strain values on a new material (assuming that a similar experiment is available for the calibration), and adjust them after the initial run, to see which regions would benefit the most from using different strain values.

Before the algorithm can start calculating these parameters, initial values need to be in place. These initial values are chosen specifically so that any material can use the algorithm and not have issues with the solver not converging. This initial fit does not necessarily have to be close to the experimental data, as all the values will be adjusted accordingly once the solver begins; but the initial fit should be close enough to the experiment, so that the algorithm does not face convergence issues. To maintain concordance with the previous section, the terms will be numbered in the same sequence to correspond to the calculated alpha terms as seen in Figure 6.1. The initial values used can be found in Table 6.1, and the resulting fit with respect to DP980 can be seen in Figure 6.3.

Table 6.1 : Initial parameters for Chaboche optimization algorithm.

| TERM | ALGORITHM VALUE |
|---|---|
| $C^{(1)}$(MPa) | 300,000 |
| $C^{(2)}$ (MPa) | 100,000 |
| $C^{(3)}$ (MPa) | 5,000 |
| $C^{(4)}$ (MPa) | 20,000 |
| $\gamma^{(1)}$ | 3,000 |
| $\gamma^{(2)}$ | 500 |
| $\gamma^{(3)}$ | 0 |
| $\gamma^{(4)}$ | 100 |

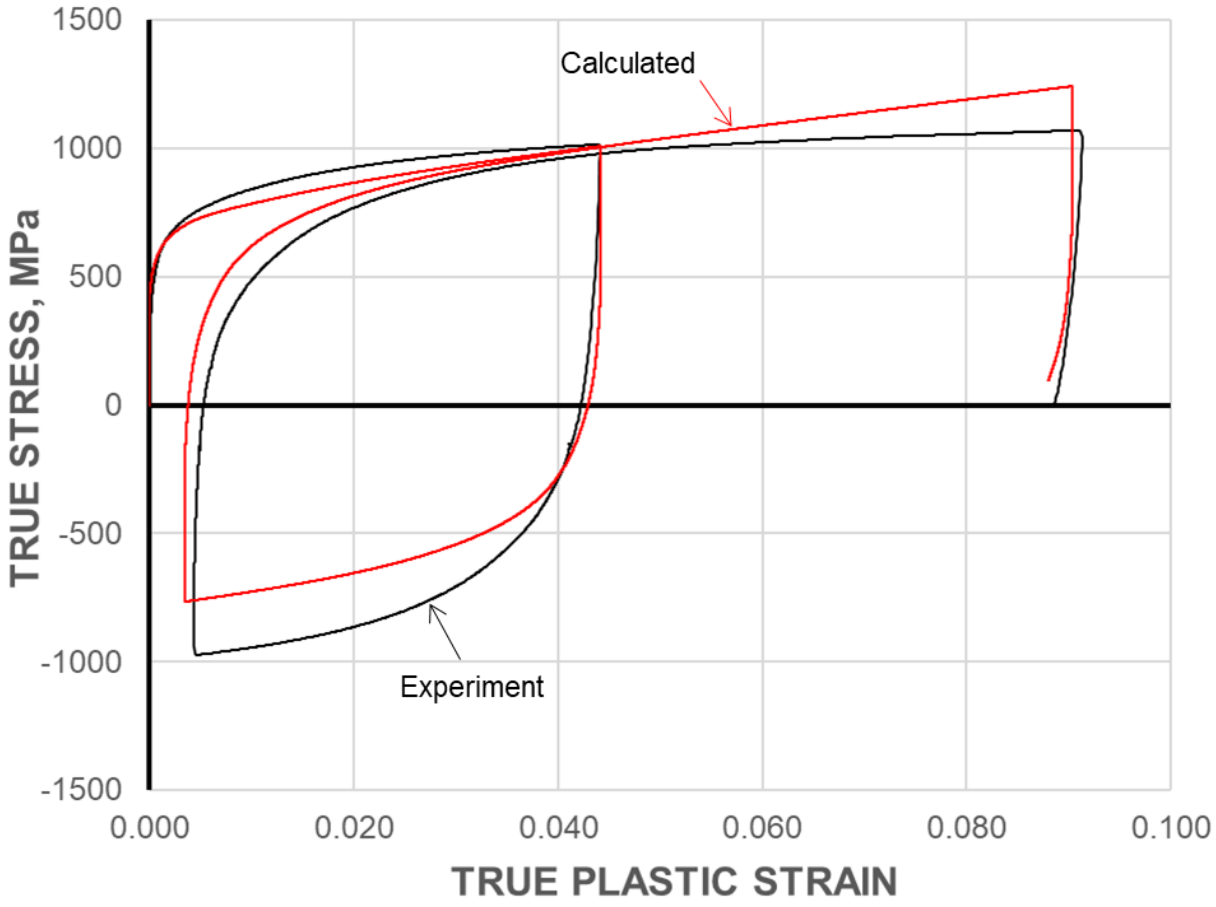


Figure 6.3 Agreement between prediction and experiment for the initial Chaboche values used in this work, for DP980 steel. Significant discrepancies after the first load reversal are seen.

Starting with the plastic tangent modulus at the large plastic deformation range, the algorithm will calculate the $\alpha^{(3)}$ term (see Figure 6.2). This calculated slope will stay the same regardless of what values are found for the remaining $\alpha^{(k)}$ components, since $\alpha^{(3)}$ will continue to grow after the other $\alpha^{(k)}$ terms have saturated. In order for the slope to always increase, the $\gamma^{(3)}$ value is set to zero and only $C^{(3)}$ will be modified, until the plastic tangent modulus matches the experimental data in the "large" deformation range, i.e., past roughly 6% plastic strain. To accomplish this, the current value of $C^{(3)}$ is increased,

if the slope is lower than the experimental one, and vice versa if it is higher. The change occurs based on a non-linear reduction scheme, i.e., the change depends on the current difference between the two slopes. When the difference is less than .5%, the iterations stop (see Figure 6.2). The calculated fit at this point can be seen in Figure 6.4.

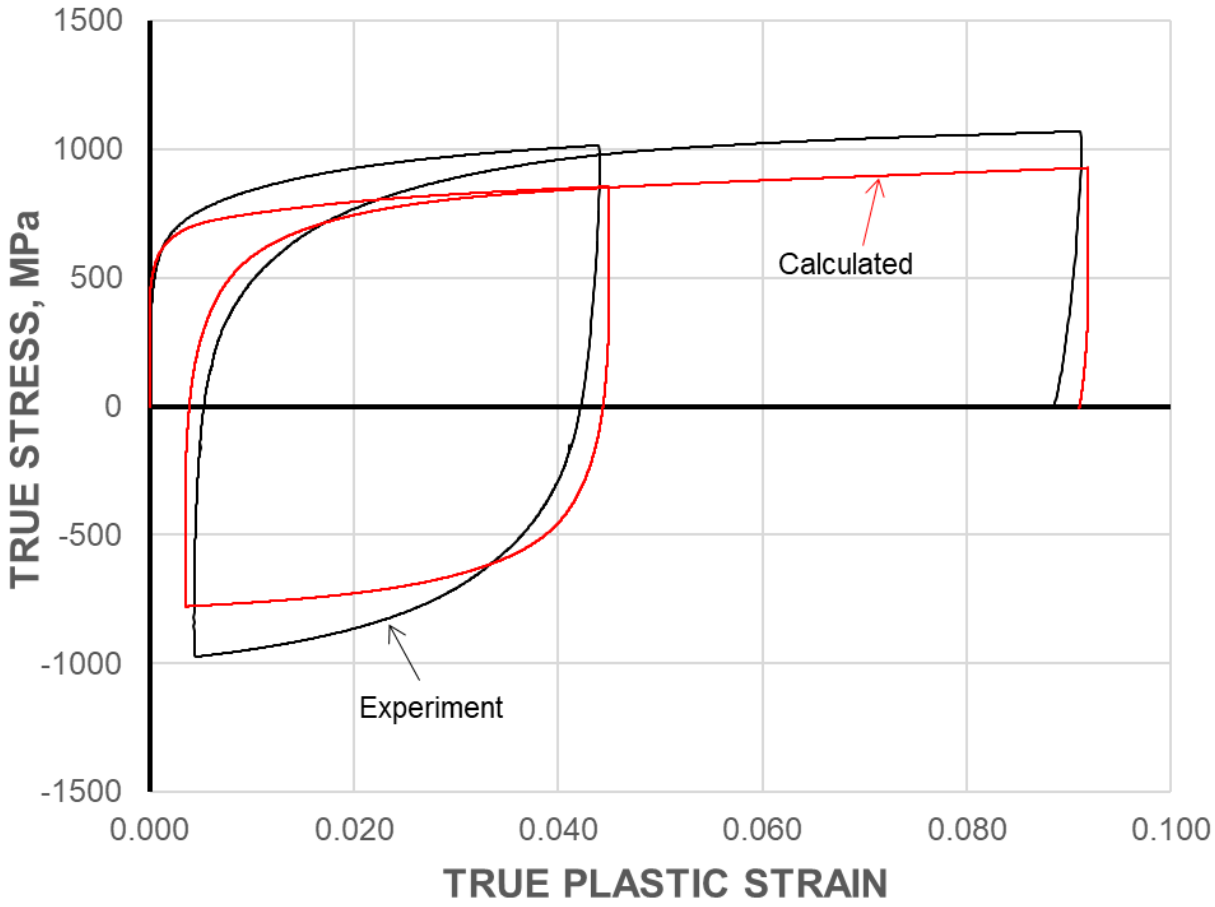


Figure 6.4 Fit of calculated curve after the plastic tangent modulus at large strains is matched to the experimental one.

Once $\alpha^{(3)}$ is determined, the next objective is to determine $S$ (Equation (6.6)), which directly correlates to the magnitude of the $\alpha$ term.

$$S = \sum_{\substack{k=1 \\ k \neq 3}}^{4} \frac{C^{(k)}}{\gamma^{(k)}} \tag{6.6}$$

This is done by varying the $C^{(1)}$ value which corresponds to $\alpha^{(1)}$. For that purpose, the stress at the final reversal point (e.g., the unloading at about 9% in Figure 6.4 is compared to the experiment; if it's too low, $C^{(1)}$ is increased; if it's too high, it is decreased. Once $S$ is determined (i.e., loop 2 in Figure 6.2 has converged), this value is then equally split between $\alpha^{(1)}$, $\alpha^{(2)}$ and $\alpha^{(4)}$ by maintaining $\gamma^{(k)}$ and only adjusting $C^{(k)}$. As long as $S$ remains the same, the calculated curve will closely match the stress saturation magnitude in the experimental data.

Using $\alpha^{(1)}$ again, the first pair of values ($C^{(1)}$ and $\gamma^{(1)}$) will be determined. To determine the magnitude of what this first set of values needs to be, the program looks for the stress saturation point of $\alpha^{(1)}$ to be at 0.3% true strain which is just after the customary .2% offset strain for the conventional determination of the yield stress. As $\alpha^{(1)}$ is increased or decreased, so is $\alpha^{(2)}$, to maintain a constant $S$ value. Once the stress saturation magnitude is satisfied (loop 3 of Figure 6.2), $\gamma^{(1)}$ is adjusted until the curvature falls within half a percent mean error of the experimental data in that strain region (loop 4 of Figure 6.2). Figure 6.5 showcases what the stress-strain response after the magnitude determination $S$ and $\alpha^{(1)}$ looks like, as well as further verifying that the large-strain plastic tangent modulus that was determined earlier for the curve past .06 plastic strain remains unchanged.

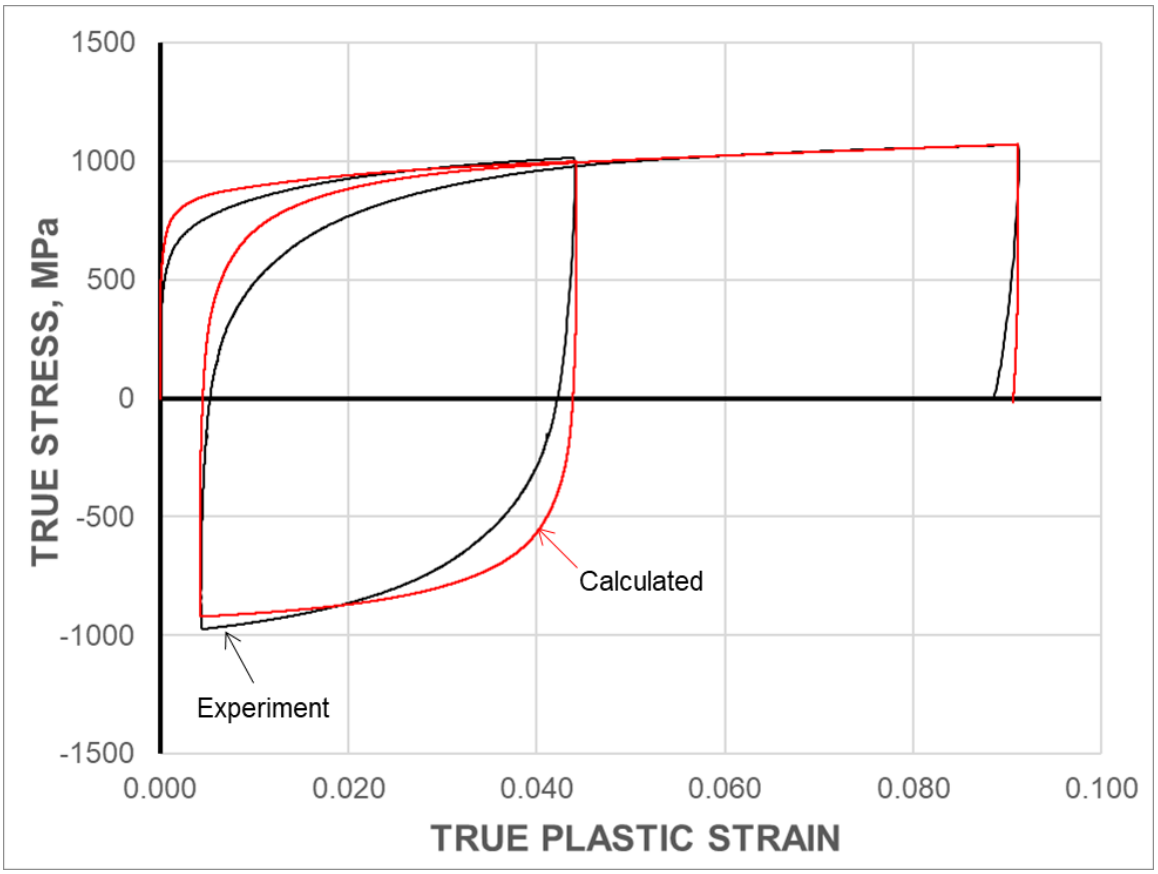


Figure 6.5 Fit of calculated curve with $S$ and $\alpha^{(1)}$ determined.

With $S$ and $\alpha^{(1)}$ calculated, the last $\alpha^{(k)}$ terms can be determined (loops 5-8 in Figure 6.2). Since $\alpha^{(2)}$ was used as an adjustment variable in the previous loop, $\alpha^{(2)}$ and $\alpha^{(4)}$ will be made equal magnitudes. Terms $\gamma^{(2)}$ will remain at 500, $\gamma^{(4)}$ at 100, and both $C^{(2)}$ and $C^{(4)}$ will be calculated by Equation (6.6) and noting that the $\frac{C^{(k)}}{\gamma^{(k)}}$ terms are kept the same throughout this process. Subsequently, $\gamma^{(2)}$ and $\gamma^{(4)}$ will be adjusted to match the curvatures in the experimental data. This process is simply taking two points on the experimental stress-strain response for each $\alpha^{(k)}$ term and changing $\gamma^{(2)}$ and $\gamma^{(4)}$ to match those designated points. In the present case, $\alpha^{(2)}$ is intended to control the curvature around the 2% strain region and $\alpha^{(4)}$ around the 6% one. The program will look

for a fit within half a percent mean error in the region of control for each term respectively with respect to curvature. With the final two terms determined, the calculated curve is complete (as far as the algorithm is concerned), as seen in Figure 6.6.

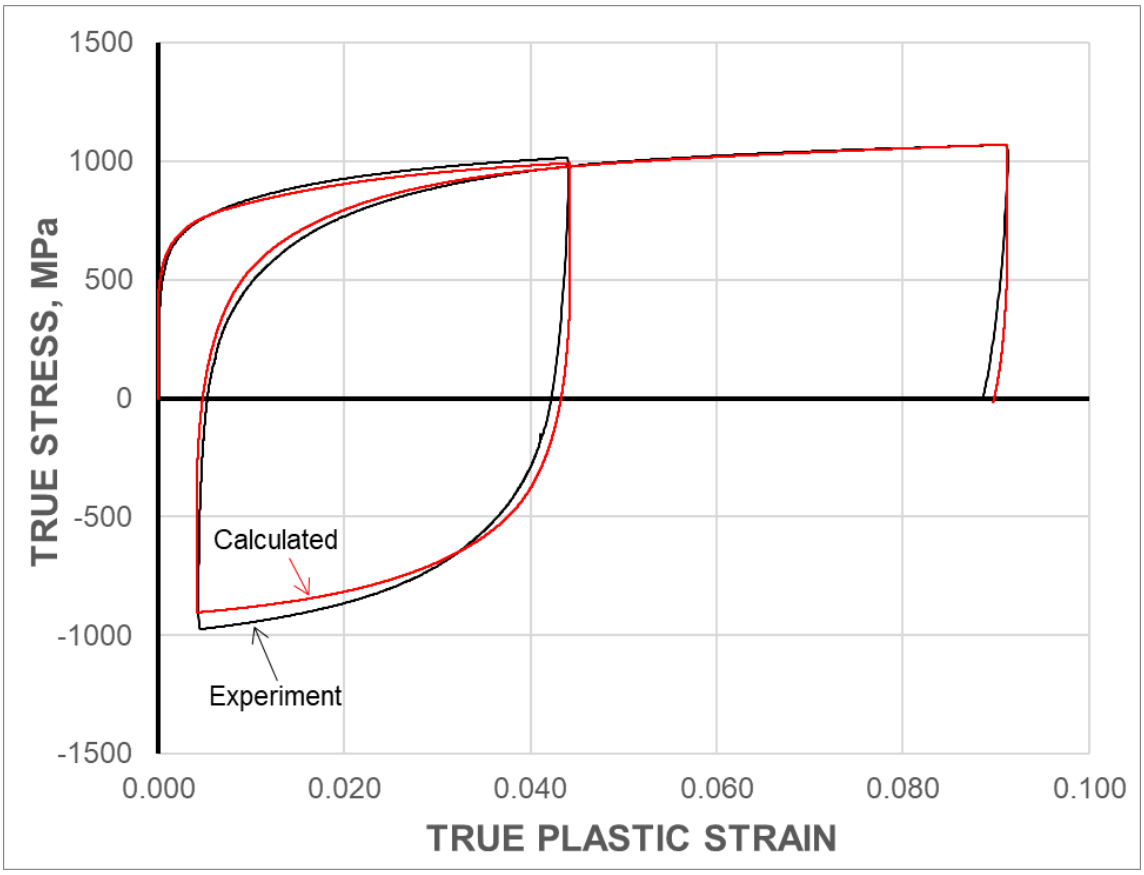


Figure 6.6 Fit of calculated curve with all terms determined.

With this best guess, the user will then have to manually modify the eight Chaboche parameters, to further improve the fit if desired. A future development of the algorithm would look at changing the percent ratio between the last two $\alpha^{(k)}$ sets rather than being 50/50. Another development that could be added would be changing $\gamma^{(3)}$ to be a value other than zero. This value would still be relatively small, but it will cause $\alpha^{(3)}$ to eventually plateau rather than infinitely increase.

### 6.3. Parameter identification for DP980 steel

Using the algorithm on DP980, an initial set of values are determined from the 0%-5%-0%-10% strain test referred to as TCTF (Tension-Compression-Tension to Failure), see Figure 5.19. The reason this test is chosen is due to its relatively large strain values, as well as the existence of additional tests with different prestrain reversals, that can be used for verification of the identified parameters (e.g., a 0%-1.5%-0%-10% strain test and a 0%-3%-0%-10% one). The other parameters that were used for the algorithm can be found in Table 6.2.

Table 6.2 : Remaining Parameters for DP980 Chaboche optimization algorithm

| TERM | VALUE |
|---|---|
| b | 200 |
| Q | -140 MPa |
| PROPRTIONAL STRESS (INITIAL YIELD STRESS) | 430 MPa |
| ELASTIC MODULUS | 201.2 GPa |
| POISSON'S RATIO | 0.27 |

The values that are initially calculated by the algorithm with a $\gamma^{(3)}$ modification (i.e., non-zero value, unlike in the previous section) are found to be an acceptable starting point but need further refinement. This manual "optimization" was done in consultation with Dr. Minki Kim [17], to produce a fit with much better agreement with the reverse loadings. Both sets of values can be found below in Table 6.3 for comparison.

Table 6.3 : Chaboche terms determined for DP980 [17]

| TERM | INITIAL FIT | OPTIMIZED VALUE |
|---|---|---|
| $C^{(1)}$ (MPa) | 300,000 | 300,000 |
| $C^{(2)}$ (MPa) | 115,500 | 110,000 |
| $C^{(3)}$ (MPa) | 1,500 | 1,500 |
| $C^{(4)}$ (MPa) | 27,720 | 30,000 |
| $\gamma^{(1)}$ | 3,000 | 3,000 |
| $\gamma^{(2)}$ | 500 | 500 |
| $\gamma^{(3)}$ | 5 | 22.5 |
| $\gamma^{(4)}$ | 80 | 80 |

Looking at Figure 6.7, the experimental data along with both fits can be seen. Starting at 0% strain, both fits have very good agreement with the experiment, up until the first load reversal. After that reversal, the optimized fit can be seen to follow the experimental data up to the second load reversal better than the initial fit. After the second load reversal, the initial fit merges back to the experimental data, whereas the manually-optimized one deviates to a plateaued value, which would be expected due to $\gamma^{(3)}$ being further away from zero.

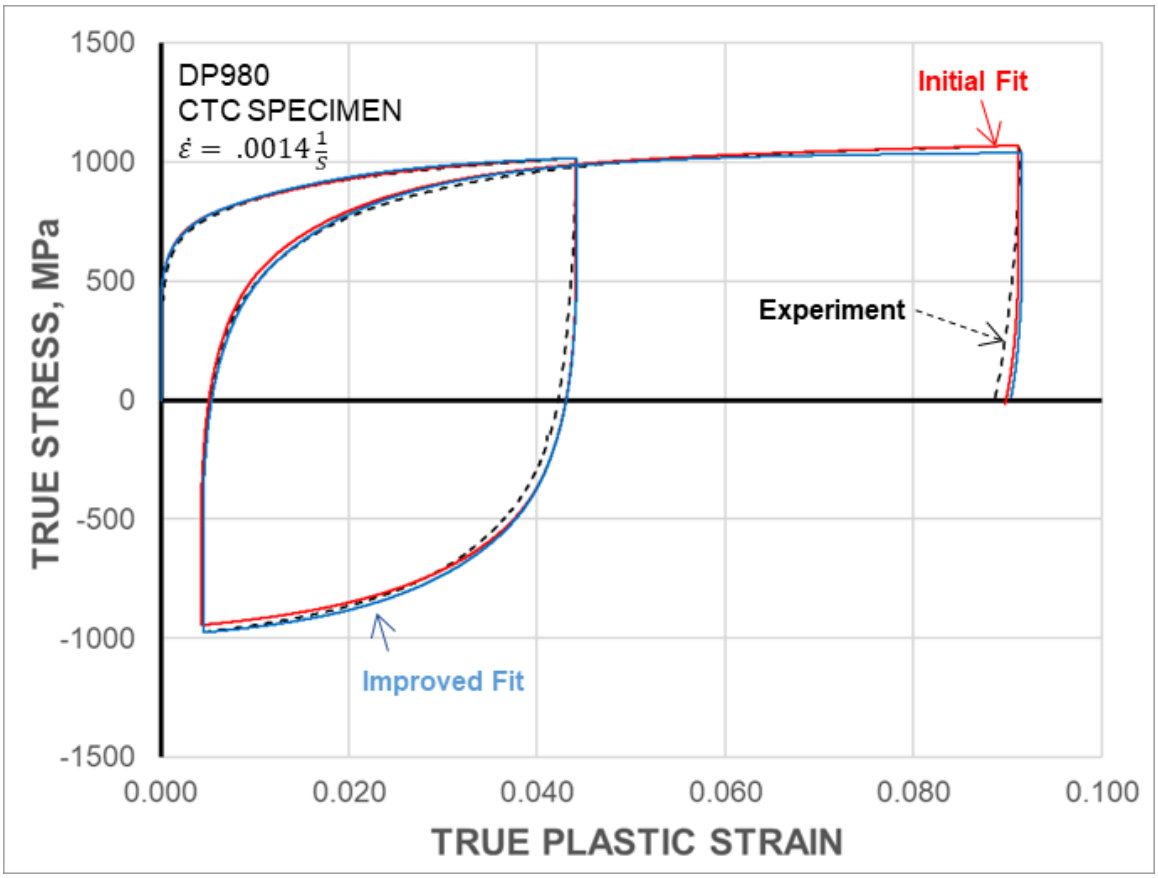


Figure 6.7 Fit of calibrated curves against DP980 TCTF experimental results.

Using the optimized values for the remaining TCTF tests further illustrates the agreement between the predicted and experimental curves. Figure 6.8 and Figure 6.9 both display the comparison of TCTF tests on the DP980 material, along with the predicted curve for each. For the smaller strain test (which had a prestrain of 1.5%), the predicted curve follows the experimental data very well up until the second load reversal. After that reversal, Figure 6.8 shows a large deviation between the experimental data and predicted curve until the stress saturation point (at about .05 strain). The agreement is much better in Figure 6.9. In both comparisons, the predicted curve saturates to a low level of work hardening, whereas the experimental data continually hardens.

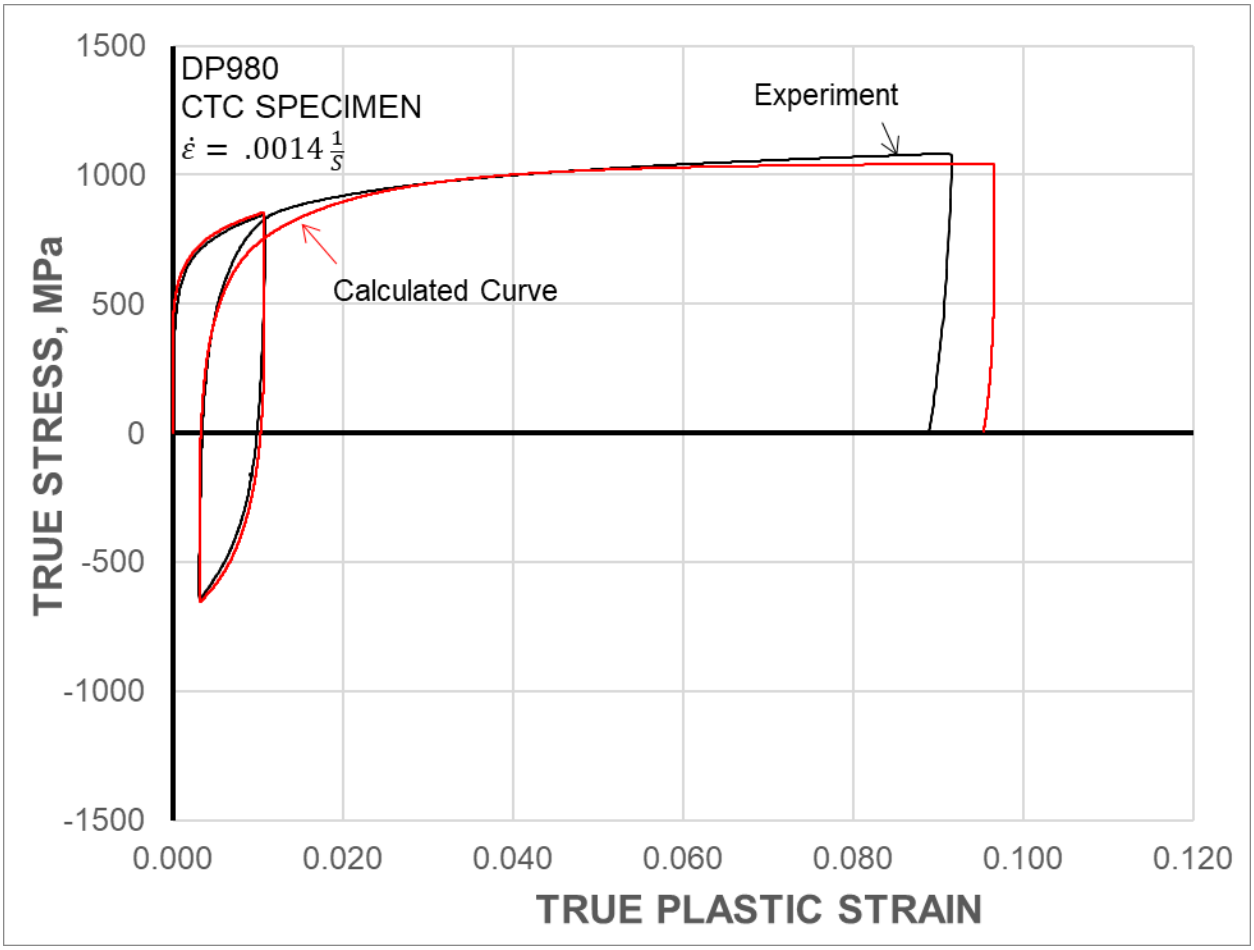


Figure 6.8 Prediction of the 0%-1.5%-0%-10% DP980 TCTF test using the manually-optimized material parameters.

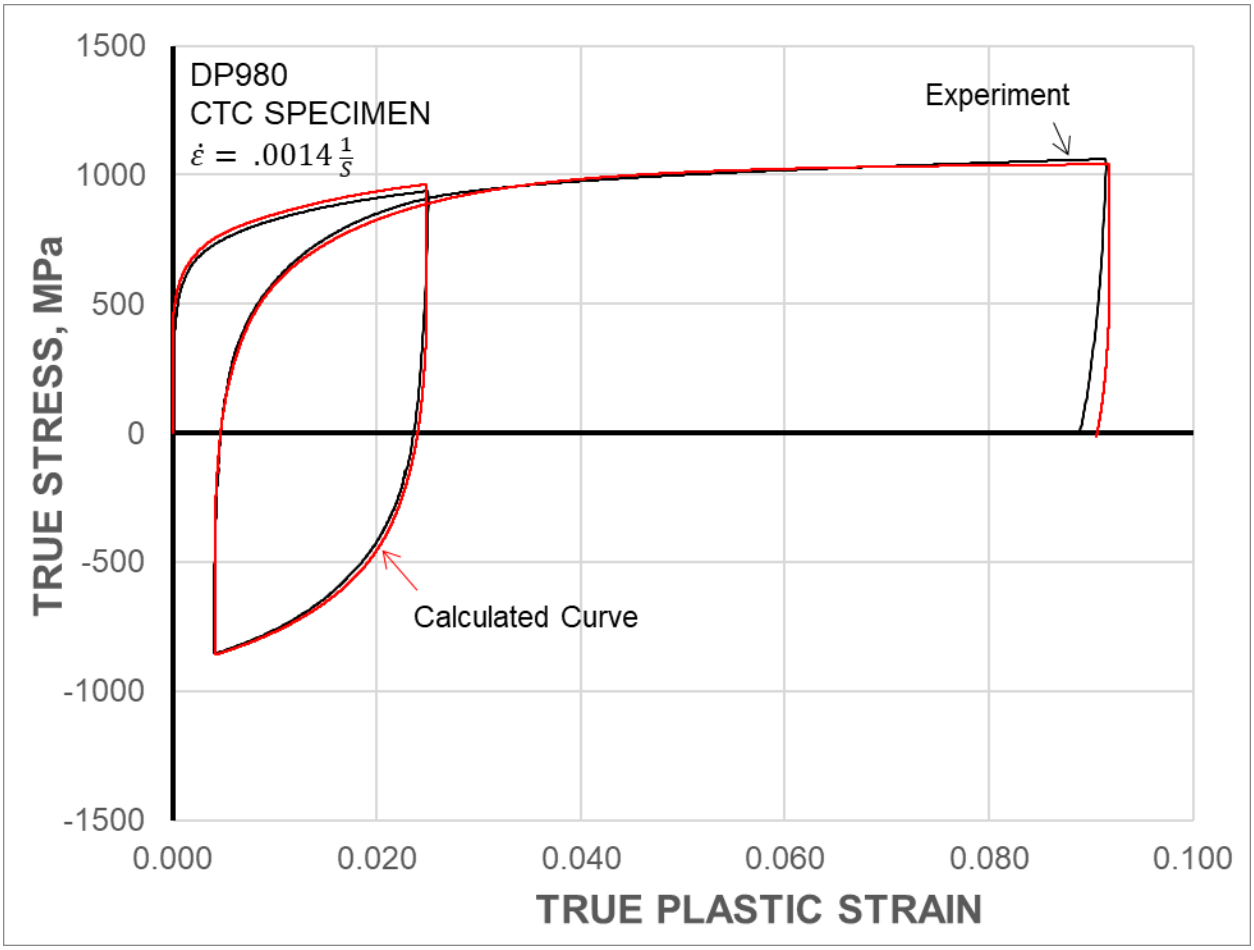


Figure 6.9 Prediction of the 0%-3%-0%-10% DP980 TCTF test using the manually-optimized material parameters.

Applying the same parameters to predict the responses under different loading histories, the agreement between the predicted curve and experimental result is still acceptable, except for large compressive strains. Looking at Figure 6.10, the calculated curve tends to under-predict the compressive stress due to the amount of tension-compression asymmetry in the material. (As a reminder, the current material model cannot capture that asymmetry.) After the first load reversal, the calculated curve eventually merges back into the experimental data around .05 true plastic strain.

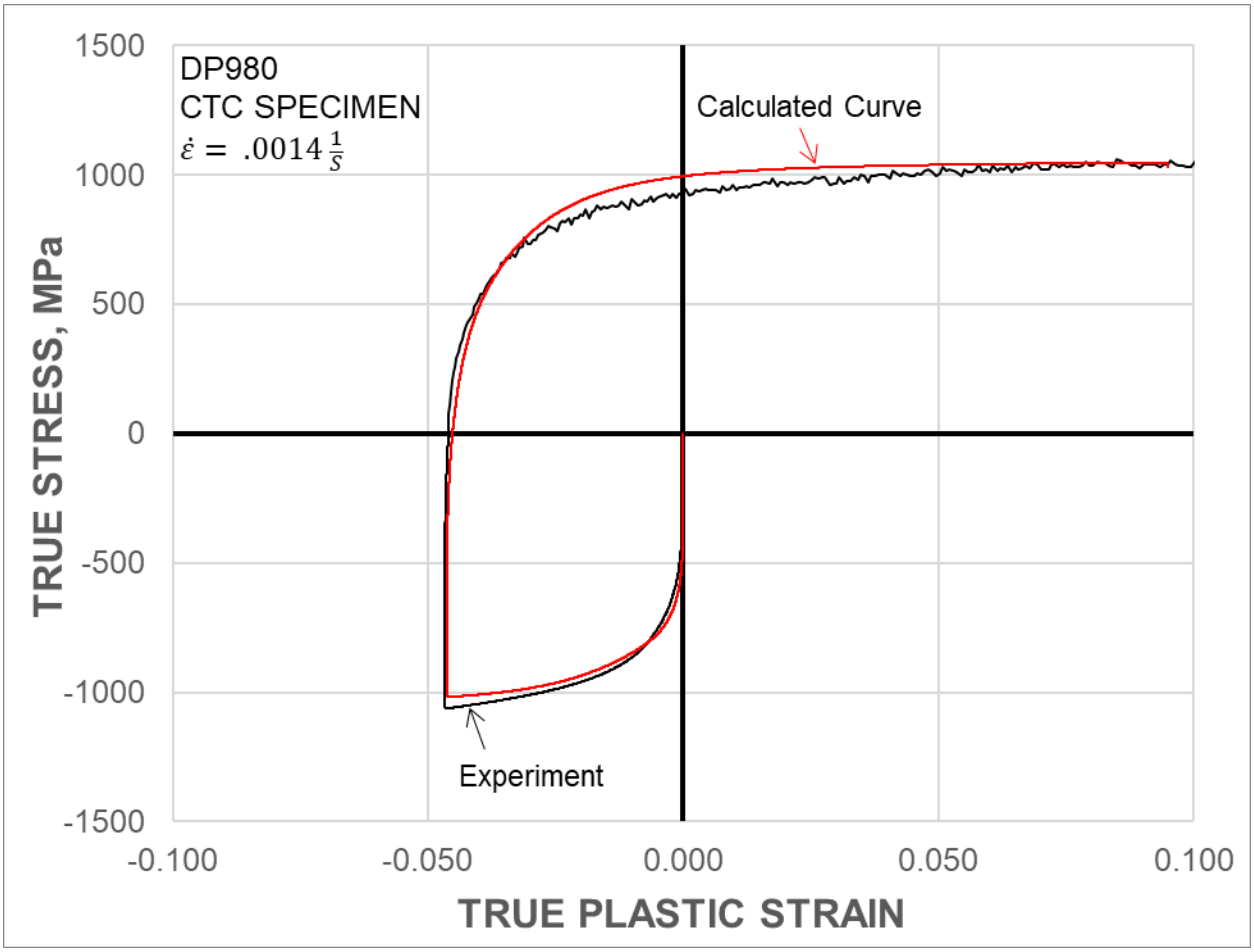


Figure 6.10 Prediction of the DP980 compression-to-tension-to-failure test using the manually-optimized material parameters.

When assessing the quality of agreement for the calculated curve on an experiment with large compressive strain, as seen in Figure 6.11, the large amount of deviation between the curves is significant. This is because the model doesn't reproduce the asymmetry in the material, and can be seen clearly in Figure 6.11, where major deviation can be seen after -.03 plastic strain. This agreement can be improved by having different Chaboche parameters for tension and compression, but this was not attempted for this study. Another reason for the discrepancy is that the change in elastic modulus is not

accounted for in this algorithm. This discrepancy is minor but is still mildly noticeable in reversals at large strains such as Figure 6.7.

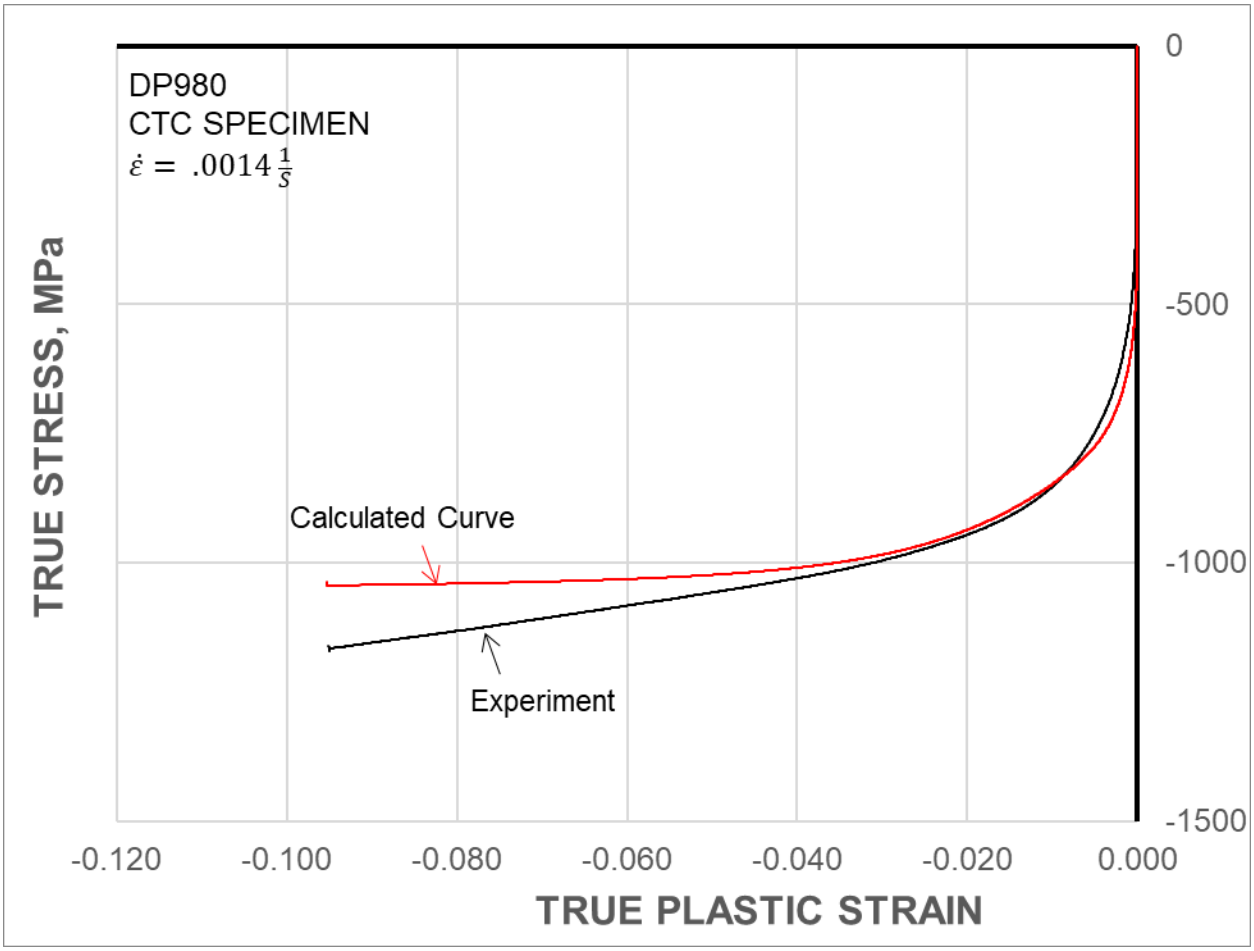


Figure 6.11 Prediction of the DP980 pure compression test using the manually-optimized material parameters.

# CHAPTER 7
# CONCLUSIONS AND FUTURE WORK

## 7.1. Introduction

In this final chapter, the major conclusions from this work, as well as improvements that can be made to the existing design will be discussed, along with future work. The design that is described in this work created a stable starting point, that will allow future users to further improve the overall system design. The biggest setback that is in this current design is based on the maximum strain that can be captured, but this setback can easily be overcome with the hardware improvements which will be described.

## 7.2. Conclusions

As the machine currently stands, the goal originally set of being able to successfully test thin sheet metal has been achieved. In the verification tests covered in CHAPTER 4, the machine has proven to provide accurate results using a unique shaped specimen, as well as producing almost identical results with the machine at the Tokyo University of Agriculture and Technology that is based on the same testing concept. CHAPTER 5 successfully showcased the capabilities of the machine by testing various materials such as aluminum AA6022-T43, EDDQ steel, and Dual Phase steels. A few of the findings in that chapter were:

- AA6022-T43 is found to be able to achieve higher stresses in a cyclic manner compared to pure tension.
- EDDQ compared the difference in cycling the material starting in tension versus compression and found that the tension-compression asymmetry is significantly higher in the compression starting test versus the tension one.
- JAC-270D is found to not have a noticeable tension-compression asymmetry compared to other materials tested in this work.
- DP590 has work-hardening stagnation in tests starting in tension but not compression. It exhibits significant tension-compression asymmetry.
- DP980 compared the different orientations to RD in pure compression and found that the lowest stress path is the rolling direction progressing towards the transverse direction.
- DP1180 is found to not have significant cyclic hardening until after being cycled past 1.5% strain. It exhibits significant tension-compression asymmetry.

Using the data obtained from the machine, CHAPTER 6 showcased how a material model can be calibrated. In addition, an algorithm was created to improve the efficiency of this task and used to determine the properties for DP980 with very satisfactory agreement between experiment and prediction.

Although further improvements can be made to bring the design to the next level, the machine is still fully capable of performing the tests needed for material parameter characterization.

## 7.3. Hardware Improvements

As suggested above, the biggest setback in the current design is related to the maximum range of strain that can be captured. At the time of this writing, the machine can reliably read about +/- 4.5% engineering strain, which significantly limits the usage when examining materials that can easily strain up to 20%. A work-around was created, as discussed in 3.2.1, which allowed the full 10% strain to be read, but this is still not practical for all types of measurements envisioned. To improve upon this, new hardware can be used to increase the strain range. The process should essentially be plug-and-play where the new hardware is plugged into the computer or DAQ chassis and the software would only need to update where the strain data is being read from. Since the software is programmed to have a single point of reading strain data, the update to where the strain is being read will update the entire program.

Another aspect that could be improved upon is the rod-alignment coupler and making this connection more rigid. Currently, the connection has a “dead” zone where a significant amount of travel occurs before the specimen deformation reverses direction. This can be seen in the force vs. displacement plots of the data, where there is a flat zone before a change in force resumes. There are a few options on how to fix this, but the quickest and simplest solution is to add a displacement sensor directly on the moving comb die assembly. That way there is no additional compliance that will be induced. Furthermore, there are open ports in the current hardware that can be used to wire up the sensor. Another solution is to remove the rod alignment coupler altogether and switch to a rigid connection. Even with this rigid connection to the rest of the load train, there will

still be compliance that can cause skewed displacement results but the flat zone for the force will be removed, and no additional sensors would be needed.

## 7.4. Machine Control Program Improvements

As far as the control program goes, user-friendliness will most likely need to be improved since this machine has not been run by many new users. An attempt was made to create help buttons to explain what certain features buttons do, but there is still more that can be done with respect to clarity. A work-instructions package will help ease the learning curve for a new user.

Another improvement that can be made is related to creating flexibility with the tests that can be performed. It is possible to create a test option which uses an excel table which can control whether the machine is in force/strain control, what strain values reversals will occur, and at what force values should loading reversals occur. By adding this to the control program, the user could test whatever they desire without needing to create a whole new test tab. This aspect could also be expanded upon further from what has been listed if more control options are desired, e.g., adding a temperature input, etc.

# REFERENCES


[1] Volvo Car, "Body Structure (with Graphics)," 22 07 2014. [Online]. Available: https://www.media.volvocars.com/uk/en-gb/media/videos/148248/body-structure-with-graphics.

[2] U.S. Department of Energy, "Vehicle Fuel Efficiency (CAFE) Requirements by Year," 25 04 2013. [Online]. Available: https://afdc.energy.gov/data/?q=cafe.

[3] World Auto Steel, "Springback," [Online]. Available: https://ahssinsights.org/forming/springback/.

[4] R. H. Wagoner, H. Lim and M.-G. Lee, "Advanced Issues in springback," *International Journal of Plasticity,* vol. 45, pp. 3-20, 2013.

[5] Product Development Services Ltd., "PDS," [Online]. Available: http://www.pdslimited.com/index_files/FEA_Forming.htm. [Accessed 27 04 2022].

[6] R. K. Boger, R. H. Wagoner, F. Barlat, M. G. Lee and K. Chung, "Continuous, large strain, tension/compression," *International Journal of plasticity,* vol. 21, no. 12, pp. 2319-2343, 2005.

[7] J. A. Miller, "A Fixutre for Compressive Tests of Thin Sheet Metal between Lubricated Steel Guides," National Advisory Committee for Aeronautics , Washington, 1946.

[8] F. Yoshida, T. Uemori and K. Fuijiwara, "Elastic–plastic behavior of steel sheets," *International Journal of Plasticity,* vol. 18, no. 5-6, pp. 633-659, 2002.

[9] Z. L. Kowalewski, L. Dietrich and G. Socha, "Experimental investigation of thin metal sheets under tension-compression cyclic loading," in *8th Australasian Congress on Applied Mechanics, ACAM 8*, Melbourne, Australia, 2014.

[10] J. Cao, W. Lee, H. S. Cheng, M. Seniw, H.-P. Wang and K. Chung, "Experimental and numerical investigation of combined isotropic-kinematic hardening behavior of sheet metals," *International Journal of Plasticity,* vol. 25, no. 5, pp. 942-972, 2009.

[11] T. Kuwabara and T. Nakajima, "Material Modeling of 980 MPa Dual Phase Steel Sheet Based on Biaxial Tensile Test and In-plane Stress Reversal Test," *Journal of Solid Mechanics and Materials Engineering,* vol. 5, no. 12, pp. 709-720, 2011.

[12] ASM International, ASM Metals Reference Book, ASM International, 1993.

[13] ASM international, ASM Specialty Handbook - Carbon and Alloy Steels, ASM international, 1996.

[14] ASTM International, *E8/E8M-13a | Standard Test Methods for Tension Testing of Metallic Materials,* ASTM International, 2013.

[15] T. J. Roemer, T. J. Barrett, M. Knezevic, B. L. Kinsey and Y. P. Korkolis, "Experimental study of continuous-bending-under-tension of AA6022-T4," *Journal of Materials Processing Technology,* vol. 266, pp. 707-714, 2019.

[16] F. Yoshida, H. Hamasaki and T. Uemori, "Modeling of anisotropic hardening of sheet metals including description of the Bauschinger effect," *International Journal of Plasticity,* vol. 75, pp. 170-188, 2015.

[17] M. Kim, J. Ha, J. McNally and Y. P. Korkolis, "Transient Hardening and R-value Behavior in Two-step Tension and Loading Reversal for DP980 Sheet," in *International Deep-Drawing Research Group Conference (IDDRG 2022)*, 2022.

[18] J. Lemaitre and J.-L. Chaboche, Mechanics of Solid Materials, New York: Cambridge University Press, 1990.

[19] N. Deng, T. Kuwabara and Y. P. Korkolis, "On the non-linear unloading behavior of a biaxially loaded dual-phase steel sheet," *International Journal of Mechanical Sciences,* Vols. 138-139, pp. 383-397, 2018.

[20] S. Bari and T. Hassan, "Anatomy of coupled constitutive models for ratcheting simulation," *International Journal of Plasticity,* vol. 16, no. 3-4, pp. 381-409, 2000.

[21] T. Maeda, N. Noma, T. Kuwabara, F. Barlat and Y. P. Korkolis, "Measurement of the strength differential effect of DP980 steel sheet and experimental validation using pure bending test," *Journal of Materials Processing Technology,* vol. 256, pp. 247-253, 2018.

[22] T. Kuwabara, Y. Kumano, J. Ziegelheim and I. Kurosaki, "Tension–compression asymmetry of phosphor bronze for electronic parts and its effect on bending behavior," *International Journal of Plasticity,* vol. 25, no. 9, pp. 1759-1776, 2009.

[23] T. Kuwabara and T. Nakajima, "Material Modeling of 980 MPa Dual Phase Steel Sheet Based on Biaxial Tensile Test and In-plane Stress Reversal Test," *Journal of Solid Mechanics and Materials Engineering,* vol. 5, no. 12, pp. 709-720, 2011.

[24] G. Joo, H. Huh and M. K. Choi, "Tension/compression hardening behaviors of auto-body steel sheets at intermediate strain rates," *International Journal of Mechanical Sciences,* Vols. 108-109, pp. 174-187, 2016.

[25] T. Hama, Y. Kariyazaki, N. Hosokawa, H. Fujimoto and H. Takuda, "Work-hardening behaviors of magnesium alloy sheet during in-plane cyclic loading," *Materials Science and Engineering: A,* vol. 551, pp. 209-217, 2012.

# APPENDIX A
# ADDITIONAL CALCULATION INFORMATION

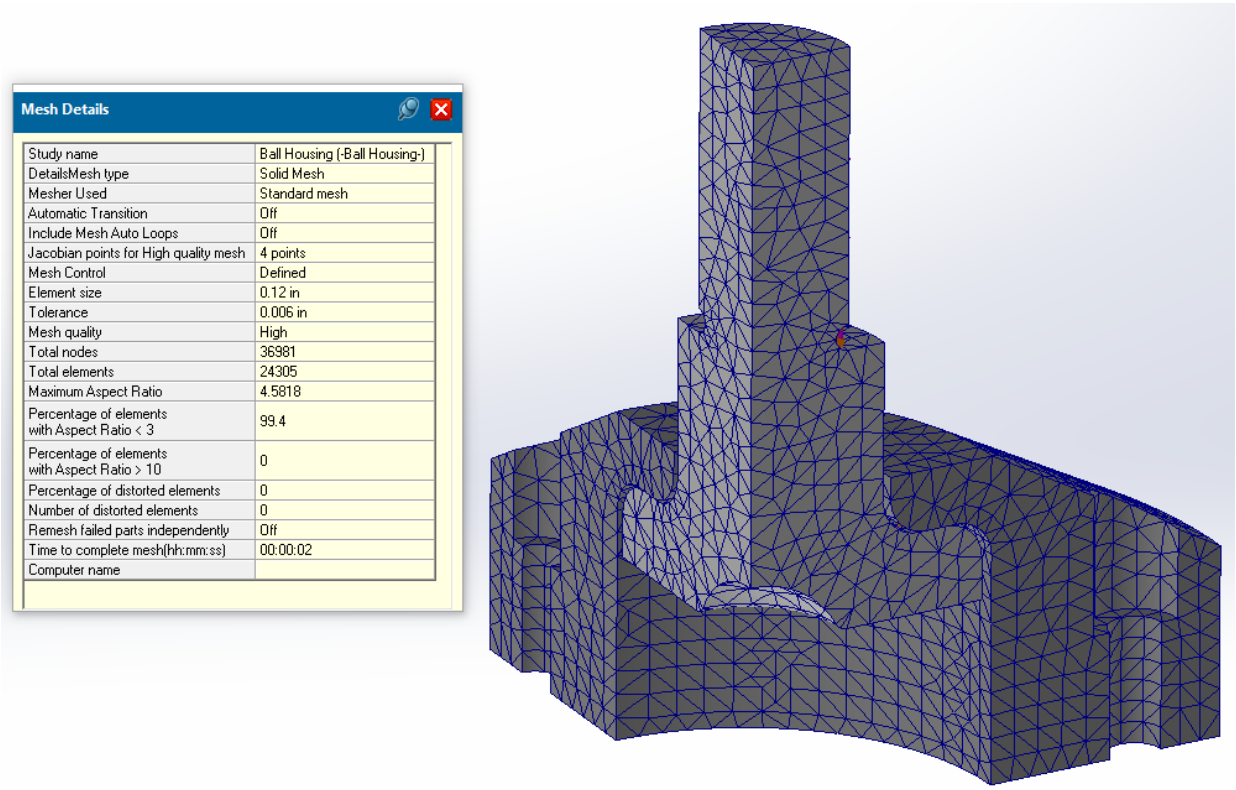

**Mesh Details**

| | |
|---|---|
| Study name | Ball Housing (-Ball Housing-) |
| DetailsMesh type | Solid Mesh |
| Mesher Used | Standard mesh |
| Automatic Transition | Off |
| Include Mesh Auto Loops | Off |
| Jacobian points for High quality mesh | 4 points |
| Mesh Control | Defined |
| Element size | 0.12 in |
| Tolerance | 0.006 in |
| Mesh quality | High |
| Total nodes | 36981 |
| Total elements | 24305 |
| Maximum Aspect Ratio | 4.5818 |
| Percentage of elements with Aspect Ratio < 3 | 99.4 |
| Percentage of elements with Aspect Ratio > 10 | 0 |
| Percentage of distorted elements | 0 |
| Number of distorted elements | 0 |
| Remesh failed parts independently | Off |
| Time to complete mesh(hh:mm:ss) | 00:00:02 |
| Computer name | |

Figure A 1 Ball housing assembly tension FEA Mesh displayed with mesh details

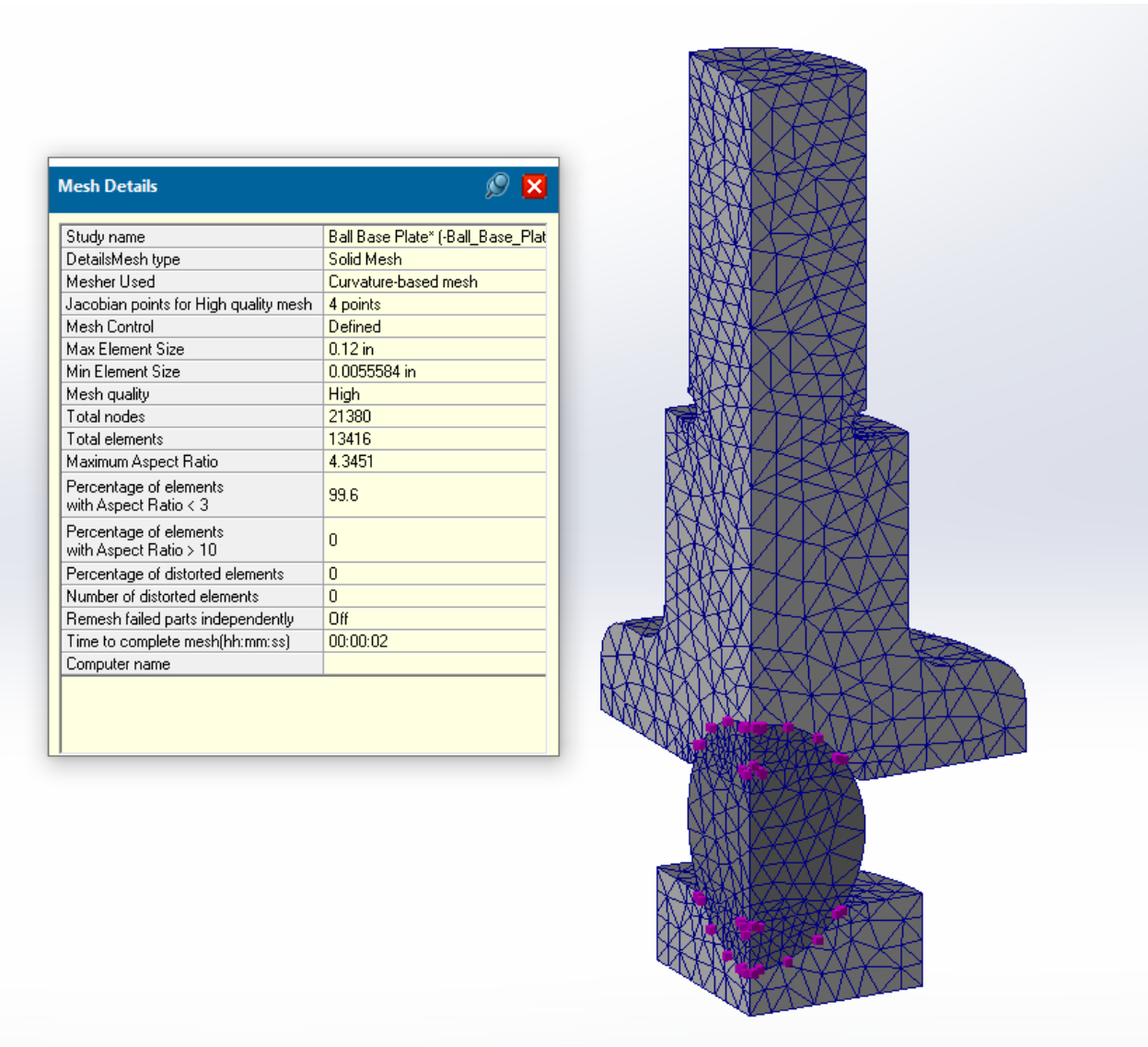


Figure A 2 Ball housing assembly compression FEA Mesh displayed with mesh details

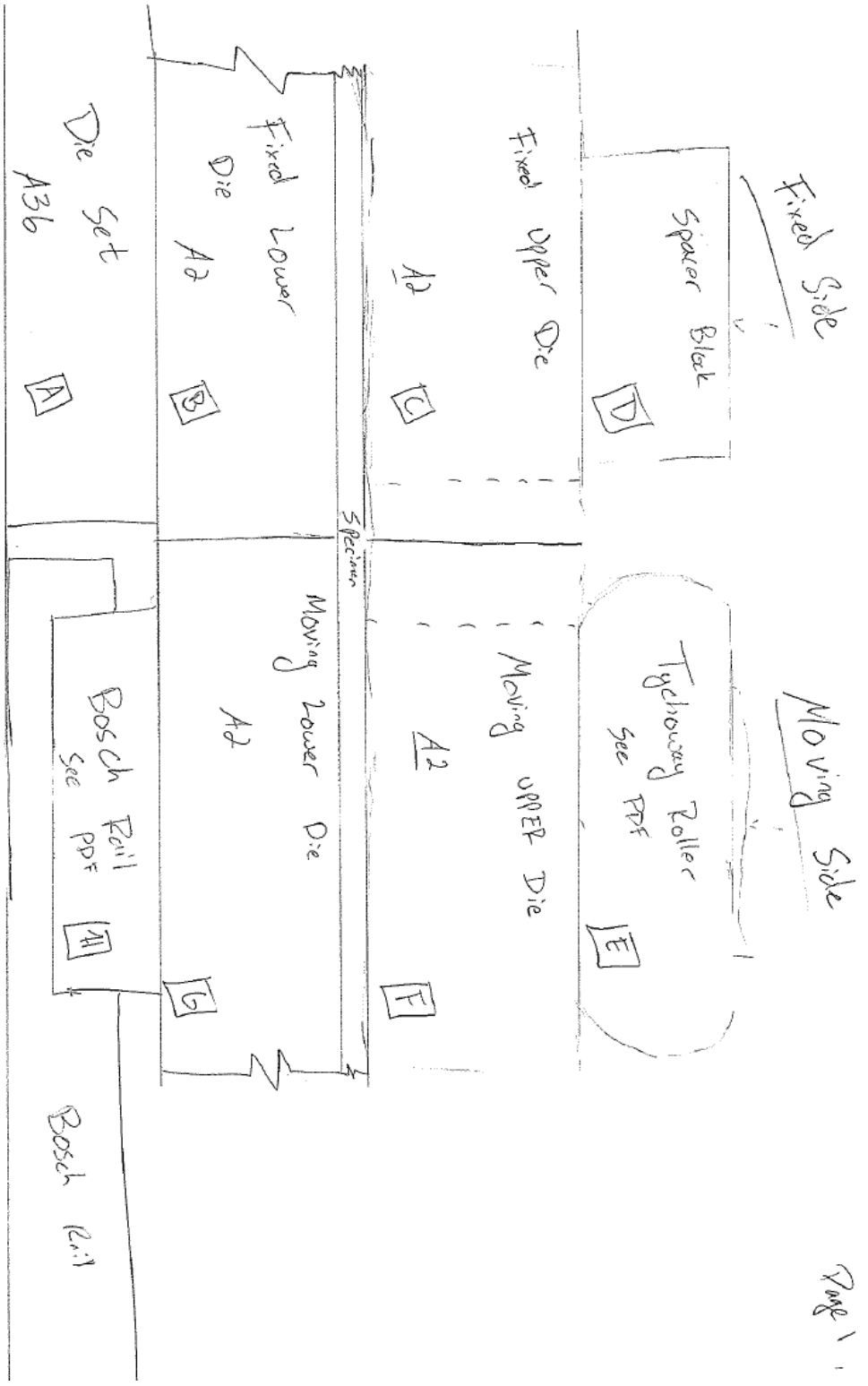


Figure A 3 Compliance of comb dies labeling major features

Fixed Lower and UPPER die are assumed to have the same stress modulus

3+6

$\delta_{B6} = \frac{FL}{AE} = \frac{443.59 \times 10^{-9}\ m}{} = 443.59 \times 10^{-6}\ mm$

$= 0.444\ \mu m$

$F = 15\ kN$

$L = 24,700\ mm$

$A = 41,758\ mm \cdot 98,425\ mm$

$E_{A36} = 29.5 \times 10^{3}\ Ksi = 203.4\ GPa$

---

4] Die set

$\delta_A = \frac{FL}{AE} = 656.93 \times 10^{-6}\ mm$

$= 0.657\ \mu m$

$F = 15\ kN$

$L = 36mm$

$A = 41,758\ mm \cdot 98,425mm$

$E_{A36} = 200\ GPa$

---

Combined elastic deformation under the Specimen

| Fixed | Moving |
|---|---|
| $0.444\ \mu m$ | $0.444\ \mu m$ |
| $0.657\ \mu m$ | $14\ \mu m$ |
| Total = $1.101\ \mu m$ | $14.444\ \mu m$ |

Difference = $13.343\ \mu m$

4] elastic deformation is assumed to be $14\ \mu m$ until official chart comes in, 4/3/16

$F = 15\ kN \quad A = 4.11 \times 10^{-3}\ m^2$

$E_{peek} = 3.45\ GPa$

$L_{Pek} = \frac{13.343\ \mu m \cdot A \cdot E}{F} = 0.012\ 6m$

$E_{UDPE} = 0.3730\ GPa \quad L = 0.00136m = 1.36mm$

$L = 2mm$

$E = \frac{FL}{AS} = 0.597\ GPa$

$L = 4mm$

$E = 1.09\ GPa$

Figure A 4 Compliance of comb dies calculations 1

$E_{HDPE} = 100\,ksi = 0.689\,GPa$

$L = \frac{18.343\,\mu m \cdot A \cdot E}{F} = 0.0025\,m = 2.5\,mm$

Adding a plastic buffer makes the system a lot more complicated. Going to check the feasibility of making the moving die slightly thicker than the fixed die.

**B** See previous calculation

$\delta_B = 0.444\,\mu m$

**A** See previous calculation

$\delta_A = 0.657\,\mu m$

**H** Value for now 8/3/16

$\delta_H = 14\,\mu m$

**b** $F = 15\,kN$ $A = 4.11 \times 10^{-3}\,m^2$ $E_{AD} = 203.4\,GPa$

$\delta_b = \delta_H - \delta_B - \delta_A = 14\,\mu m - 0.444\,\mu m - 0.687\,\mu m = 12.869\,\mu m$

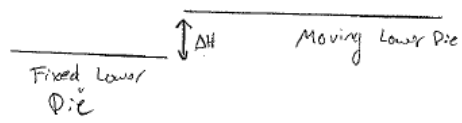


W/o ΔH: $L_b = \frac{\delta_b \cdot A \cdot E_{AD}}{F} = 0.717\,m$

W/ ΔH = 0: $\delta_H = \delta_b$

$\delta_{b'} = \frac{F L_b}{AE}$ $L_b = 24.722\,mm + 12.869\,\mu m$

$= 0.444\,\mu m$

W/ ΔH = 0.0005": $L_b = 24.722\,mm + 0.0005" \cdot 25.4\,\frac{mm}{in} = 24.735\,mm$

$\delta_{b'} = \frac{F L_b}{AE} = 0.443\,\mu m + \delta_b \Rightarrow 0.612\,\mu m$

$\delta_b = 12.869\,\mu m - 0.0005" \cdot 25.4\,\frac{mm}{in} = 0.169\,\mu m$

W/ ΔH = 0.0005": $L_b = 24.722\,mm + 0.00055" \cdot 25.4\,\frac{mm}{in} = 24.736\,mm$

$\delta_{b'} = \frac{F L_b}{AE} = 0.444\,\mu m \Rightarrow -0.657\,\mu m$

$\delta_b = 12.869\,\mu m - 0.00055" \cdot 25.4\,\frac{mm}{in} = -1.101\,\mu m$

W/ ΔH = 0.0006": $L_b = 24.722\,mm + 0.0006" \cdot 25.4\,\frac{mm}{in} = 24.737\,mm$

$\delta_{b'} = \frac{F L_b}{AE} = 0.444\,\mu m \Rightarrow -1.927\,\mu m$

$\delta_b = 12.869\,\mu m - 0.0006" \cdot 25.4\,\frac{mm}{in} = -2.371\,\mu m$

Figure A 5 Compliance of comb dies calculations 2

$F = 12{,}5\ kN$ $A = 4{,}11 \times 10^{-3}\ m^2$ $E_A = 203{,}4\ GPa$ $\Delta H = 0{,}000\,5$ $L_b = 24{,}735\ mm$ rapk 7

$\delta_H = 11\ \mu m$ $\delta_A = \frac{12{,}5\ kN \cdot 36\ mm}{4{,}11 \times 10^{-3}\ m^2 \cdot 200\ GPa} = 0{,}547\ \mu m$ $\delta_B = \frac{12{,}5\ kN \cdot 24{,}735\ mm}{4{,}11 \times 10^{-3} \cdot 203{,}4\ GPa} = 0{,}370\ \mu m$

$\delta_b = 11\ \mu m - 0{,}547\ \mu m - 0{,}370\ \mu m = 10{,}059\ \mu m$ $\delta_{b'} = \frac{F L}{A E} = 0{,}364\ \mu m = 2 \cdot 0{,}280\ \mu m$

$\delta_b = 10{,}059\ \mu m - 0{,}000\,5 \cdot 24{,}735\ mm = -2{,}644\ \mu m$

---

$F = 6{,}25\ kN$ $A = 4{,}11 \times 10^{-3}\ m^2$ $E_B = 203{,}4\ GPa$ $L_b = 24{,}735\ mm + \Delta H$

$\delta_H = 6\ \mu m$ $\delta_A = \frac{6{,}25\ kN \cdot 36\ mm}{4{,}11 \times 10^{-3}\ m^2 \cdot 200\ GPa} = 0{,}274\ \mu m$ $\delta_B = \frac{6{,}25\ kN \cdot 24{,}735\ mm}{4{,}11 \times 10^{-3} \cdot 203{,}4\ GPa} = 0{,}185\ \mu m$

לולאה 1

$\Delta b = \delta_H - \delta_A - \delta_B = 6\ \mu m - 0{,}274\ \mu m - 0{,}185\ \mu m = 5{,}541\ \mu m$ $\Delta H = 0{,}000\,2"$

לולאה 2

$\delta_b = \frac{6{,}25\ kN \cdot (24{,}735\ mm + 0{,}000\,2")}{4{,}11 \times 10^{-3}\ m^2 \cdot 203{,}4\ GPa} = 0{,}220\ \mu m$ $\Delta b = 0{,}000\,2" \cdot 25{,}4 \frac{mm}{in} = 0{,}481\ \mu m$

Figure A 6 Compliance of comb dies calculations 3

# APPENDIX B

# REFERENCE DOCUMENTS

## Cushions and Pressure

### Cushions

Sheffer pioneered tapered cushions, designed to provide gradual deceleration and eliminate shock upon entrance of the cushion pistons, have now been considerably improved. The tapered cushion has been married with a fine thread, wide range, adjusting screw. This new combination offers a positive, low-shock deceleration and a method to adjust the cushioning effect for speeds and loads.

The adjusting screw is identified by a tag affixed to the head (or cap) and can be further distinguished by the fact that it is captivated with the Sheffer exclusive captivator This allows full open to close adjustment without concern for damaging seals.

The cushion check, which does not require adjustment, has a single slot in its head. It does not project beyond the surface of the head (or cap). The cushion check plus the tapered cushion piston provides rapid acceleration out of cushioning. There is no spring in the cushion check to fatigue, hence, no worry of mechanical failure.

Cushioning is designed to properly cushion the cylinder and is not intended to cushion large inertia loads. Cushions do not substitute for speed controls or deceleration valves on most installations.

As indicated on page HH-6, the standard positions for ports are 1 and 5. Where possible, the standard positions for cushion adjusting screws will be 2 and 6 and the standard positions for cushion checks will be 4 and 8. With some mounting styles, it is not possible to so locate the adjusting screws and checks. For example, a Trunnion Front Mount has the trunnion pins located in positions 2 and 4 on the head. With the port in position 1, the only side available for both adjusting screw and check is position 3. Since both will then be located on the same side, they will be located off-center. This example would hold true with the TR, CL, FHF and RHF mounts. See **Chart A** for standard positions that will be supplied unless otherwise specified. When requested, other positions can be supplied so long as there is no interference with mounting.

Where access to an adjusting screw or check could be made difficult because of proximity to a mount, the locations of the screws will be slightly off-center. An example of this would be a small bore cylinder with a side lug mount.

### HH SERIES Cylinder Weight Chart

| BORE | 1 1/8 | 1 1/2 | 2 | 2 1/2 | 3 1/4 | 4 | 5 | 6 | 7 | 8 | 10 | 12 | 14 |
|---|---|---|---|---|---|---|---|---|---|---|---|---|---|
| ZERO STROKE | 3 | 8 | 14 | 19 | 37 | 50 | 90 | 140 | 210 | 290 | 650 | 975 | 1600 |
| ADD PER INCH OF STROKE | .25 | .5 | .8 | 1.3 | 1.8 | 2.5 | 4 | 5.8 | 6.5 | 9 | 16 | 25 | 35 |

Note: The above weights are based on an average value for cushioning, rod size, and the various types of mountings for uncrated cylinders to establish approximate shipping weights. Add 10% of cylinder weight to determine estimate weight of crated cylinder.

### Chart A

| MOUNT | CUSHION ADJUSTING SCREW | CUSHION CHECK |
|---|---|---|
| TF AND FHF | 3 and 6 | 3 and 8 |
| CL | 3 and 7 | 3 and 7 |
| TR AND RHF | 2 and 7 | 4 and 7 |
| ALL OTHER MOUNTS | 2 and 6 | 4 and 8 |

Standard positions for cushion adjusting screws and cushion checks in relation to port positions by style of mounting.

**Position Diagram for Ports, Air Bleeds, Cushion Adjusting Screws and Cushion Checks**

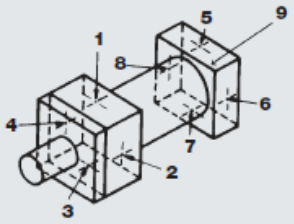


### Chart B
### Maximum Pressure Ratings

| BORE SIZE | HEAVY DUTY SERVICE PSI | MAX. SHOCK SERVICE PSI | 3:1 SAFETY FACTOR (YIELD) PSI |
|---|---|---|---|
| 1 1/8 | 3,000 | 5,000 | 3,612 |
| 1 1/2 | 3,000 | 5,000 | 3,085 |
| 2 | 3,000 | 5,000 | 3,412 |
| 2 1/2 | 3,000 | 5,000 | 2,783 |
| 3 1/4 | 3,000 | 5,000 | 2,842 |
| 4 | 3,000 | 5,000 | 2,667 |
| 5 | 3,000 | 5,000 | 2,778 |
| 6 | 3,000 | 5,000 | 2,760 |
| 7 | 3,000 | 5,000 | 2,558 |
| 8 | 3,000 | 5,000 | 2,391 |
| 10 | 3,000 | 5,000 | 2,936 |
| 12 | 3,000 | 5,000 | 2,549 |
| 14 | 3,000 | 5,000 | 2,443 |

All above figures are based on the cylinder as a pressure vessel. Some styles of mountings will not withstand the thrust generated at these pressures. See information on specific mounts.

Note: Because of space limitations, neither cushion adjusting screws nor cushion ball checks can be put into 1 1/2" and 2" bore sizes for cushioned front when they are specified with 2:1 rod diameters.

### Pressure and Shock

HH SERIES Cylinders are suitable for working pressures to 3,000 psi and maximum pressure including any shock to 5,000 psi. Refer to **Chart B** for the maximum operating pressure that can be used with a 3:1 safety factor based on yield. It is felt that this is an adequate safety factor for any well designed hydraulic system where shock conditions have been considered and reduced to an acceptable level. Not all mounting styles will take the thrust generated at these pressures. See separate Accessories Brochure.

The following factors in shock loading should be considered:

- Relief valves in the circuit do not protect the components from shock because of the time lag.
- Gauges do not necessarily register shock conditions, either because of their position in the circuit, or the short duration of shock.
- The two general types of shock loading to be considered are pressure rise caused by quick stop of the flow in the circuit and quick pressure drop. Decompression shock is particularly important in large bore cylinders and can be as destructive as compression shock.
- The magnitude of the pressure difference and the duration that the maximum pressure exists are the factors that determine the damage from shock.



Figure B 1 Hydraulic safety information

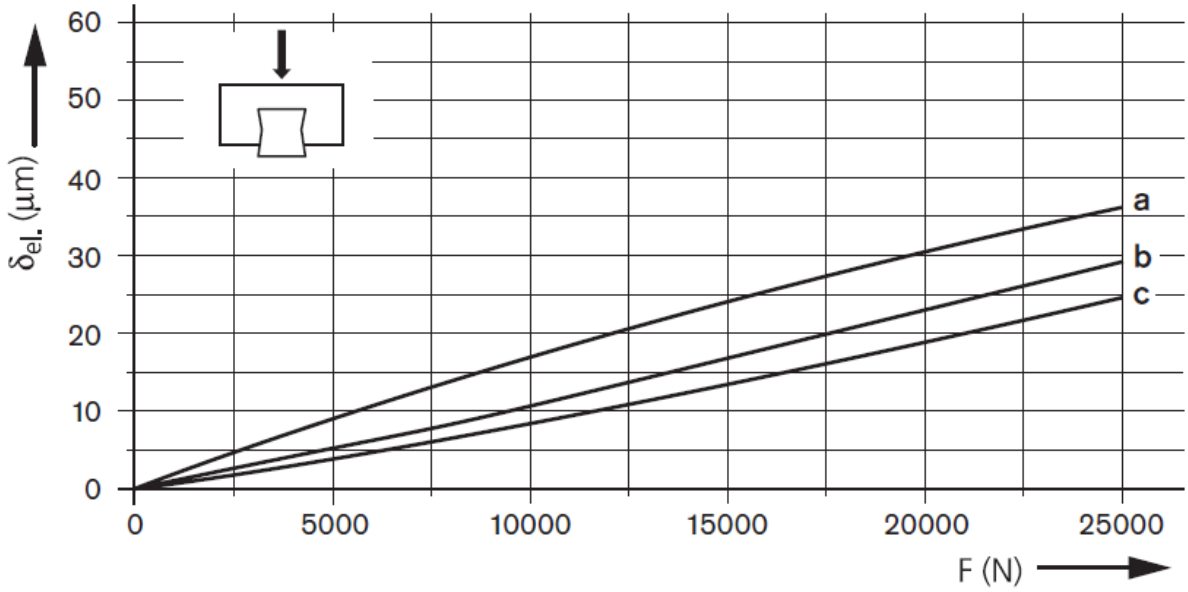


Figure B 2 Bosh Rexroth guide rail information

| Deflection of 21250 Bearing | |
|---|---|
| Load in lbs. | Deflection in inches |
| 10,000 | 0.00073 |
| 20,000 | 0.00173 |
| 30,000 | 0.00204 |
| 40,000 | 0.00270 |
| 50,000 | 0.00332 |
| 60,000 | 0.00393 |
| 70,000 | 0.00457 |

Figure B 3 Tychoway information

# APPENDIX C
# ADDITIONAL MATERIAL RESULTS

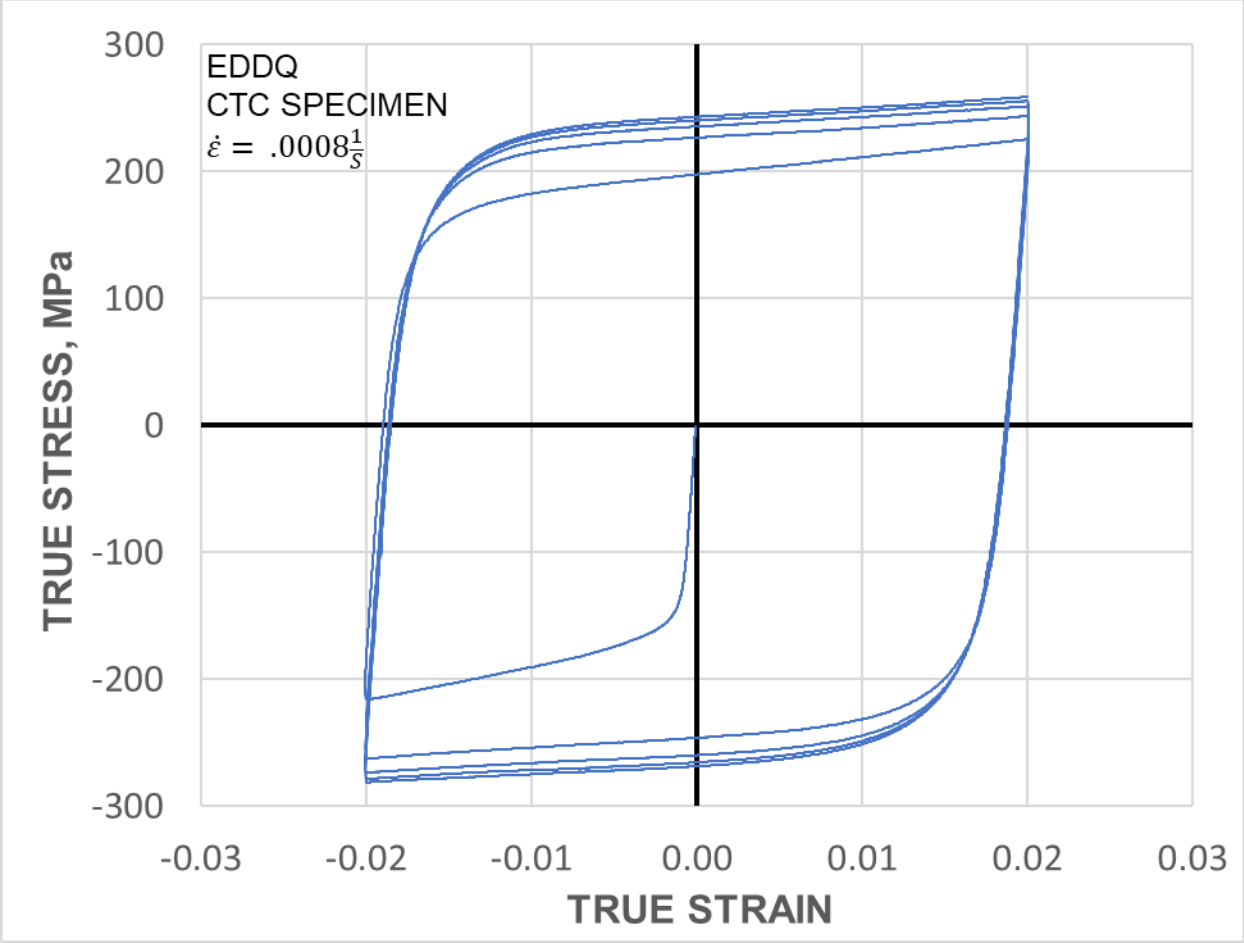


Figure C 1 EDDQ 5x cycle test starting in compression.

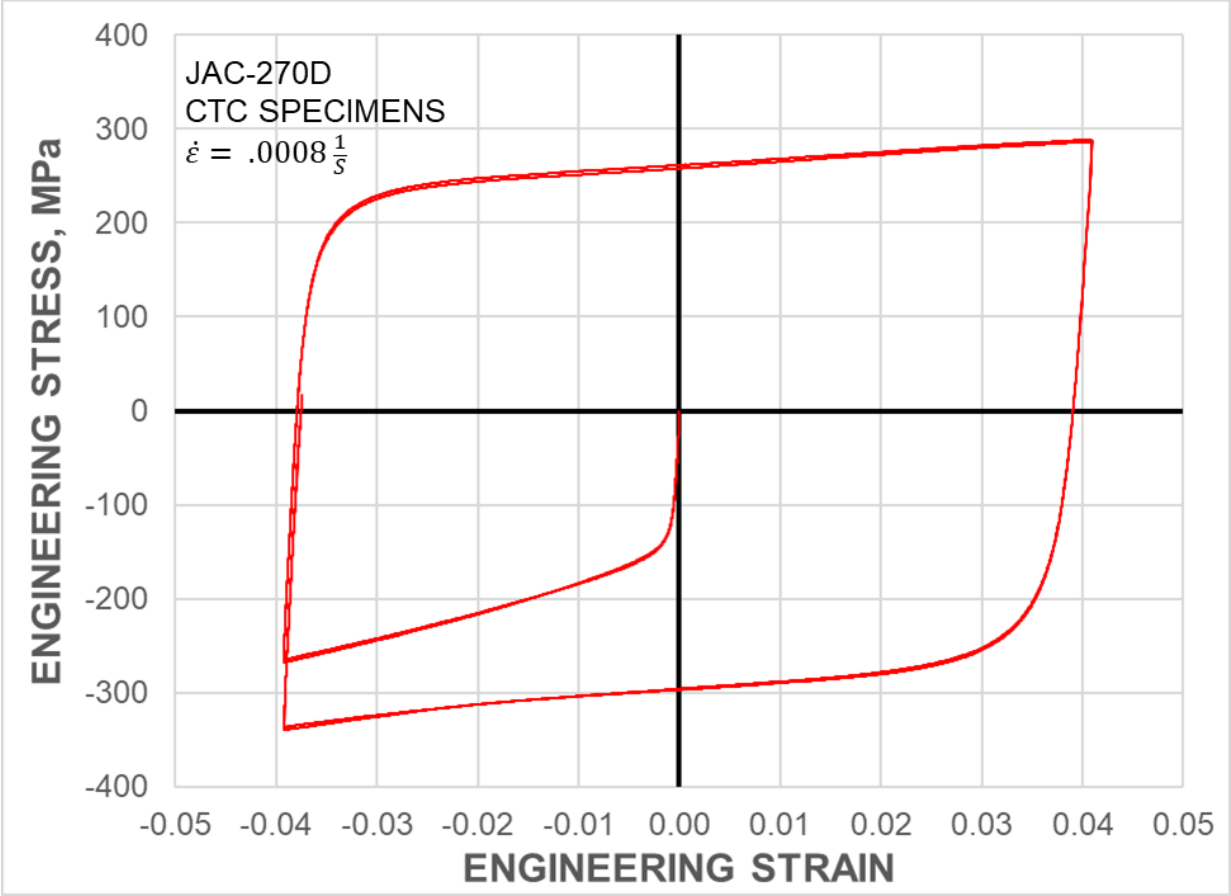

Figure C 2 JAC-270D cycle test starting in compression.

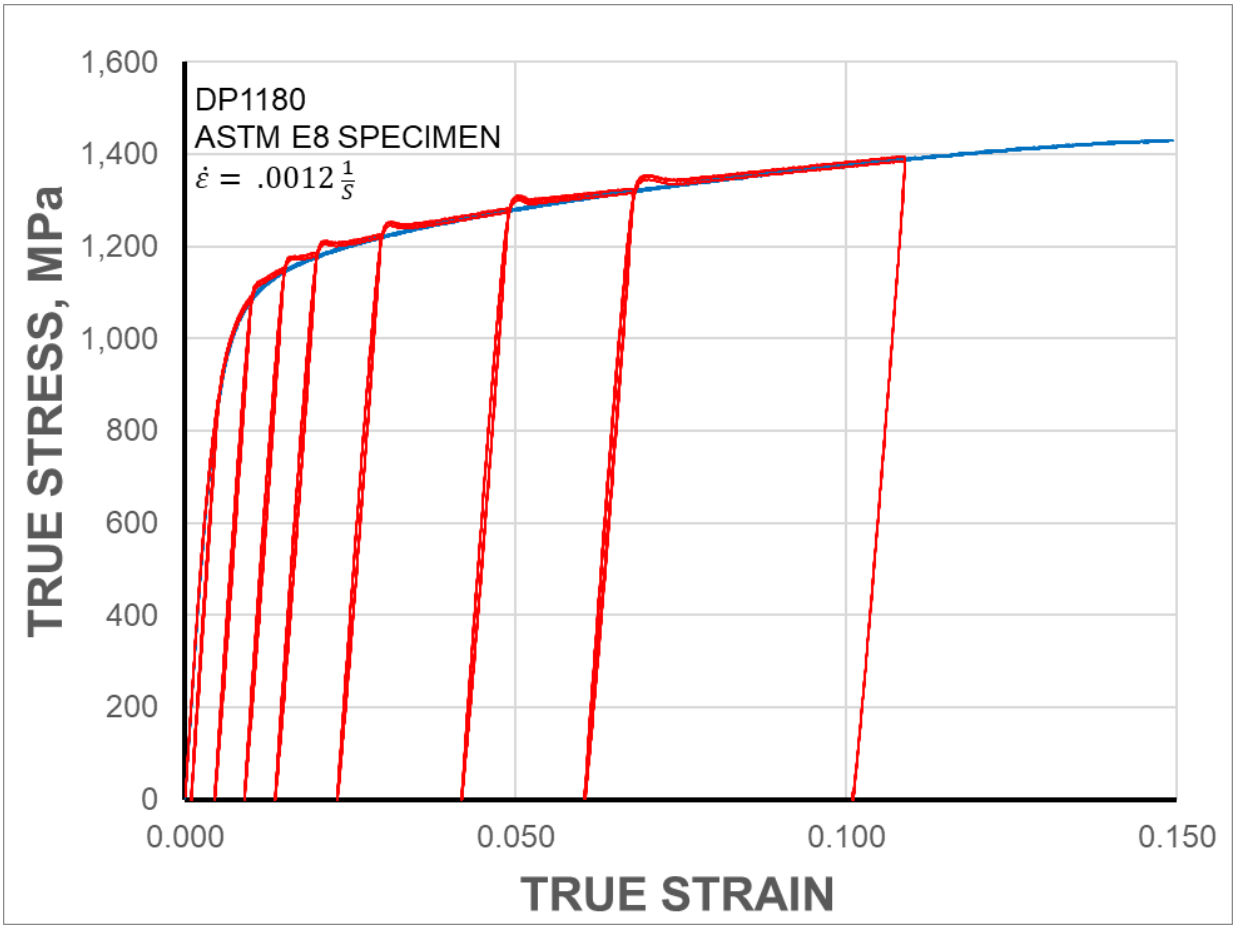

Figure C 3 DP1180 Load-unload test overlayed on tension test.

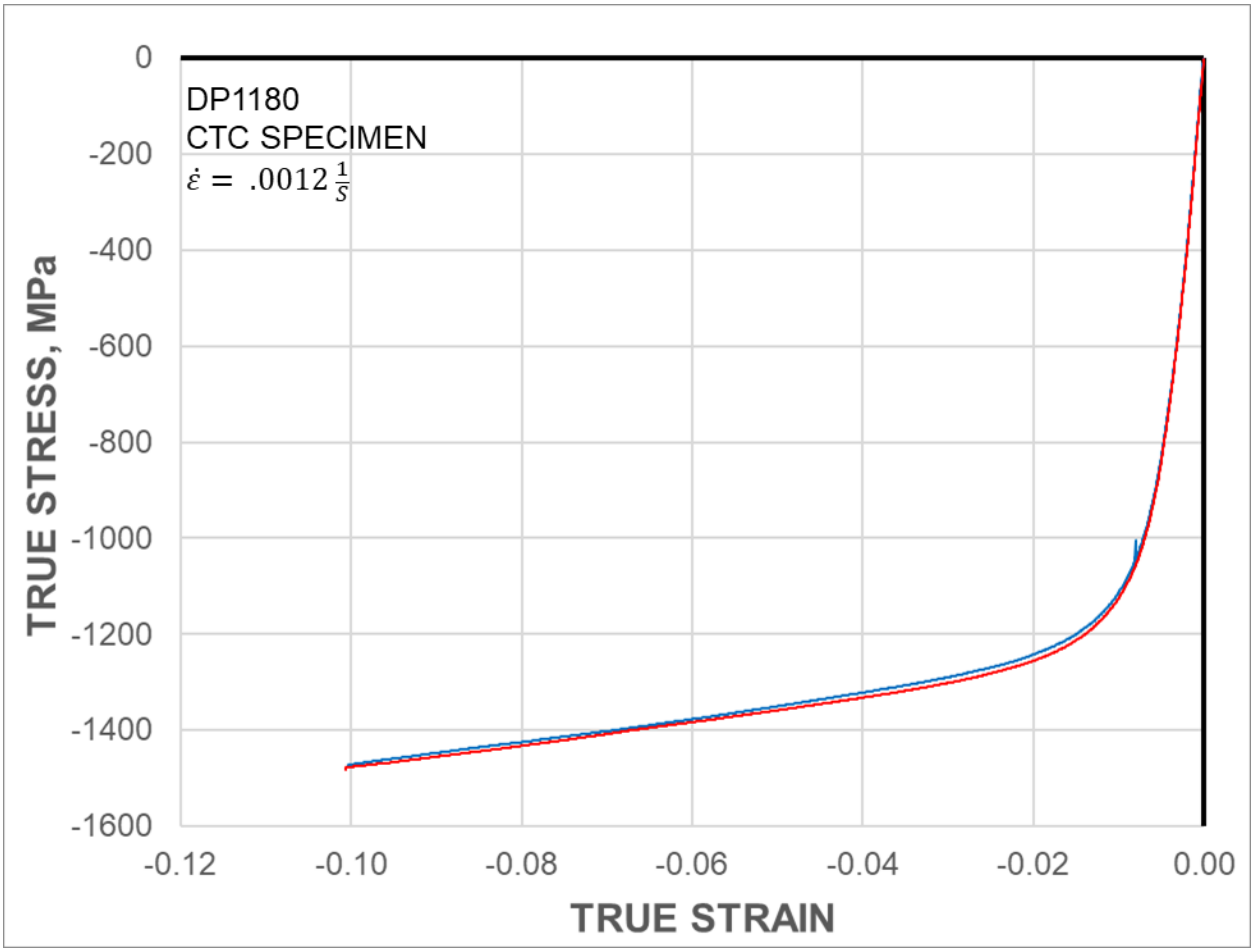


Figure C 4 DP1180 Pure compression test.

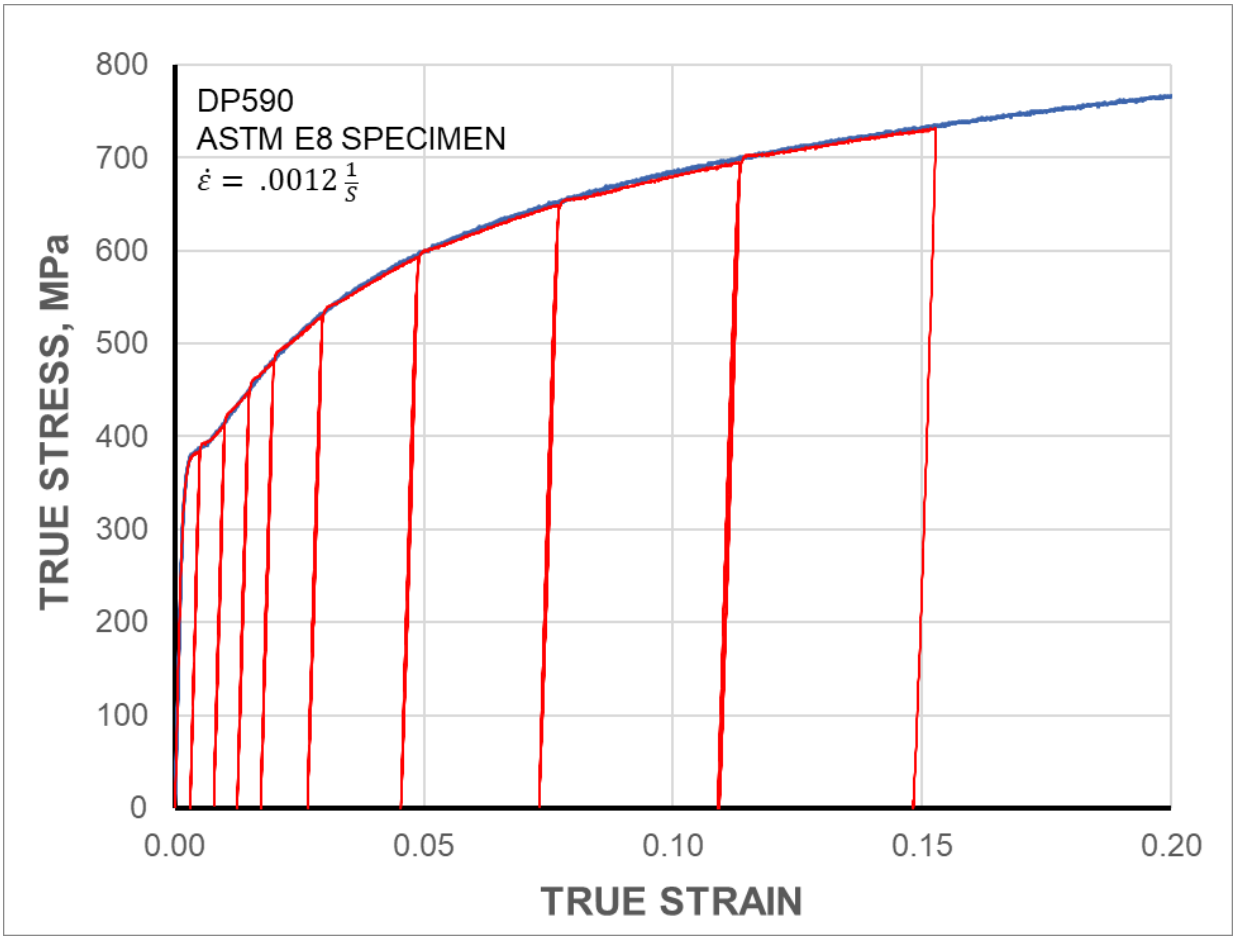


Figure C 5 DP590 Load-unload test overlayed on tension test.

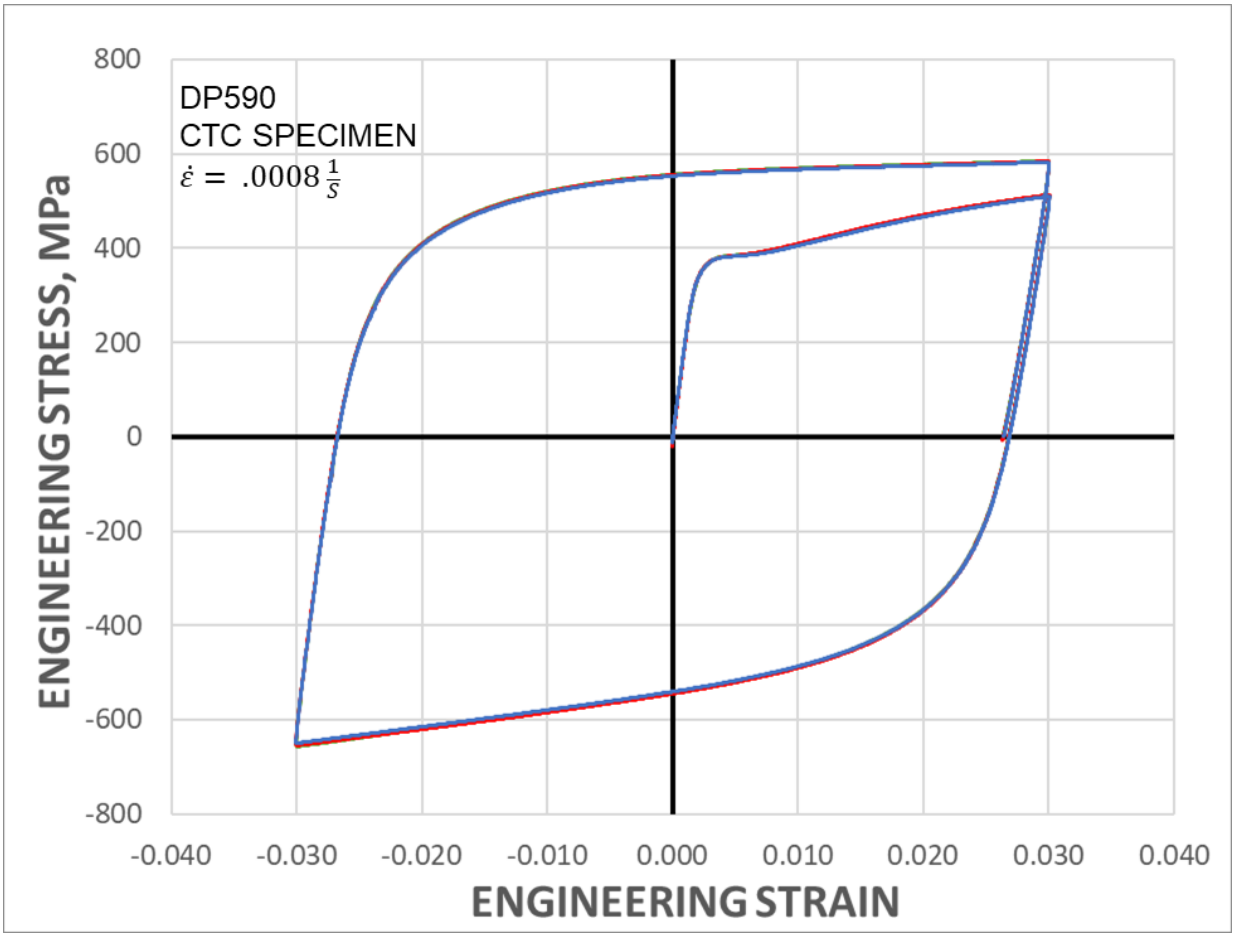


Figure C 6 DP590 1x cycle starting in tension.

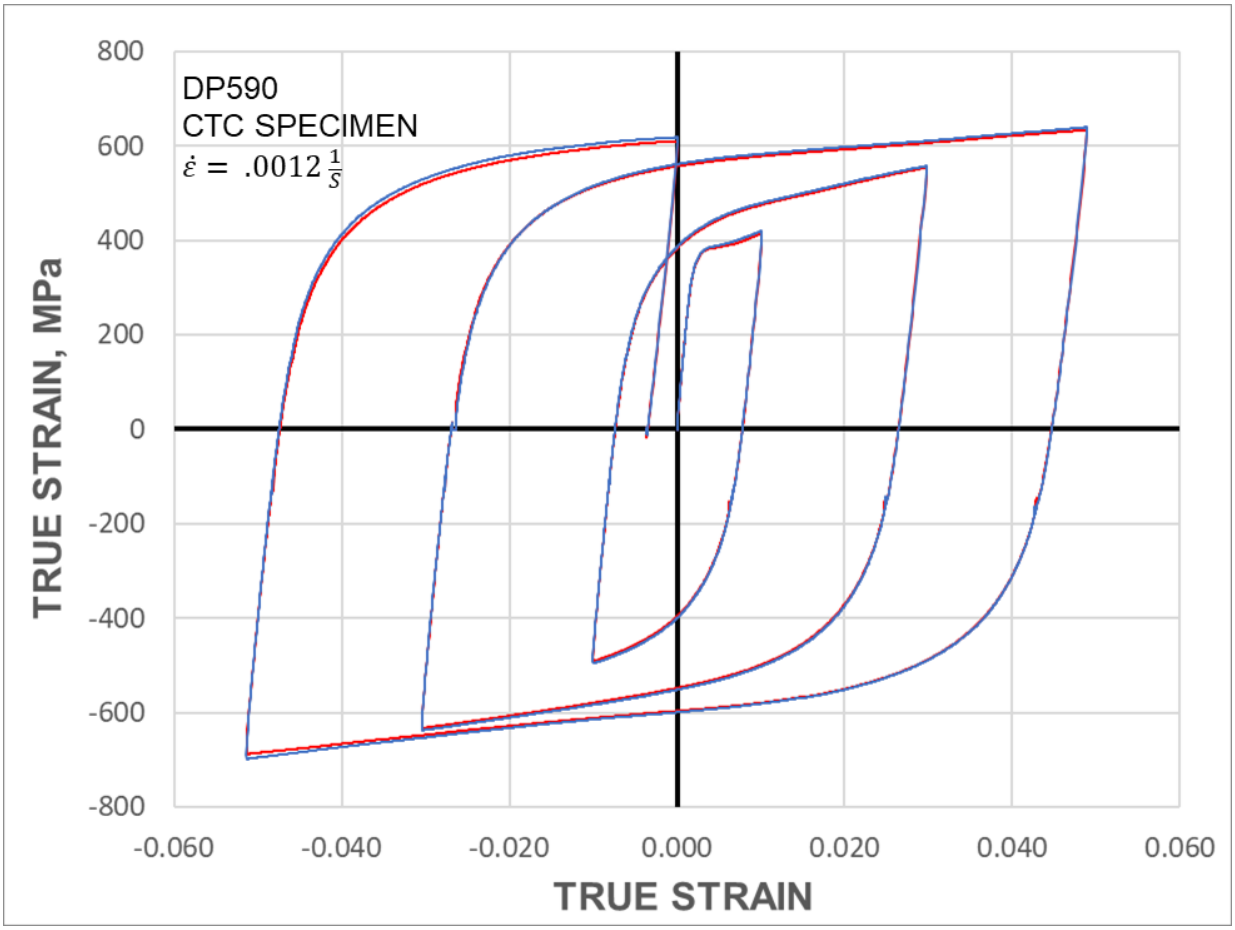


Figure C 7 DP590 Multiple cycle test.